CIMAT Lectures in Mathematical Sciences

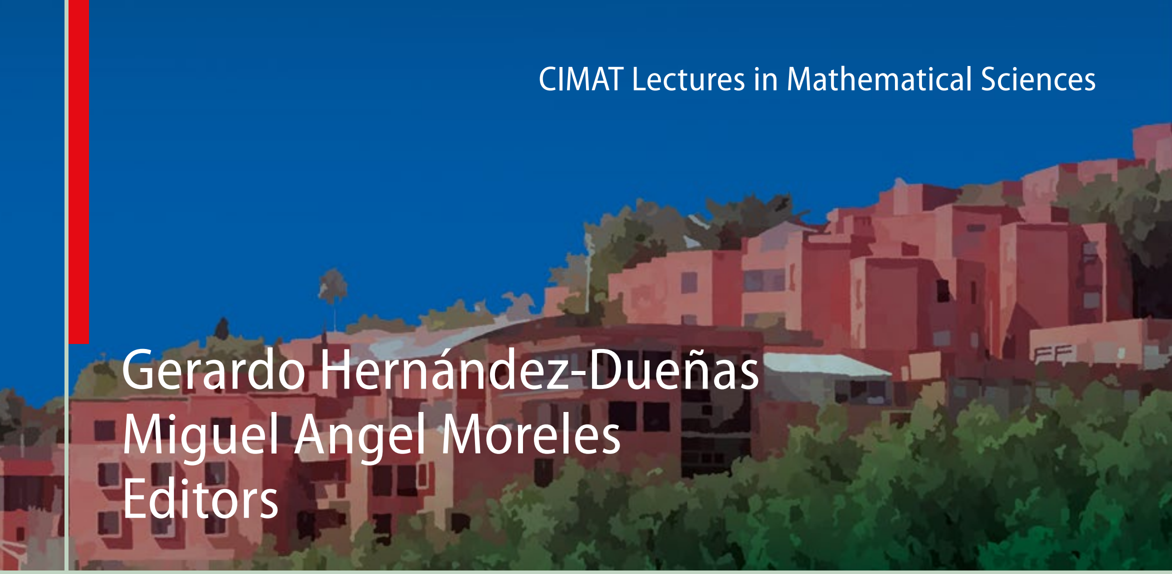

Gerardo Hernández-Dueñas
Miguel Angel Moreles
Editors

Mathematical and Computational Models of Flows and Waves in Geophysics

CIMAT

Birkhäuser

Birkhäuser

CIMAT Lectures in Mathematical Sciences

This series, published by Birkhäuser in collaboration with CIMAT, reports recent developments in mathematics and its applications, including those in computer science, mathematical statistics, economics, biology, etc., which are close to the research fields cultivated at CIMAT. The texts to be considered will be sets of lecture notes on current or new topics with a strong mathematical content, as well as presentations of classic fields from novel perspectives. The volumes can be the product of specialized lecture courses, advanced summer/winter schools, or collaborative efforts by research groups to present various facets of a given field in an insightful and unified manner.

Gerardo Hernández-Dueñas •
Miguel Angel Moreles
Editors

Mathematical and Computational Models of Flows and Waves in Geophysics

Birkhäuser

Editors
Gerardo Hernández-Dueñas
Institute of Mathematics
National Autonomous University of Mexico
Juriquilla, Querétaro, Mexico

Miguel Angel Moreles
Department of Mathematics
CIMAT
Guanajuato, Mexico

ISSN 2731-6521 ISSN 2731-653X (electronic)
CIMAT Lectures in Mathematical Sciences
ISBN 978-3-031-12006-0 ISBN 978-3-031-12007-7 (eBook)
https://doi.org/10.1007/978-3-031-12007-7

© The Editor(s) (if applicable) and The Author(s), under exclusive license to Springer Nature Switzerland AG 2022
This work is subject to copyright. All rights are solely and exclusively licensed by the Publisher, whether the whole or part of the material is concerned, specifically the rights of translation, reprinting, reuse of illustrations, recitation, broadcasting, reproduction on microfilms or in any other physical way, and transmission or information storage and retrieval, electronic adaptation, computer software, or by similar or dissimilar methodology now known or hereafter developed.
The use of general descriptive names, registered names, trademarks, service marks, etc. in this publication does not imply, even in the absence of a specific statement, that such names are exempt from the relevant protective laws and regulations and therefore free for general use.
The publisher, the authors, and the editors are safe to assume that the advice and information in this book are believed to be true and accurate at the date of publication. Neither the publisher nor the authors or the editors give a warranty, expressed or implied, with respect to the material contained herein or for any errors or omissions that may have been made. The publisher remains neutral with regard to jurisdictional claims in published maps and institutional affiliations.

This book is published under the imprint Birkhäuser, www.birkhauser-science.com by the registered company Springer Nature Switzerland AG
The registered company address is: Gewerbestrasse 11, 6330 Cham, Switzerland

Preface

This volume proposes an integral approach to studying the geophysics of Earth. It is motivated by a variety of phenomena from nature with deep and direct impacts in our lives. Such events may evolve across a large range of spatial and time scales and may be observed in the ocean, the atmosphere, the volcanic surface, as well as underground.

The physical laws dictating the evolution of such phenomena lead to the unifying theme of this manuscript, that is, the mathematical and computational modeling of flows and waves. Consequently, the underlying models are given in terms of partial differential equations (PDEs) whose solutions are approximated using numerical methods, thus providing simulations of the aforementioned phenomena, which are to be given the appropriate geophysical validation and interpretation.

The outline of the book is as follows. The first chapter considers rapidly rotating convectively driven flows in extreme parameter regimes, which are of relevance in geophysical and astrophysical settings. The underlying model is the rapidly rotating Rayleigh-Bénard convection (RRRBC) primitive equations. It is well known that laboratory explorations and direct numerical simulations of the governing equations are limited. Consequently, alternative methodologies are required. For instance, the chapter introduces an asymptotic reduction based on small Rossby (Ro) number. The resulting equations, the non-hydrostatic balanced geostrophic equations (NHBGE), form a closed system in which the small parameter Ro no longer appears. The asymptotic procedure eliminates the impediments to using the primitive equations to describe geophysical and astrophysical flows. In particular, the reduced equations describe four important dynamical regimes: cellular convection, convective Taylor columns, convective plumes, and geostrophic turbulence. Some of these are relevant to both astrophysical and oceanographic applications. The latter connects the chapter that follows.

Chapter 2 deals with interactions of the ocean and the atmosphere, with emphasis on wave theory. The chapter is concerned with some important applications related to the influence of ocean surface waves on present challenging issues. One particular issue is the gas transfer across the interface and its potential impact on climate and its changes. Another one is the upper ocean dynamics and the behavior of surface currents and drift, greatly associated with transport of pollutants and objects on the sea surface. It is noteworthy that the chapter develops the underlying theory, complementing it with data to provide insightful information on the air-sea transfer mechanisms. The aim is to obtain the best knowledge in that respect, in order to be able to predict in the most appropriate fashion the ocean-atmosphere exchange processes of greenhouse gases for instance, and in due course to predict climate and its changes through the use of powerful numerical models.

As illustrated by the first two chapters, in recent decades, computational resources have made possible the simulation of complex phenomena. While the first chapter delves into the mathematical physics to understand geophysical flows, the second chapter relies on data and observation. Both use numerical methods to complement their respective theses. It is apparent that an in depth knowledge of these methods is essential. Thus, Chap. 3 provides a state-of-the-art contribution for one of such methods. Namely, the work proposes a second-order accurate and robust numerical method for the conservative level-set approach, which is applied for capturing the interface between two fluids. The first two chapters include problems of this sort. The exposition will appeal to a numerical specialist, and specifics of the method are included. For instance, the time integration is based on a method that allows the selection between complete explicit and implicit first-order time formulations or a second-order Crank-Nicolson (implicit) method. The space discretization is based on a finite-volume method on prisms elements consisting of unstructured triangular grids on the horizontal directions and several layers in the vertical. Numerical results for three-dimensional simulations require significant computational time to be carried out. Thus, the entire code is developed in parallel. The parallelization of the algorithm is based on a domain decomposition into several sub-domains in the horizontal direction, one for each parallel process, and a parallel solution of the linear system using a multi-color SOR (MSOR) method.

The second part of the book deals with problems associated to solid Earth. In Chap. 4, granular flows in volcanic environments are considered. As a primer, continuum models can be used for modeling this flow phenomenon. However, unlike the equations governing Newtonian fluids, such as the Navier-Stokes equations, granular models may require additional terms that take into account frictional and collisional loss of energy both between particles and between the medium and its substrate. Also, they fail to describe phenomena inherent to the granularity of the medium, such as particle-size segregation and high-speed ejection of individual particles. This failure can be of crucial importance when assessing hazard maps for locations prone to rock avalanches and pyroclastic density currents. Consequently, the chapter focuses instead on the description of discrete models. These models take into account the mechanics of individual particles and are used to explain the behavior of granular flows. This approach uses molecular dynamics (MD) algorithms, which first calculate the sum of forces experienced by each of the individual grains, and afterwards solve the equations of motion with an appropriate integrator. The basics of the method are fully described. An application to active volcanoes is presented.

Chapter 5 addresses geophysical exploration of underground resources. The exploration of a region of interest requires the measurements of several geophysical datasets which need to be interpreted for characterization. A scheme for cooperative inversion of seismic and gravity measurements is presented. The seismic method has been particularly successful, becoming the basis for other state-of-the-art methods such as full waveform inversion (FWI). FWI is a powerful seismic-imaging method used to estimate a seismic-velocity model such that the discrepancies between observed and synthetic seismograms are minimized. The gravimetric inversion method is an inversion method (GI) for density estimation. This method is well known for estimating structures with horizontal changes of mass distribution. The solution is straightforward using Gauss-Newton minimization to obtain a density model inverting the square matrix on a single step. This method is widely used by geophysicists because of its fast convergence. However, it is computationally expensive and unfeasible for large-scale problems. Full-waveform inversion (FWI) and gravimetric inversion (GI) are carried out in tandem. First, FWI is used to estimate a seismic-velocity model. Then, using Gardner's density-velocity relationship, GI is performed to update the density model. Again, using Gardner's velocity density relation, a velocity model is obtained and the process is iterated. For FWI, minimization is approximated by a gradient-based algorithm. To compute the gradient, the adjoint state method is used. For the reader's convenience, gravimetric and waveform forward modeling are introduced, as well as the numerical methods of solution. Results are illustrated with the well-known Marmousi model, a highly nontrivial benchmark problem in the literature.

The last chapter deals also with wave phenomena. The motivation is the use of electromagnetic methods in geophysics exploration to map the resistive structure of the subsurface using instruments that work at low induction numbers (LINs). These methods have been successfully applied to archaeological studies, groundwater characterization, contaminant migration, and mineral alteration mapping. To interpret electromagnetic measurements, the electric and magnetic fields are computed by solving numerically the Maxwell's equations in the low induction-number domain. The geophysical applications under study lead to high scale computations. Consequently, the differential forms of Maxwell's equations are solved using the parsimonious finite-difference method. Such method is implemented in Fortran and parallelized with OpenMP.

Acknowledgments The editors thank the Mexican Research Center in Mathematics for its hospitality. Both editors were partially supported by the grants UNAM-DGAPA-PAPIIT IN112222 & Conacyt A1-S-17-634. The co-editor G. H-D would like to thank the hospitality of NorthWest Research Associates and the support of NSF Award 2123740, CTIC and DGAPA during his sabbatical visit.

Juriquilla, Mexico Gerardo Hernández-Dueñas
Guanajuato, Mexico Miguel Angel Moreles

Contents

Geostrophic Turbulence and the Formation of Large Scale Structure

Edgar Knobloch

Abstract This Chapter summarizes recent progress in understanding rapidly rotating convectively driven flows. The emphasis is on the behavior in extreme parameter regimes of relevance in geophysical and astrophysical settings. These regimes are described by an asymptotically reduced system of equations valid in the limit of small Rossby numbers. The equations describe four regimes as a scaled Rayleigh number $\widetilde{Ra}$ increases: a disordered cellular regime near threshold, a regime of weakly interacting convective Taylor columns at larger $\widetilde{Ra}$, followed for yet larger $\widetilde{Ra}$ by a breakdown of the convective Taylor columns into a disordered plume regime characterized by reduced heat transport efficiency, and finally by a turbulent state called geostrophic turbulence. Properties of these states are described and illustrated using direct numerical simulations of the reduced equations. These simulations reveal that geostrophic turbulence is unstable to the formation of large scale barotropic vortices or jets, via a process known as spectral condensation. The details of this process are quantified and its implications explored. The results are corroborated via direct numerical simulations of the governing Navier-Stokes equations. In the presence of lateral boundaries robust boundary zonal flows resembling topologically protected edge states in chiral systems are present.

1 Introduction

Typical flows of astrophysical and geophysical relevance represent a challenge for both laboratory explorations and direct numerical simulations of the governing equations. In rapidly rotating flows this is for two reasons: the very large Reynolds numbers governing such flows, requiring high spatial resolution, and the low values of the Rossby number (equivalently, the Ekman number) for such flows implying the presence of high frequency inertial waves requiring high temporal resolution.

E. Knobloch (✉)
Department of Physics, University of California at Berkeley, Berkeley, CA, USA
e-mail: knobloch@berkeley.edu

G. Hernández-Dueñas, M. A. Moreles (eds.), *Mathematical and Computational Models of Flows and Waves in Geophysics*, CIMAT Lectures in Mathematical Sciences, https://doi.org/10.1007/978-3-031-12007-7_1

These requirements make direct numerical simulation of such flows inaccessible even to state of the art computers. Likewise laboratory experiments, particularly those mounted on a rotating turntable, are limited in size and hence the Reynolds and Rossby numbers that can be reached. These considerations motivate the alternative approach that is explored in this chapter.

Planetary scale rotating flows are described by a very successful theory called quasigeostrophy [42]. Briefly, the theory is based on the idea that large scale, rapidly rotating flows are in approximate geostrophic balance, i.e., that in the low Rossby number regime the Coriolis force is balanced by pressure gradients. This type of balance is seen in everyday weather maps, where air masses circulate counterclockwise or cyclonically around low pressure regions and clockwise or anticyclonically around regions of high pressure. Fluid motions that govern what we call weather develop on top of this balanced flow, and are described by the equations of quasigeostrophy, obtained by going to next order in powers of the Rossby number $\mathrm{Ro} \ll 1$. Here $\mathrm{Ro} = UL/f$, where U represents a typical horizontal flow velocity, L its horizontal scale and f is the local rotation rate at latitude Λ, $f = 2\Omega \sin \Lambda$.

The quasigeostrophic description implies that the flow is horizontal at leading order in Ro, i.e., that the flow is nearly hydrostatic. This type of approximation therefore works well for planetary scale flows in the atmosphere or the oceans such as the Gulf Stream (Fig. 1) but does not apply in regions where vertical, i.e. nonhydrostatic, flows are important [25, 40]. An important example is provided by the regions where the thermohaline circulation descends to the bottom of the ocean, as occurs in the Labrador Sea (Fig. 2). Other situations where the quasigeostrophic description breaks down arise in convectively driven flows since convection is fundamentally nonhydrostatic.

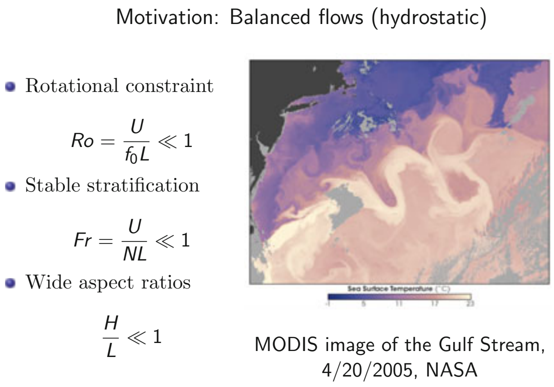

Fig. 1 The quasigeostrophic description applies to large scale flows such as the Gulf Stream

Motivation: Balanced flows (hydrostatic)

- Rotational constraint

$$Ro = \frac{U}{f_0 L} \ll 1$$

- Stable stratification

$$Fr = \frac{U}{NL} \ll 1$$

- Wide aspect ratios

$$\frac{H}{L} \ll 1$$

MODIS image of the Gulf Stream, 4/20/2005, NASA

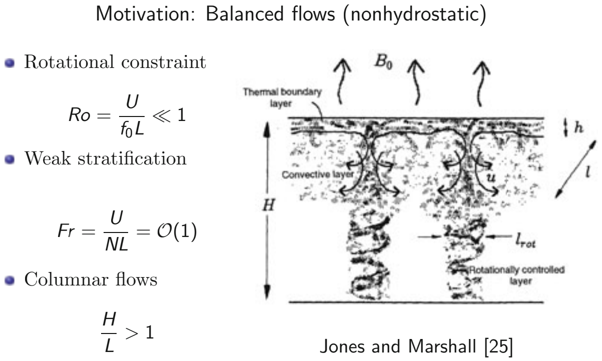

Motivation: Balanced flows (nonhydrostatic)

- Rotational constraint

$$Ro = \frac{U}{f_0 L} \ll 1$$

- Weak stratification

$$Fr = \frac{U}{NL} = \mathcal{O}(1)$$

- Columnar flows

$$\frac{H}{L} > 1$$

Jones and Marshall [25]

Fig. 2 Nonhydrostatic but rotationally constrained flows are present in the Labrador Sea where the thermohaline circulation dives towards the bottom of the ocean

At first sight it appears that nonhydrostatic processes cannot be included within the quasigeostrophic approximation. This is indeed true for large scale phenomena. However, convective forcing generally occurs on smaller scales and we show below that a nonhydrostatic quasigeostrophic description can be developed, that applies to geostrophically balanced flows on these small scales when the corresponding Ro remains small.

Figure 3 shows an example of such a convectively driven flow in the laboratory. The figure shows a side view of a rotating tank experiment, heated from below and cooled from above, and visualized using a liquid crystal suspension with the property that warm regions turn blue and cold regions turn red. The figure shows

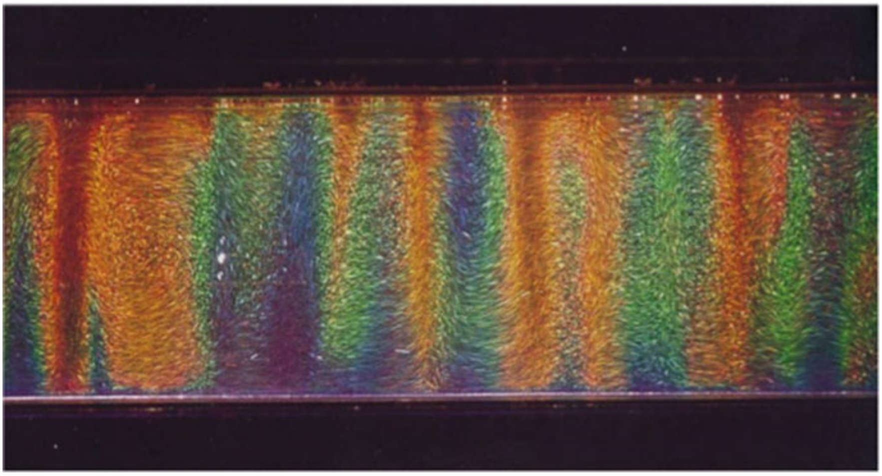

Fig. 3 Side view of a rotating convection experiment with $H = 6\,\text{cm}$, $\Delta T = 2.6\,^\circ\text{C}$, $\Omega = 14.3\,\text{rpm}$. From [45]

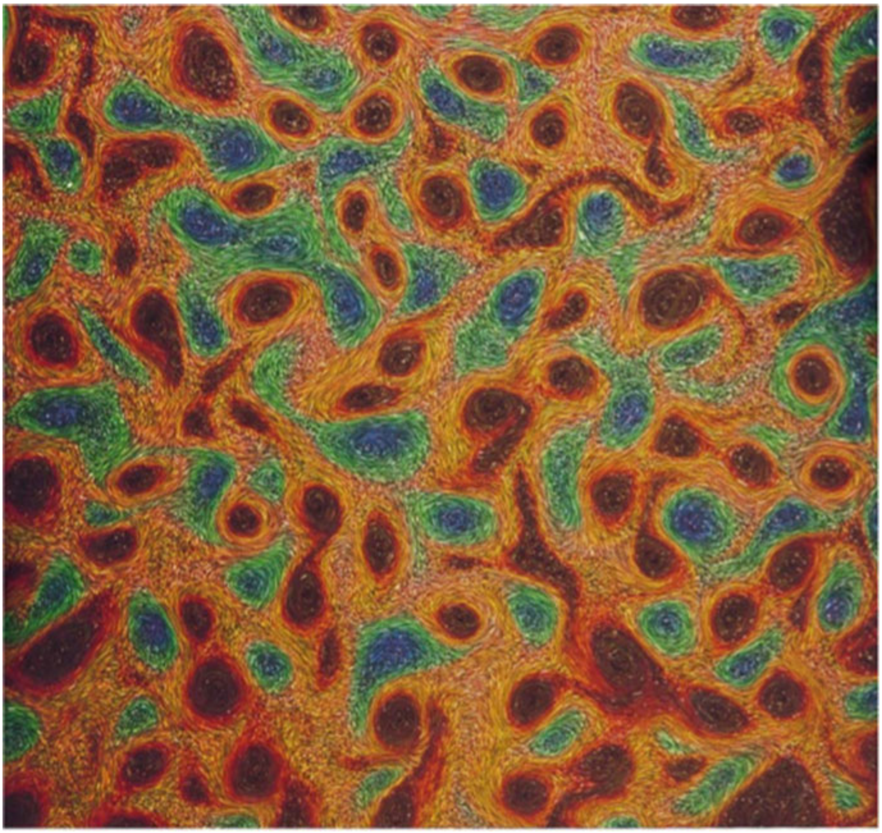

Fig. 4 Top view of the same experiment. From [45]

a snapshot of a state consisting of Taylor-Proudman columns that extend from the bottom to the top (rising warm regions) or from the top to the bottom (descending cold regions). Figure 4 shows a top view, well away from the lateral walls, showing a ‘gas’ of cyclonic (red) and anticyclonic (blue) structures. Observe that cyclonic structures dominate at the top of the layer.

Figure 5 shows the basic parameter plane of the problem for a thermally forced horizontal layer at the North Pole. In (a) we show a log-log plot of the Taylor number $\mathrm{Ta} = \mathrm{E}^{-2}$, proportional to the square of the rotation rate Ω, on the horizontal axis and the Rayleigh number, a dimensionless measure of the temperature difference ΔT across the layer, on the vertical axis. The solid line represents the onset of convective instability in an unbounded layer, $\mathrm{Ra}_c(\mathrm{Ta})$, from [6] and reveals that rotation has a stabilizing effect: a larger Ra is required to generate motion at larger Ta. Panel (b) superposes some of the experiments, including those of Sakai [45] on this plot, providing an indication of the parameter regime that is accessible to laboratory experiments. Geophysical or astrophysical flows are characterized by much larger values of these parameters, in the region of 10^{20}, well outside of the realm of both laboratory experiments and direct numerical simulations (DNS).

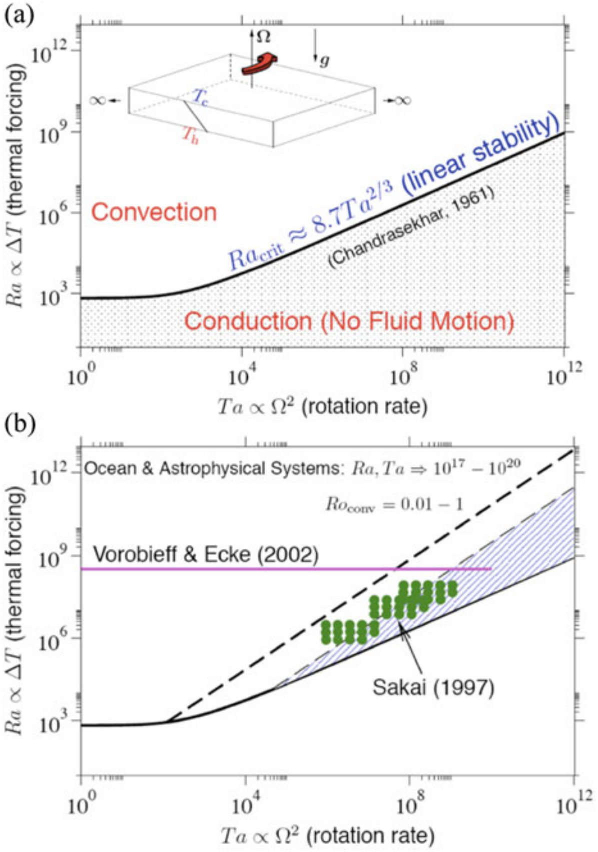

Fig. 5 (**a**) The (Ta, Ra) parameter plane, where $\mathrm{Ta} = E^{-2}$ is the Taylor number and Ra is the Rayleigh number. (**b**) The asymptotic wedge, shaded in blue. In (**b**) the heavy dashed line represents $\mathrm{Ro_{conv}} = 1$ while the thin dashed line represents $\mathrm{Ro_{conv}} = 0.01$. Here $\mathrm{Ro_{conv}} \equiv U_{\rm conv}/\Omega L = \sqrt{\mathrm{Ra}/\sigma}\, E$ is the convective Rossby number, $E \equiv \nu/2\Omega H^2$ is the Ekman number and $\sigma \equiv \nu/\kappa$ is the Prandtl number

Figure 5b shows two lines of constant convective Rossby number $\mathrm{Ro_{conv}}$. Flows with $\mathrm{Ro_{conv}} \lesssim 1$ are beginning to be affected by the presence of rotation, while those for which $\mathrm{Ro_{conv}} \lesssim 0.01$ are strongly impacted, a regime that is difficult to access in the laboratory. In the following we shall be interested in exploring the wedge region shaded in blue corresponding to strongly rotationally constrained flows with $\mathrm{Ra} - \mathrm{Ra}_c = O(1)$, i.e. fully developed flows of this type. Since we are interested in geophysical and astrophysical conditions, we explore this regime in the limit of very large Ra and very large Ta.

2 Asymptotic Reduction of the Primitive Equations

In order to explore this regime we nondimensionalize the primitive equations describing rapidly rotating Rayleigh-Bénard convection (RRRBC) using an arbitrary horizontal length L and an arbitrary horizontal velocity U:

$$\mathbf{u}_t + \mathbf{u}\cdot\nabla\mathbf{u} + \frac{1}{\mathrm{Ro}}\hat{\mathbf{z}}\times\mathbf{u} = -P\nabla p + \Gamma T\hat{\mathbf{z}} + \frac{1}{\mathrm{Re}}\nabla^2\mathbf{u}, \tag{1}$$

$$T_t + \mathbf{u}\cdot\nabla T = \frac{1}{\mathrm{Pe}}\nabla^2 T, \tag{2}$$

$$\nabla\cdot\mathbf{u} = 0, \tag{3}$$

where

$$\mathrm{Ro} = \frac{U}{2\Omega L}, \quad P = \frac{\tilde{P}}{\rho_0 U^2}, \quad \mathrm{Re} = \frac{UL}{\nu}, \quad \mathrm{Pe} = \frac{UL}{\kappa}, \quad \Gamma = -\frac{g\alpha\tilde{T}L}{U^2}. \tag{4}$$

Here $\mathbf{u} \equiv (u, v, w)$ is the velocity field in Cartesian coordinates relative to a frame rotating with angular velocity 2Ω and T is the temperature field (equivalently, the buoyancy field), and the Boussinesq approximation is employed. The dimensionless parameters specifying the system are the Rossby number Ro, the pressure scale P and the buoyancy parameter Γ. Dissipative effects are measured by the Reynolds number Re and the Péclet number Pe. Note that the magnitudes of these parameters depend on the scales of interest, and that Ro is a derived quantity, in contrast to $\mathrm{Ra}_{\mathrm{conv}}$ which may be fixed a priori.

In the following we suppose that $\mathrm{Ro} \equiv \epsilon \ll 1$ and consider scales L for which $L/H = \epsilon$, i.e. tall, thin structures like those revealed in the Sakai experiment. Here H is the dimensional layer depth. Motivated by this choice of L relative to the (presumed fixed) depth H we scale Eqs. (1)–(3) according to

$$\partial_x \to \epsilon^{-1}\partial_x, \quad \partial_y \to \epsilon^{-1}\partial_y, \quad \partial_z \to \epsilon^{-1}\partial_z + \partial_Z, \quad \partial_t \to \epsilon^{-2}\partial_t + \partial_\tau.$$

The slow spatial scale Z is required by the boundary conditions at top and bottom. The fast timescale ϵ^2 is the inertial wave timescale while the $\mathcal{O}(1)$ timescale τ represents the time scale for adjustment of the mean temperature profile.

We now sketch the main steps in the derivation of the reduced equations valid in the limit $\mathrm{Ro} \to 0$. See [28, 29] for a detailed derivation. We suppose that $u \sim v \sim w = \mathcal{O}(1)$ in order to incorporate nonhydrostatic effects, and perform an asymptotic expansion in ϵ with $T = \overline{T} + \epsilon\theta$, and $\Gamma = \mathcal{O}(\epsilon^{-1})$, $P = \mathcal{O}(\epsilon^{-1})$. Here the overbar indicates averaging over $\mathbf{x}$ *and* t, i.e. over fast scales. At $\mathcal{O}(\epsilon^{-1})$ this Ansatz leads to **geostrophic balance**:

$$\hat{\mathbf{z}}\times\mathbf{u}_\perp = -\nabla_\perp p, \quad \nabla_\perp\cdot\mathbf{u}_\perp = 0$$

and hence to

$$\mathbf{u}_\perp = (-\psi_y, \psi_x), \quad \psi \equiv p.$$

Here $\nabla_\perp \equiv (\partial_x, \partial_y)$. Thus the pressure p is nothing but the streamfunction for the horizontal flow, as seen in weather maps.

At $\mathcal{O}(1)$ the vertical vorticity $\omega \equiv \nabla_\perp^2 \psi$ and vertical velocity w satisfy

$$\partial_t \omega + J[\psi, \omega] - \partial_Z w = \mathrm{Re}^{-1} \nabla_\perp^2 \omega, \tag{5}$$

$$\partial_t w + J[\psi, w] + \partial_Z \psi = \Gamma \theta + \mathrm{Re}^{-1} \nabla_\perp^2 w. \tag{6}$$

Here $J[\psi, (\cdot)] \equiv \mathbf{u}_\perp \cdot \nabla_\perp (\cdot)$ represents advection by the horizontal flow. It follows that vertical vorticity is advected by the horizontal flow and intensified by vertical stretching. Vertical velocity is likewise advected but is generated in response to the term $\partial_Z \psi$ which is nothing but the vertical pressure gradient.

At $\mathcal{O}(\epsilon^1)$ we obtain the fluctuating buoyancy equation

$$\partial_t \theta + J[\psi, \theta] + w \partial_Z \overline{T} = \mathrm{Pe}^{-1} \nabla_\perp^2 \theta, \tag{7}$$

and the mean buoyancy equation

$$\partial_\tau \overline{T} + \partial_Z \overline{w\theta} = \mathrm{Pe}^{-1} \partial_{ZZ} \overline{T}. \tag{8}$$

Thus the temperature fluctuation θ is advected horizontally and generated via vertical transport of the mean temperature, while the mean thermal profile adjusts on the slow time τ owing to a nonzero divergence of the vertical convective heat flux. In each equation the error is $\mathcal{O}(\mathrm{Ro})$ and so becomes asymptotically small as $\mathrm{Ro} \to 0$.

The above equations arise as solvability conditions for a sequence of linear inhomogeneous problems on the fast scale together with the requirement of impenetrable boundaries at top and bottom. The latter imply that the fast scale z drops out in the leading order description of the flow. The resulting equations form a *closed* system in which the small parameter Ro no longer appears, thereby relaxing spatial resolution requirements, since Ekman boundary layers no longer need to be resolved, as well as temporal resolution requirements since high frequency inertial waves are no longer present. In other words, the asymptotic procedure sketched above eliminates the primary impediments to using the primitive equations to describe geophysical and astrophysical flows. Moreover, it appears that the adopted scaling of the dependent fields together with the choice of the horizontal scale L are uniquely determined by the closure requirement.

The above equations have a broad regime of applicability: $\mathrm{Ro} \ll 1$. This regime includes a wide range of horizontal scales L but for laboratory applications it is useful to connect these equations to the predictions of linear theory. Since these are determined by dissipative processes we choose $\mathrm{Ro} = E^{1/3}$, where $E = \nu/2\Omega H^2$ is the Ekman number, so that L/H takes its onset value $L/H = O(E^{1/3})$ [6], and take $U = \nu/L$ to obtain the rescaled system

$$\partial_t \omega + J[\psi, \omega] - \partial_Z w = \nabla_\perp^2 \omega + O(E^{1/3}) \tag{9}$$

$$\partial_t w + J[\psi, w] + \partial_Z \psi = \sigma^{-1} \mathrm{Ra} E^{4/3} \theta + \nabla_\perp^2 w + O(E^{1/3}) \tag{10}$$

$$\partial_t \theta + J[\psi, \theta] + w \partial_Z \overline{T} = \sigma^{-1} \nabla_\perp^2 \theta + O(E^{1/3}) \tag{11}$$

$$\partial_\tau \overline{T} + \partial_Z \overline{w\theta} = \sigma^{-1} \partial_{ZZ} \overline{T} + O(E^{1/3}), \tag{12}$$

where $\mathrm{Ra} \equiv g\alpha \Delta T H^3/\nu\kappa$ is the usual Rayleigh number and $\sigma \equiv \nu/\kappa$ is the Prandtl number; for consistency we assume that $\mathrm{Ra}E^{4/3} = O(1)$, $\sigma = O(1)$. These equations are to be solved subject to the boundary conditions

$$w = \psi_Z = \theta = 0, \quad \overline{T} = 1, \quad \text{on} \quad Z = 0, \tag{13}$$

$$w = \psi_Z = \theta = 0, \quad \overline{T} = 0, \quad \text{on} \quad Z = 1, \tag{14}$$

obtained by applying the same asymptotic expansion to the boundary conditions. Note that the resulting boundary conditions are stress-free implying that Ekman pumping from the boundaries becomes subdominant in this regime [33]. In the following we solve these equations with periodic boundary conditions (PBC) in the horizontal.

The equations constitute a **closed reduced system** referred to as NHBGE (non-hydrostatic balanced geostrophic equations). In contrast to the primitive equations they depend on the Rayleigh number and the Ekman number only in the combination $\widetilde{Ra} \equiv \mathrm{Ra}E^{4/3}$, assumed to be $O(1)$. In the asymptotic wedge Ra is large to overcome the stabilizing effects of rotation, while E is small.

2.1 *Properties of the NHBGE*

The NHBGE have the following beneficial properties: they

- eliminate thin Ekman boundary layers; thermal layers remain
- filter out fast inertial waves on $O(E^{1/3}H)$ vertical scales as can be seen from the inviscid dispersion relation for isothermal modes $\propto \exp i(\lambda t + \mathbf{k}_\perp \cdot \mathbf{x}_\perp + k_z Z)$:

$$\lambda^2_{\text{reduced}} = \frac{k_z^2}{k_\perp^2}, \qquad \text{cf.} \quad \lambda^2_{\text{NS}} = \frac{k_z^2}{k_\perp^2 + E^{2/3} k_z^2}.$$

- predict the correct critical Rayleigh number Ra_c and onset wavelength λ_c appropriate to the limit $E \to 0$, viz., $\mathrm{Ra}_c \approx 8.6956E^{-4/3}$ and $\lambda_c \approx 4.8154E^{1/3}H$ for steady onset [6].

These facts allow us to integrate the NHBGE with less resolution and much larger time step than required when solving the primitive equations. In the following we report on the solutions of these equations on a domain of nondimensional size $20\lambda_c \times 20\lambda_c \times 1$ with PBC in the horizontal plane and the boundary conditions (13) and (14) in the vertical. To solve the equations the horizontal directions were discretized using Fourier-Galerkin modes in the x and y directions. The vertical direction was treated using Chebyshev-tau discretization [19] allowing for an efficient clustering of gridpoints in the remaining thermal boundary layers near the top and bottom of the fluid layer. All directions were dealiased using the standard 2/3 rule. Integration in time was done using the semi-implicit Runge–Kutta scheme developed in [50], which is formally third-order accurate in time for the nonlinear terms and second-order accurate for the linear terms. However, the parameters were chosen to minimize the coefficient of the second-order error and in practice the method yields third-order accuracy in time. In all cases the computations were initialized using either a small amplitude random temperature fluctuation θ or a small amplitude unstable roll pattern.

Note that the NHBGE

- describe asymptotically precisely the fluid problem even though they do not look like the primitive equations
- are fully three-dimensional
- are fully nonlinear
- moreover, they are $D_4\dot{+}T^2$-symmetric, i.e., the equations are equivariant under translations in the x and y directions (modulo the spatial period) together with invariance under $x \leftrightarrow -x$ and $x \leftrightarrow y$. It follows there is no handedness to the flow at leading order. Thus the number of cyclonic and anticyclonic vortices is expected to be the same as $E \to 0$, unless *spontaneous* symmetry-breaking leads to the prevalence of one or other vortex type.

Two additional properties are useful. For the Prandtl numbers considered here the system rapidly equilibrates to a statistically steady state with $\partial_\tau \overline{T} \approx 0$ although this mean state may drift over long times owing to the formation of large scale structures. In the equilibrated state Eq. (11) yields the relation

$$\overline{w\theta}\partial_Z\overline{T} = -\frac{1}{\sigma}\overline{|\nabla_\perp\theta|^2}, \tag{15}$$

while (12) yields

$$\frac{1}{\sigma}\partial_Z\overline{T} = \overline{w\theta} - \frac{\mathrm{Nu}}{\sigma}, \tag{16}$$

where Nu is the Nusselt number, i.e. the total heat flux across the layer normalized by the flux which would be achieved in the absence of motion. These two equations provide an exact relation between the gradient of the mean temperature $\partial_Z\overline{T}$, the thermal dissipation rate $\overline{|\nabla_\perp\theta|^2}$, and Nu,

$$\partial_Z\overline{T} = -\frac{1}{2}\mathrm{Nu} \pm \frac{1}{2}\left[\mathrm{Nu}^2 - 4\overline{|\nabla_\perp\theta|^2}\right]^{1/2}. \tag{17}$$

This result provides an upper bound for the thermal dissipation rate, namely $\overline{|\nabla_\perp\theta|^2} \leq \mathrm{Nu}^2/4$. For sufficiently supercritical Rayleigh numbers, the $-$ sign describes the dynamics in the thermal boundary layer while the $+$ sign describes the well-mixed bulk; the transition between the two must therefore occur where $\overline{|\nabla_\perp\theta|^2} = \mathrm{Nu}^2/4$. This relation determines the width of the thermal boundary layers at the top and bottom but is special to rapidly rotating convection. In nonrotating Rayleigh-Bénard convection (16) is replaced by

$$\overline{w\theta}\partial_Z\overline{T} + \frac{1}{2}\partial_Z\overline{w\theta^2} = -\frac{1}{\sigma}\overline{|\nabla_\perp\theta|^2} + \frac{1}{\sigma}\overline{\theta\partial_Z^2\theta}$$

and this relation is *not* closed and no similar characterization holds.

In addition, the NHBGE admit exact single mode solutions of the form $(\psi, w, \theta) = \mathrm{Re}\{(\sigma^{-1}A(Z), \sigma^{-1}B(Z), C(Z))\exp i\mathbf{k}_\perp\cdot\mathbf{x}\}$, where [26, 27]

$$\frac{d^2B}{dZ^2} - k_\perp^2\mathrm{Nu}\widetilde{Ra}B\left(1 + \frac{1}{2k_\perp^2}|B|^2\right)^{-1} = 0; \quad \mathrm{Nu}^{-1} = \int_0^1\left(1 + \frac{1}{2k_\perp^2}|B|^2\right)^{-1}dZ.$$

This is a nonlinear eigenvalue problem for the Nusselt number Nu given $\widetilde{Ra}$ which can be used to generate highly nonlinear (but unstable!) states for large $\widetilde{Ra}$ as shown in Fig. 6.

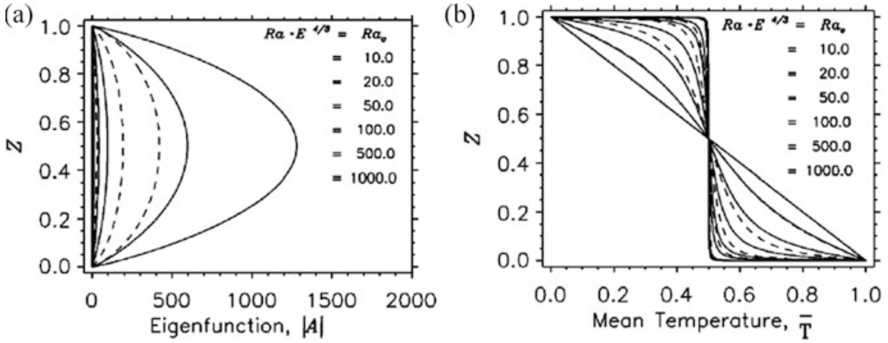

Fig. 6 (**a**) The eigenfunction $|B(Z)|$ and (**b**) the mean temperature profile $\overline{T}(Z)$ for square pattern convection at different values of $\widetilde{Ra} \equiv \mathrm{Ra}E^{4/3}$. Dashed lines show the results for steady convection with $k_c = |\mathbf{k}_\perp| = 1.3048$ while solid lines show the corresponding results for oscillations in the form of standing squares at $\sigma = 0.4574$ and $k_c = 0.8867$. Oscillatory convection with PBC in a plane is only present for $\sigma < \sigma^* \approx 0.676605$ [10] and is therefore omitted from what follows. From [27]

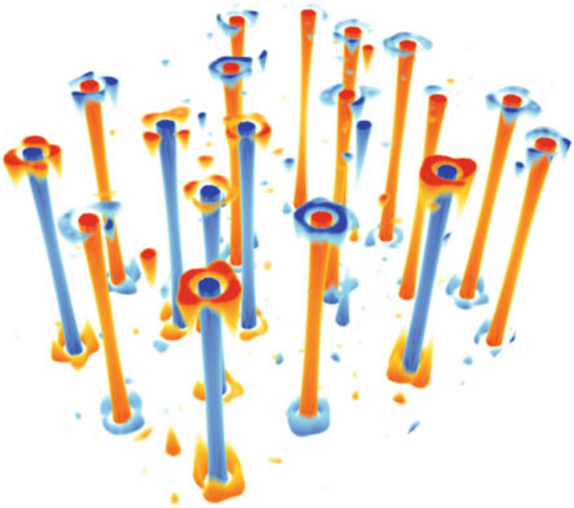

Fig. 7 Snapshot of the temperature fluctuation θ in the low Rossby number regime. Hot (red) and cold (blue) convective Taylor columns span the entire depth of the layer but are shielded by a sheath in which θ takes the opposite sign. Parameters: $\widetilde{Ra} = 40$, $\sigma = 7$. From [20]

The reduced equations describe four distinct dynamical regimes, depending on the values of the scaled Rayleigh number $\widetilde{Ra}$ and the Prandtl number σ [32, 51]:

- Cellular convection (C)
- Convective Taylor columns (T)
- Convective plumes (P)
- Geostrophic turbulence (G)

Nonlinear but cellular convection is the first state that appears as $\widetilde{Ra}$ crosses the instability threshold. With increasing $\widetilde{Ra}$ this state organizes into unsteady Taylor-Proudman columns that extend across the whole depth. These columns are *shielded* [20] as shown in Fig. 7; a similar nonmonotonic profile is also present in the vertical vorticity implying reduced mutual advection, i.e. the Taylor columns resemble a two-dimensional gas of weakly interacting particles. Upon further increase in $\widetilde{Ra}$ these columns begin to break up into plumes that no longer extend across the layer, and these eventually give rise to a state of geostrophic turbulence [7], i.e. turbulence characterized by geostrophic balance on all inertial scales. The associated regime diagram is shown in Fig. 8 with sample snapshots of the corresponding solutions shown in Fig. 9.

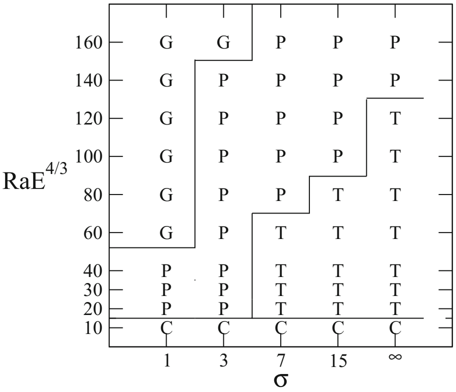

Fig. 8 Regime diagram, showing the approximate boundaries between cellular convection (C), Taylor columns (T), convective plumes (P) and geostrophic turbulence (G). From [32]

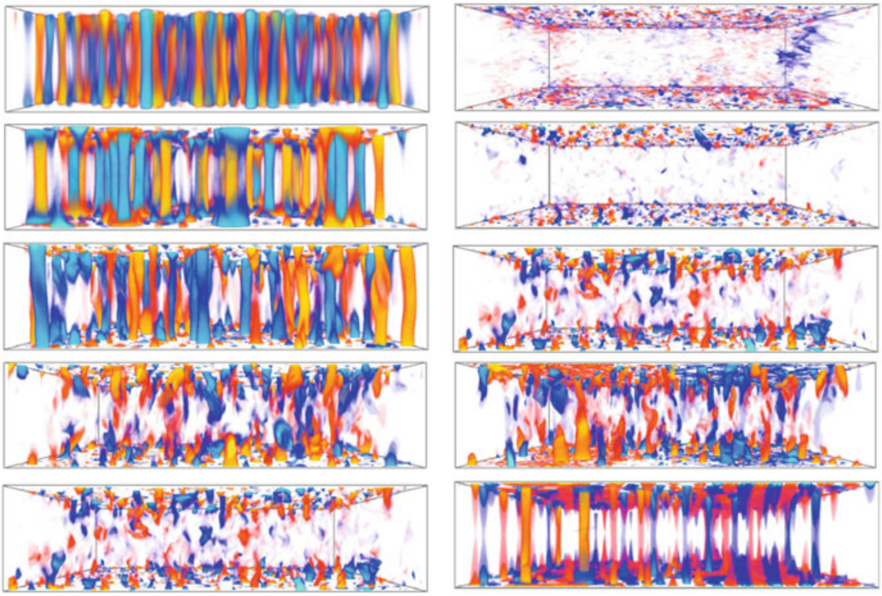

Fig. 9 Volume renders of the temperature fluctuation θ for $\widetilde{Ra} = 20, 40, 80, 120, 160$ and $\sigma = 7$ (left) and $\widetilde{Ra} = 160$ and $\sigma = 1, 3, 7, 15, \infty$ (right). From [32]

3 Spontaneous Formation of Large Scale Vortices

One of the more remarkable predictions of the NHBGE is the spontaneous appearance of large scale vortices from geostrophic turbulence. The first indication of this highly significant phenomenon came in the form of a slow drift in the

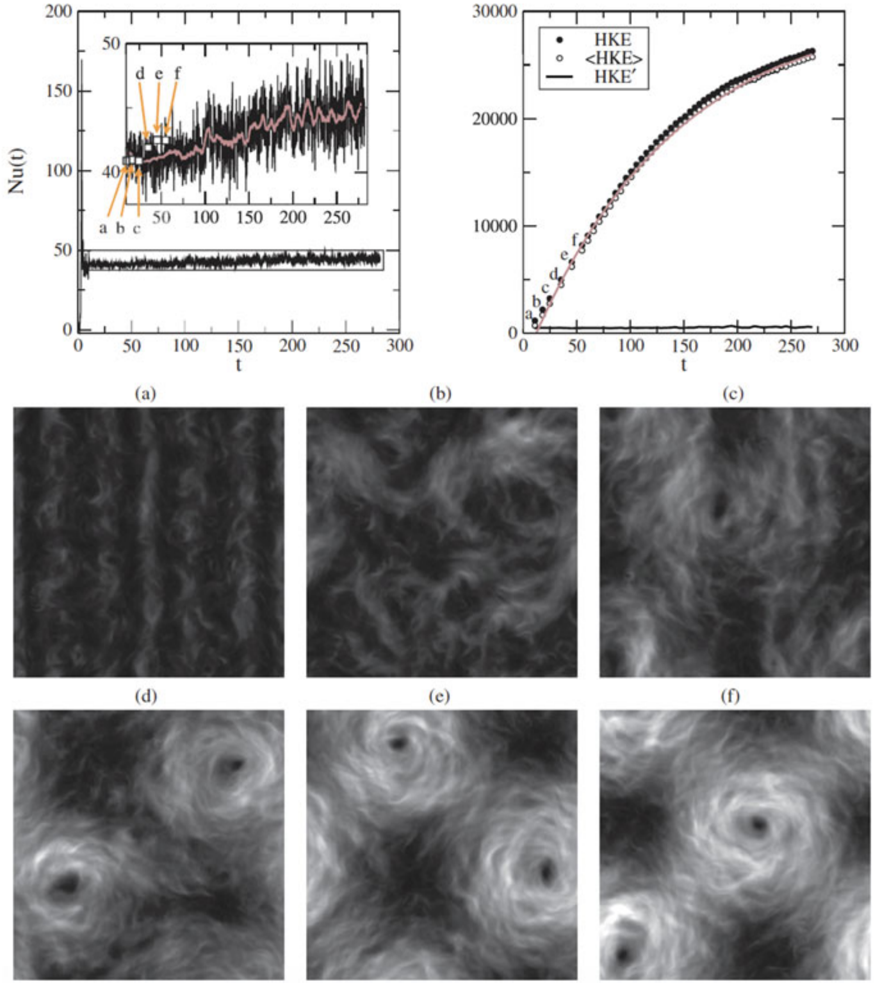

Fig. 10 Emergence of large scale vortex structures from geostrophic turbulence. Top left: Nusselt number drift. Top right: Growth of the horizontal kinetic energy $(u^2 + v^2)/2$ (HKE). Lower panels: Snapshots of the midplane HKE at the six different times indicated in the top right panel. Parameters: $\widetilde{Ra} = 100$, $\sigma = 1$. From [32]

Nusselt number with time (Fig. 10a). Further examination revealed that this drift is associated with the formation of a pair of large scale vortices (LSV) that slowly emerge from the turbulent background as the computation proceeds (Fig. 10b). The LSV are turbulent vortex structures that span the depth of the layer (Fig. 11), i.e., they represent two-dimensional coherent structures embedded in the background geostrophic turbulence. The LSV do not form via mergers of smaller vortices, but instead appear to suck energy directly from the small scales, bypassing the turbulent energy cascade (Fig. 12). Indeed, it appears that the RRRBC system

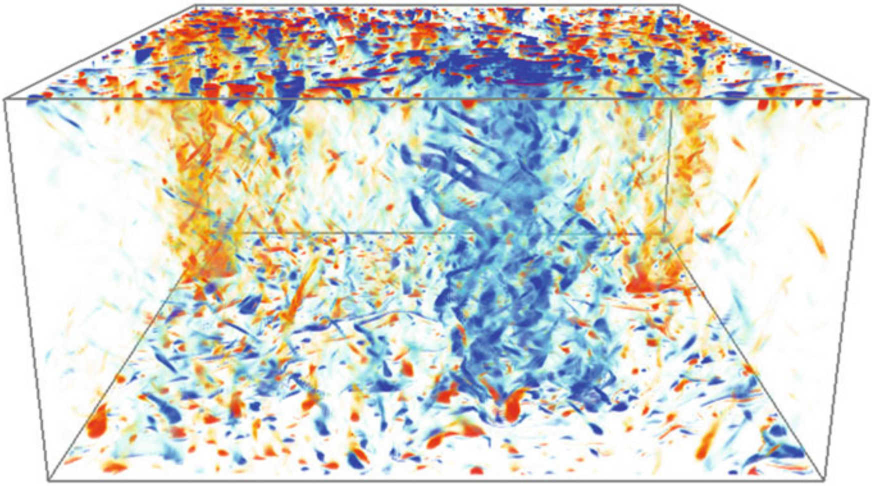

Fig. 11 Three-dimensional rendering in θ of a pair of large scale vortices in a geostrophic turbulence background. Parameters: $\widetilde{Ra} = 100$, $\sigma = 1$. From [44]

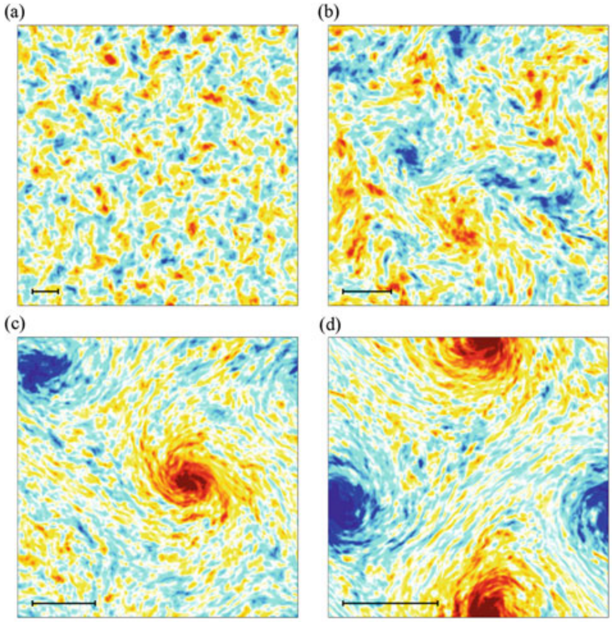

Fig. 12 Large scale vortices in a geostrophic turbulence background at (**a**) $t = 1$, (**b**) $t = 10$, (**c**) $t = 37.5$, (**d**) $t = 100$. From [44]

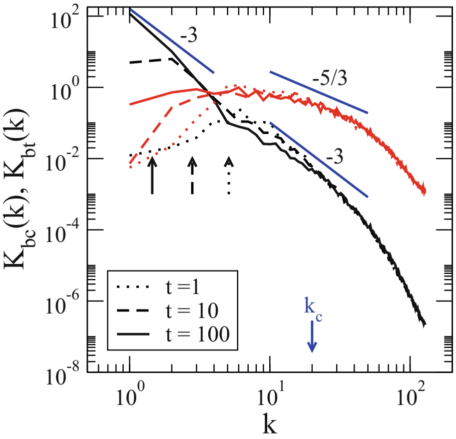

Fig. 13 Spectra of the kinetic energy in the two-dimensional barotropic mode, $K_{\rm bt}(k_\perp)$ (black), and in the three-dimensional baroclinic fluctuations, $K_{\rm bc}(k_\perp)$ (red), both at three different times. The arrows indicate the dominant barotropic mode in each case. From [44]

exhibits a split cascade [1, 41]: three-dimensional baroclinic fluctuations exhibit a forward energy cascade characterized by a Kolmogorov $k_\perp^{-5/3}$ spectrum. The two-dimensional barotropic ($k_z = 0$) component in contrast exhibits a $k_\perp^{-3}$ forward enstrophy cascade, but a $k_\perp^{-5/3}$ inverse cascade to large scales (Fig. 13) as expected of two-dimensional turbulence [3]. The latter is masked by the gradual appearance of the LSV which are also associated with a $k_\perp^{-3}$ energy spectrum [48]. Because of the spontaneous formation of the LSV the peak wavenumber of the barotropic mode migrates to ever larger scales (Fig. 13), eventually reaching domain size. In our calculations, which use PBC, the growing LSV ultimately interact with their images, leading to strong shears that presumably arrest their growth, but our system has not been integrated long enough to see and study this state. If the domain size is increased the LSV size increases accordingly, i.e. the LSV have no characteristic scale and energy piles up at the smallest available wavenumber, in a process that has been called spectral condensation [38]. See also [1, 8, 44, 55, 57, 58].

To understand this process better we decompose the vertical vorticity equation (9) into its barotropic and baroclinic components. Let $\omega = \langle\omega\rangle + \omega'$, $\psi = \langle\psi\rangle + \psi'$, where $\langle \dots \rangle$ denotes a depth average. Thus $\langle\omega\rangle$ represents the 2D part of the vertical vorticity while ω' represents zero vertical mean 3D vorticity. We refer to the former as the barotropic mode and the latter as the baroclinic mode. It follows that

$$\langle\omega\rangle_t + J[\langle\psi\rangle, \langle\omega\rangle] + \langle J[\psi', \omega']\rangle = \nabla_\perp^2 \langle\omega\rangle \tag{18}$$

and

$$\omega'_t + J[\langle\psi\rangle, \omega'] + J[\psi', \langle\omega\rangle] + J[\psi', \omega']' - \partial_Z w = \nabla_\perp^2 \omega'. \tag{19}$$

In the absence of the baroclinic-baroclinic term $\langle J[\psi', \omega']\rangle$ Eq. (18) is identical to the 2D vorticity equation and an inverse energy cascade to large scales is expected.

However, in the present case this equation is forced by the baroclinic-baroclinic term which acts as a source term for the barotropic mode. Of course, to find this source term one must solve the fluctuating equation (19) for ω' and hence for ψ'. These quantities in turn depend on the 2D vorticity $\langle\omega\rangle$ and so have to be determined self-consistently. We have seen that the transfer of energy to large scales persists even in this case but that it takes a dramatically different form. The inverse energy cascade familiar from 2D is now superseded by the $k_\perp^{-3}$ pile up at large scales, eg., Smith and Waleffe [48], powered by energy extraction directly from small scale baroclinic modes. However, the fluctuation equation is fully 3D and hence exhibits the usual $k_\perp^{-5/3}$ energy spectrum expected from Kolmogorov theory.

To quantify the above processes we partition the kinetic energy K into barotropic and baroclinic parts, $K = K_{\text{bt}} + K_{\text{bc}}$, where $K_{\text{bt}} = \frac{1}{2}(\langle u^2\rangle + \langle v^2\rangle)$ and $K_{\text{bc}} = \frac{1}{2}(u'^2 + v'^2 + w'^2)$ and examine the growth of both terms arising from mode-mode interactions. For example, the growth of barotropic kinetic energy at horizontal wavenumber $\mathbf{k}$, $K_{\text{bt}}(\mathbf{k})$, arises from triads of the form $\mathbf{k}+\mathbf{p}+\mathbf{q}=0$ where $(\mathbf{p},\mathbf{q})$ are either both 2D or both 3D. Thus

$$\partial_t K_{\text{bt}}(\mathbf{k}) = T_{\mathbf{k}} + F_{\mathbf{k}} + D_{\mathbf{k}}.$$

Here $T_{\mathbf{k}} \equiv \sum_{\mathbf{pq}} T_{\mathbf{kpq}}$ and $F_{\mathbf{k}} \equiv \sum_{\mathbf{pq}} F_{\mathbf{kpq}}$ represent, respectively, the symmetrized transfer of energy between Fourier modes within the barotropic component and the transfer of energy between baroclinic and barotropic modes; $D_{\mathbf{k}} \equiv -k^2 K_{\text{bt}}$ represents viscous dissipation of the barotropic mode. Specifically,

$$\begin{aligned}
T_{\mathbf{kpq}} &= b_{\mathbf{pq}} \mathrm{Re}\left[\langle\psi_{\mathbf{k}}\rangle\langle\psi_{\mathbf{p}}\rangle\langle\psi_{\mathbf{q}}\rangle\right]\delta_{\mathbf{k}+\mathbf{p}+\mathbf{q},\mathbf{0}},\\
F_{\mathbf{kpq}} &= b_{\mathbf{pq}} \mathrm{Re}\left[\langle\psi_{\mathbf{k}}\rangle\langle\psi'_{\mathbf{p}}\psi'_{\mathbf{q}}\rangle\right]\delta_{\mathbf{k}+\mathbf{p}+\mathbf{q},\mathbf{0}},\\
b_{\mathbf{pq}} = b_{\mathbf{qp}} &\equiv \frac{1}{2}(p^2 - q^2)(p_x q_y - p_y q_x).
\end{aligned}$$

These transfer rates can be computed from the simulations and the migration to large scales of the dominant barotropic mode quantified. The results can be used to identify three distinct regimes in the time evolution of the system [44]. The left panels of Fig. 14 show that barotropic-barotropic interactions rapidly populate the box scale (regime II, the black histogram on the right of each panel sums the contribution to $\mathbf{k}$ of all the modes $\mathbf{p}$ and $\mathbf{q} = -\mathbf{k} - \mathbf{p}$), ultimately leading to energy accumulation at the box scale (regime III). In parallel, the baroclinic-baroclinic interactions (right panels) reveal a gradual increase in the energy containing scale, culminating in the box scale in regime III. We see that while both types of mode-mode interactions feed the box scale, the baroclinic-baroclinic interaction ultimately dominates. Thus the energy transfer process largely bypasses the barotropic manifold.

Time evolution of baroclinic (red) and barotropic (black) modes in regimes I, II and III is shown in Fig. 15. We see that in regime I the box scale mode

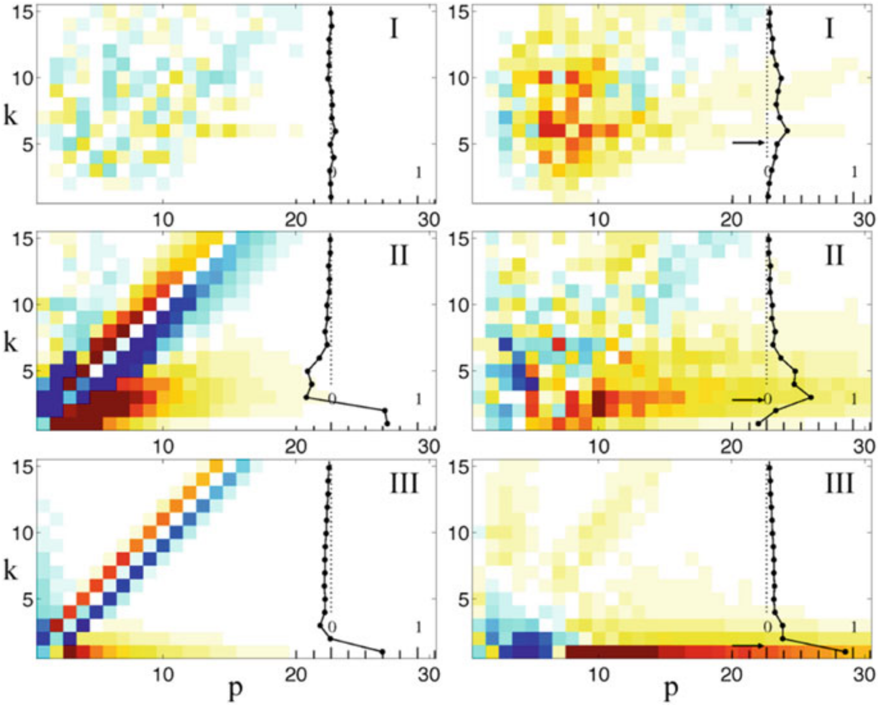

Fig. 14 Transfer rates $T_{\mathbf{k}}$ (left) and $F_{\mathbf{k}}$ (right) in regimes I, II and III. From [44]

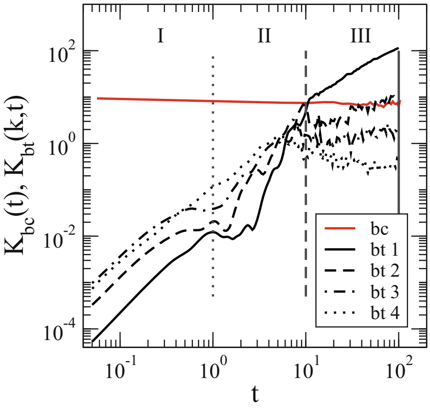

Fig. 15 The box scale mode (solid black line) extracts energy directly from small scales and continues to grow while other barotropic modes saturate. The energy in the baroclinic state remains almost constant. From [44]

grows algebraically (recall that the turbulence is driven by energy injection into the baroclinic modes) but takes off in regime II before a transition to slower but continued growth in regime III. The growth continues even when other barotropic modes saturate and is a consequence of continued energy extraction by the box scale mode from the small scale baroclinic fluctuations (Fig. 14). We discuss this process in greater detail later in this chapter.

4 Validation

Before proceeding we pause to validate the NHBGE against DNS of the primitive equations, solved at finite Ekman number. These comparisons are most easily done for $\sigma = 1$ for which the geostrophic turbulence regime can be reached for lower values of $\widetilde{Ra}$. The first such comparison was performed by S Stellmach (2012, unpublished) for a remarkably low value of the Ekman number, $E = 10^{-7}$, establishing qualitative agreement with the NHBGE (Fig. 16). Indeed, with some imagination one may even see an LSV in the last panel. We point out that the NHBGE results are shown on a domain scaled with $E^{1/3}$; this is not the case for the DNS of the primitive equations. Figures 17, 18, and 19 show more detailed comparisons at less extreme values of E.

These DNS computations confirm that the NHBGE capture correctly the behavior of the primitive equations at low Ekman numbers, and indeed suggest that no

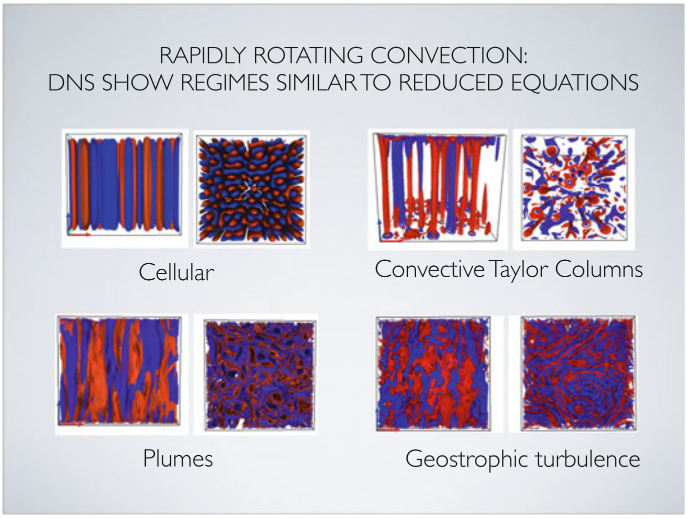
RAPIDLY ROTATING CONVECTION:
DNS SHOW REGIMES SIMILAR TO REDUCED EQUATIONS

Fig. 16 Cellular regime (C): $\sigma = 1$, $\widetilde{Ra} = 11$; Taylor column (T) regime: $\sigma = 15$, $\widetilde{Ra} = 15$; Plume (P) regime: $\sigma = 3$, $\widetilde{Ra} = 50$; Geostrophic turbulence (G) regime: $\sigma = 1$, $\widetilde{Ra} = 90$. In each case a top view (right) is shown next to a side view (left). Courtesy S Stellmach (2012, unpublished)

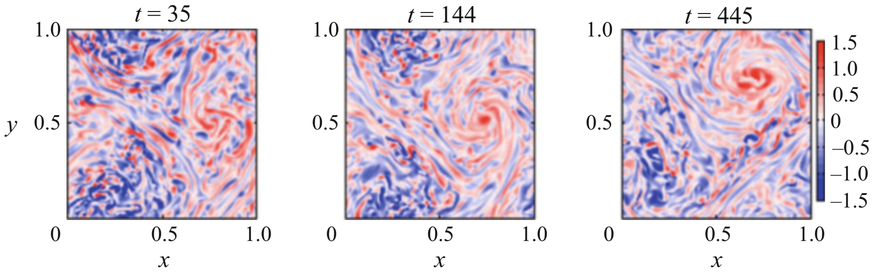

Fig. 17 Spontaneous generation of LSV at $E = 5 \times 10^{-6}$, $\widetilde{Ra} = 68$, $\sigma = 1$ in terms of the vorticity ω at height $z = 0.25$. From [22]

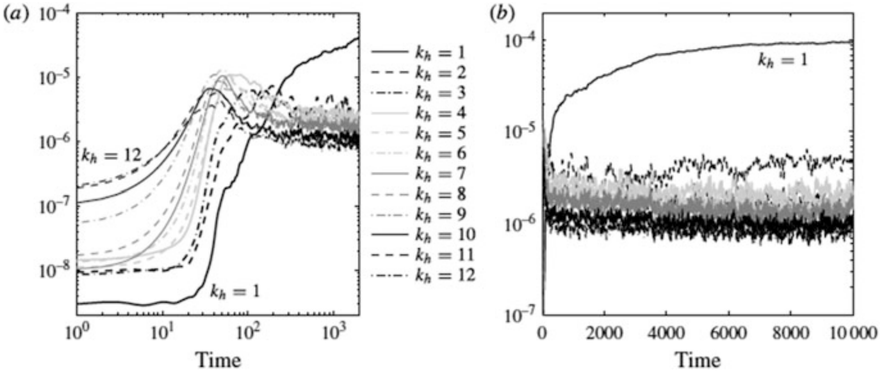

Fig. 18 Evolution of the energy of the box scale mode $k_h = 1$ at $E = 5 \times 10^{-6}$, $\widetilde{Ra} = 34$, $\sigma = 1$, showing behavior similar to Fig. 15. From [22]

fundamentally new phenomena arise between $E \sim 10^{-6}$ and the asymptotic regime $E \to 0$. This observation argues in favor of NHBGE even outside of the asymptotic limit used in their derivation, and in fact over a broad range of Ekman (and indeed Rossby) numbers outside of this limit. Note, however, that when E is finite the RRRBC system favors cyclonic vortices over anticyclonic vortices. This is not the case in the limit $E \to 0$ (Fig. 12).

A further test of the NHBGE can be made by integrating the equations in periodic rectangles in the horizontal instead of periodic square domains. Anisotropic domains of this type favor the spontaneous formation of jets parallel to the short side resulting in a Kolmogorov type of flow superposed on geostrophic turbulence. We find that jets of this type are generated already for domain aspect ratios of order 1.1, i.e. 10% off a square cross-section (Fig. 20). These conclusions are confirmed by DNS of the primitive equations as shown in Fig. 21. At present it is unclear what sets the wavelength of the jets in Figs. 20 and 21 but it is likely the result of a growing LSV reaching the short scale first and then imprinting this scale in the orthogonal direction. If this is the case then it is the short side that determines the

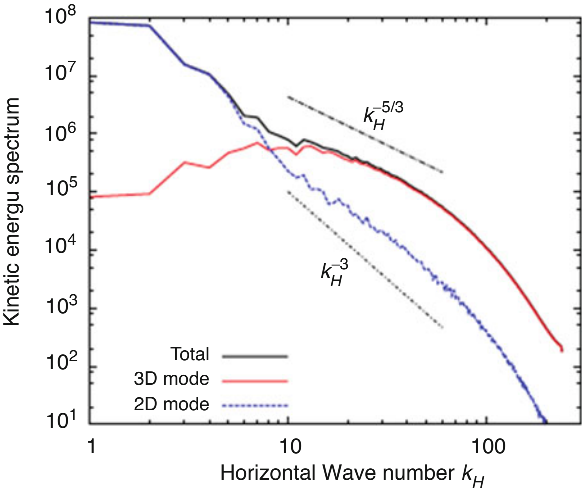

Fig. 19 Barotropic and baroclinic energy spectra at $E = 10^{-5}$, $\widetilde{Ra} = 107.7$, $\sigma = 1$, showing behavior similar to Fig. 13. From [16]

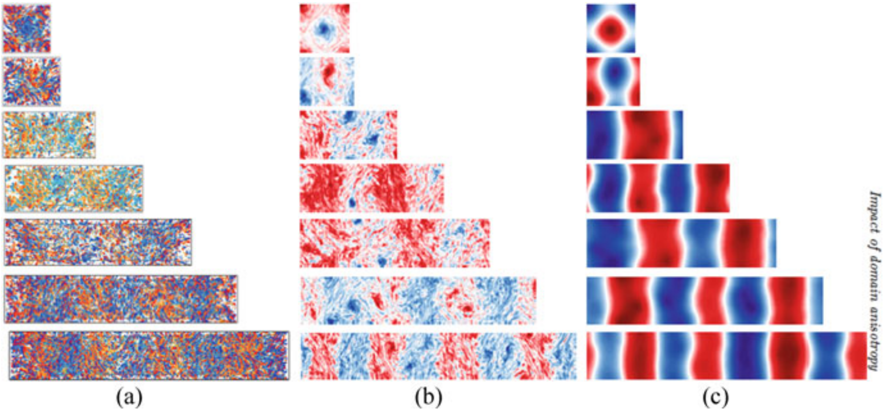

Fig. 20 Top view of large scale structures in periodic domains in the horizontal with aspect ratios $L_y/L_x = 1, 1.1, 2, 3, 4, 5$ and 6, showing snapshots of vertical vorticity (left), barotropic vertical vorticity (middle) and barotropic streamfunction (right) for $\widetilde{Ra} = 90$, $\sigma = 1$. From [34]. (**a**) ω. (**b**) $\langle\omega\rangle$. (**c**) $\langle\Psi\rangle$

wavelength of the turbulent Kolmogorov flow, in contrast to, say, the β-effect that sets the latitude scale of planetary jets.

Figure 22 shows the asymmetry parameter $\alpha \equiv \frac{\langle u^2\rangle - \langle v^2\rangle}{\langle u^2\rangle + \langle v^2\rangle}$ as a function of the domain length L_y in the y direction ($L_x = 1$). The figure confirms that LSV ($\alpha = 0$) are present when the domain has square cross-section ($L_y = 1$) and that fully developed jets parallel to the short side ($\alpha \sim 1$) are present when $L_y \approx 1.1$.

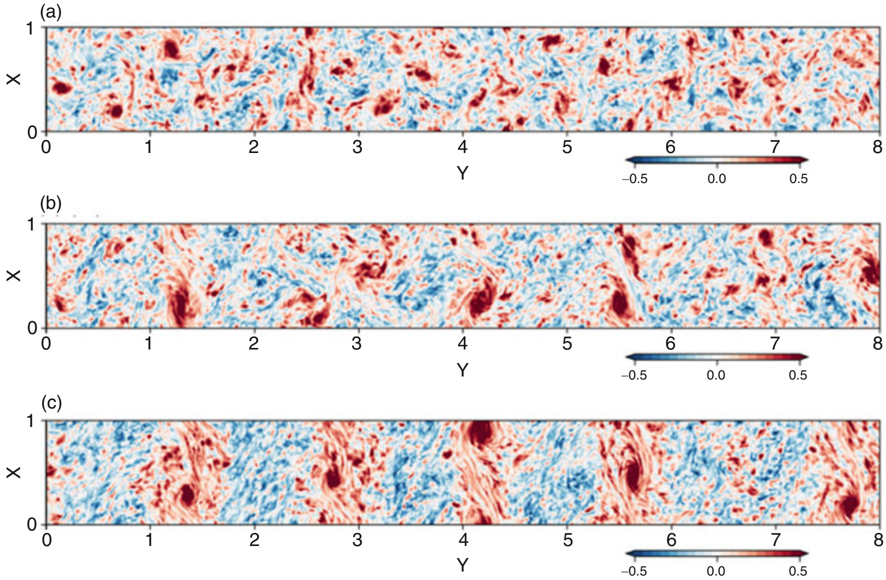

Fig. 21 Jet formation in an $L_y/L_x = 8$ domain in DNS of the primitive equations shown at three different times. Parameters: $E = 10^{-5}$, $\widetilde{Ra} = 62$. From [21]. (**a**) $\langle\omega\rangle_z$ at $t = 326$. (**b**) $\langle\omega\rangle_z$ at $t = 788$. (**c**) $\langle\omega\rangle_z$ at $t = 2167$

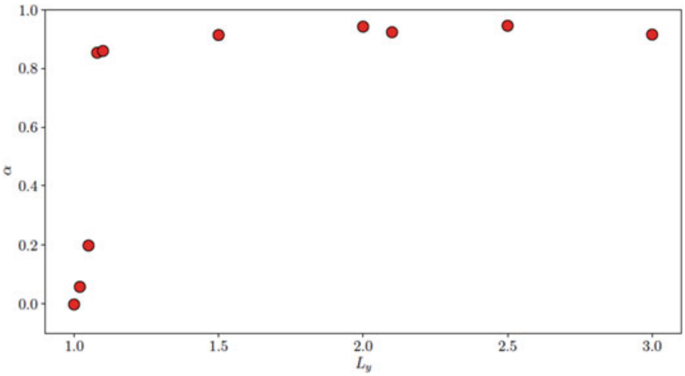

Fig. 22 The asymmetry parameter α as a function of the domain length L_y in the y direction for $L_x = 1$, $E = 10^{-5}$, $\widetilde{Ra} = 62$. LSV ($\alpha = 0$) evolve into turbulent jets parallel to the short side ($\alpha \sim 1$) at $L_y \approx 1.1$. From [21]

Remarkably, this observation coincides with a similar prediction from equilibrium statistical mechanics [4] even though the present system is a driven dissipative system.

We conclude this section by summarizing the advantages and disadvantages of the NHBGE.

Advantages of the Asymptotic Approach

- The reduced equations are asymptotically exact as $E \to 0$, Ra $E^{4/3} = \mathcal{O}(1)$
- The reduced equations permit study of regimes relevant to geophysical and astrophysical flows
- The equations contain no small or large parameters
- The equations capture, apparently correctly, the physics of RRRBC, including Taylor columns, plumes and geostrophic turbulence
- They capture the formation of large scale structure: domain-size vortices and jets
- Equations offer opportunity to study fundamental properties of 2+ϵ-dimensional flows.

Disadvantages of the Asymptotic Approach

- The equations focus on one particular regime: $L/H = \mathcal{O}(\text{Ro})$ and may not describe other regimes
- Applications always require finite Ro or finite E: when are the dynamics at a given Ro captured by the reduced equations?
- The equations only represent slow dynamics; inertial wave turbulence has been eliminated
- Ekman pumping is absent; may be added as subdominant boundary forcing [33].

5 Finite Rossby Number

In this section we discuss some consequences of employing finite values of the Rossby or Ekman numbers, and use these to shed light on the mechanism whereby the LSV extract energy from small scales. We are interested in exploring two questions: (1) is the development of LSV due to an instability of geostrophic turbulence, and (2) what is the mechanism whereby the LSV extract energy from the small scale 3D fluctuations?

To explore the first question we take a modest Ekman number $E = 10^{-4}$ together with Ra $= 3 \times 10^7$ (Ro $= 0.55$, $\widetilde{Ra} = 139$). For these parameters LSV do not develop and we suppose that the geostrophic turbulence state is therefore 'stable'. However, we encourage the formation of LSV by superposing a box scale barotropic vortex dipole of amplitude A on the small amplitude random initial conditions. Figure 23 shows that for small values of A the turbulent state decays to homogeneous geostrophic turbulence ($A = 0$); in fact it does so faster than the laminar viscous decay (dashed lines) since in this regime turbulence enhances dissipation. However, for sufficiently large A this is no longer the case, and after an initial decay interval we see that the kinetic energy in the 2D barotropic mode begins to grow and continues to do so as time proceeds—classic signature of the growth of LSV. As expected, the LSV that forms is a single cyclonic vortex; the anticyclonic vortex eventually decays. The result shows that in this parameter regime the system is bistable: the states with no LSV and with a single cyclonic LSV are both stable

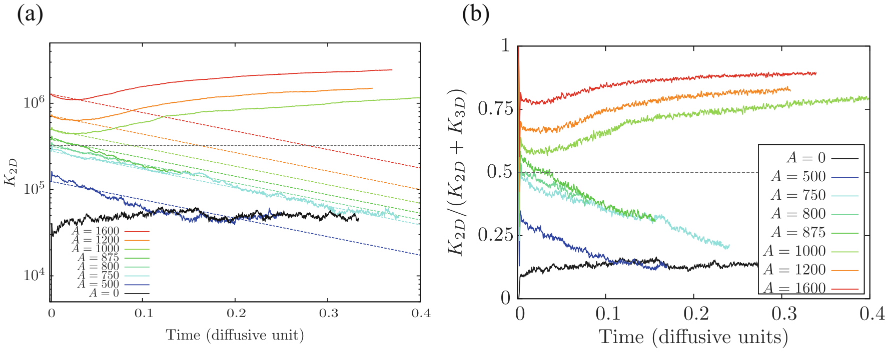

Fig. 23 (**a**) Time evolution of the kinetic energy density K_{2D} of the 2D flow for different values of A showing subcritical behavior of the vortex state. (**b**) Ratio $K_{2D}/(K_{2D}+K_{3D})$ for different A. Sufficiently large perturbation amplitude A leads to a self-sustained vortex. Parameters: $\widetilde{Ra} = 139$ and $\sigma = 1$. Adapted from [17]

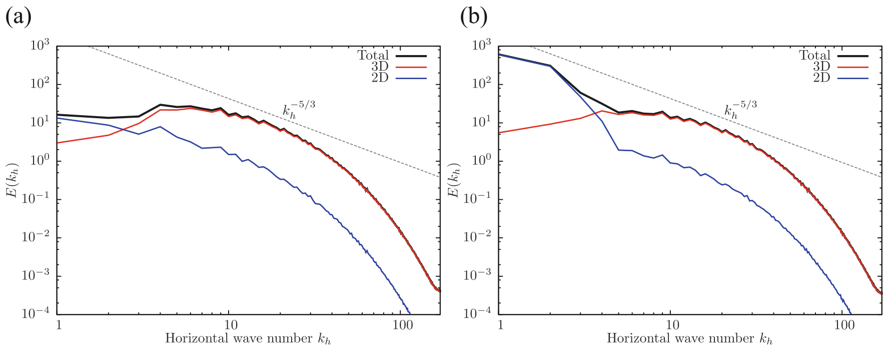

Fig. 24 Kinetic energy spectra averaged over time and depth as a function of the horizontal wavenumber k_h when $\widetilde{Ra} = 139$, $\sigma = 1$. (**a**) $A = 0$. (**b**) $A = 1600$. From [17]

states of the system. This result suggests that if geostrophic turbulence is indeed unstable with respect to the formation of LSV at larger $\widetilde{Ra}$ then this bifurcation is *subcritical*. Figure 24 shows that the kinetic energy spectra of these two states are as expected, with no k_h^{-3} spectrum at large scales when $A = 0$.

In Fig. 25 we compare the rate of energy injection into the 2D mode via the convective instability, and the overall energy dissipation rate of this mode, as defined by the expression

$$\frac{d}{dt}K_{2D} \propto \iint \langle \mathbf{u}\rangle_z \cdot \langle \mathbf{u}' \cdot \nabla \mathbf{u}'\rangle_z \mathrm{d}x\mathrm{d}y + \sigma \iint \langle \mathbf{u}\rangle_z \cdot \nabla_h^2 \langle \mathbf{u}\rangle_z \mathrm{d}x\mathrm{d}y \equiv \mathcal{F} + \mathcal{D}.$$

When $A = 0$ (homogeneous geostrophic turbulence) the instantaneous energy injection rate and the dissipation rate are in close balance, and on average there is no net energy input into the 2D mode (Fig. 25a). This is no longer so when

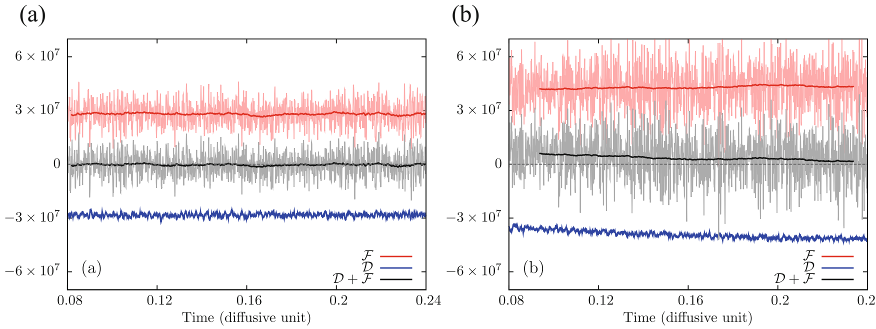

Fig. 25 Time evolution of the forcing $\mathcal{F}$ and dissipation $\mathcal{D}$ for the 2D barotropic mode when $\widetilde{Ra} = 139$, $\sigma = 1$. (**a**) $A = 0$. (**b**) $A = 1600$. From [17]

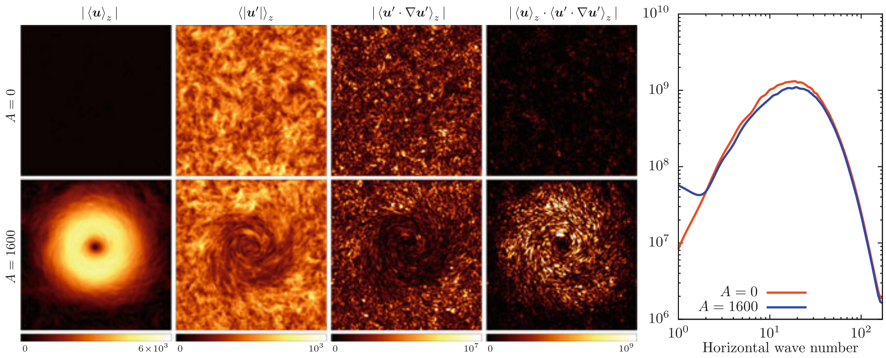

Fig. 26 Left: amplitude of the 2D flow, vertical average of the 3D fluctuation amplitude, amplitude of the fluctuating forcing and its rate of working for $A = 0$ (top) and $A = 1600$ (bottom) showing the footprint of the LSV in the 3D baroclinic fluctuations. Right: spectra of the fluctuation forcing $\left\langle \mathbf{u}' \cdot \nabla \mathbf{u}' \right\rangle_z$ in the two cases shown on the left. From [17]

a self-sustained LSV is present ($A > A_c$). In this case the energy injection rate continues to slowly increase, but even more significantly, the dissipation rate drops substantially as the LSV strengthens. The result is persistent net energy injection into the system that continues to grow the cyclonic vortex that remains.

How does this unexpected behavior come about? We believe that the fully developed LSV has a profound effect on the small scale baroclinic (3D) fluctuations in that it introduces correlations among the phase of these scales. These correlations are such that they enable efficient energy extraction from these scales by the 2D barotropic mode, and that, at the same time, reduce viscous dissipation. Traditional approaches to turbulence ignore the role of the phases of different modes and focus on the properties of the energy spectrum. In this type of description all phase information is lost; in effect one is making a random phase assumption, asserting that phase correlations are unimportant. Figure 26 shows that this is not so. The figure compares the properties of the $A = 0$ state with the LSV state ($A = 1600$)

focusing on vertically averaged quantities (indicated by the subscript z). The figure shows clearly that the presence of the LSV impacts the small scale fluctuations [46], and leaves a substantial footprint in these scales, both in the small scale forcing $\left\langle \mathbf{u}' \cdot \nabla \mathbf{u}' \right\rangle_z$ and in its rate of working $\langle \mathbf{u} \rangle_z \cdot \left\langle \mathbf{u}' \cdot \nabla \mathbf{u}' \right\rangle_z$, clearly violating the random phase assumption.

In the present system energy is injected via unstable convective modes which are both advected and sheared by an ambient vortex, thereby modifying the energy injection mechanism as well as its efficiency. Such an *active* injection process differs from systems driven by a stochastic force with fixed statistical properties. In the latter, passive case, a statistically stationary state requires no net injection of energy, in other words, $\iint \mathbf{u} \cdot \mathbf{f} \, dx dy = 0$, i.e. the flow $\mathbf{u}$ reflects the prescribed statistical properties of $\mathbf{f}$. In the active case these statistical properties develop self-consistently and may as a result be inhomogeneous in space.

6 Cylindrical Domain: Robust Boundary Flow

In the presence of lateral boundaries, for example in Rayleigh-Bénard convection in a uniformly rotating vertical cylinder, new behavior is found. In his original experiments Rossby [43] discovered that convection sets in at Rayleigh numbers Ra_w below the critical Rayleigh number Ra_c for the onset of bulk convection predicted by Chandrasekhar [6]. Subsequent work by Goldstein et al. [18] showed that this surprising behavior was due to the presence of a new mode of instability, a precessing wall-attached mode. This prediction was confirmed in [23, 39] and in associated experiments [62, 63], generating new interest in the properties of this laterally confined mode [13].

In retrospect it is easy to understand the properties of this state [13]. We employ polar coordinates (r, ϕ, z) and suppose that the wall mode has azimuthal wavenumber $m > 0$, i.e. that the mode breaks the azimuthal invariance of the system. Near onset we may write the temperature departure from the conduction state in the form

$$\theta(r, \phi, z, t) = \mathcal{R}\{a_m(t) \exp(-im\phi) \, f_m(r, z)\} + \dots,$$

where $f_m(r, z)$ is the eigenfunction of the mode m and a_m is its amplitude. When the cylinder does not rotate and the boundary conditions are ϕ-independent, the equation satisfied by a_m must commute with the symmetries

$$\begin{aligned} \text{rotations}: \quad & \phi \to \phi + \phi_0 : \qquad a_m \to a_m \exp(-im\phi_0), \\ \text{reflection}: \quad & \phi \to -\phi : \qquad a_m \to \bar{a}_m . \end{aligned} \tag{20}$$

It follows that $\dot{a}_m = g(|a_m|^2, \varepsilon) a_m$, where g is necessarily real. The parameter $\varepsilon \equiv (\mathrm{Ra} - \mathrm{Ra}_w)/\mathrm{Ra}_w$ measures the distance from onset; Ra_w also depends on the mode number m. Thus near onset $\varepsilon \ll 1$ and the function g may be expanded in a Taylor series:

$$\dot{a}_m = \varepsilon a_m + \alpha |a_m|^2 a_m + \dots \tag{21}$$

Writing $a_m = A_m \exp(i\Phi_m)$ we see that the onset of a steady-state instability is described by equations of the form

$$\dot{A}_m = \varepsilon A_m + \alpha A_m^3 + \dots, \qquad \dot{\Phi}_m = 0.$$

The second equation is a consequence of neutral stability of the mode with respect to rotations and shows that the bifurcation is a pitchfork of revolution.

Now suppose that the cylinder rotates with a small angular velocity Ω. The rotation breaks the reflection symmetry but not the rotation symmetry. The coefficients in Eq. (21) consequently acquire nonzero imaginary parts:

$$\dot{a}_m = (\varepsilon + i\Omega\delta) a_m + (\alpha + i\Omega\beta)|a_m|^2 a_m + \dots, \tag{22}$$

where ε, δ, α and β are all functions of Ω^2 and the mode number m. In terms of the real variables we now have

$$\dot{A}_m = \varepsilon A_m + \alpha A_m^3 + \dots, \qquad \dot{\Phi}_m = \Omega(\delta + \beta A_m^2 + \dots)$$

and conclude that the bifurcation is a Hopf bifurcation leading to a precessing state of the form

$$\theta = \mathcal{R}\{A_m \exp[i(\omega_d t - m\phi)]\, f_m(r, z)\} + \dots$$

with drift frequency

$$\omega_d = \Omega\left(\delta - \frac{\beta}{\alpha}\varepsilon\right) + O(\varepsilon^2).$$

The predictions of this simple theory have been successfully tested in experiment [13] and Fig. 27 summarizes the region in parameter space where precessing wall modes are the first mode of instability for different Prandtl numbers Pr and aspect ratios $\Gamma \equiv D/H$, where D is the cylinder diameter and H is its height.

Figure 28 shows the evolution of the wall modes in the nonlinear regime when $E = 10^{-6}$, $\sigma = 1$, $\Gamma = 1.5$. Close to onset ($\mathrm{Ra} = 5 \times 10^7$) the predictions of the weakly nonlinear theory are borne out, and a steadily precessing retrograde mode with $m = 6$ is found. At larger Ra a small amplitude random initial condition grows more rapidly, and as it does so the pattern coarsens, selecting the mode number $m = 4$. The figure shows that the system is bistable: both $m = 6$ and $m = 4$ states are simultaneously stable at $\mathrm{Ra} = 5 \times 10^7$, cf. [35]. With increasing Ra the wall modes become unsteady (Fig. 29a) but persist into the regime $\mathrm{Ra} > \mathrm{Ra}_c$ where the

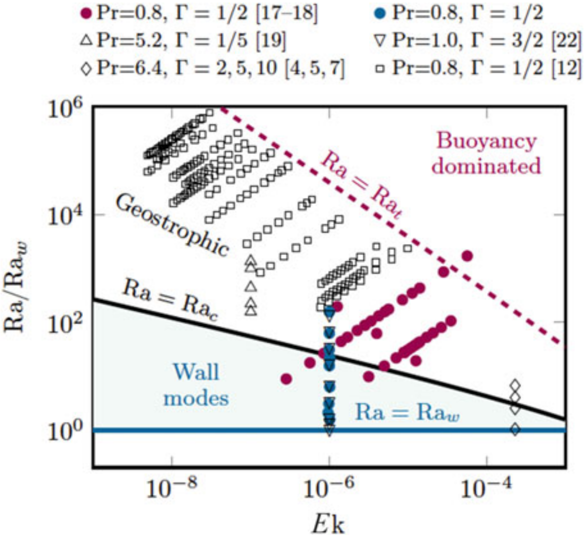

Fig. 27 The (Ra, E) parameter space for convection in a rapidly rotating cylinder. Wall modes are found between Ra_w and the onset of bulk convection at Ra_c. From [14]

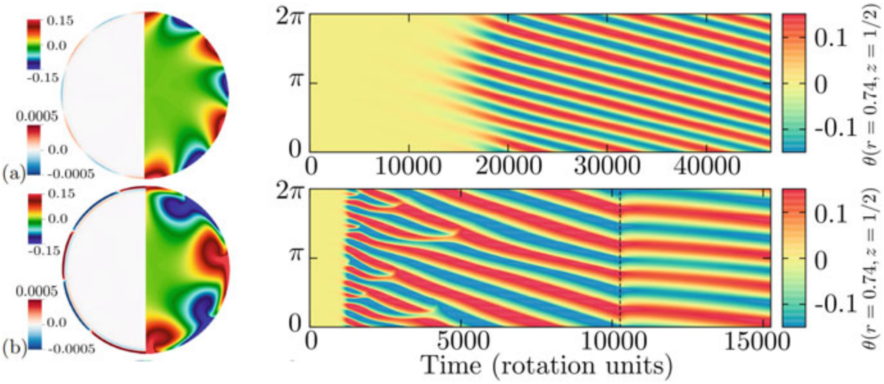

Fig. 28 Midplane vertical velocity w (left) and fluctuating temperature θ at $r = 0.74$ (right) at (**a**) $\mathrm{Ra} = 5 \times 10^7$ and (**b**) $\mathrm{Ra} = 2 \times 10^8$ together with associated temperature space-time plots. In (**b**) Ra is reduced to $\mathrm{Ra} = 5 \times 10^7$ at the dashed line to demonstrate multistability. Adapted from [15]

interior of the domain fills with bulk turbulence (Fig. 29b). Favier and Knobloch [15], see also [47], suggest that these wall modes are responsible for the strong boundary zonal flows observed in high Rayleigh number experiments [12, 60, 61], a suggestion confirmed in recent work by Ecke et al. [14].

While it is surprising that the wall modes persist into the geostrophic turbulence regime, it is even more remarkable that they are robust with respect to changes in the geometry. To illustrate this fact we show in Fig. 30 a DNS of Rayleigh-Bénard convection in a rotating cylinder with a thin, no-slip barrier along a half-diameter.

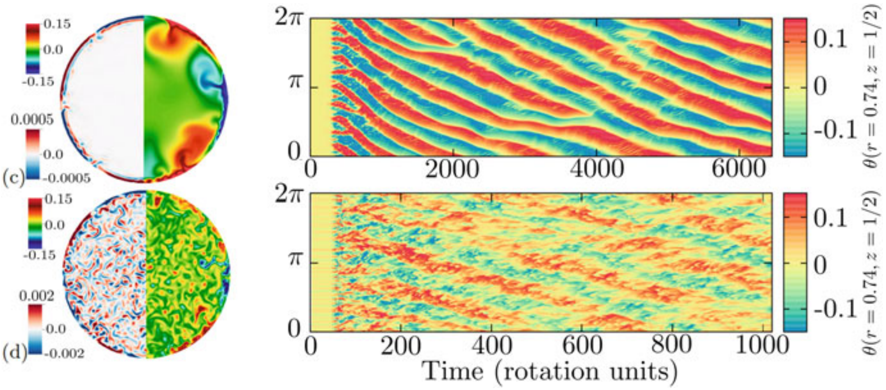

Fig. 29 Midplane vertical velocity w (left) and fluctuating temperature θ (right) at (**a**) Ra $= 5 \times 10^8$ and (**b**) Ra $= 2 \times 10^9$ together with associated temperature space-time plots. The wall states persist in the presence of a turbulent bulk state in the interior. Adapted from [15]

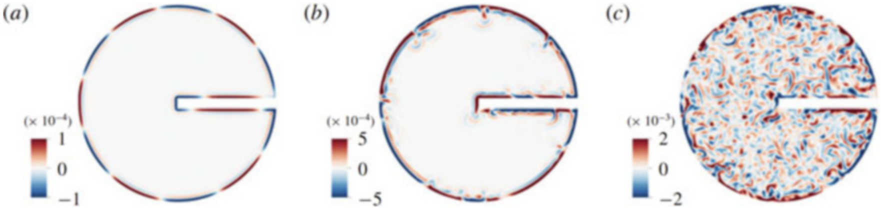

Fig. 30 Vertical velocity in the midplane $z = 0.5$ for a cylinder with a barrier. The Rayleigh number increases from left to right: (**a**) Ra $= 5 \times 10^7$, (**b**) Ra $= 5 \times 10^8$ and (**c**) Ra $= 2 \times 10^9$. Parameters are $\Gamma = 1.5$, $E = 10^{-6}$ and $\sigma = 1$. From [15]

Figure 31 shows that the wall mode simply travels along the extra wall, but remains essentially unchanged. Indeed, its radial profile (Fig. 31) and precession frequency (Fig. 32) are essentially unchanged in the presence of the barrier.

The robustness of the boundary zonal flow is reminiscent of topologically protected states in two-dimensional insulators [54]; see also [11, 53]. We describe here a system of this type with a fluid dynamical flavor, and describe the generation of sound waves in a chiral material described by a linear equation for density changes ($\partial_t \rho = -\rho_0 \nabla \cdot \mathbf{v}$) and a linear equation for the associated velocity $\mathbf{v} \equiv (u, v)$ ($\mathbf{v}_t = -c^2 \nabla \rho / \rho_0 + \omega_B \mathbf{v}^* + \nu^o \nabla^2 \mathbf{v}^*$). Here ρ_0 is the background density, c the sound speed and ω_B the chiral frequency. The latter couples linearly to $\mathbf{v}^* \equiv (v, -u)$ and thus corresponds to a Coriolis-like term. The important difference from usual hydrodynamics is provided by the last term, which resembles viscous dissipation but involves $\mathbf{v}^*$ instead of $\mathbf{v}$. The corresponding viscosity, called *odd viscosity*, therefore acts like dispersion but does not result in energy dissipation. The resulting system is therefore nondissipative and exhibits all the hallmarks of a system with a topologically protected edge current [49]. Figure 33 shows a typical consequence of this property. A localized perturbation initiated at the point indicated by a red star leads to unidirectional propagation of sound along the boundary. Since

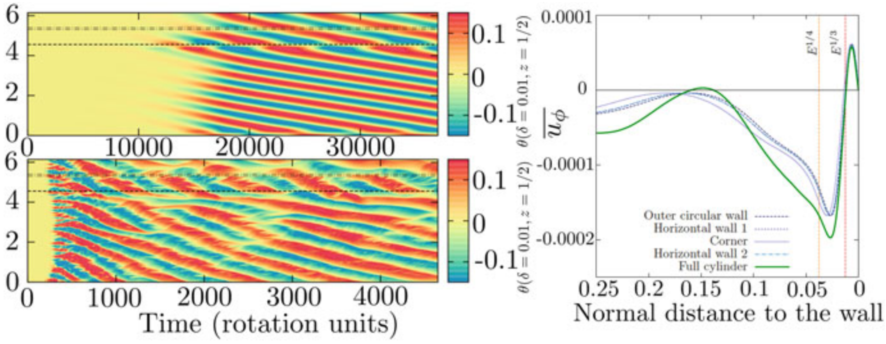

Fig. 31 Spatio-temporal plots showing the temperature fluctuation θ at $z = 0.5$ and a fixed distance $\delta = 10^{-2}$ from the boundary at (**a**) Ra $= 5 \times 10^7$ and (**b**) Ra $= 5 \times 10^8$. The dotted lines indicate the positions of the four corners of the barrier. (**c**) Vertically and temporally averaged velocity tangential to the boundary at Ra $= 5 \times 10^8$ as a function of the radial coordinate r. We distinguish between the cylindrical boundary and the different faces of the barrier. The results are compared to the case without barrier. Positive values correspond to cyclonic motions while negative values correspond to anticyclonic motions. The two vertical lines indicate the Stewartson layer scales $E^{1/3}$ and $E^{1/4}$ [52]. Parameters are $\Gamma = 1.5$, $E = 10^{-6}$ and $\sigma = 1$. Adapted from [15]

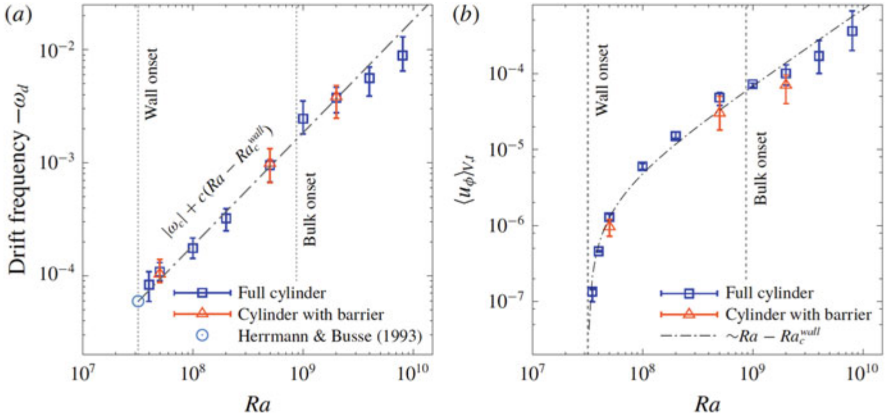

Fig. 32 (**a**) Drift frequency $-\omega_d$ as a function of Ra for $\Gamma = 1.5$, $E = 10^{-6}$ and $\sigma = 1$. The results for the full cylinder (blue color square) and the cylinder with a barrier (orange color triangle) coincide. The theoretical onset value $\omega_w \approx -59E/\sigma$ predicted in [23] for the onset of the instability in the presence of a planar wall is also reported (open circle). (**b**) Corresponding volume- and time-averaged zonal velocity $\langle u_\phi \rangle_{V,t}$. The dot-dashed line corresponds to the scaling $\langle u_\phi \rangle_{V,t} \sim \text{Ra} - \text{Ra}_w$. The volume integration is performed only over the left half of the cylinder when the barrier is present. From [15]

the edge current is topologically protected the wave travels past obstacles along the boundary with essentially no change, much like the zonal currents associated with the wall modes in RRRBC. However, in our system the wall modes are fully three-dimensional nonlinear waves maintained against dissipation by thermal forcing

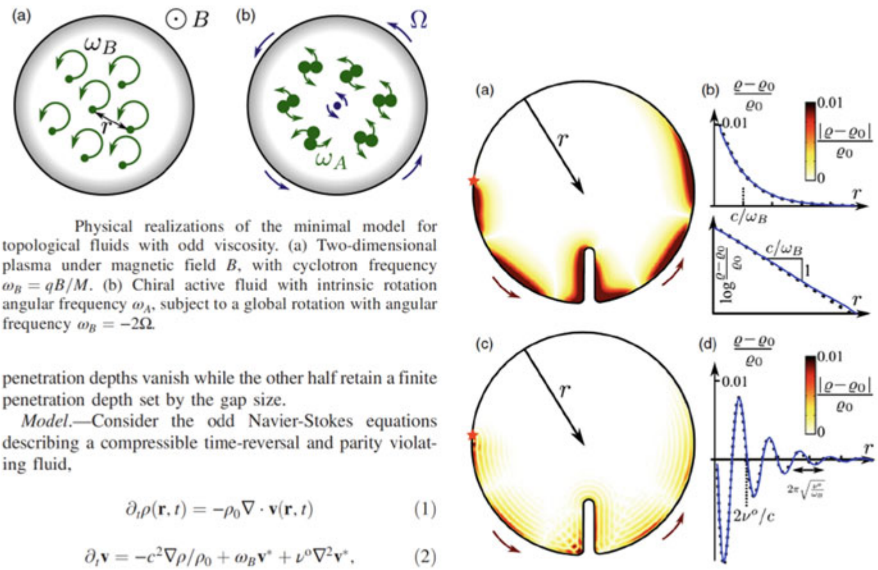

Physical realizations of the minimal model for topological fluids with odd viscosity. (a) Two-dimensional plasma under magnetic field B, with cyclotron frequency $\omega_B = qB/M$. (b) Chiral active fluid with intrinsic rotation angular frequency ω_A, subject to a global rotation with angular frequency $\omega_B = -2\Omega$.

penetration depths vanish while the other half retain a finite penetration depth set by the gap size.

Model.—Consider the odd Navier-Stokes equations describing a compressible time-reversal and parity violating fluid,

$$\partial_t\rho(\mathbf{r},t) = -\rho_0\nabla\cdot\mathbf{v}(\mathbf{r},t) \qquad (1)$$

$$\partial_t\mathbf{v} = -c^2\nabla\rho/\rho_0 + \omega_B\mathbf{v}^* + \nu^o\nabla^2\mathbf{v}^*, \qquad (2)$$

Fig. 33 Left: chiral fluid and basic equations. Right: simulation of two-dimensional topological edge states in a cylinder for two different values of $m \equiv \omega_B\nu^o/c^2$, showing a plan view of a wave emanating from a low-frequency source at the red star together with its radial profile. (**a**) $m = 0.0625$. (**b**) $m = 9.0$. From [49]

from below, and with their own intrinsic dynamics. It is unclear whether waves of this type are topologically protected, despite the similar behavior [15], and indeed we observe a multiplicity of such unidirectional waves in RRRBC with transitions between them. In contrast, in the odd viscosity problem the wavenumber is selected by the frequency of the source, instead of dissipation.

7 Discussion

In this article we have provided a brief review of an asymptotic approach that has proved useful in a number of fluid systems with strong restraints, including salt-finger convection [59], magnetoconvection [28, 30], magnetorotational instability [24, 37], dynamo instability [5], Langmuir circulation [9], shear flow instability [2] and many others. In each case a similar procedure generates simplified equations that are valid for extreme parameter values inaccessible to both laboratory and DNS studies.

We have focused on RRRBC as a prototypical system, largely because it is the system that is best studied both in the laboratory and in DNS. In this system the restraint is provided by rapid rotation, as measured by the convective Rossby number $\mathrm{Ro}_{\mathrm{conv}} \ll 1$. This regime favors small horizontal scales and our asymptotic procedure was designed to take full advantage of this fact. The reduced equations we derived, the NHBGE, are a closed set of equations with $\mathcal{O}(1)$ parameters, providing a non-stiff system characterized by a single key parameter, $\widetilde{Ra} \equiv \mathrm{Ra}E^{4/3}$, that is eminently suitable for numerical study. Comparison with the primitive equations is possible if the reduced equations are scaled with respect to the viscous scale. We presented results that show convincingly that the reduced system captures the essential properties of RRRBC over a broad range of parameters. Indeed the spontaneous evolution of large scale vortices and jets predicted by the reduced equations was confirmed in subsequent DNS studies of the primitive equations, a significant success of the proposed approach.

We emphasize that in strongly forced systems the primary balances are inevitably inviscid. Thus for geophysical and astrophysical applications it is inappropriate to use viscous lengths and times to nondimensionalize the equations. Instead of using the primitive equations with conventional nondimensionalization we may scale all fluid variables and the spatial and temporal derivatives based on the distinguished powers of Ro identified here to obtain the rescaled equations [31]

$$(\partial_t+\mathbf{u}_\perp\cdot\nabla_\perp+\mathrm{Ro}\,w\partial_Z)\mathbf{u}_\perp+\frac{1}{\mathrm{Ro}}\hat{\mathbf{z}}\times\mathbf{u}_\perp=-\frac{1}{\mathrm{Ro}}\nabla_\perp\hat{p}+\frac{1}{\mathrm{Re}}(\nabla_\perp^2+\mathrm{Ro}^2\partial_{ZZ})\mathbf{u}_\perp, \quad (23)$$

$$(\partial_t+\mathbf{u}_\perp\cdot\nabla_\perp+\mathrm{Ro}\,w\partial_Z)w=-\partial_Z\hat{p}+\frac{1}{\mathrm{Re}}(\nabla_\perp^2+\mathrm{Ro}^2\partial_{ZZ})w+\mathcal{F}_w, \quad (24)$$

$$\nabla_\perp\cdot\mathbf{u}_\perp+\mathrm{Ro}\partial_Z w=0. \quad (25)$$

In fact, as shown in [31], the parameter Ro appearing in these equations can be replaced by $E^{1/3}\widetilde{Ra}^{2\lambda}$, where the arbitrary scaling exponent λ $(1/3 < \lambda \leq 1)$ emphasizes the large range of horizontal scales described by the theory.

The anisotropic rescaling $\nabla \mapsto \nabla_\perp + \mathrm{Ro}\partial_Z$ and $p \mapsto \mathrm{Ro}^{-1}\hat{p}$ ensures that the rescaled equations converge smoothly to the asymptotic system (5)–(6) in the limit $\mathrm{Ro} \to 0$. For RRRBC $\mathcal{F}_w$ represents buoyancy forcing whose strength Re_H is directly related to Ro through $\mathrm{Re}_H = \mathrm{Re}\mathrm{Ro}^{-1}$. We believe that the primitive equations rescaled in the above manner may be more suitable for DNS at finite Ro than the isotropically (and viscously) scaled equations conventionally used in DNS studies.

We close with a list of open questions raised by our asymptotic approach:

- What is special about $L/H = \mathcal{O}(\mathrm{Ro})$ that allows closure?
- Are there other regimes where closure is possible?
- The approach points to the importance of phases of the small scales: can this be confirmed and the interaction between the large scales and the phases of the small scales be understood?
- Is homogeneous anisotropic turbulence in some sense (which?) unstable to the formation of large scale structure?
- Is this a subcritical bifurcation? Or are the large scale structures noise-sustained?
- Can a similar description of the fast dynamics be developed and the two descriptions coupled?

- Can vortices be computed as localized structures [36] of the NHBGE and interactions among them studied?
- What is the origin of the robustness of the boundary zonal flows?
- How useful is the anisotropic rescaling (23)–(25) for DNS at finite Ro?

We hope that some of these questions will be answered in ongoing work.

Acknowledgments EK thanks Benjamin Favier and Keith Julien for collaboration that has led to the insights reported here, and to Adrian Van Kan for a careful reading of the manuscript. The preparation of this chapter was supported in part by NSF grant DMS-2009563.

References

1. A. Alexakis, L. Biferale, Cascades and transitions in turbulent flows. Phys. Rep. **767–769**, 1–102 (2018)
2. C. Beaume, G.P. Chini, K. Julien, E. Knobloch, Reduced description of exact coherent states in parallel shear flows. Phys. Rev. E **91**, 043010 (2015)
3. G. Boffetta, R.E. Ecke, Two-dimensional turbulence. Annu. Rev. Fluid Mech. **44**, 427–451 (2012)
4. F. Bouchet, A. Venaille, Statistical mechanics of two-dimensional and geophysical flows. Phys. Rep. **515**, 227–295 (2012)
5. M.A. Calkins, K. Julien, S.M. Tobias, J.M. Aurnou, A multiscale dynamo model driven by quasi-geostrophic convection. J. Fluid Mech. **780**, 143–166 (2015)
6. S. Chandrasekhar, *Hydrodynamic and Hydromagnetic Stability* (Oxford University Press, Oxford, 1961)
7. J. Charney, Geostrophic turbulence. J. Atm. Sci. **28**, 1087–1095 (1971)
8. M. Chertkov, C. Connaughton, I. Kolokolov, V. Lebedev, Dynamics of energy condensation in two-dimensional turbulence. Phys. Rev. Lett. **99**, 084501 (2007)
9. G.P. Chini, K. Julien, E. Knobloch, An asymptotically reduced model of turbulent Langmuir circulation. Geophys. Astrophys. Fluid Dyn. **103**, 179–197 (2009)
10. T. Clune, E. Knobloch, Pattern selection in rotating convection with experimental boundary conditions. Phys. Rev. E **47**, 2536–2550 (1993)
11. P. Delplace, J.B. Marston, A. Venaille, Topological origin of equatorial waves. Science **358**, 1075–1077 (2017)
12. X.M. de Wit, A.J.A. Guzman, M. Madonia, J.S. Cheng, H.J. Clercx, R.P. Kunnen, Turbulent rotating convection confined in a slender cylinder: the sidewall circulation. Phys. Rev. Fluids **5**, 023502 (2020)
13. R.E. Ecke, F. Zhong, E. Knobloch, Hopf bifurcation with broken reflection symmetry in rotating Rayleigh-Bénard convection. Europhys. Lett. **19**, 177–182 (1992)
14. R.E. Ecke, X. Zhang, O. Shishkina, Connecting wall modes and boundary zonal flows in rotating Rayleigh-Bénard convection. Phys. Rev. Fluids **7**, L011501 (2022)
15. B. Favier, E. Knobloch, Robust wall states in rapidly rotating Rayleigh-Bénard convection. J. Fluid Mech. **895**, R1 (2020)
16. B. Favier, L. Silvers, M.R.E. Proctor, Inverse cascade and symmetry breaking in rapidly rotating Boussinesq convection. Phys. Fluids **26**, 096605 (2014)
17. B. Favier, C. Guervilly, E. Knobloch, Subcritical turbulent condensate in rapidly rotating Rayleigh-Bénard convection. J. Fluid Mech. **864**, R1 (2019)
18. H.F. Goldstein, E. Knobloch, I. Mercader, M. Net, Convection in a rotating cylinder. Part 1: linear theory for moderate Prandtl numbers. J. Fluid Mech. **248**, 583–604 (1993)

19. D. Gottlieb, S. Orszag. *Numerical Analysis of Spectral Methods: Theory and Applications* (SIAM, Philadelphia, 1977)
20. I. Grooms, K. Julien, J.B. Weiss, E. Knobloch, Model of convective Taylor columns in rotating Rayleigh-Bénard convection. Phys. Rev. Lett. **104**, 224501 (2010)
21. C. Guervilly, D.W. Hughes, Jets and large-scale vortices in rapidly rotating Rayleigh-Bénard convection. Phys. Rev. Fluids **2**, 113503 (2017)
22. C. Guervilly, D.W. Hughes, C.A. Jones, Large-scale vortices in rapidly rotating Rayleigh-Bénard convection. J. Fluid Mech. **758**, 407–435 (2014)
23. J. Herrmann, F.H. Busse, Asymptotic theory of wall-attached convection in a rotating fluid layer. J. Fluid Mech. **255**, 183–194 (2014)
24. B. Jamroz, K. Julien, E. Knobloch, An asymptotically exact reduced PDE model for the magnetorotational instability: derivation and numerical simulations. Phys. Scripta **T132**, 014027 (2008)
25. H. Jones, J. Marshall, Convection with rotation in a neutral ocean: a study of open-ocean deep convection. J. Phys. Oceanograph. **23**, 1009–1039 (1993)
26. K. Julien, E. Knobloch, Fully nonlinear oscillatory convection in a rotating layer. Phys. Fluids. **9**, 1906–1913 (1997)
27. K. Julien, E. Knobloch, Fully nonlinear three-dimensional convection in a rapidly rotating layer. Phys. Fluids. **11**, 1469–1483 (1999)
28. K. Julien, E. Knobloch, Reduced models for fluid flows with strong constraints. J. Math. Phys. **48**, 065405 (2007)
29. K. Julien, E. Knobloch, J. Werne, A new class of equations for rotationally constrained flows. Theor. Comput. Fluid Dyn. **11**, 251–261 (1998)
30. K. Julien, E. Knobloch, S. Tobias, Strongly nonlinear magnetoconvection in three dimensions. Phys. D **128**, 105–129 (1999)
31. K. Julien, E. Knobloch, A.M. Rubio, G.M. Vasil, Heat transport in low-Rossby-number Rayleigh-Bénard convection. Phys. Rev. Lett. **109**, 254503 (2012)
32. K. Julien, A.M. Rubio, I. Grooms, E. Knobloch, Statistical and physical balances in low Rossby number Rayleigh-Bénard convection. Geophys. Astrophys. Fluid Dyn. **106**, 392–428 (2012)
33. K. Julien, J.A. Aurnou, M.A. Calkins, E. Knobloch, P. Marti, S. Stellmach, G.M. Vasil, A nonlinear model for rotationally constrained convection with Ekman pumping. J. Fluid Mech. **798**, 50–87 (2016)
34. K. Julien, E. Knobloch, M. Plumley, Impact of domain anisotropy on the inverse cascade in geostrophic turbulent convection. J. Fluid Mech. **837**, R4 (2018)
35. E. Knobloch, Bifurcations in rotating systems, in *Lectures on Solar and Planetary Dynamos*, ed. by M.R.E. Proctor, A.D. Gilbert (Cambridge University Press, Cambridge, 1994), pp. 331–372
36. E. Knobloch, Spatial localization in dissipative systems. Annu. Rev. Cond. Matter Phys. **6**, 325–359 (2015)
37. E. Knobloch, K. Julien, Saturation of the magnetorotational instability. Phys. Fluids **17**, 094106 (2005)
38. R.H. Kraichnan, Inertial ranges in 2D turbulence. Phys. Fluids **10**, 1417–1423 (1967)
39. E.Y. Kuo, M.C. Cross, Traveling-wave wall states in rotating Rayleigh-Bénard convection. Phys. Rev. E **47**, R2245–R2248 (1993)
40. J. Marshall, F. Schott, Open-ocean convection: observations, theory and models. Rev. Geophys. **37**, 1–64 (1999)
41. S. Musacchio, G. Boffetta, Split energy cascade in turbulent thin fluid layers. Phys. Fluids **29**, 111106 (2017)
42. J. Pedlosky, *Geophysical Fluid Dynamics* (Springer, Berlin, 1979)
43. H.T. Rossby, A study of Bénard convection with and without rotation. J. Fluid Mech. **36**, 309–335 (1969)
44. A.M. Rubio, K. Julien, E. Knobloch, J.B. Weiss, Upscale energy transfer in three-dimensional rapidly rotating turbulent convection. Phys. Rev. Lett. **112**, 144501 (2014)

45. S. Sakai, The horizontal scale of rotating convection in the geostrophic regime. J. Fluid Mech. **333**, 85–95 (1997)
46. M.G. Shats, H. Xia, H. Punzmann, G. Falkovich, Suppression of turbulence by self-generated and imposed mean flows. Phys. Rev. Lett. **99**, 164502 (2007)
47. O. Shishkina, Tenacious wall states in thermal convection in rapidly rotating containers. J. Fluid Mech. **898**, F1 (2020)
48. L.M. Smith, F. Waleffe, Transfer of energy to two-dimensional large scales in forced, rotating three-dimensional turbulence. Phys. Fluids **11**, 1608–1622 (1999)
49. A. Souslov, K. Dasbiswas, M. Fruchart, S. Vaikuntanathan, V. Vitelli, Topological waves in fluids with odd viscosity. Phys. Rev. Lett. **122**, 128001 (2019)
50. P. Spalart, R. Moser, M. Rogers, Spectral methods for the Navier-Stokes equations with one infinite and two periodic directions. J. Comput. Phys. **96**, 297–324 (1990)
51. M. Sprague, K. Julien, E. Knobloch, J. Werne, Numerical simulation of an asymptotically reduced system for rotationally constrained convection. J. Fluid Mech. **551**, 141–174 (2006)
52. K. Stewartson, On almost rigid rotations. J. Fluid Mech. **3**, 17–26 (1957)
53. C. Tauber, P. Delplace, A. Venaille, A bulk-interface correspondence for equatorial waves. J. Fluid Mech. **868**, R2 (2019)
54. C. Tauber, P. Delplace, A. Venaille, Anomalous bulk-edge correspondence in continuous media. Phys. Rev. Res. **2**, 013147 (2020)
55. A. van Kan, A. Alexakis, Condensates in thin-layer turbulence. J. Fluid Mech. **864**, 490–518 (2019)
56. P. Vorobieff, R.E. Ecke, Turbulent rotating convection: an experimental study. J. Fluid Mech. **458**, 191–218 (2002)
57. H. Xia, H. Punzmann, G. Falkovich, M.G. Shats, Turbulence-condensate interaction in two dimensions. Phys. Rev. Lett. **101**, 194504 (2008)
58. H. Xia, D. Byrne, G. Falkovich, M. Shats, Upscale energy transfer in thick turbulent fluid layers. Nat. Phys. **7**, 321–324 (2011)
59. J. Xie, B. Miquel, K. Julien, E. Knobloch, A reduced model for salt-finger convection in the small diffusivity limit. Fluids **2**(6), 1–26 (2017)
60. X. Zhang, D.P.M. van Gils, S. Horn, M. Wedi, L. Zwirner, G. Ahlers, R.E. Ecke, S. Weiss, E. Bodenschatz, O. Shishkina. Boundary zonal flow in rotating turbulent Rayleigh-Bénard convection. Phys. Rev. Lett. **124**, 084505 (2020)
61. X. Zhang, R.E. Ecke, O. Shishkina, Boundary zonal flows in rapidly rotating turbulent Rayleigh-Bénard convection. J. Fluid Mech. **915**, A62 (2021)
62. F. Zhong, R.E. Ecke, V. Steinberg, Asymmetric modes and the transition to vortex structures in rotating Rayleigh-Bénard convection. Phys. Rev. Lett. **67**, 2473–2476 (1991)
63. F. Zhong, R.E. Ecke, V. Steinberg, Rotating Rayleigh-Bénard convection: asymmetric modes and vortex states. J. Fluid Mech. **249**, 135–159 (1993)

Ocean Surface Waves and Ocean-Atmosphere Interactions

Francisco J. Ocampo-Torres, Pedro Osuna, Héctor García-Nava, and Nicolas G. Rascle

Abstract The relevance of ocean surface wave dynamics is briefly reviewed. Some aspects are acknowledged from the traditional point of view, regarding mainly coastal and oceanic engineering applications, ship design, as well as maritime operations. More recently, interest is well focused at the exchange processes between the ocean and the atmosphere, to deal with weather and sea state forecast, as well as prediction and climate projections. We are mainly concerned with some of the most important applications, very much related to the influence of ocean surface waves on present challenging issues. One particular issue is the gas transfer across the interface and its potential impact on climate and its changes. Another one is the upper ocean dynamics and the behavior of surface currents and drift, greatly associated with transport of pollutants and objects on the sea surface (a very key issue when ocean and atmosphere are not in equilibrium in the interface sense). Furthermore, fundamental processes associated with observing the ocean with remote sensors are also a challenging aspect that requires a great knowledge of ocean surface waves behaviour. For instance, from ocean surface images acquired with synthetic aperture radars it is possible to indirectly determine the wave directional spectrum, essentially since ocean waves modulate the microwave reflectors, which represent a rather small scale roughness of the very sea surface. The main challenge to estimate the directional wave spectrum is shown and some preliminary results are presented. This challenge is also approached from aspects more related to the upper ocean dynamics, with another example of laboratory experiments aiming to obtain

---

F. J. Ocampo-Torres (✉)
CEMIE-Océano, Instituto de Ingeniería, UNAM, Ensenada, Mexico
e-mail: pocampotorres@gmail.com

H. García-Nava
Universidad Autónoma de Baja California, Ensenada, Mexico
e-mail: hector.garcia.nava@uabc.edu.mx

P. Osuna · N. G. Rascle
CICESE, Ensenada, Mexico
e-mail: osunac@cicese.mx; nrascle@cicese.mx

G. Hernández-Dueñas, M. A. Moreles (eds.), *Mathematical and Computational Models of Flows and Waves in Geophysics*, CIMAT Lectures in Mathematical Sciences, https://doi.org/10.1007/978-3-031-12007-7_2

the fluid velocity field in a layer just beneath the sea surface when acoustic Doppler methods are used, and subsequently estimate the surface drift induced jointly by wind and waves. Final remarks suggesting the way ahead regarding ocean surface wave dynamics research are delineated.

1 Introduction

Even if waves on water surfaces represent probably one of the most studied fluid phenomenon, wind generated ocean surface waves are of a rather complex nature and they still remain as one of the most difficult geophysical problems to be fully understood. Understanding its dynamics and having the proper skills to forecast them is a critical issue in many oceanic applications, covering a wide range of particular subjects within maritime and coastal engineering.

It has been recognized since long time ago that large amount of information about the behaviour of ocean surface waves is needed to many practical applications regarding mainly to planning and design of coastal and oceanic infrastructure, to programe maintenance activities and even for the design of ships as naval architects rely on historic data. This relevance of ocean surface wave information may be considered as classical fact. As Mitsuyasu [1, 2] pointed out, it can be said that surface wave dynamics modern studies started a few decades ago [3], while before, ocean surface waves were considered to be too disordered to be treated properly.

Nevertheless, very important and complete mathematical treatment and physical understanding of water waves have been achieved decades ago. Mainly regarding waves over water surfaces, their form and propagation were described by very relevant studies by Laplace, Poisson, Lagrange, Stokes, Airy, Rayleigh and Boussinesq in the eighteenth and nineteenth centuries. Weber and Weber [4] have presented a very comprehensive compilation and included experimental observations and results, while recent reviews of the historical development have been advanced by Darrigol [5] and Craik [6].

Furthermore, first attempts to deal with the generation of waves by wind were described by Jeffreys [7, 8]. Therefore, we can say that modern wave forecasting started in the 1920s with swell forecasts for Morocco coastal region [9, 10], although a more general approach was developed by Sverdrup and Munk [3] considering the full life cycle of waves, particularly including the description of processes such as generation by the wind and dissipation in the middle of the ocean, coastal regions and on beaches. Ocean surface wave studies were advanced towards the applications of forecasting in the coastal regions very much linked to maritime operations and disembark. Nevertheless, great deal of work and research has also been devoted to other types of engineering applications and this is reviewed in the book of Dean and Dalrymple [11].

Advance in research in the 1950s and 1960s was rather more associated with the understanding of the physics and dynamical processes of ocean surface waves and to properly incorporate that knowledge into development of numerical models for the forecast of the wave spectrum.

A spectral model of wind waves was presented by Pierson [12] somehow influenced by the fundamentals of the theory of random noise [13]. Meanwhile Neumann [14], determined a spectral form of developing ocean surface waves by using his observed wave data. Joint efforts resulted in a seminal paper on practical methods for observing and forecasting ocean waves by means of wave spectra and statistics [15].

Through fundamental studies and theoretical work it was shown that wind wave growth was initially linear [16] but ultimately exponential [17] in time, and later Miles [18] combined those two previous theories. Based upon the idea of an equilibrium range in the wave spectrum and through a dimensional analysis, Phillips [19] showed that for large values of the frequency, the spectrum reached a definite form which only depends on the frequency.

With the increase of ocean wave data great effort was devoted to determine the similarity form of the ocean surfaces wave spectrum. Based upon the similarity theory by Kitaigorodskii [20], probably the most successful result was given by Pierson and Moskowitz [21].

Besides the needs for better understanding of ocean surface waves for the classical applications i.e. design of coastal and oceanic infrastructure, and the design of ships and regulations for safety at sea, further research since few decades ago was fostered by the relevance of ocean waves on processes at both sides of the sea surface and essentially on the exchange between ocean and atmosphere as well as on mixing at the upper ocean layer, with some emphasis also on basic knowledge required for ocean remote sensing applications. A great number of field experiments and very important theoretical developments were carried out in the last decades that provided much needed basic and fundamental knowledge.

From the point of view of theoretical work, a very important and complete scheme to deal with nonlinear wave-wave interactions was proposed by Phillips [22], and further extensions and generalized form was advanced by Hasselmann [23–25]. Therefore, on one hand important theoretical framework has been established, while on the other, great numerical difficulties and computer limitations of the time, prevented from further development especially in operational forecasting numerical models. Nevertheless, practical approximations have been developed since the first scheme (Discrete Interactions Approximation) was presented by Hasselmann et al. [26], and they are now being used in forecast numerical routines. It is still important to mention a very relevant challenge. It seems it remains as a very difficult task to provide field measurements evidence for the nonlinear interactions being as relevant as the theory predicts. Maybe this aspect of ocean surface wave dynamics requires a lot more of attention and efforts to make an appropriate progress.

From the Stereo Wave Observation Project (SWOP), the first field campaign to estimate the directional wave spectrum as a function of the wavenumber vector **k** from stereo pairs of photographs of the sea surface [27], when they observed a narrow directional wave spectrum for the longer waves (in comparison with the shorter ones) and a remarkably close results to theoretical spectrum derived by Neumann, to the Joint North Sea Wave Project (JONSWAP) when a classical spectral form was defined and basic elements were developed to advance on the relative importance of non-linear energy transfer among wave components for the evolution of the spectrum [28]. Wave measurements were also carried out with an array of wave staffs in Lake Ontario [29], and it was determined that the frequency spectrum in the rear face is inversely proportional to ω^{-4} while the directional spreading of the wave energy has the form $\mathrm{sech}(\theta)$, where ω is the wave frequency and θ the wave propagation direction relative to the wind.

The relevance of surface waves on air-water interaction processes was more recognized with time, and with results from very detailed laboratory experiments a clear influence of waves besides the wind speed was identified [30] especially in the transfer of carbon dioxide and water vapour under smooth and rough flow conditions.

More recently during the Surface Wave Dynamics Experiment [31], wave directional spectra were measured along with estimates of fluxes between ocean and atmosphere. The presence of swell, both counter and cross direction relative to the wind, showed that the drag coefficient was larger than under conditions of pure wind sea. Later on new experiments were designed and carried out, for instance: The "Flux, etat de la mer, et télédétection en conditions de fetch variable" ETCH experiment [32]. Some of the objectives of this experiment were closely linked to the estimation of turbulent fluxes in the open ocean and to determine the effect of the sea state on those fluxes when fetch-limited wave growth was also considered.

As it is pointed out in a rather comprehensive analysis [33], the ocean-atmosphere coupled system deserves further attention and it is a future challenge to include simultaneous measurements of winds, currents and waves, since they are crucial for the air-sea exchange of momentum, energy, heat, freshwater gases and other tracer gases.

The focus of this contribution is on the relevance of ocean surface waves in air-sea interaction processes, and in Sect. 2, recent developments are described very much linked to momentum and gas exchange. Specific aspects associated with the influence of ocean surface waves in the CO_2 exchange in relation to our planet's climate and its future scenarios is presented in Sect. 3. In Sect. 4 emphasis is given to remote sensing measurements of the ocean and its relation to direct observations of dynamical processes of the upper ocean. Finally, some concluding remarks are provided in Sect. 5.

2 Recent Developments on Air-Sea Exchange of Momentum and Gases

In order to properly address ocean-atmosphere interactions and to study their associated processes, it is important to be able to obtain direct measurements of the relevant variables and the fluxes of interest from appropriate observing platforms. They could be fixed structures, research vessels, floating platforms and buoys. Quite a number of experimental field campaigns have been organized and carried out in the last decades with various different platforms and devices. From the Floating Instrument Platform (FLIP) to other various research vessels, fixed platforms in the coastal region and continental shelf, surface buoys, among others, important results have been put forward to advance our knowledge regarding the influence of ocean surface waves in air-sea interaction processes. Now, remote sensing of the ocean is also considered as an essential and needed component for a complete and robust global ocean observing system, and a very detailed description of the relevance of different measuring techniques associated with studying the sea state is given by Ardhuin et al. [34].

In this section, at least when dealing with the air-sea momentum fluxes, we will rather focus our attention to observations obtained from buoys and in a specific case from FLIP. An air-sea interaction spar (ASIS) buoy has been designed and successfully tested since some time ago (Graber et al., 35) and this type of measuring platform has been used later on in various field experiments [32, 36, 37]. A view of the first ASIS type buoy deployed in Mexican waters is given in Fig. 1.

Even if the global coupling between the ocean and atmosphere is of outmost relevance to climate and general circulation, this time we are more concerned with the specific air-sea interaction problem trying to define the particular processes and the influence of ocean surface waves, to merely work towards establishing the

Fig. 1 Air-sea interaction spar (ASIS) buoy deployed in 2005 in the Gulf of Tehuantepec, Mexico, during the INTOA Experiment [36], with the support of the DR06 Bahía Tepoca vessel from the Mexican Navy (Secretaría de Marina-Armada de México), as seen in the background (Photo: S. Ramos)

boundary conditions that are to be applied to the sea surface (the ocean-atmosphere interface) in order to determine the specific mean conditions on either side of that interface. The main constraint on the mean horizontal momentum equation is the vertical flux of horizontal momentum i.e. the surface stress, which in this case comes from the wind effect upon the sea surface (or vice versa in some cases in the real ocean). In a similar fashion, the vertical flux of a property or gas, such as CO_2, is the main constraint in the mean concentration equation. Probably a common practice is to determine the surface fluxes from mean values, which might be reasonable if we have appropriate parametric description of the transfer process. We rely on the so-called bulk aerodynamic formulae to estimate [38] the air-sea fluxes such as:

$$\overline{w'q'} = \frac{E}{\rho} = -C_E(Q_z - Q_s)(U_z - U_s) \tag{1}$$

$$\overline{w'm'} = \frac{F}{\rho} = -C_F(M_z - M_s)(U_z - U_s) \tag{2}$$

where E stands for evaporation and F is the gas flux across the interface. The fluctuations of the vertical wind velocity is denoted with w', while q' and m' are the fluctuations of the concentration of water (specific humidity) and gas, respectively. The bar over the fluctuating variables denotes the covariance. The subscripts z and s indicate the height where the measurement is taken and the surface, respectively. Water vapor saturated value at the surface is Q_s. The bulk transfer coefficients are then identified as C_E, the Dalton number for water vapor, and C_F for gas flux.

While we can establish a way of determining the fluxes directly, through the measurements of fluctuating quantities, this is not an easy task to perform regularly in the field, neither there is a simple way to include this type of information in numerical models that are routinely operated to forecast the weather and sea state or to predict future scenarios of our planet's climate. Often, the bulk formulae are used and they are considered as the only available alternative. One concern is the knowledge or the meaning of the transfer coefficients, which are over charged with many details and we tend to include unknown processes behaviour into them.

We certainly can advance our knowledge of specific air-sea interaction processes when we measure directly the fluxes and every other relevant environmental variable, in our case it should mean we need to properly measure the ocean surface wave field simultaneously.

2.1 On the Transfer of Momentum Between the Ocean and Atmosphere

Although fluxes described with Eqs. (1) and (2) relate to scalar properties, a similar form of equation can be considered for the vertical flux of horizontal momentum.

From wind velocity components measured by a sonic anemometer, for instance, the wind stress ($\boldsymbol{\tau}$) can be directly calculated through the eddy-correlation method as

$$\boldsymbol{\tau} = -\rho \left(\overline{u'w'}\hat{\boldsymbol{i}} + \overline{v'w'}\hat{\boldsymbol{j}} \right), \tag{3}$$

where u', v', and w' are the turbulent velocity components, ρ is the air density, the over-bar represents time averaging over a certain period of time (typically 30 minutes or so), and $\hat{\boldsymbol{i}}$ and $\hat{\boldsymbol{j}}$ represent unit vectors. The sign is such that $\boldsymbol{\tau}$ is in the direction of the horizontal velocity vector for a downward flux.

Furthermore, the wind friction velocity (u_*) can be directly estimated as $u_* = [|\boldsymbol{\tau}|/\rho]^{1/2}$. We see that we relay on the bulk formula and wind stress is typically expressed in terms of the drag coefficient, C_D, by

$$|\boldsymbol{\tau}| = \rho C_D U_z^2, \tag{4}$$

where we usually avoid a dependance of C_D on measuring height and atmospheric stability, and C_D is computed for neutral conditions at the 10 m standard height. Wind speed is typically converted to a neutral conditions value using the flux profile relation [38], such that

$$U_{zN} = U_z + \frac{u_*}{\kappa}\psi_u \ , \tag{5}$$

where κ is the von Kármán constant, $\psi_u = \psi_u(z/L)$ represents the non-dimensional gradient suggested by Donelan [38], and L is the Obukhov length. Wind speed at standard 10 m height is then calculated assuming a logarithmic wind profile

$$U_{10N} = U_{zN} + \frac{u_*}{\kappa}\log\frac{10}{z} \tag{6}$$

and the drag coefficient directly determined through Eq. (4).

We may then investigate the behaviour of the drag coefficient in order to determine and study the influence or effect on the wind stress that comes from the various different processes involved. A simple examination of C_D results as a function of wind speed will readily show that the wind stress does not only depend on the wind itself, but some other processes are present and owe to be considered in order to properly describe the momentum transfer and to be able to incorporate all pieces of information for the ocean-atmosphere coupled numerical models best performance.

Recent results from a field campaign carried out during winter 2017–2018 are shown in Fig. 2. The drag coefficient is estimated upon the direct calculation of the wind stress according to Eq. 3. General sea state conditions include the simultaneous presence of swell and wind sea [39], with swell dominance during most of the measurements period of time. It is important to mention that swell

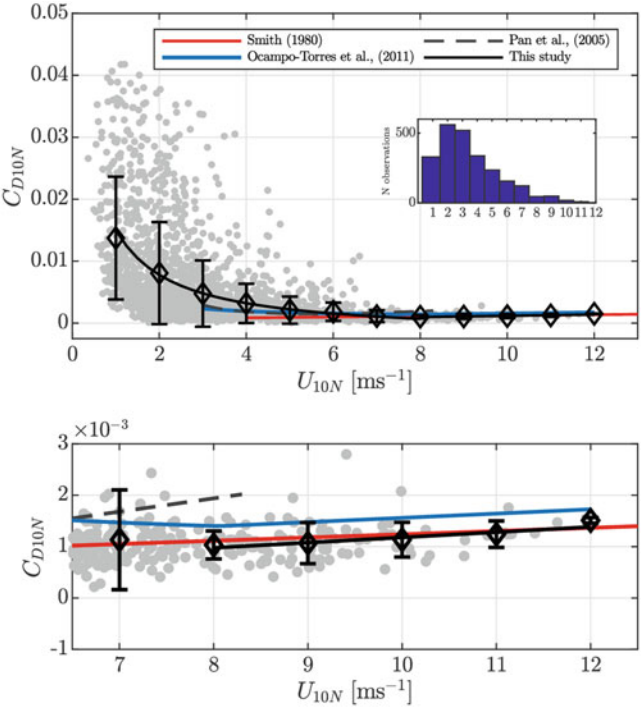

Fig. 2 Drag coefficient (C_{D10N}) as a function of wind speed (U_{10N}) as obtained from measurements with an ASIS buoy offshore Bahía Todos Santos, Baja California, Mexico, during the field experiment carried out between November 2017 and February 2018. Each dot represents the results from eddy covariance using an average over 10 min. Diamonds correspond to wind speed bin average in 1 ms^{-1} classes. The relationships obtained from previous experiments are also shown, Smith (1980) as red line, Ocampo-Torres et al. [36] as blue line, and Pan et al. [41] as grey dashed line. The inset histogram recalls in the number of data considered as a function of wind speed [ms^{-1}]

propagation direction was practically the same as the wind sea. Under low to moderate conditions, the drag coefficient decreases with wind speed, a behaviour already observed in some previous studies [36]. When wind conditions are moderate to strong, the drag coefficient increases with the wind speed, and the values reported are rather similar to those associated with the relationship provided by Smith [40], resembling more open ocean conditions. It is most likely that the differences shown with respect to the results obtained in the Gulf of Tehuantepec [36] and those in the Gulf of Mexico [41], are associated to the swell presence and their characteristics. Conditions in those studies were rather particular, swell opposing locally wind generated sea in the Gulf of Tehuantepec, and rather short and young swell in the Gulf of Mexico.

So far, we here draw attention to the study of momentum transfer from the analysis of its magnitude only. However, it should be bear in mind that the horizontal momentum is a vector quantity. Therefore, when dealing with the potential effect of swell, it should be important to also consider the swell propagation direction, probably not only in the local and micro scale of the processes we are trying to understand, but also in a wider view and larger scales. The challenge should be taken and then study the behaviour of swell even from their generations spot, considering that it will might affect somehow air-sea interaction processes and the weather patterns all along its travel to the coast. It should also be taken into account that there most likely will be a two-way interaction between swell and the atmosphere boundary sub-layer just above, and into larger scales, there might be implications to and from climate patterns.

Nevertheless, coming back to the results from the INTOA experiment [36], the relative importance of the swell present during the field measurement period on the sea surface roughness is shown in Fig. 3. The wind-sea energy E_{ol} is shown as function of friction velocity u_*, while the relative swell importance as given by the swell index is indicated with the colour scale. Also, black dashed line is the best fit to the BHDDB data ensemble [28, 29, 42–44], under near-neutral and steady wind conditions.

It is readily noticed that for a specific wind friction velocity, locally generated waves are higher when swell is less important. This apparent inhibition to wind-sea grow due to the presence of swell in the opposite direction is still a matter of research, where definitely more efforts and new measurements are required.

Let's now address some results and analysis regarding the wind stress direction. If we stick to the bulk formulae, wind stress direction will always be the same as the

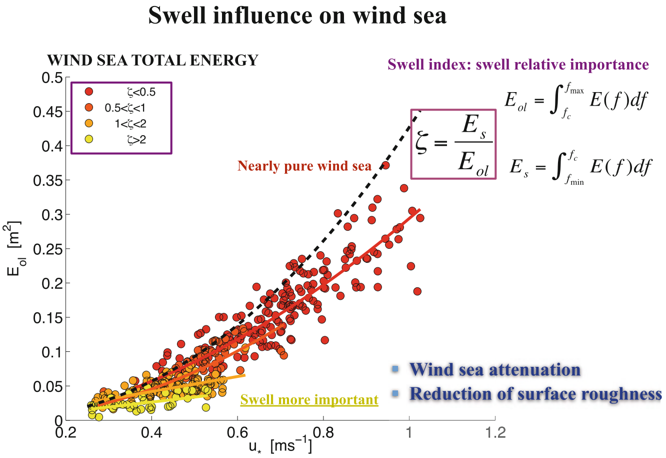

Fig. 3 Wind-sea energy E_{ol} as a function of friction velocity u_* from data obtained during the INTOA experiment [36]. Swell index is indicated with the colour scale. Black dashed line is the best fit to the BHDB data ensemble [28, 29, 42–44], under near-neutral and steady wind conditions

mean wind direction, for it is only the magnitude $|\boldsymbol{\tau}|$ what it is considered, and the actual direction is disregarded.

From measurements acquired from FLIP, and through one of the first descriptions of the deviation of wind stress with respect to the mean wind direction [45], it is now recognized that in general mean wind and wind stress not necessarily are alligned. This deviation comes from surface or near-surfaces effects, which might be due to the sea surface geometrical structure, the presence and dynamics of swell, and also from surface currents (mean and large scale, wind induced and wave generated surface currents) and from the dynamics within the upper ocean.

Results from the INTOA experiment show that the deviation of the wind stress relative to the mean wind might be considerable, and that the presence of swell plays a significant role, as it can be seen in Fig. 4.

Further efforts are required to better understand the wind stress resultant direction, since this is of paramount importance for ocean-atmosphere coupled numerical models to properly describe the transfer of momentum which ultimately will determine the amount of kinetic energy into (and out from) the oceans. It is

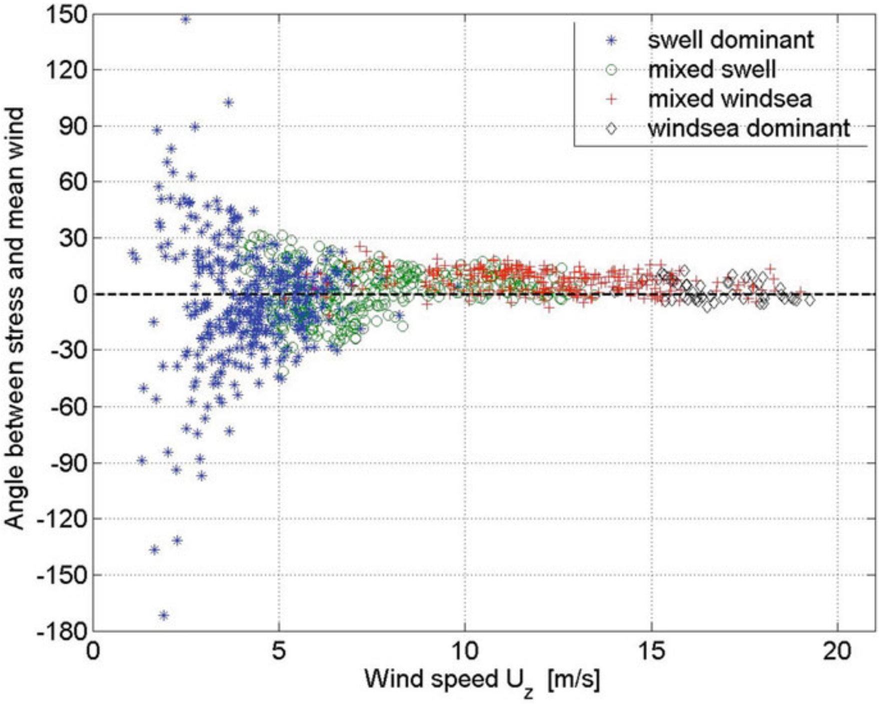

Fig. 4 Relative direction of wind stress with respect to the mean wind [degrees], as a function of reference wind speed at $z = 10$ m height. The horizontal dashed line refers to wind stress aligned with the mean wind direction. The relative importance of wind-sea and swell are indicated with symbols. Each symbol correspond to eddy covariance results with average over 30 min, from data obtained during the INTOA experiment [36]

this knowledge probably much more critical when dealing with the important small scale processes at, and on both sides of the interface, the generation of ocean surface waves, upper ocean turbulence and surface drift, for instance. The wind stress vector may deviate considerably from the mean wind flow [46]. This might include cases when stress is directed across or even opposite to the wind. Proper determination of the wind stress vector is very important in many other applications, end especially those associated with oceanography from space or remote sensing of the ocean surface, particularly when considering that with most remote sensing techniques we can directly detect details and processes right at the sea surface only.

2.2 *On the Transfer of Mass and Carbon Dioxide Between Air and Water*

Here we now deal with the idea regarding the influence of ocean surface waves in the transfer of scalar quantities, in some detail on the evaporation process and with further expansion on the transfer of carbon dioxide between the ocean and atmosphere.

Besides the natural curiosity of understanding the actual processes driving and affecting somehow the overall air-sea transfer mechanisms, it has been clear that we aim to obtain the best of our knowledge in that respect, in order to be able to predict in the most appropriate fashion the ocean-atmosphere exchange processes of greenhouse gases for instance, and in due course to predict our climate and its changes. Weather and climate predictions are now possible mainly through the use of powerful numerical models, where the best of our knowledge is incorporated and coded in a computer language.

For the specific case of climate description and prediction, as well as for the generation of future scenarios and projections, these powerful models, among many other tools and schemes, make use of parameterizations of the formulae that represent physical, chemical, and other relevant, processes. And specially when dealing with the fluxes of important greenhouse gasses like carbon dioxide F_{CO_2}, then an expression [47] such as

$$F_{CO_2} = k_{CO_2}([CO_2]_{sat} - [CO_2]), \tag{7}$$

is considered, where $[CO_2]$ is the gas concentration and $[CO_2]_{sat}$ is its corresponding saturation concentration in equilibrium with the water-vapor-saturated atmosphere at a total atmospheric pressure P_a. As it is seen, the gas transfer velocity k_w plays a crucial role in the estimation of the fluxes between ocean and atmosphere, and it is definitely important to rely in its most complete version, for it is through this velocity where the most important processes driving and affecting the CO_2 transfer are incorporated into the models.

From a series of laboratory experimental runs it was determined that the exchange of slightly soluble gases, such as CO_2, as well as the evaporation process, do not depend solely on wind speed [30]. The experiments were carried out in a specially designed and tightly closed gas transfer flume, including smooth and rough flow conditions. With the very detailed results of this classical work, the importance of establishing and studying the mass transfer velocity as well as the exchange coefficients was recalled.

The wind-speed dependance of k_{CO_2} showed to be stronger than linear. For the case of evaporation, a wind-speed dependance of k_{H_2O} was also clearly observed, and it was noticed that k_{H_2O} increased with wind speed for all range of speeds considered, while for the case of CO_2, its transfer velocity remained constant when wind was lower than 3 ms^{-1}. Furthermore, a clearly increase in k_{CO_2} was observed associated with the onset of initial waves, that occurred when wind speed reached about 3 ms^{-1}. As expected k_{H_2O} did not show any sudden increase associated with the onset of initial waves, showing evidence on the difference on water phase and air phase limited compounds. Micro breaking of small waves are much associated with an effect of ventilating the water side diffusive sub-layer, and with a much smaller effect on the turbulence in the air side.

As it was considered earlier, it is convenient to make use of the bulk parameterization of the transfer rates or velocity in terms of wind speed, we then refer to the bulk transfer coefficient or Dalton number. Both, Dalton number for evaporation $\mathcal{D}_{H_2O}$ and for the CO_2 exchange process showed a minimum when wind was between 2 and 3 ms^{-1}. That very detailed dependance of the bulk transfer coefficient was presented for the first time, stressing the influence and the relevance of other processes besides wind speed on the air-sea interaction processes.

When trying to compare the mass transfer velocity of gases that are limited in different phases, a proper alternative is to convert them to a common reference. We owe to consider the most important physical and flow characteristics. These are viscosity for air and water, ν_a and ν_w, respectively, as well as the Schmidt numbers for H_2O and for CO_2, and friction velocity in both air u_{*a} and in water u_{*w}, and the mean square slope of the waves. The mass transfer velocities for H_2O and for CO_2 are then normalized by the corresponding friction velocity, such as:

$$K_{H_2O} = k_{H_2O}/u_{*a} \tag{8}$$

$$K_{CO_2} = k_{CO_2}/u_{*w} \tag{9}$$

The results were given as a function of the appropriate Reynolds number [30], such as:

$$Re_{*a} = \frac{z_0\ u_{*a}}{\nu_a} \tag{10}$$

$$Re_{*w} = \frac{z_0\ u_{*w}}{\nu_w} \tag{11}$$

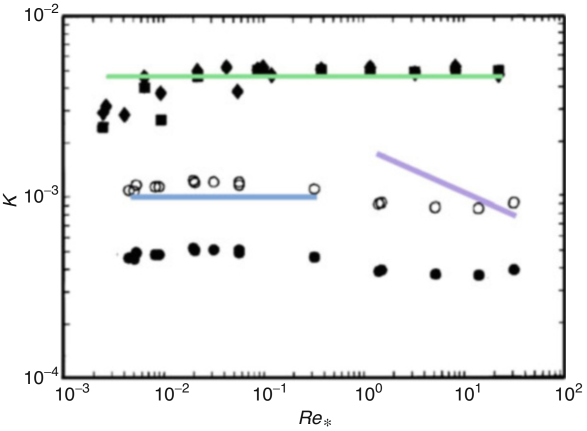

Fig. 5 Results for normalized mass transfer rate K as a function of Reynolds number Re_*. Estimations were obtained in laboratory experiments [30], K_{CO_2} as calculated from rate of change in concentration in air are black diamonds, and those in water are black squares. Results of Jahne et al. [48] linear fit is shown (green line). For comparison K_{H_2O} was adjusted to a Schmidt number equal to 600 using exponent of -0.704 (filled circles) and -0.58 (open circles). Solid wall results of Shaw and Hanratty [49] for smooth flow (blue line) and of Dawson and Trass [50] for rough flow (purple line) are also shown. Modified from Ocampo-Torres et al. [30]

and they are reproduced in Fig. 5

The transfer of H_2O is determined by the near-surface turbulence in the air and the dense water surface is more appropriately viewed as a solid wall that as a free surface. On the other hand, since CO_2 is a slightly soluble gas, the resistance to its transfer takes place most importantly in the aqueous phase, then the transfer properties are determined by the turbulence in the water near the free surface.

The K_{CO_2} results [30] show higher normalized mass transfer rates than those corresponding to a solid wall (blue and purple lines). Jahne et al. [48] have demonstrated this enhancement in comparison to the transfer over a solid wall results, they showed that the normalized mass transfer rate are well represented by a dependance on as 0.11Sc (green line). These experimental results confirm those from Jahne et al. [48].

The experimental results of K_{H_2O} are not in agreement with the empirical results from mass transfer at solid wall, a factor of 2 lower at low Reynolds numbers (compare filled circles with blue line). At high Reynolds numbers, experimental results of K_{H_2O} intersect the results of Dawson and Trass [50] but they are not in agreement with their $Re_*^{-1/4}$ (compare open circles with purple line). This is an important warning and show inadequacies of the solid wall results in predicting transfer rates of air phase limited compounds at the air-water interface.

A better modeling of air-water exchange of gases requires new experiments and insights, and definitely further and detailed measurements both in laboratory and in the open ocean, to clearly establish Schmidt number, Reynolds number and wave slope dependancies of normalized mass transfer rate of both air phase and water phase limited constituents.

It is rather well known that air-gas exchange has been of intensive scientific research for several decades for its great importance to biogeochemical cycles of climate and weather, at least. Also, it has been recognized that gas exchange contributes to reduce green-house effect through absorption of CO_2 by the ocean. Accordingly, excellent reviews have already been provided [51, 52] where the authors stress, among other issues, about the increasing evidence that the gas transfer cannot be adequately quantified solely with wind speed. A summary of selected key contributions in that respect follows.

Direct covariance method to obtain air-sea CO_2 fluxes is proven to be effective and provide best results, as it has already been reported [53]. The authors describe the very relevant results of an interdisciplinary air-sea gas exchange experiment (GasEx-98) carried out in May and June, 1998, in the North Atlantic.

The oceanographic cruise included a wide range of independent air-sea gas exchange measurement techniques. Of particular importance for this section are those associated with estimates of air-sea gas exchange as they were derived from CO_2 atmospheric gradients, and from direct covariance CO_2 measurements. As main results, the authors pointed out that the air-sea gas exchange measurements when wind conditions were in excess of $11\,\mathrm{ms}^{-1}$ show a general enhancement of gas transfer velocity with respect to other previous indirect measurements. This enhancement might be well explained by the fact that the indirect methods cannot discriminate important surface process variability such as atmospheric stability upper ocean mixing, and specially ocean surface wave characteristics like wave age, wave steepness and wave breaking. It is definitely clear that in order to better understand the relationship between gas physical properties, surface processes, and air-sea CO_2 exchange, direct CO_2 flux measurements are very relevant and certainly needed.

Even if specific wave influence is already refer to, the authors advanced an expression for the gas transfer velocity k, such as

$$k_{660} = 3.3 + 0.025 U_{10}^3 \tag{12}$$

where it has been related to Schmidt number equal to 660. Furthermore, with some more analysis incorporating de drag coefficient (exchange coefficient for momentum) and considering the CO_2 exchange associated Dalton number, a modified and certainly more complete representation is given as,

$$k_{CO_2} = C_D^{-1/2} U_r \mathcal{C}_{CO_2} \tag{13}$$

where $\mathcal{C}_{CO_2}$ is the CO_2 transfer coefficient when u_* is considered and it is defined as $\mathcal{C}_{CO_2} = k_{CO_2}/u_*$. Results from the open ocean as in the GasEx-98 Experiment also showed a minimum in Dalton number $\mathcal{D}_{CO_2}$ when wind speed U_{10} was near 3 ms^{-1} (see Fig. 10 in McGillis et al. [53]), confirming previous laboratory experiments results [30]. This also helps to emphasize that processes controlling air-water CO_2 transfer, those processes in the aqueous boundary layer, are not the same as those processes controlling the water vapor fluxes.

Further air-sea gas exchange measurements were needed and some were carried out during the GasEx-2001 Experiment [54], which took place in the equatorial Pacific in the South Equatorial Current, in February 2001. Other physical processes, in addition to wind, were observed to control the rate of CO_2 transfer from the ocean to the atmosphere confirming that these processes owe to be taken into account in local and global biogeochemical models. The results strongly establish the fact that gas transfer parameterizations that rely solely on wind will be insufficient for regions with low to moderate winds and specially with strong insolation. The persistence of low to moderate wind over the ocean and relatively high values of air-sea pCO_2 difference (CO_2 partial pressure), proved to be effective for the region to prevail with high mean transfer of CO_2 to the atmosphere. From a regression analysis with the air-sea gas transfer data on wind speed a parameterization for the gas transfer velocity is

$$k_{660} = 8.2 + 0.014 U_{10N}^3, \tag{14}$$

although it is clear that ocean surface wave characteristics have to be considered properly especially for the low wind conditions prevailing, when it is clear that the wave field is not necessarily coupled or directly linked with the local wind field. Gas transfer velocity is readily noticed to be higher than other parameterizations for low wind conditions (see Figure 12 from McGillis et al. [54]), however, data and regression analysis provide values well between previous and classical parameterizations. Special care should be taken when swell waves are predominant and the surface wave spectrum is not associated with waves in equilibrium with the wind.

In one of the first attempts to incorporate the wave breaking effect on the gas transfer of gases [55], it was assumed that the transfer velocity k was the sum of two contributions,

$$k = k_0 + k_b, \tag{15}$$

where the non-breaking k_0 contribution [48] was given as,

$$k_0 = 1.57 \times 10^{-4} u_* (600/Sc)^{1/2}, \tag{16}$$

and the breaking contribution is proportional to W the fractional whitecap coverage, such as $k_b = 850\,\mathrm{W}$. This model and description provided much promise, mainly due to the incorporation of a relevant form of Reynolds number, which is defined approximately to W, therefore

$$W \sim R_{H_w} \tag{17}$$

and

$$R_{H_w} = u_* H / \nu_w \tag{18}$$

being ν_w the kinematic viscosity in water.

With another important modeling work [56], a mixing length model was proposed specially for the aqueous boundary layer including the effect of wave breaking on enhancing gas transfer. Wave breaking is a source of vertical turbulent energy to the aqueous boundary layer. Breaking therefore acts to disrupt the very thin viscous sub-layer near the surface. An important consideration is that dissipation rate, overall variance integrated over all wavenumbers, corresponds to an unambiguous connection with the effect of wave breaking on the mixing length. The resulting model is rather general, it can be used for all sparingly soluble gases and any gas-liquid interface. The model established for the air boundary layer, is then applied to the water boundary layer with the important role of wave breaking in mixing the sub-layer, once it is included through wave dissipation rate.

In both studies previously referred to, wave breaking was assumed very linked to the local wind, which is very much the case when wind is acting to force upon the sea surface, generating wind-waves, making them to grow, and maybe leading to reach well developed sea, in all these conditions there is wind-wave coupling. However, wave conditions out of equilibrium with the local wind is commonly observed in coastal regions, therefore modeling air-sea fluxes in those regions are even more limited if parameterizations used rely solely on wind speed. Typical conditions nearshore can be seen in Fig. 6 and, where most of the time it is swell waves what arrives to shore, beaches or cliffs.

Therefore, direct calculations of gas transfer fluxes (through eddy-covariance method) are still much needed in order to properly take into account those processes besides the wind. Recent measurements in a coastal region near Ensenada B.C., Mexico, show a sink of CO_2 into the coastal ocean during the period of the field campaign carried out from May 2014 to April 2015 [57]. Results of air-sea fluxes in the coastal region are shown in Fig. 7.

Although, it was not possible to estimate the transfer velocities, direct measurements during this experiment allowed us to calculate the fluxes for both, evaporation and CO_2. As expected from the coastal region conditions, air-sea fluxes results showed no direct association with the local wind speed (see Fig. 8).

However, the significant wave height H_S was found to be best correlated with F_{CO_2} based on quantile-regression analysis. Simultaneous measurements of CO_2 concentration in both sides of the interface are necessary to fully assess the effect of waves and their breaking process both on the fluxes and on the gas transfer velocity. We are continuing to explore these ideas in the coastal region, we therefore anticipate our plans to deploy an ASIS type buoy (see Fig. 9) in the vicinity of Todos Santos Islands, offshore Ensenada B.C., Mexico, in the near future, with a suite of instruments that will include fast response CO_2 infra-red sensors.

While it is generally understood that air-sea flux of CO_2 is a critical part of the climate system, its contemporary behaviour is investigated with the use of an air-

Fig. 6 Coastal region where experiments to calculate CO_2 fluxes directly were carried out [57]. Swell is very common in this region, then wind conditions are not in equilibrium with the sea state. Waves effect in the gas transfer between atmosphere and ocean in the coastal region should be appropriately included, besides wind speed, in transfer velocity descriptions. Light wind is readily apparent in the scene

sea flux equation [59], with special attention to some uncertainties. In particular, uncertainties derived from the gas transfer velocity when using a set of eight formulations. Even if there is growing evidence on the effect of ocean surface waves on the gas transfer velocity, with this work the various gas transfer formulations used are given as a function of wind speed through polynomial expressions. The traditional wind-speed-dependent parameterization is used, as

$$k = (600/Sc)^{1/2}(c_0 + c_1U + c_2U^2 + c_3U^3), \tag{19}$$

where U is the wind speed corrected to an equivalent value in a neutrally stable atmosphere (U_{10N}, already defined before), and the coefficients c are provided (see Table 1 in Woolf et al. [59]). These expressions are an example of those found experimentally somewhere else, but they provide a reasonable test for uncertainties in fluxes as they result from the uncertainties in the gas transfer velocity.

At least within the global context of this analysis, it seems that the primary cause of uncertainty in the contemporary global annual value of net air-sea CO_2 flux (-3.0 ± 0.6 Pg C/year) is the uncertainty in the transfer velocity. It is still expected

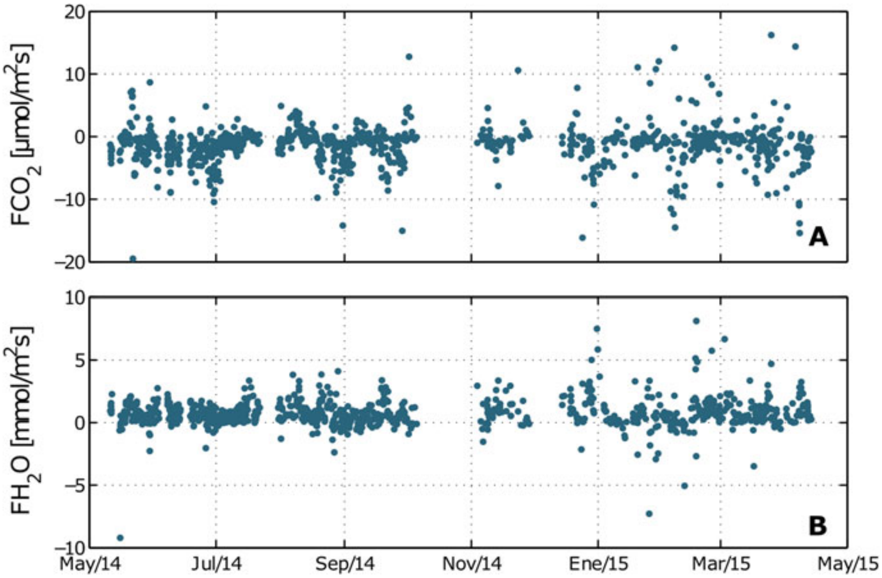

Fig. 7 Time series of fluxes calculated through eddy covariance method in the coastal region near Ensenada, B. C., Mexico during 2014–2015, for both carbon dixode and evaporation. Positive flux is towards the atmosphere

that better and more consistent models of air-sea gas transfer velocity (probably more refined than those associated with Eq. 19) being generated by different authors would contribute to greater confidence in those estimates. It might be crucial the proper incorporation of better description of the effect of ocean surface waves in the gas exchange, mainly because these type of expressions are the ones used in the most advanced climate system models to predict the future climate in our planet.

Research aim at determining wave characteristics influencing gas transfer originated some decades ago [30, 48] where it was shown that the mean square slope was an appropriate index for the gas transfer velocity. Wave breaking and the fractional area coverage of microbreakers in laboratory experiments [60, 61], as well as whitecap coverage at open ocean were also considered to scale the gas transfer velocity. Meanwhile, wind-sea Reynolds number was proved to be somehow better than wind speed in describing whitecap coverage [62]. Making use of the idea of wind-sea Reynolds number, some more elaborated results have been reported very recently [63] where a nondimensional version of gas transfer velocity $\tilde{K}$ has been presented, from observations obtained in laboratory experiments. Two expressions were developed such that

$$\tilde{K} = 4.6 \times 10^{-9}[b_T R_{\mathrm{HB}}(1+\tilde{U})]^{-0.70} \quad \text{and} \tag{20}$$

$$\tilde{K} = 2.0 \times 10^{-9}[R_{\mathrm{HM}}(1+\tilde{U})]^{-0.69}, \tag{21}$$

Fig. 8 Coastal region scene where swell is observed to be present, another clear example when wind conditions are not in direct association with ocean waves. Rather strong wind is affecting the waves in such a way that fluid separation is observed in some wave crests. Swell waves arriving are present regardless of wind conditions

where

$$R_{\mathrm{HM}} = \frac{H_s U_{wm}}{\nu_w} \quad \text{and} \qquad R_{\mathrm{HB}} = \frac{H_b U_{wb}}{\nu_w}, \tag{22}$$

are a novel version of wind-sea Reynolds numbers. They both have the same structure but include different wave parameters: in R_{HM} some statistical characteristics of all waves are then considered, the significant wave height H_s and the mean orbital velocity U_{wm} are taken into account, while in R_{HB}, wave breaking features are highlighted, therefore height H_b and orbital velocity U_{wb} associated with breaking waves are considered. When estimating the nondimensional gas transfer velocity $\tilde{K}$ through Eqs. 20 and 21, the wave breaking probability b_T and a nondimensional version of the wind speed $\tilde{U} = u_*/\sqrt{gH_s}$ are to be considered.

It should be clear now that we need better physical models for k_{CO_2} where wave effects are explicitly included in order to reach improved flux estimates over specific and limited spatial domains, as well as over certain temporal events that might lay away from the mean behavior of the wind-based formulas. It is recognized that k_{CO_2} is critical to the prediction of CO_2 fluxes in the global climate system,

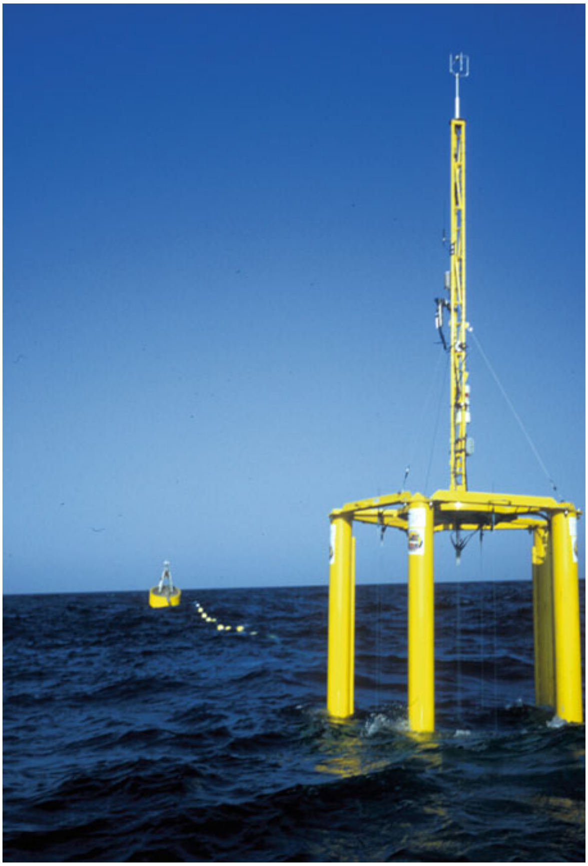

Fig. 9 Air-sea interaction spar buoy to be deployed offshore Isla Todos Santos, Ensenada, Mexico. It will include fast response CO_2 sensors, besides a sonic anemometer located on top of the mast which is needed to measuring wind turbulent fluctuations. An array of wave staff will provide sea surface elevation to estimate the ocean surface wave directional spectrum with a fine directional resolution. Following the Wavelet Directional Method, proposed by Donelan et al. [58], it is also possible to estimate de spectrum as a function of the wavenumber vector (Photo: S. Ramos)

therefore its parameterization is still a major research topic that requires further efforts. Ultimately, we need the correct transfer velocity to be incorporated in the modern numerical models to predict the future climate and generate scenarios under the possible alternatives of carbon use, and mainly to properly address the CO_2 gas flux between the atmosphere and ocean.

3 Air-Sea Exchange of Carbon Dioxide and the Relevance of Ocean Surface Waves Within the Context of Climate Prediction

The sea surface is well recognized as of paramount importance, since it actually is the air-sea interface a key gateway in the Earth system [64]. The sea surface is right where the atmosphere transfers energy to the ocean and set it in motion, and it is right there where climate and weather-relevant air-sea forcing and feedback processes occur. Besides, anthropogenic carbon dioxide enters the ocean mainly through its surface. Once we realize that it is ocean surface waves what form the actual surface, their relevance in diverse processes taking place in the vicinity is somehow very clear. It might be wise to emphasize in these ideas pointing out to some explanation originally expressed by Benton [65] and Donelan [38]: On average the ocean absorbs more than 2.5 times the incoming solar radiation (which is in the form of short wave) than does the atmosphere. The energy from the warmed ocean surface is transferred to the atmosphere by infrared (long-wave) radiation and by sensible and latent heat transfer. Therefore, we can realize that the atmosphere, to a large extent, is heated from below. Zonal differences in heating and the Earth's rotation drive the large scale atmospheric circulation, from which the oceans acquire most of their energy and momentum. It is now clear that there is exchange through the interface, and the energy originally provided by the sun, crosses the sea surface in one form or another, at least three times before it becomes the kinetic energy of oceanic waves and currents.

The impact of surface wave dynamics on the air-sea fluxes has been readily shown [66], through the global distribution of the ratio of the wave induced momentum transfer computed with the WAM model, to the total momentum transfer into the ocean, computed using the standard Charnok drag law.

The effect of ocean surface waves has also been identified in the mixing process of the uppermost layer of the ocean, just below the sea surface. It is in fact this thin layer what greatly influences and control the exchange of heat and gases such as CO_2 between the ocean and atmosphere. Through a diagnostic study it is suggested that the turbulent energy available for mixing in the upper ocean layer is underestimated when surface waves are not included as forcing [67]. This direct us to the recommendation for global climate models to compute and take into account the wave field, specially to represent wave forcing of Langmuir turbulence acting within the uppermost layer of the ocean.

Let's now address some specific details the global climate models deal with, regarding the exchange of CO2 between ocean and atmosphere. It seems that modelers [47] use the instantaneous gas transfer velocity k as parameterized by Wanninkhof [68], which is a quadratic function of the wind speed U_{10} referred as to be measured 10 m above the mean sea surface, such that

$$k = a(\frac{Sc}{660})^{-1/2} U_{10}^2, \tag{23}$$

where the constant a is normally adjusted so that wind speeds used to force the model are consistent with the observed global inventory of bomb ^{14}C (the bomb effect refers to additional radioactive carbon in the atmosphere that comes from nuclear weapons testing).

While classical parameterizations are still being used in global climate models, great effort is devoted to promote more and better in-situ measurements of air-sea fluxes, along with all the most relevant environmental variables in order to improve our understanding of the whole process. Authors have been put forward ideas and strategies to produce gridded information of fluxes and wind stress fields over the global ocean [69]. The strategy incorporates the expansion of already established buoys network, ocean surface wave information has to be included in the recorded data.

Cronin et al. [69] conclude indicating that there are some research challenges that could lead to improve bulk flux parameterizations to be used in the global climate numerical models, such as the development of wave-dependent surface flux parameterization. In particular, it is needed to perform better than wind-speed-only dependent parameterizations specially under a wider range of wind, wave and current conditions, among others.

Above all, our main concern is still the gas transfer velocity description and its incorporation into the global climate models. In the previous sections, we have addressed the effect of ocean surface waves in the gas exchange process and mainly in relation to evidences from several sources. The main issue here is if we still keep and use parameterizations of the gas transfer velocity that relay solely in wind speed, then we will look at pictures like what it is plotted in Fig. 10.

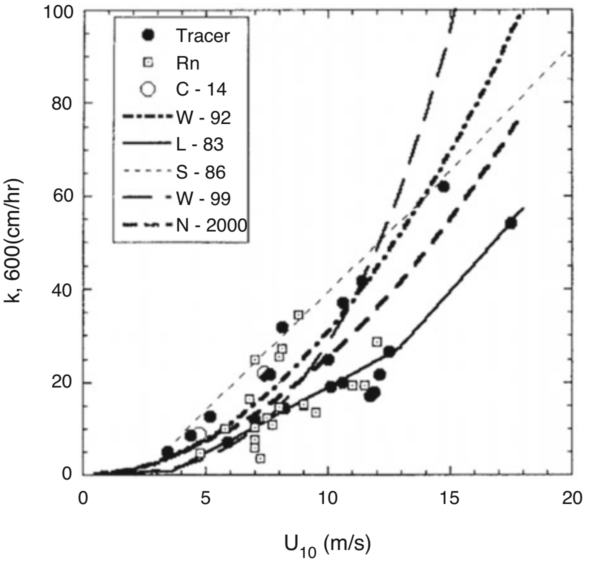

Fig. 10 Gas exchange results in the ocean and from empirical relationships, specifically, gas transfer velocity k is provided as a function of U_{10}. All data is normalized to $Sc = 600$. Dual tracer results are indicated as Tracer, ^{222}Rn results as Rn, and global estimate based on bomb-radiocarbon as C-14. Results from some empirical relationships are also shown, Liss and Merlivat (1983) indicated as L-83, Wanninkhof [68] as W-92, Smethie et al. [70] as S-86, Wanninkhof and McGillis [71] as W-99, and Nightingale et al. [72] as N-2000. From Donelan and Wanninkhof [73]

It is readily apparent from Fig. 10, that depending on the relationship or parameterization we decide to use in the corresponding numerical model, the predicted gas transfer velocity could easily be doubled when wind conditions are at low to moderate speed (6 ms^{-1} approximately), or even nearly tripled if wind speed were higher.

4 Remote Sensing Ocean Measurements and Their Relation to Upper Ocean Processes Direct Observations

Remote sensing techniques provide novel tools and unprecedent information regarding the upper ocean dynamics and characteristics. Great advantages are associated with the capabilities of observing the sea surface without protruding and over wide areas around the global oceans. Besides, measurements over the ocean surface can be obtained continuously, in some cases even during day and night. Although there are some limitations, we all agree that great amount of information can be retrieved from sensors in satellites and airplanes. Caution is advised, however, especially when calibration and validation are needed for it is imperative to be sure about the exact geophysical variable which is being acquired as well about the quality of its final value. Most information obtained by remote sensors are associated with the very surface of the ocean, except for some wavebands of the electro-magnetic signals that can penetrate (or come from) some centimeters to few meters into the water [74].

In this section we deal with some remote sensing ocean information that is useful to improve our knowledge regarding the link between air-sea interactions and ocean surface waves, and with some direct measurements of upper ocean processes that might be considered when retrieving dynamic variables from satellite derived data. While it is true that sea surface roughness, currents and winds over the oceans can also be retrieved from remote sensors [75], we are interested this time to focus on ocean surface waves.

Within the context of Earth observation data, radar images can be considered one of the most valuable information acquired from satellites. Sea surface information from synthetic aperture radar (SAR) images are popular since 1978 Seasat mission, the first satellite with a SAR on board dedicated to study the global seas [76].

Various different features can be detected from this type of images, and they are associated with specific surface or near-surface processes. In fact, features can be linked to ocean interior processes, as long as those processes interact in some way or another with, and can induce certain modulation to, the very short waves (ripples) present right at the surface, since these short waves are the actual reflectors or scatterers to the incident microwaves coming from the radar (Raney, 1983).

Great effort has been devoted to build the conceptual and theoretical framework to understand how ocean surface waves are detected by SAR, as well as to develop the numerical schemes to retrieve wave information from sea surface images acquired with SAR [77, 78]. From the rather large images obtained with ERS-1 for instance, a study has been prepared to track the waves generated by intense storms [79]. A brief overview about ocean wave measurements has been presented by Lehner and Ocampo-Torres [80], while a recent assessment of the ocean wave spectrum estimation using global Envisat-ASAR data has been provided by Li et al. [81].

Here we only approach the analysis of ocean swell as a matter of example, as it is well known that it can be detected and studied through images of the sea surface acquired with SAR. It is demonstrated by Li et al. [82] and Díaz-Méndez et al. [83], that high resolution SAR imagery in general and TerraSAR-X imagery in particular, is a suitable tool to observe the spatial variability of ocean surface wave behaviour.

The spatial variability of the wave field during the INTOA experiment [36] was studied through the analysis of SAR images of the ocean surface. Results from a set of 4 consecutive SAR images acquired by Envisat ASAR on 02 March 2005 at 16:20–16:21 h over the Gulf of Tehuantepec region [84] are shown in Fig. 11. SAR-inverted spectra, derived following Collard et al. [85], revealed a strong variability of the wave field along its propagation over approximately 400 km, with frequently observed multi-peaked spectra. Results are shown for two wave systems found, both with similar wavelength but with different mean propagation direction.

These results demonstrate the capabilities of SAR onboard satellites to provide images over ocean areas where variability and spatial evolution of swell can be determined with outstanding resolution. It is worth mentioning that a simple analysis was also performed to look in detail at the wavelength variation along the propagation of the ocean swell over approximately 400 km, showing longer waves in the forefront due to its greater wave celerity.

Besides the possibility of obtaining wave field information from SAR images, which ultimately could assist on dynamical processes details to better understand air-sea fluxes, it is important to bear in mind that the technique to retrieve the directional wave spectrum from the SAR image spectrum requires important resources and a general and open scheme is still not available. Further efforts are required to develop optimal numerical schemes to deal with the inversion of image spectrum with stronger and more robust theoretical basis. Some advance has been reported not requiring the inversion of the image spectrum, and it is based on a new SAR image spectral parameter, the Mean rAnge Cross-Spectrum (MACS) that focuses on the isolated wave scales along the radar line-of-sight direction [63]. It is claimed that MACS is an efficient variable in that it characterizes the local wave spectra properties without need of the non-linear wave inversion procedure.

Another example of ocean wave features that can be detected through ocean surface SAR images is still associated with the spatial evolution of the wave field. In Fig. 12 two wave systems are easily observed, generating a diamond grid pattern. This type of spatial evolution is still to be studied, and it is important to recall on the possibility of determining wave parameters that could be tightly associated with the groupiness and with the characteristic nonlinearities along wave propagation.

Now we would like to focus on an important consequence of the momentum transfer from air to water. This is being analyzed from laboratory experiments

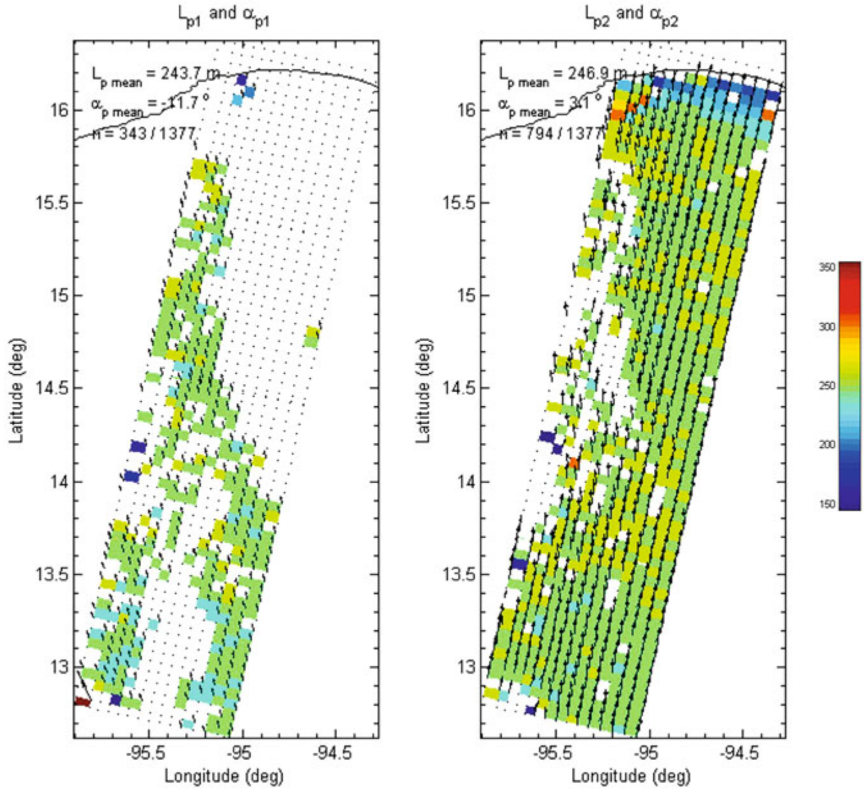

Fig. 11 Maps of SAR-derived wavelength L_p and propagation direction α_p corresponding to the different partitions identified from the March 2 set. Colors indicate wavelength scale in meters; arrows, direction where waves propagate to. System 1 shows 243 m wavelength and propagation direction $-11.7^c irc$, while system 2 is 246 m wavelength and propagation direction towards $3.1^c irc$

in a wind-wave flume as described in Robles-Díaz et al. [86], carried out in the IRPHE/Institut Pythéas in Marseille, France. Typical relations to describe the surface wave growth process must be modified when non-stationary wind is considered. It is important to mention that non-stationary and non-homogeneous wind fields are encountered in nature most of the time.

In this particular case we simply describe the results of the horizontal velocity vertical profile as obtained with a Doppler based current profiler (see Fig. 13), when experimental runs were performed under constantly accelerated wind was acting upon the water surface. As the wind speed increased from 1 ms^{-1} to 13 ms^{-1} approximately, the surface current evolved showing a vertical profile varying with time. Outstanding vertical shear was observed, as it is shown in Fig. 14.

The fate of surface drift is critical in the ocean upper layer, since it is linked to an enhancement of air-sea interaction processes mainly through its influence in

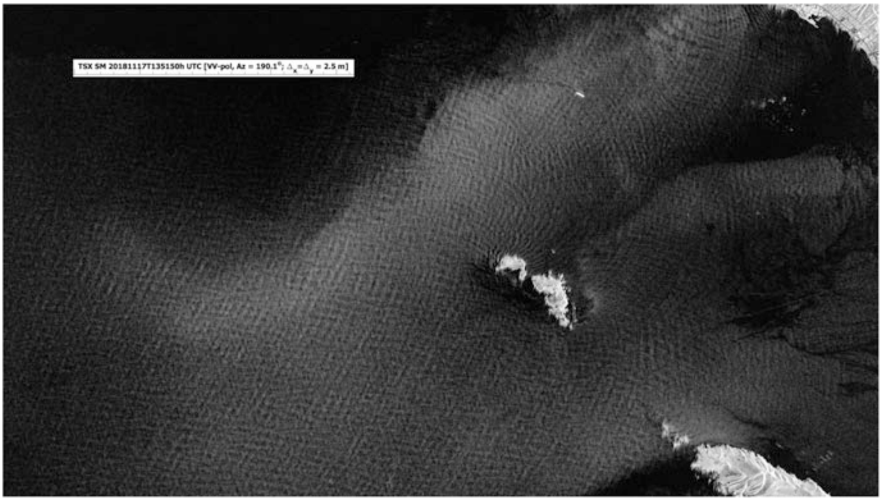

Fig. 12 Example of a TerraSAR-X SAR image acquired over Todos Santos Bay area in Mexico. Two ablique wave systems are readily apparent and both show refraction and diffraction patterns nearshore and in the vicinity of the islands. Ensenada port can be seen in the upper right corner

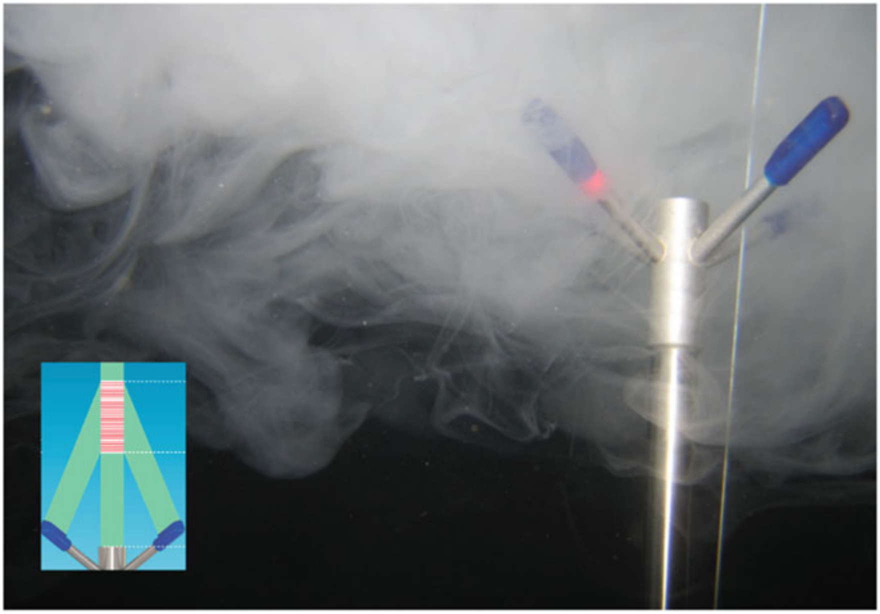

Fig. 13 Velocity profiler during an experimental run in the wind wave flume. Acoustic profiling technique requires some seeds in the water in order to reflect the acoustic signal. A capacitance wire can be seen just besides the profiler, it was used to record water level in order to analyze the wave field

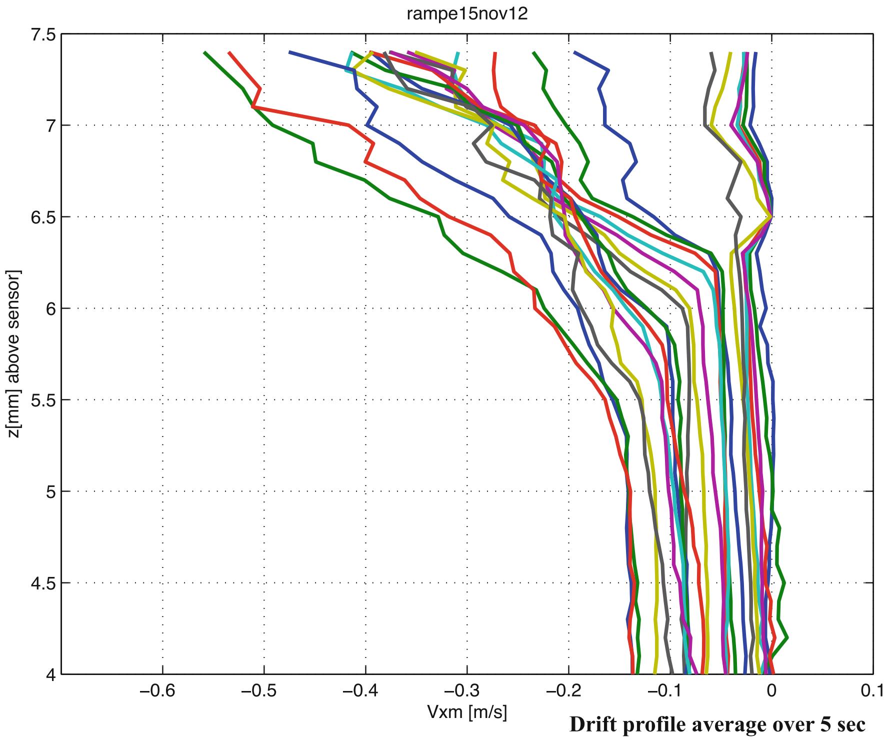

Fig. 14 Drift velocity profiles during an experimental run rampe15 in the wind wave flume. A profile is estimated every 5 s. As the experimental run progresses, wind speed increases with constant acceleration, drift current increases (towards negative values) accordingly. The evolution of the profile and the variation in vertical shear is noticeable. The determination of the wind acceleration influence represents work still under progress

turbulent kinetic energy dissipation rate, and for it also plays an important role in the dispersion and movement of contaminants and all types of organic matter, sargassum for instance. Furthermore, the evolution of surface drift under accelerated winds might be easily observed through remote sensors, and this is a topic that requires greater research efforts to achieve a better understanding within the context of air-sea exchange processes.

5 Final Remarks

A brief review of ocean surface wave studies have been presented, with some emphasis in the influence on air-sea interaction processes. Gas exchange between ocean and atmosphere is a critical issue when dealing with understanding and predicting sea state, the weather and climate. Global scale model to predict the climate and to generate future scenarios normally rely on exchange velocity of gases such as CO_2, which are parameterized taking into account the wind speed only. Great effort are being devoted and new measurements and insight are required in order to properly include wave information into the gas transfer velocity taken into account within climate models. Remote sensing techniques to retrieve ocean information has provided very valuable knowledge, however, it is important to elaborate new schemes to retrieve wave field information from ocean surface images (acquired by synthetic aperture radars, for instance) and to make it available to be used by air-sea interaction novel models. Conditions under accelerated winds (non-stationary fields) are considered very relevant, since those are encountered in nature most of the time.

Acknowledgments We acknowledge the availability of SAR images from DLR and from ESA. We are grateful to funding for laboratory experiments from Excellence Initiative of Aix-Marseille University-A*MIDEX, a French "Investissements d'Avenir" program.

References

1. H. Mitsuyasu, A historical note on the study of ocean surface waves. J. Oceanograph. **58**, 109–120 (2002)
2. H. Mitsuyasu, Reminiscences on the study of wind waves. Proc. Jpn. Acad. Ser. B **91**, 109–130 (2015)
3. H.U. Sverdrup, W.H. Munk, Wind, sea, and swell: theory of relations for forecasting. H. O. Pub. No. 601, U. S. Hydrographic Office Tech. Rep. Number 1. vi+44pp. (1947)
4. E.H. Weber, W.E. Weber, *Wellenlehre auf Experimente gegründet* (Gerhardt Fleischer, Leipzig, 1825)
5. O. Darrigol, The spirited horse, the engineer, and the mathematician: water waves in nineteenth-century hydrodynamics. Arch. Hist. Exact Sci. **58**, 21–95 (2003). https://doi.org/10.1007/s00407-003-0070-5
6. A.D.D. Craik, The origins of water wave theory. Annu. Rev. Fluid Mech. **36**, 1–28 (2004)
7. H. Jeffreys, On the formation of waves by wind. Proc. R. Soc. A **107**, 189–206 (1924)
8. H. Jeffreys, On the formation of waves by wind, II. Proc. R. Soc. A **110**, 341–347 (1925)
9. L. Gain, La prédiction des houles au Maroc. Ann. Hydrograph. **4**, 65–75 (1918)
10. R. Montagne, Le service de prédiction de la houle au Maroc. Ann. Hydrograph. 157–186 (1922)
11. R.G. Dean, R.A. Dalrymple, *Water Wave Mechanics for Engineers and Scientists*, 2nd edn. (World Scientific, Singapore, 1991), 353 pp.
12. W.J. Pierson, A unified mathematical theory for the analysis, propagation and refraction of storm generated ocean surface waves, Parts I and II, N.Y.U., College of Engineering, Research Division, Department of Meteorology and Oceanography, 461pp. (1953)
13. S.O. Rice, *Mathematical Analysis of Random Noise*. Reprint in Selected Papers on Noise and Stochastic Proceses (Dover Publications, Mineola, 1944), pp. 133–294
14. G. Neumann, On ocean wave spectra and a new method of forecasting wind-generated sea. Beach Erosion Board, Tech. Mem., No. 43 (1953), 42pp.
15. W.J. Pierson, G. Neumann, R.W. James, Practical methods for observing and forecasting ocean waves by means of wave spectra and statistics. U.S. Navy Hydrographic Office, Pub. No. 603 (1955). 284pp.
16. O.M. Phillips, On the generation of waves by turbulent wind. J. Fluid Mech. **2**, 417–445 (1957)

17. J.W. Miles, On the generation of surface waves by shear flow. J. Fluid Mech. **3**, 185–204 (1957)
18. J.W. Miles, On the generation of surface waves by turbulent shear flow. J. Fluid Mech. **7**, 469–478 (1960)
19. O.M. Phillips, The equilibrium range in the spectrum of wind-generated ocean waves. J. Fluid Mech. **4**, 426–434 (1958)
20. S.A. Kitaigorodskii, Applications of the theory of similarity to the analysis of wind-generated wave motion as a stochastic process. Izv. Geophys. Ser. Acad. Sci. USSR **1**, 105–117 (1962)
21. W.J. Pierson, L. Moskowitz, A proposed spectral form for fully developed wind seas based on the similarity theory of S. A. Kitaigorodskii. J. Geophys. Res. **69**, 5181–5190 (1964)
22. O.M. Phillips, On the dynamics of unsteady gravity waves of finite amplitude, part 1. J. Fluid Mech. **9**, 193–217 (1960)
23. K. Hasselmann, Grundgleichungen der Seegangsvoraussage. Schiffstechnik, **1**, 191–195 (1960)
24. K. Hasselmann, On the non-linear energy transfer in a gravity wave spectrum. Part 1. J. Fluid Mech. **12**, 481–500 (1962)
25. K. Hasselmann, On the non-linear energy transfer in a gravity wave spectrum. Part 2. J. Fluid Mech. **15**, 273–281; Part 3. **15**, 385–398 (1963)
26. S. Hasselmann, K. Hasselmann, J. Allender, T. Barnett, Computation and parameterizations of the nonlinear energy transfer in a gravity-wave spectrum. Part II: parameterizations of the nonlinear energy transfer for application in wave models. J. Phys. Oceanogr. **15**, 1378–1391 (1985)
27. J. Chase, L.J. Cote, W. Marks, E. Mehr, W.J. Pierson Jr., F.C. Rönne, G. Stephenson, R.C. Vetter, R.G. Walden, The Directional Spectrum of a Wind Generated Sea as Determined from Data Obtained by the Stereo Wave Observation Project, Rep. ONR 285(03), College of Engineering, N.Y.U (1957), 267pp.
28. K. Hasselmann, T.P. Barnett, E. Bouws, H. Carlson, D.E. Cartwright, K. Enke, J.A. Ewing, H. Gienapp, D.E. Hasselmann, P. Kruseman, A. Meerburg, P. Müller, D.J. Olbers, K. Richter, W. Sell, H. Walden, Measurements of wind-wave growth and swell decay during the Joint North Sea Wave Project. Deut. Hydrogr. Z. **8**, 1–95 (1973)
29. M.A. Donelan, J. Hamilton, W.H. Hui, Directional spectra of wind-generated waves. Phil. Trans. Roy. Soc. Lond. A **315**, 509–562 (1985)
30. F.J. Ocampo-Torres, M.A. Donelan, N. Merzi, F. Jia, Laboratory measurements of mass transfer of carbon dioxide and water vapour for smooth and rough flow conditions. Tellus. **46B**, 16–32 (1994). https://doi.org/10.3402/tellusb.v46i1.15746
31. M.A. Donelan, W.M. Drennan, K. Katsaros, The air-sea momentum flux in conditions of wind sea and swell. J. Phys. Oceanogr. **27**, 2087–2099 (1997)
32. D. Hauser, H. Branger, S. Bouffies-Cloché, S. Despiau, W.M. Drennan, H. Dupuis, P. Durand, X. Durrieu de Madron, C. Estournel, L. Eymard, C. Flamant, H.C. Graber, C. Guérin, K. Kahma, G. Lachaud, J.-M. Lefèvre, J. Pelon, H. Pettersson, B. Piguet, P. Queffeulou, D. Tailliez, J. Tournadre, A. Weill, The FETCH experiment: an overview. J. Geophys. Res. Oceans **108**, C3 (2003)
33. A.B. Villas Bôas, F. Ardhuin, A. Ayet, M.A. Bourassa, P. Brandt, B. Chapron, B.D. Cornuelle, J.T. Farrar, M.R. Fewings, B. Fox-Kemper, S.T. Gille, C. Gommenginger, P. Heimbach, M.C. Hell, Q. Li Q, M.R. Mazloff, S.T. Merrifield, A. Mouche, M.H. Rio, E. Rodriguez, J.D. Shutler, A.C. Subramanian, E.J. Terrill, M. Tsamados, C. Ubelmann, E. van Sebille, Integrated observations of global surface winds, currents, and waves: requirements and challenges for the next decade. Front. Mar. Sci. **6**, 425 (2019)
34. F. Ardhuin, J.E. Stopa, B. Chapron, F. Collard, R. Husson, R.E. Jensen, J. Johannessen, A. Mouche, M. Passaro, G.D. Quartly, V. Swail, I. Young, Observing sea states. Front. Mar. Sci. **6**, 124 (2019)
35. H. Graber, E. Terray, M. Donelan, W. Drennan, V. Leer, D. Peters, ASIS - A new Air-Sea Interaction Spar buoy: Design and performance at sea. J. Atmos. Ocean. Technol. **17**, 707–720 (2000). http://dx.doi.org/10.1175/1520-0426(2000)017<0708:AANASI>2.0.CO;2

36. F.J. Ocampo-Torres, H. García-Nava, R. Durazo, P. Osuna, G. Díaz-Méndez, H.C. Graber, The INTOA experiment: a study of ocean-atmosphere interactions under moderate to strong offshore winds and opposing swell conditions in the Gulf of Tehuantepec, Mexico. Bound.-Lay. Meteorol. **138**, 433–451 (2011)
37. C.O. Collins, B. Lund, R.J. Ramos, W.M. Drennan, H.C. Graber, Wave measurement intercomparison and platform evaluation during the ITOP (2010) experiment. J. Atmos. Ocean. Technol. **31**, 2309–2329 (2014)
38. M.A. Donelan, Air-sea interaction, in *The Sea: Ocean Engineering Science* (Wiley, Hoboken, 1990), pp. 239–292
39. D. Larios Rodríguez, Efecto del oleaje en la transferencia de momento a través de la interfase océano atmósfera. M.Sc. Thesis, CICESE (2019), 62pp.
40. S.D. Smith, Water vapour flux at the sea surface. Boundary-Layer Meteorol. **47**, 277–283 (1980)
41. J. Pan, D.W. Wang, P.A. Hwang, A study of wave effects on wind stress over the ocean in a fetch-limited case. J. Geophys. Res. **110**, C02020 (2005)
42. R.W. Burling, The spectrum of waves at short fetches. Ocean Dyn. **12**(2), 45–64 (1959)
43. F. Dobson, W. Perrie, B. Toulany, On the deep-water fetch laws for wind–generated surface gravity waves. Atmos. Ocean **27**(1), 210–236 (1989)
44. M.L. Babanin, Y.P. Soloviev, Field investigation of transformation of the wind wave frequency spectrum with fetch and stage of development. J. Phys. Oceanogr. **28**, 563–576 (1998)
45. K.F. Rieder, J.A. Smith, R.A. Weller, Observed directional characteristics of the wind, wind stress, and surface waves on the open ocean. J. Geophys. Res. **99**, 22589–22596 (1994)
46. A.A. Grachev, C.W. Fairall, J.E. Hare, J.B. Edson, S.D. Miller, Wind stress vector over ocean waves. J. Phys. Oceanogr. **33**(11), 2408–2429 (2003)
47. J.C. Orr, R.G. Najja, O. Aumont, L. Bopp, J.L. Bullister, G. Danabasoglu, S.C. Doney, J.P. Dunne, J.-C. Dutay, H. Graven, S.M. Griffies, J.G. John, F. Joos, I. Levin, K. Lindsay, R.J. Matear, G.A. McKinley, A. Mouchet, A. Oschlies, A. Romanou, R. Schlitzer, A. Tagliabue, T. Tanhua, A. Yool, Biogeochemical protocols and diagnostics for the CMIP6 ocean model inter-comparison project (OMIP). Geosci. Model Develop. **10**(6), 2169–2199 (2017)
48. B. Jähne, K. Münnich, R. Bösinger, A. Dutzi, W. Huber, P. Libner, On the parameters influencing air-water gas exchange. J. Geophys. Res. **92**(C2), 1937–1949 (1987)
49. D.A. Shaw, T.J. Hanratty, Turbulent mass transfer rate to a wall for large Schmidt numbers. AIChE J. **23** 28–37 (1977)
50. D.A. Dawson, O. Trass, Mass transfer at rough surfaces. Int. J. Heat Mass Transf. **15**, 1317–1336 (1972)
51. R. Wanninkhof, Relationship between gas exchange and wind speed over the ocean. J. Geophys. Res. **97**, 7373–7381 (1992)
52. M. Donelan, W. Drennan, E. Saltzman, R.H. Wanninkhof, Gas transfer at water surfaces. Washington DC, AGU., Geophys. Monograph Series, 10.1029/GM127 (2002)
53. W. McGillis, J. Edson, J. Hare, C. Fairall, Direct covariance air-sea CO2 fluxes. J. Geophys. Res. **106**(C8), 16729–16745 (2001)
54. W.R. McGillis, J.B. Edson, C.J. Zappa, J.D. Ware, S.P. McKenna, E.A. Terray, J.E. Hare, C.W. Fairall, W. Drennan, M. Donelan, M.D. DeGrandpre, R. Wanninkhof, R.A. Feely, Air-sea CO2 exchange in the equatorial Pacific. J. Geophys. Res. **109** C08S02, 1–17 (2004)
55. D.K. Woolf, Parametrization of gas transfer velocities and sea-state-dependent wave breaking. Tellus **57B**, 87–94 (2005)
56. M.A. Donelan, A.V. Soloviev, A mixing length model for the aqueous boundary layer including the effect of wave breaking on enhancing gas transfer. IOP Conf. Ser. Earth Environ. Sci. **35** 012001 (2016)
57. L. Gutiérrez-Loza, F.J. Ocampo-Torres, H. García-Nava, The effect of breaking waves on CO2 air–sea fluxes in the coastal zone. Boundary-Layer Meteorol. **168**, 343–360 (2018)
58. M. Donelan, W. Drennan, A.-K. Magnusson, Nonstationary analysis of the directional properties of propagating waves. J. Phys. Oceanogr. **26**, 1901–1914 (1996)

59. D.K. Woolf, J.D. Shutler, L. Goddijn–Murphy, A.J. Watson, B. Chapron, P.D. Nightingale, C.J. Donlon, J. Piskozub, M.J. Yelland, I. Ashton, T. Holding, U. Schuster, F. Girard–Ardhuin, A. Grouazel, J.-F. Piolle, M. Warren, I. Wrobel-Niedzwiecka, P.E. Land, R. Torres, J. Prytherch, B. Moat, J. Hanafin, F. Ardhuin, F. Paul, Key uncertainties in the recent air-sea flux of CO2. Global Biogeochem. Cycles **33**, 1548–1563 (2019)
60. C.J. Zappa, W. Asher, A. Jessup, Microscale wave breaking and air-water gas transfer. J. Geophys. Res. **106**, 9385–9391 (2001)
61. C.J. Zappa, W. Asher, A. Jessup, J. Klinke, S. Long, Microbreaking and the enhancement of air-water transfer velocity. J. Geophys. Res. **109**, C08S16 (2004)
62. D. Zhao, Y. Toba, Dependence of whitecap coverage on wind and wind-wave properties. J. Oceanogr. **57**, 603–616 (2001)
63. S. Li, A.V. Babanin, F. Qiao, D. Dai, S. Jiang, C. Guan, Laboratory experiments on CO2 gas exchange with wave breaking. J. Phys. Oceanogr. **51**, 3105–3116 (2021)
64. L.R. Centurioni, J. Turton, R. Lumpkin, L. Braasch, G. Brassington, Y. Chao, E. Charpentier, Z. Chen, G. Corlett, K. Dohan, C. Donlon, C. Gallage, V. Hormann, A. Ignatov, B. Ingleby, R. Jensen, B.A. Kelly-Gerreyn, I.M. Koszalka, X. Lin, E. Lindstrom, N. Maximenko, C.J. Merchant, P. Minnett, A. O'Carroll, T. Paluszkiewicz, P. Poli, P.-M. Poulain, G. Reverdin, X. Sun, V. Swail, S. Thurston, L. Wu, L. Yu, B. Wang, D. Zhang, Global in situ observations of essential climate and ocean variables at the air-sea interface. Front. Mar. Sci. **6**, 419 (2019)
65. G.S. Benton, Interaction between the atmosphere and the ocean. Rep. Joint P. Air-Sea Interaction. G. S. Chairman. Nat. Acad. Sci., Publ. 983 (1962)
66. K. Hasselmann, Ocean circulation and climate change. Tellus, 43AB, 82–103 (1991)
67. S.E. Belcher, A.L.M. Grant, K.E. Hanley, B. Fox-Kemper, L. Van Roekel, P.P. Sullivan, W.G. Large, A. Brown, A. Hines, D. Calvert, A. Rutgersson, H. Pettersson, J.-R. Bidlot, P.A.E.M. Janssen, J.A. Polton, A global perspective on Langmuir turbulence in the ocean surface boundary layer. Geophys. Res. Lett. **39**, L18605 (2012)
68. R. Wanninkhof, Relationship between wind speed and gas exchange over the ocean. J. Geophys. Res. **97**(C5), 7373–7382 (1992)
69. M. F. Cronin, C.L. Gentemann, J. Edson, I. Ueki, M. Bourassa, S. Brown, C.A. Clayson, C.W. Fairall, J.T. Farrar, S.T. Gille, S. Gulev, S.A. Josey, S. Kato, M. Katsumata, E. Kent, M. Krug, P.J. Minnett, R. Parfitt, R.T. Pinker, P.W. Stackhouse Jr., S. Swart, H. Tomita, D. Vandemark, R.A. Weller, K. Yoneyama, L. Yu, D. Zhang, Air-sea fluxes with a focus on heat and momentum. Front. Mar. Sci. **6**, 430 (2019)
70. W.M. Smethie Jr., H.G. Ostlund, H.H. Loosli, Ventilation of the deep Greenland and Norwegian seas: evidence from krypton-85, tritium, carbon-14 and argon-39. Deep Sea Res A Oceanograph. Res. Pap. **33**(5), 675–703 (1986)
71. R. Wanninkhof, W. McGillis, A cubic relationship between air-sea CO2 exchange and wind speed. Geophys. Res. Let. **26**(13), 1889–1892 (1999)
72. P.N. Nightingale, P.S. Liss, P. Schlosser, Measurement of air- sea gas transfer during an open ocean algal bloom. Geophys. Res. Lett. **27**, 2117–2120 (2000)
73. M.A. Donelan, R. Wanninkhof, Gas transfer at water surfaces–concepts and issues, in *Gas Transfer at Water Surfaces*, ed. by M.A. Donelan, W.M. Drennan, E.S. Saltzman, R. Wanninkhof, vol. 127 (2002), pp: 1–10
74. I.S. Robinson, *Measuring the Oceans from Space: The Principles and Methods of Satellite Oceanography* (Springer, Berlin, 2004), pp. xlvi, 670
75. N. Rascle, B. Chapron, J. Molemaker, F. Nouguier, F.J. Ocampo-Torres, J.P. Osuna Cañedo, L. Marié, B. Lund, J. Horstmann, Monitoring intense oceanic fronts using sea surface roughness: satellite, airplane, and in situ comparison. J. Geophys. Res. Oceans **125**, 1–22 (2020) https://doi.org/10.1029/2019JC015704
76. L.-L. Fu, B. Holt, Seasat views oceans and sea ice with synthetic-aperture radar. JPL Pub. 81–120, pp: ix, 200 (1982)
77. K. Hasselmann, S. Hasselmann, On the non-linear mapping of an ocean wave spectrum into a Synthetic Aperture Radar image spectrum and its inversion. J. Geophy. Res. **96**, 10713–10729 (1991)

78. R.A. Shuchman, J.S. Zelenka, Processing of ocean wave data from synthetic aperture radar. Boundary-Layer Meteorol. **13**, 181–191 (1978)
79. B. Holt, A.K. Liu, D.W. Wang, A. Gnanadesikan, H.S. Chen, Tracking storm-generated waves in the northeast Pacific Ocean with ERS-1 synthetic aperture radar imagery and buoys. J. Geophys. Res. **103**(C4) 7917–7929 (1998)
80. S. Lehner, F.J. Ocampo-Torres, The SAR measurements of ocean waves: wave session white paper, in *Proceedings of the Second Workshop Coastal and Marine Applications of SAR, 8–12 September 2003, Svalbard, Norway*. ESA SP-565 (2004)
81. H. Li, J.E. Stopa, A. Mouche, B. Zhang, Y. He, B. Chapron, Assessment of ocean wave spectrum using global Envisat/ASAR data and hindcast simulation. Remote Sens. Environ. **264**, 112614 (2021)
82. X. Li, S. Lehner, W. Rosenthal, Investigation of ocean surface wave refraction using TerraSAR-X data. Trans. Geosci. Remote Sens. **48**, 830–840 (2010)
83. G.M. Díaz Méndez, S. Lehner, F.J. Ocampo-Torres, X. Ming Li, S. Brusch, Wind and wave observations off the south Pacific Coast of Mexico using TerraSAR-X imagery. Int. J. Remote Sens. **31**, 4933–4955 (2010)
84. G.M. Díaz Méndez, Análisis de la evolución del espectro direccional del oleaje libre en el Golfo de Tehuantepec bajo condiciones de viento intensos utilizando imágenes de radar de apertura sintética. Ph.D. Thesis, F. Ciencias Marinas, UABC (2011)
85. F. Collard, F. Ardhuin, B. Chapron, Extraction of coastal ocean wave fields from SAR images. IEEE J. Ocean. Eng. **30**(3), 526–533 (2005)
86. L. Robles-Díaz, F.J. Ocampo-Torres, H. Branger, H. García-Nava, P. Osuna, N. Rascle, On the early stages of wind-wave generation under accelerated wind conditions. Eur. J. Mech. B Fluids **78**, 106–14 (2019)
87. M. Broy, Software engineering—from auxiliary to key technologies, in *Software Pioneers*, ed. by M. Broy, E. Dener (Springer, Heidelberg, 2002), pp. 10–13
88. J. Dod, Effective substances, in *The Dictionary of Substances and Their Effects*. Royal Society of Chemistry (1999). Available via DIALOG. http://www.rsc.org/dose/titleofsubordinatedocument. Accessed 15 Jan 1999
89. K.O. Geddes, S.R. Czapor, G. Labahn, *Algorithms for Computer Algebra* (Kluwer, Boston, 1992)
90. C. Hamburger, Quasimonotonicity, regularity and duality for nonlinear systems of partial differential equations. Ann. Mat. Pura. Appl. **169**, 321–354 (1995)

A 3D Two-Phase Conservative Level-Set Method Using an Unstructured Finite-Volume Formulation

Miguel Uh Zapata and Reymundo Itzá Balam

Abstract Mathematical and computational modeling of two-phase flows simulations is widely used in many physical and industrial applications. Moreover, a numerical model with an unstructured level-set method allows for flexible applications to geophysical flows of arbitrary domains with the presence of many obstacles. In this work, we introduce a new second-order time- and space-accurate method developed to solve in parallel a conservative level-set equation in three-dimensional geometries. We employ a θ-method for the time integration and a finite-volume method on prisms elements consisting of triangular cells on the horizontal plane and several layers in the vertical direction for the space discretization. We apply an upwind scheme with a Local Extremum Diminishing flux limiter to approximate the convective terms that solves the level-set equation using either the Heaviside function or the regularized characteristic function. Moreover, we present a parallelization strategy using a block domain decomposition technique and Message Passing Interface. The numerical method is initially validated against classical advection test cases and unstructured grids. Finally, several interface-capturing tests, including topology changes, are used to demonstrate the capabilities and performance of the proposed scheme.

M. Uh Zapata (✉) · R. Itzá Balam
CONACYT–Centro de Investigación en Matemáticas A. C., CIMAT Unidad Mérida, Mérida, Yucatán, Mexico
e-mail: angeluh@cimat.mx; reymundo.itza@cimat.mx

G. Hernández-Dueñas, M. A. Moreles (eds.), *Mathematical and Computational Models of Flows and Waves in Geophysics*, CIMAT Lectures in Mathematical Sciences, https://doi.org/10.1007/978-3-031-12007-7_3

1 Introduction

A wide variety of problems in geological fluid mechanics require capturing interfaces with great precision or involving a jump in physical properties across a sharp boundary [1–4]. However, solving these problems can be a challenging task because they have sharped discontinuities in some regions. Thus numerical instabilities appear, which prevent the local use of high order numerical schemes. Although several approaches have been proposed, the level-set method has shown to be a successful formulation to overcome this difficulty. For instance, level-set methods have been implemented in computational volcanology problems to trace flow fronts and interfaces in a lava dome evolution [5–7]. Another example of level-set application is modeling geodynamical flows that require advecting compositional fields with discontinuities, as presented in [8, 9].

In general, many numerical methods have been proposed to solve two-phase flows in recent years [10]. These methods can be classified into Lagrangian methods that modify the grid to match the interface location and Eulerian methods that extract the interface location from a fixed grid.

In a Lagrangian method, the interface can be specifically delineated and precisely followed; however, the computational mesh moves with the interface. Although these methods are successful for small interface deformations, re-meshing is required when the interface undergoes large deformations [11, 12]. In an Eulerian method, an interface moves through a fixed grid. The two main approaches are interface tracking and capturing. An interface tracking method uses a set of Lagrangian points to mark and track an interface. Examples of interface tracking methods include the front-tracking method [13, 14] and the ghost fluid method [15, 16]. On the other hand, with interface-capturing methods, the interface is implicitly captured by a contour of a scalar function. The volume-of-fluid (VOF) method [17, 18] and the level set (LS) method [19, 20] are popular examples of interface capturing. The VOF method determines the interface location by the volume fraction occupied by each fluid in each cell. In the LS method, an interface is represented as a zero set of an auxiliary scalar function. In general, interface-capturing methods are based on the spatial discretization of a characteristic function to distinguish between two phases. Here, the position of the interface is computed at each time step by solving a convective equation.

We remark that structured grids have many limitations for their application to arbitrary three-dimensional (3D) geometries. To overcome this issue, we can employ unstructured grids, which are more flexible for geophysical flows applications. Most of the LS methods used for unstructured grids were developed in the framework of the finite-element method. However, the finite-volume (FV) method is attractive due to its local conservation property, which is not the case for standard finite-difference or finite-element methods.

The literature that involves numerical interface-capturing methods applying a finite-volume approach is limited; most numerical methods have been developed for rectangular grids and only a few strategies for unstructured grids [21–28]. Moreover, there exist only a limited number of these models that combine a 3D finite-volume method and unstructured grids, and most of them are based on VOF algorithms, for example, see [26, 28]. To the best of the authors' knowledge, Balcázar et al. [27] is the only one presenting a 3D conservative level-set (CLS) method based on an unstructured FV method. Moreover, their analysis is limited to a few test cases.

As previously discussed, level-set/finite-volume methods for unstructured grids have rarely been reported. Motivated by this, the present work aims to develop a new unstructured finite-volume method (UFVM) with arbitrary-shaped triangular cells. Furthermore, the transport equation is initially studied to directly analyze the effect of the convective approximation on unstructured grids. Next, the problem considers a re-initialization process [29] to improve the results. In general, accurate approximations of the convective equation are not simple to obtain due to different difficulties such as false diffusion, non-conservative, overshoot/undershoot and phase error [30]. Numerical methods employ second-order schemes to mitigate this diffusion effect. Central schemes perform well in smooth regions [31]; however, they produce oscillations around sharp gradient regions. On the other hand, second-order upwind schemes work well near discontinuities. However, oscillations still exist, which can be reduced or eliminated by the introduction of a Flux-Limiter technique [30].

This work proposes a second-order accurate and robust numerical method for the conservative level-set approach, which is applied for capturing the interface between two fluids. The time integration is based on a method that allows us to select between complete explicit and implicit first-order time formulations or a second-order Crank-Nicolson (implicit) method. The space discretization is based on a finite-volume method on prisms elements consisting of unstructured triangular grids on the horizontal and several layers in the vertical. Balcázar et al. [27] calculate the convective equation as the sum of a diffusive first-order upwind part and an anti-diffusive term. In contrast to their method, the proposed convective approximation applies a second-order upwind interpolation scheme. We calculate the corresponding gradients using a least-square technique [32]. In order to eliminate non-desirable oscillations, the approximations also incorporate a flux limiter which is determined by the Local Extremum Diminishing (LED) technique [33].

Finally, numerical results require significant computational time to compute, in particular, for three-dimensional simulations. Thus, the whole code is developed in parallel. The parallelization of the algorithm is based on a domain decomposition into several sub-domains in the horizontal direction, one for each parallel process, and a parallel solution of the linear system using a Multi-Color SOR (MSOR) method [34, 35].

This chapter is organized as follows. The second section introduces the conservative level-set method. The third section is devoted to time integration and finite-volume discretization. The following section deals with the parallelization technique. Next, the numerical techniques are tested over different benchmark problems. We present the performance of the proposed model in Sect. 6. Finally, the last section includes the conclusions and ideas to be pursued in future work.

2 Conservative Level-Set Method

For interface motion, we assumed that the fluids are immiscible and that their movement is defined by the unique divergence-free velocity field. In the classical LS method [19, 20], we consider the conservative transport equation:

$$\frac{\partial \phi}{\partial t} + \boldsymbol{u} \cdot \nabla \phi = 0, \quad \boldsymbol{x} \in \Omega, \tag{1}$$

where t is the time, $\boldsymbol{u}$ is the known velocity field, and $\phi(\boldsymbol{x}) = d(\boldsymbol{x})$ is the signed distance function given by

$$d(\boldsymbol{x}) = \sigma \min_{x_\Gamma} \left(|\boldsymbol{x} - \boldsymbol{x}_\Gamma|\right). \tag{2}$$

Here, Γ denotes the interface; the sign value, σ, is set positive on one side and negative in another; and with the zero level set of ϕ indicating the interface $\Gamma = \{\boldsymbol{x} | \phi(\boldsymbol{x}) = 0\}$.

However, standard numerical formulations for (1) may have unacceptable mass conservation errors. Thus, instead of the signed distance function to represent the interface, we can employ the conservative level-set formulation [29]:

$$\frac{\partial \mathcal{H}(\phi)}{\partial t} + \nabla \cdot \left[\boldsymbol{u}\mathcal{H}(\phi)\right] = 0, \quad \boldsymbol{x} \in \Omega, \tag{3}$$

where $\mathcal{H}$ is the Heaviside function given by

$$\mathcal{H}(\phi) = \begin{cases} 1, & \phi(\boldsymbol{x}) > 0, \\ 1/2, & \phi(\boldsymbol{x}) = 0, \\ 0, & \phi(\boldsymbol{x}) < 0. \end{cases} \tag{4}$$

However, if not proper numerical techniques are applied, the strong discontinuity at the interface may cause instabilities of the numerical solutions. To avoid this problem, Olsson and Kreiss [29] employed a regularized characteristic function, as follows

$$\mathcal{H}_\epsilon(\boldsymbol{x}) = \frac{1}{2}\left(1 + \tanh\left(\frac{d(\boldsymbol{x})}{2\epsilon}\right)\right), \tag{5}$$

where $d(\boldsymbol{x})$ is the same signed distance function previously defined in (2), ϵ controls the interface thickness and $\mathcal{H}_\epsilon$ varies from 0 to 1. In this work, the width ϵ of the transition region is given by $\epsilon = 0.5\Delta^\beta$ [27], with $\Delta = \sqrt{V_c}$ where V_c is taken as the minimum area of the triangular cells, and $\beta = 1$ is set as a default value.

As time simulations evolve, approximation of (3) presents numerical inaccuracies that eventually change the profile of the Heaviside function at the interface.

To keep H with the profile and thickness of the interface constant, we introduce a reinitialization equation as follows [29]:

$$\frac{\partial \mathcal{H}}{\partial \tau} + \nabla \cdot \left[\mathcal{H}(1-\mathcal{H})\right] \boldsymbol{n}_{\tau=0} = \nabla \cdot (\epsilon \nabla \mathcal{H}), \quad \boldsymbol{x} \in \Omega, \tag{6}$$

where τ is a pseudo time, $\boldsymbol{n} = \nabla H / |\nabla H|$ is the normal of Γ before applying the re-initialization, and ϵ is the same value employed in (5). The left-hand side term is a compressive flux to keep the profile sharp, and the diffusive right-hand side term aims to avoid discontinuities at the interface [29, 36].

3 Numerical Method for the Level-Set Equation

In this work, the θ-method and an unstructured finite-volume method are used to discretize the integral form of the conservative transport equation (3) in time and space, respectively. Initial conditions are determined by the characteristic function (5). Dirichlet or Neumann boundary conditions are applied at the boundaries.

3.1 Time Integration: θ-Method

Explicit or implicit numerical methods can be proposed depending on the convection approximation. If this term is evaluated at the previous time step, t^n, a simple forward approximation for the time derivative results in an explicit first-order time-accurate approximation for Eq. (1). However, the stability of the explicit scheme is restricted by a Courant-Friedrichs-Lewy (CFL) condition. To overcome this time-step restriction, we can select an implicit formulation by evaluating the convective term at the new time step, t^{n+1}.

Although the implicit treatment of the convective term eliminates the numerical stability restriction, the method is still a first-order time-accurate approximation. This study also proposes a second-order implicit time-advancement scheme based on the Crank-Nicolson (C-N) method. We can summarize all these options in the following scheme for Eq. (3):

$$\frac{H^{n+1} - H^n}{\Delta t} + \nabla \cdot \left(\theta H^{n+1} \boldsymbol{u}^{n+1} + (1-\theta) H^n \boldsymbol{u}^n\right) = 0,$$

where H^n denotes the approximation of $\mathcal{H}$ at time level t^n, Δt is the computational time step, and θ is equal to 0, 1 or $1/2$ if the method is explicit, implicit or the C-N method, respectively. Thus, the time-advancement scheme for the level-set equation can be written as follows:

$$H^{n+1} + \theta \Delta t \nabla \cdot \left(H^{n+1} \boldsymbol{u}^{n+1} \right) = H^n - (1-\theta) \Delta t \nabla \cdot \left(H^n \boldsymbol{u}^n \right). \tag{7}$$

Note that the right-hand side corresponds to known values because it only includes terms of the previous step and the velocity field $\boldsymbol{u}$.

3.2 Space Discretization: Finite-Volume Method

The computational domain in the horizontal plane is discretized into N_{cell} triangular cells. The 3D domain discretization is formed by prisms, V_i, using the exact horizontal 2D triangular discretization and extending into N_z layers in the vertical direction. Thus, the total number of prism elements is given by $N_V = N_{cell} N_z$.

Each prism-shaped control volume has five faces, S_j: three with vertical orientation (lateral faces $j = 1, 2, 3$) and two with horizontal direction (top face $j = 4$ and bottom face $j = 5$). The cell-centered node of each prism is denoted by $\boldsymbol{x}_i = (x_i, y_i, z_i)$. We use a staggered grid where the face-normal velocity $U = \boldsymbol{u} \cdot \boldsymbol{n}$ is located at the centers of the cell faces, named $\boldsymbol{x}_{ij} = (x_{ij}, y_{ij}, z_{ij})$, and H is calculated at the cell-centered point $\boldsymbol{x_i}$ of the cell. Here, $\boldsymbol{n}$ denotes the outward normal unit vector at each face. A schematic plot of the triangular prism element and its components is shown in Fig. 1a–c.

Following the standard finite-volume formulation, Eq. (7) is integrated over each control volume, which formally gives (assuming sufficient regularity):

$$\int_{V_i} H^{n+1} dV + \theta \Delta t \int_{V_i} \nabla \cdot (H\boldsymbol{u})^{n+1} \, dV = \int_{V_i} H^n dV - (1-\theta) \Delta t \int_{V_i} \nabla \cdot (H\boldsymbol{u})^n \, dV. \tag{8}$$

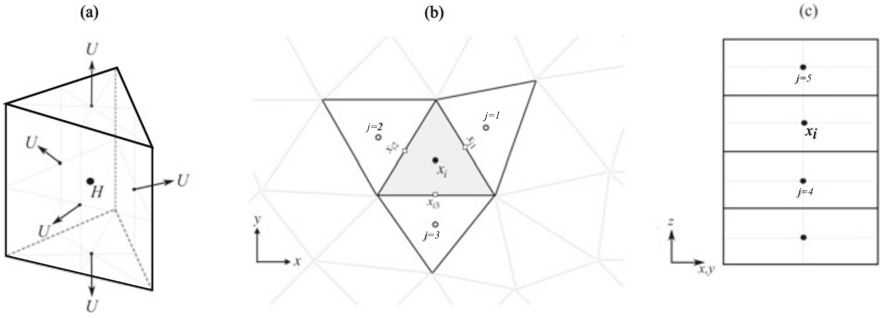

Fig. 1 Sketch of the three and two-dimensional control volumes used for discretization

After application of the Green's theorem, we get

$$\int_{V_i} H^{n+1} dV + \theta \Delta t \sum_{j=1}^{5} \oint_{S_j} (H\boldsymbol{u})^{n+1} \cdot \boldsymbol{n} dS = \int_{V_i} H^{n} dV - (1-\theta) \Delta t \sum_{j=1}^{5} \oint_{S_j} (H\boldsymbol{u})^{n} \cdot \boldsymbol{n} dS \tag{9}$$

where index j accounts for any V_j sharing a face S_j with V_i. We remark that up to this point we have not introduced any approximation in space.

A second-order scheme is obtained by applying the midpoint rule integral approximation for the prism element and its corresponding faces. Thus, we get

$$m_{V_i} H_i^{n+1} + \theta \Delta t \sum_{j=1}^{5} m_{S_j} (H\boldsymbol{u})_{ij}^{n+1} \cdot \boldsymbol{n}_j = m_{V_i} H_i^{n} - (1-\theta) \Delta t \sum_{j=1}^{5} m_{S_j} (H\boldsymbol{u})_{ij}^{n} \cdot \boldsymbol{n}_j, \tag{10}$$

where $(\cdot)_{ij}$ denotes a variable at the midpoint of S_j, see Fig. 1. Here, m_{V_i} and m_{S_j} are the volume of V_i and the area of S_j, respectively. The outward normal directed from V_i to V_j is defined as $\boldsymbol{n}_j$. Finally, we can write the level-set discretization as follows

$$H_i^{n+1} + \theta c_i \sum_{j=1}^{5} m_{S_j} H_{ij}^{n+1} U_{ij}^{n+1} = H_i^{n} - (1-\theta) c_i \sum_{j=1}^{5} m_{S_j} H_{ij}^{n} U_{ij}^{n}, \tag{11}$$

where $c_i = \Delta t / m_{V_i}$ and the normal-face flux crossing the face is given by

$$U_{ij} = (\boldsymbol{u} \cdot \boldsymbol{n})_{ij}, \quad j = 1, \ldots, 5. \tag{12}$$

The discretization is complete by approximating H_{ij} in Eq. (11) as a function of the discrete unknowns H_i and H_j associated to V_i and its neighbors V_j.

3.3 Interpolation: Upwind Scheme

The unknown variable H at the face midpoint can be approximated in several ways, and the method accuracy depends on how precise is this approximation. These midpoints values are approximated using a second-order upwind scheme based on Taylor expansions around $\boldsymbol{x}_{ij}$. Let us denote $H_{ij}(V_i)$ and $H_{ij}(V_j)$ the approximations of the variable H at S_j, respectively. Thus, a common flux is approximated as [37]:

$$H_{ij} U_{ij} = \max(U_{ij}, 0)\ H_{ij}(V_i) + \min(U_{ij}, 0)\ H_{ij}(V_j), \quad j = 1, \ldots, 5, \tag{13}$$

where a second-order interpolation at the cell-face is calculated as follows

$$H_{ij}(V_i) \approx H_i + \psi_i \Theta_i, \quad \text{where} \quad \Theta_i = \nabla H_i \cdot (\boldsymbol{x}_{ij} - \boldsymbol{x}_i). \tag{14}$$

Note that Eq. (14) also incorporates a flux limiter as ψ_i. It is to eliminate non-desirable oscillations. In this work, this flux limiter is determined by the Local Extremum Diminishing technique [33] satisfying $H_{\min} \leq H_{ij} \leq H_{\max}$, where $H_{\min}$ and $H_{\max}$ are the minimum and the maximum taken over V_i and its surrounding neighbors. We obtain a unique value of the flux limiter per control volume V_i as follows

$$\psi_i = \min_j(\psi_{ij}), \qquad \psi_{ij} = \begin{cases} \min\left(1, \left[H_{\max} - H_j\right]/\Theta_i\right), & \text{if } \Theta_i > 0, \\ \min\left(1, \left[H_{\min} - H_j\right]/\Theta_i\right), & \text{if } \Theta_i < 0, \\ 1, & \text{if } \Theta_i = 0. \end{cases} \tag{15}$$

This technique ensures that local maximum cannot increase and local minimum cannot decrease [33]. In a similar way, we obtain the coefficients of $H_{ij}(V_j)$.

Equation (14) can be further simplified such that H_{ij} is calculated by different techniques in the horizontal and vertical faces of each prism. For the horizontal case, the problem is reduced at the two-dimensional case

$$H_{ij}(V_i) \approx H_i + \psi_i \left(\frac{\partial H_i}{\partial x}(x_{ij} - x_i) + \frac{\partial H_i}{\partial y}(y_{ij} - y_i) \right), \quad j = 1, 2, 3. \tag{16}$$

For the vertical case, it will be simply necessary an approximation of the third derivative component as follows

$$H_{ij}(V_i) \approx H_i + \psi_i \left(\frac{\partial H_i}{\partial z} \right) (z_{ij} - z_i), \quad j = 4, 5. \tag{17}$$

Finally, Eqs. (16) and (17) require the gradient approximation at each cell-centered point. In the vertical direction, a central scheme is applied to obtain the corresponding derivatives in the z-direction. In the horizontal plane, we use a least-square technique, as described in the work of Lien [32]. In this method, the solution is assumed to be linear in each control volume such that

$$H(x, y) = \mathfrak{a}x + \mathfrak{b}y + \mathfrak{c}, \quad \text{and} \quad \nabla H = (\mathfrak{a}, \mathfrak{b}). \tag{18}$$

The coefficients $\mathfrak{a}$, $\mathfrak{b}$ and $\mathfrak{c}$ are determined using the values H_i and the horizontal neighbors H_j $(j = 1, 2, 3)$. Although the resulting gradient approximation is only first-order accurate, Eqs. (16) and (17) result in a second-order approximation.

3.4 Boundary Conditions

Boundary conditions are included into the problem as updates of ghost values. Let us denote H_g the corresponding ghost cell of H_i. Dirichlet boundary conditions are updated as the average of both values and Neumann boundary conditions are calculated as a central difference formula as follows

$$H_g = 2H_E - H_i \quad \text{and} \quad H_g = \Delta_g \left(\frac{dH}{d\boldsymbol{n}} \right)_E + H_i,$$

respectively, where $(\cdot)_E$ indicates the known values at the boundary and Δ_g represents the distance from the cell-centered point to its ghost point.

3.5 Linear System and Solver

In summary, a finite-volume discretization of Eq. (7) at each control volume V_i $(i = 1, 2, \ldots, N_V)$ results in the following linear system of equations

$$H_i^{n+1} + \theta c_i \left(a_0 H_i^{n+1} + \sum_{j=1}^{5} a_j H_j^{n+1} + a_G^{n+1} \right) = f_i^n, \tag{19}$$

where the coefficients corresponding to the upwind scheme are given by

$$a_0 = \sum_{j=1}^{5} \max(U_{ij}, 0), \quad \text{and} \quad a_j = \min(U_{ij}, 0), \quad j = 1, \ldots, 5. \tag{20}$$

and a_G includes all the terms related with the gradient approximation and flux limiter choice. Here, f_i^n is the right-hand side given by

$$f_i^n = H_i^n - (1-\theta)c_i \left(a_0 H_i^n + \sum_{j=1}^{5} a_j H_j^n + a_G^n \right). \tag{21}$$

Besides the explicit formulation ($\theta = 0$), Eq. (19) results in a linear system for the unknown vector $\overrightarrow{H}$ of the form

$$A\,\overrightarrow{H} + \overrightarrow{r_H} = \overrightarrow{f}, \tag{22}$$

where matrix A only contains the coefficients obtained from the geometric values and velocity, $\overrightarrow{r_H}$ contains all the values related to the gradient, and $\overrightarrow{f}$ is the known right-hand side. Vector $\overrightarrow{r_H}$ significantly complicates the computer implementation and parallelization. Thus, $\overrightarrow{r_H}$ is iteratively solved with the linear solver.

The efficiency of the scheme depends on the selection of the solver for linear system (22). Many solvers can be chosen such as the Generalized Minimal Residual and the Bi-Conjugate Gradient Stabilized. However, in reason of their efficiency and simplicity in implementation in parallel, we consider a classical stationary iterative methods, such as the Successive Over-Relaxation (SOR) method [38]. It solves the new iteration for $\overrightarrow{H}$ using the previous one as

$$(D + \omega L)\overrightarrow{H}^{(k+1)} = \omega\left(\overrightarrow{f} - \overrightarrow{r_H}^{(k)}\right) - (\omega U + (\omega - 1)D)\,\overrightarrow{H}^{(k)}, \tag{23}$$

where L, U and D are the lower, upper and diagonal matrices of A, respectively. The value ω is the relaxation factor. Superscripts k and $k+1$ indicates the values of the previous and current iteration, respectively. Note that the proposed SOR method is not the same as their original definition because of $\overrightarrow{r_H}^{(k)}$. This vector should include some values at $k+1$, but all are updated using k. Second, the gradient should be updated at each iteration to obtain $\overrightarrow{r_H}^{(k)}$.

The convergence of the SOR method can be greatly improved by choosing an appropriate choice of the relaxation factor $0 < \omega < 2$. However, the optimal value depends on the particular problem to solve. This paper uses the SOR method with a relaxation value of $\omega = 1.2$ and a tolerance value of $\epsilon = 10^{-8}$.

4 Numerical Method for the Reinitialization Equation

The reinitialization equation (6) is also discretized using similar methodologies as the level-set equation (3), as presented in this section. However, this equation is non-linear that contributes to the higher complexity of the problem.

For the time integration, the θ-method can be also applied to Eq. (6) as follows:

$$H^{m+1} + \theta\Delta\tau\nabla\cdot\left(H^{m+1}\boldsymbol{v}^m + \epsilon\nabla H^{m+1}\right) = H^m - (1-\theta)\Delta\tau\nabla\cdot\left(H^m\boldsymbol{v}^m + \epsilon\nabla H^m\right), \tag{24}$$

where $\boldsymbol{v}^m = (1 - H^m)\boldsymbol{n}^{m=0}$ and $\boldsymbol{n} = \nabla H/|\nabla H|$. Here H^m denotes the approximation of $\mathcal{H}$ at pseudo-time level τ^m, $\Delta\tau$ is the computational pseudo-time step, and θ is equal to 0, 1 or 1/2 if the method is explicit, implicit or the C-N method, respectively. Opposite to the level-set equation where the velocity field is always known, the field $\boldsymbol{v}$ depends on H. Thus this term is always calculated at the previous step in the pseudo-time marching. Note that we also calculate the diffusive term using an implicit formulation.

For the space discretization, we follow the standard finite-volume discretization as described in Eq. (8) for the level-set equation. The main difference relies in the approximation of $\boldsymbol{v}^m$ and the diffusive term. For the vector $\boldsymbol{v}$, we require the gradient approximation of H. This is calculated using the same least-square technique shown in (18). On the other hand, the diffusive term is given by

$$\int_{V_i} \nabla \cdot \nabla H dV = \sum_{j=1}^{5} \oint_{S_j} \nabla H^{n+1} \cdot \boldsymbol{n} dS \approx \sum_{j=1}^{5} m_{S_j} \nabla H_{ij} \boldsymbol{n}_{ij} \tag{25}$$

In this work, we propose to approximate the diffusive term as proposed by Kim and Choi [39]. This formulation decomposed $\left(\frac{\partial H}{\partial \boldsymbol{n}}\right)_{ij} = \nabla H_{ij} n_{ij}$ in two terms: the first one corresponds to the principal diffusion and the second one corresponds to the cross diffusion, as follows

$$\left(\frac{\partial H}{\partial \boldsymbol{n}}\right)_{ij} = \frac{H_j - H_i}{\delta_i + \delta_j} + \frac{H_{\mathrm{V}_2} - H_{\mathrm{V}_1}}{\delta_{\mathrm{V}_1 \mathrm{V}_2}} \tan(\alpha), \tag{26}$$

where δ_i and δ_j are the normal distances to the cell face from $\boldsymbol{x}_i$ and $\boldsymbol{x}_j$, respectively; $\delta_{\mathrm{V}_1 \mathrm{V}_2}$ is the distance from the vertex point $\boldsymbol{x}_{\mathrm{V}_1}$ to $\boldsymbol{x}_{\mathrm{V}_2}$; and α is the angle between $\boldsymbol{n}$ and the line containing $\boldsymbol{x}_i$ and $\boldsymbol{x}_j$. We remark that Eq. (26) is reduced to a central approximation at the vertical faces. Moreover, for orthogonal grids, the cross diffusion is equal to zero as $\alpha = 0$.

A vertex value H_{V} is obtained by averaging over all surrounding cell centers as follows

$$H_{\mathrm{V}} = \sum_k \left(\frac{1}{L_k} H_k\right) \Big/ \sum_k \frac{1}{L_k}, \tag{27}$$

where L_k is a weighting value calculated as the distance between the vertex and the cell-centered point.

Finally, a finite-volume discretization of Eq. (6) at each control volume V_i $(i = 1, 2, \ldots, N_V)$ results in the following linear system of equations

$$H_i^{m+1} + \theta c_i \left((a_0 + b_0) H_i^{m+1} + \sum_{j=1}^{5} (a_j + b_j) H_j^{m+1} + a_G^{m+1} + b_{\mathrm{V}}^{m+1} \right) = f_i^m, \tag{28}$$

where the a_i and b_i coefficients correspond to the convective and diffusive terms, respectively; and f_i^m is the corresponding right-hand side of known values from the previous pseudo-time step. Here, a_G represents the values obtained from the least-square gradient approximation and b_{V} corresponds to the values resulting from the vertex interpolation. Equation (28) is traditionally solved for a few pseudo-time steps.

5 Parallelization

As previously pointed out, three-dimensional numerical simulations require considerable computational time due to the amount of data. Furthermore, for implicit formulations, linear systems (19) and (28) have to be solved for each time step. Thus, the complete code can be performed in parallel, as described in this section.

The computational domain is divided into several sub-domains of almost the same number of elements. Every sub-domain is extended to create an overlap region such that all the elements surrounding boundary nodes are included, see Fig. 2. This block domain decomposition guarantees that an unknown value H_i and its five surrounding values, H_j, are included in the same sub-domain. However, the discretization links cell-centered unknowns assigned by different sub-domains. Therefore, communication between processors is required. In order to ensure efficient data communication, the data changed through overlapping points is grouped in vectors. Then, a standard Message Passage Interface (MPI) is used to implement the algorithm.

On the other hand, the SOR solver can not be parallelized in its original form. Instead, we employ the Multi-color SOR method to solve linear system (22). The idea is to divide the whole domain into different colors such that the evaluation of each unknown involves the values of another color only [34, 35]. Thus, sets of points of the same color can be computed using the SOR method (23) as follows

$$\overrightarrow{H}^{(k+1)} = D^{-1}\left[\omega(\overrightarrow{f} - \overrightarrow{r_H}^{(k)}) - (\omega(L+U) + (\omega-1)D)\overrightarrow{H}^{(k)}\right]. \tag{29}$$

Note that Eq. (29) is equivalent to a Jacobi solvers. Although communication after each color calculations required, this method is well-suited to parallel implementation because all new values only depends on the previous iteration. Moreover, numerical results have shown that the convergence of this method is similar to the original SOR method [35].

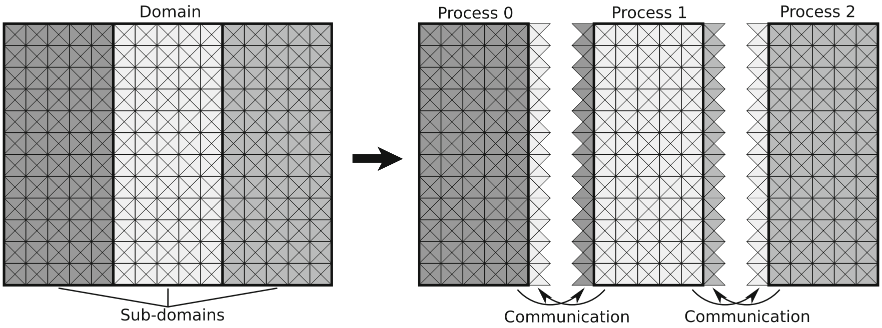

Fig. 2 An example of horizontal computational domain with a block domain decomposition

6 Accuracy

In this section, we study the accuracy and performance of the proposed time integration and finite-volume formulation used to approximate the partial differential equations of the level-set model.

Numerical simulations employ structured and unstructured grids in the horizontal plane. For structured grids, the domain is firstly divided into $(N_x - 1) \times (N_y - 1)$ uniform rectangles and then each rectangle is split into two right-angled triangles as shown in Fig. 3a. For unstructured grids, triangles change size and different number of cells share a node, as shown in Fig. 3b. Table 1 shows the number of vertex points, cell-centered points and prisms used to discretize a square and cube domain of resolution $N = N_x = N_y = N_z$. Here, $\Delta x = L/(N_x - 1)$ is the length of the triangle in the x-direction, where L is the 2D domain width. For unstructured grids, the mesh was generated by taking a mean triangle edge close to the corresponding Δx.

To study the order of the method in time and space, we propose a solid-body rotation example. As shown in the numerical results, presented in the following section, the proposed method produces significant errors close to the sharp gradient

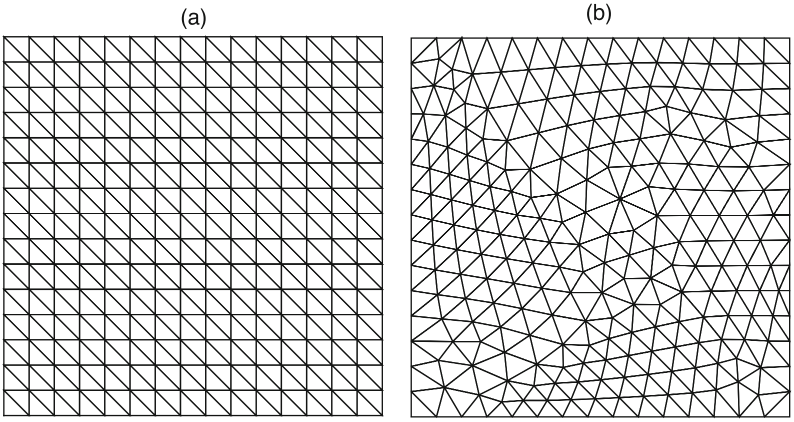

Fig. 3 (**a**) Structured right-angled and (**b**) unstructured grid of resolution $N = 16$

Table 1 Size of the structured and unstructured grids used in numerical experiments for the computational domain

	Structured			Unstructured		
N	Vertex points	Cell-centered points	Prisms	Vertex points	Cell-centered points	Prisms
32	1024	1922	59,582	1188	2234	69,254
64	4096	7938	500,094	4752	9234	58,1742
128	16,384	32,258	4,129,024	18,355	36,121	4,587,367
256	65,536	130,050	33,162,750	72,351	143,473	36,585,615

regions using $\mathcal{H}_\epsilon$ to solve the conservative level-set equation, even for fine mesh resolutions. It is expected as the numerical methods are originally designed to solve problems with enough regularity. Thus, a convergence analysis using this characteristic function will not give us helpful information about the accuracy of the approximated solution. Instead, in this section, we study the accuracy using the well-known cosine-bell example to test convective equations. In the cosine-bell example, the characteristic function is given by

$$\varphi(\boldsymbol{x}) = \begin{cases} \cos^2(2\pi r), & r \le r_0, \\ 0, & r > r_0, \end{cases} \tag{30}$$

where $r = ||\boldsymbol{x} - \boldsymbol{x}_0||$. Although this is not the function that we employ to obtain the interface location, it give us an idea how accurate the method behaves in ideal situations. Thus, we impose $H = \varphi$ as initial condition for Eq. (3). For all the simulations, homogeneous Dirichlet conditions are imposed at all boundaries.

6.1 2D Pure Convective Test

The computational domain is set as the square $[-1, 1] \times [-1, 1]$ and the velocity field is given by

$$\boldsymbol{u} = 2\pi\Big(- y, x\Big), \tag{31}$$

where the angular velocity was chosen such that one full revolution takes place within final time $t = 1$. Initial condition is given by the cosine-bell example (30) with $r_0 = 0.25$ and $(x_0, y_0) = (-1/2, 0)$.

Figure 4a shows the numerical solution at five stages: $t = 0.2, 0.4, 0.6, 0.8, 1.0$ using the upwind scheme with the flux-limiter technique, $\Delta t = 10^{-4}$ and a

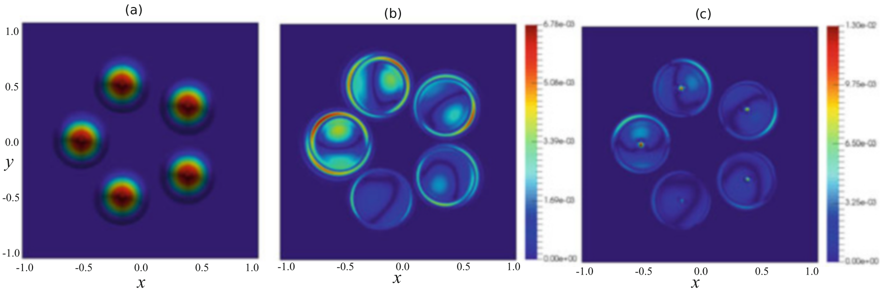

Fig. 4 Numerical solution and absolute errors with and without flux limiter for the 2D cosine-bell rotation example at $t = 0.2, 0.4, 0.6, 0.8, 1.0$ using $N = 256$. (**a**) Numerical solution. (**b**) Error: upwind. (**c**) Error: upwind with flux-limiter

structured grid resolution of $N = 256$. The numerical solution nicely preserves the round shape of the initial condition. Figure 4b and c show the absolute error and the influence of the flux limiter technique in the numerical solution. In all cases, the maximum errors are concentrated near the interface region ($H = 0$). Note that the upwind scheme begins to show small oscillations. However, the flux-limiter technique either reduces or eliminates them. From now on every simulation is run with the flux limiter.

The temporal accuracy is investigated by varying the time step, but keeping the grid size constant. A structured grid of $N = 256$ is used to minimize spatial error. Figure 5 shows the norm errors for the explicit ($\theta = 0$), implicit ($\theta = 1$), and C-N ($\theta = 0.5$) methods. There is a clear difference when we change the temporal formulation. The explicit scheme is only stable to values close to $\Delta t = \Delta x^2$; the implicit scheme is first-order accurate in time; and the C-N method is second-order accurate, as expected. The order of accuracy is calculated by the slope of the least-square (LSM) regression line of the norm errors.

Now, the space accuracy is investigated by varying the grid size but keeping the C-N method with $\Delta t = 10^{-5}$ constant. Table 2 convergence analysis indicates that the method is close to second-order accurate. Results also show that the flux-limiter technique produces smaller L_2-norm errors than the original upwind solution. However, the L_∞-norm differs from one resolution to another. Table 2 also shows the absolute error of the cosine-bell peak values. Note that we obtain more precise peak values for the upwind scheme. This behavior is expected because the flux limiter can reduce the method to a first-order approximation in some regions. In this way, spurious oscillations are reduced in the whole domain, but additional numerical diffusion is introduced.

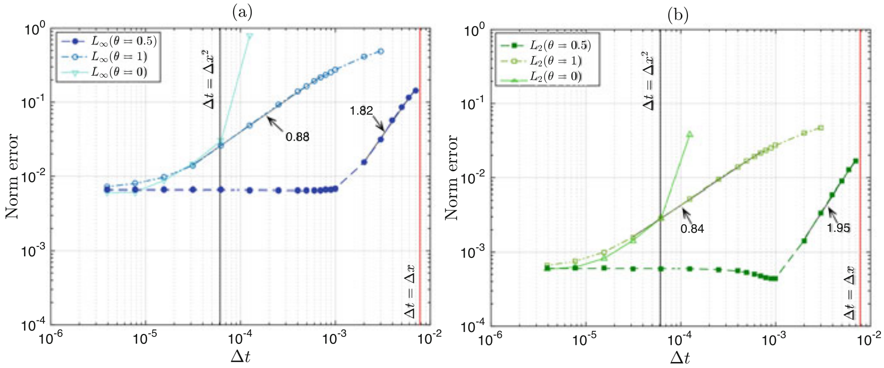

Fig. 5 Temporal convergence analysis of the 2D cosine-bell rotation example at $t = 1$ using (**a**) L_∞-norm and (**b**) L_2-norm error

Table 2 Convergence spatial analysis for the 2D cosine-bell example using different structured grids resolutions at $t = 1$

	Upwind scheme					Upwind scheme with flux-limiter technique				
	L_∞-norm		L_2-norm		Peak value	L_∞-norm		L_2-norm		Peak value
N	Error	Order	Error	Order	Error	Error	Order	Error	Order	Error
32	3.73e−01	–	3.24e−02	–	3.58e−01	4.67e−01	–	3.52e−02	–	4.67e−01
64	9.37e−02	1.99	9.21e−03	1.81	6.82e−02	1.45e−01	1.69	8.24e−03	2.09	1.45e−01
128	1.83e−02	2.36	2.25e−03	2.03	8.40e−03	4.05e−02	1.84	1.84e−03	2.16	4.01e−02
256	6.51e−03	1.49	5.89e−04	1.93	1.12e−03	1.21e−02	1.74	4.95e−04	1.89	1.19e−02
LSM		**1.83**		**1.91**			**1.74**		**1.98**	

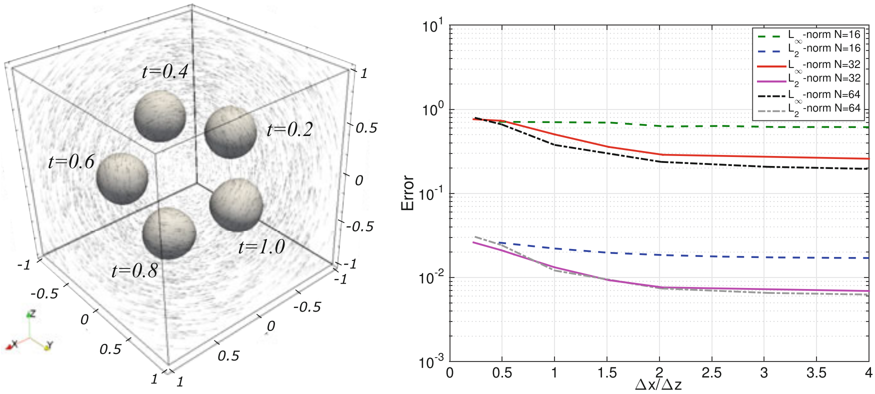

Fig. 6 Numerical solution of the 3D cosine-bell rotation example at different stages, and the error at $t = 1$ using different number of layers in the z-direction

6.2 3D Pure Convective Test

For the 3D case, the domain is $[-1, 1] \times [-1, 1] \times [-1, 1]$ and the velocity is given by

$$\boldsymbol{u} = 2\pi/\sqrt{3}\big(z - y,\ x - z,\ y - x\big). \tag{32}$$

As the 2D case, the numerical solution of Eq. (3) is quantified using the cosine-bell example (30) with $r_0 = 0.25$ and $\boldsymbol{x}_0 = (-0.5, -0.5, -0.5)$. The domain is divided into several horizontal structured grid resolutions and number of vertical layers. We use $\Delta t = 5 \times 10^{-4}$ in these simulations. The contour line $H = 0.01$ and velocity field using $N = 128$ are shown at different time stages in Fig. 6. The scheme recovers the shape of the sphere when it moves around the domain.

The error magnitude is different in the horizontal and vertical direction because these approximations are not calculated in the same way. Figure 6 also shows the errors for different horizontal grids as the vertical resolution is increased. The value

Table 3 Convergence analysis for the 3D solid-body rotation example using a structured grid

N	L_∞-norm	Order	L_2-norm	Order	Peak numerical	Peak exact	Peak error
32	5.70e−01	–	1.48e−02	–	0.359340	0.999800	6.40e−01
64	2.01e−01	1.50	4.84e−03	1.61	0.782000	0.984350	2.02e−01
128	4.27e−02	2.23	9.57e−04	2.34	0.952840	0.999930	4.71e−02
256	1.34e−02	1.67	2.47e−04	1.95	0.986430	0.998700	1.23e−02
LSM		**1.83**		**1.98**			

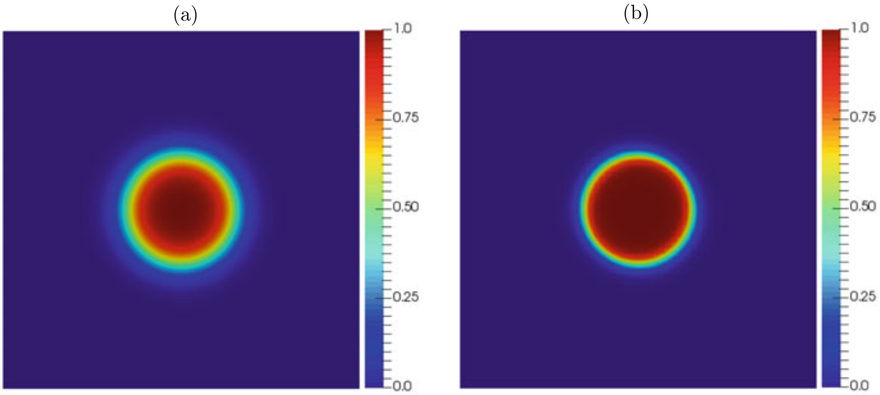

Fig. 7 (**a**) Initial and (**b**) numerical solution of the reinitialization equation at 20 pseudo-time steps

of Δz should be the half of Δx to obtain the minimum error for the convective problem. However, $\Delta z = \Delta x$ already gives a precise solution, as shown in the convergence analysis of Table 3. The method is close to a second order of accuracy. Note that, by increasing the grid resolution, the peak value is closer to the exact one.

6.3 *Reinitialization Test*

Now, we analyze the solution of the reinitialization equation (6). For this test, the initial condition is a smooth function given by $0.5\left(1 + \tanh\left(d/\sqrt{2A}\right)\right)$, where d is the distance function and A is the minimum area among all triangular cells, see Fig. 7a. Figure 7b shows the effect of the reinitialization equation after 20 pseudo-time steps. Here, we use a structured grid resolution of $N = 64$ for $\Omega = [0, 1]^2$, and an explicit formulation with $\Delta\tau = 2 \times 10^{-3}$. Note that the solution now resembles the Heaviside function.

Figure 8a shows that the numerical solution becomes sharper as the number of pseudo-time step increases. However, the solution does not change significantly after 50 pseudo-time steps. As a criteria for steady-state, we used Error =

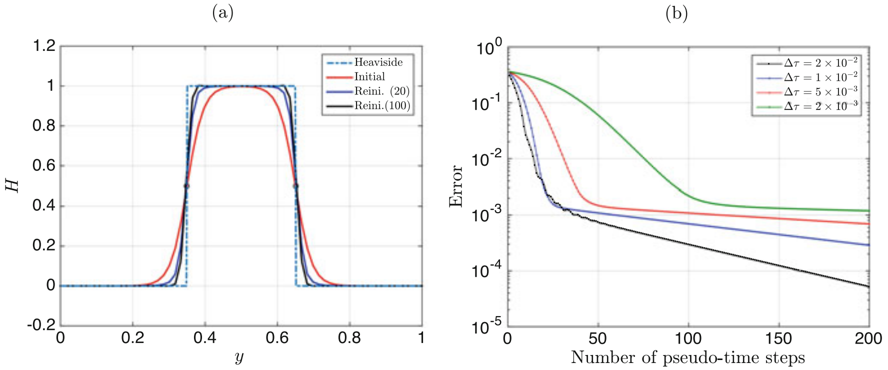

Fig. 8 (**a**) Reinitialization solution at $x = 0.5$, and (**b**) convergence error for different $\Delta\tau$ values

$\int_\Omega \left((H^{m+1} - H^m)/\Delta\tau\right) < tol$, for some tolerance tol [29]. Figure 8b displays the error versus the number of pseudo-time steps. As expected, the convergence depends on $\Delta\tau$. The steps required to reach a given tolerance reduces significantly for larger $\Delta\tau$ values. Although the results are not shown here, similar results are obtained for the 3D case.

7 Two-Dimensional Numerical Results

In this section, three well-known problems are used to study the proposed conservative level-set approach: the solid-body rotation problem, the Zalesak's disk, and the single vortex.

In the following examples, the initial condition is the regularized $\mathcal{H}_\epsilon$ function. However, we also perform simulations using the original Heaviside function $\mathcal{H}$. For both cases, the interface is defined as the level sets $H = 0.5$. To quantify the error, we use the normalized mass conservation errors defined as

$$E_0(t) = \left(\int_\Omega H(\boldsymbol{x}, t)dV - \int_\Omega H(\boldsymbol{x}, 0)dV\right) \Big/ \int_\Omega H(\boldsymbol{x}, 0)dV, \tag{33}$$

$$E_1(t) = E_0(t), \quad \text{for} \quad 0.5 \leq H \leq 1. \tag{34}$$

Note that E_0 measures the mass conservation in the whole domain; meanwhile, E_1 only the mass inside the interface.

7.1 Solid-Body Rotation

For the first example, we consider the solid-body rotation problem resulting from the conservative level-set equation (3). The domain is $[-1, 1] \times [-1, 1]$ and the interface is circular with $r_0 = 0.25$ and $\boldsymbol{x}_0 = (-0.5, -0.5)$. The velocity field is given by Eq. (31). Figure 9 shows the numerical results at different stages using $\Delta t = 10^{-4}$ and a structured grid of resolution $N = 256$. Accurate solutions are obtained for both $\mathcal{H}_\epsilon$ and $\mathcal{H}$. However, as the solid-body rotates, the numerical solution produce some numerical diffusion close to the sharp gradient regions. On the other hand, Fig. 10 shows the normalized mass conservation errors for each case. Both errors are small indicating that the numerical method is conservative, as expected.

Previous results have shown high accuracy due to the fine mesh; however, as expected, the solution becomes more diffusive as the spatial resolution decreases. This behavior is in part a consequence of the proposed regularized function $\mathcal{H}_\epsilon$. For example, Fig. 11 shows the initial and final results at $x = -0.5$ for different $\epsilon = 0.5\Delta^\beta$ values and a structured grid of resolution $N = 64$. As β is smaller, ϵ is larger and the initial solution becomes smoother. Note that for $\beta = 0.8$, the initial and final profiles are very similar. However, the solution is not sharp enough to describe the profile of the Heaviside function. In this work, we use $\mathcal{H}_\epsilon$ with $\beta = 1$ as a default value. Note that its corresponding final stage is almost the same as $\mathcal{H}$ for this example.

Finally, we improve the results by applying the reinitialization step, as shown in Fig. 12. As expected, the numerical solution is significantly improved. We remark that there is not much difference for cases with higher resolution as the conservative level-set equation already gives accurate results.

The effect of the unstructured mesh will be discussed in the following two more complex examples. In the Zalesak's disk problem, we study how accurately sharp

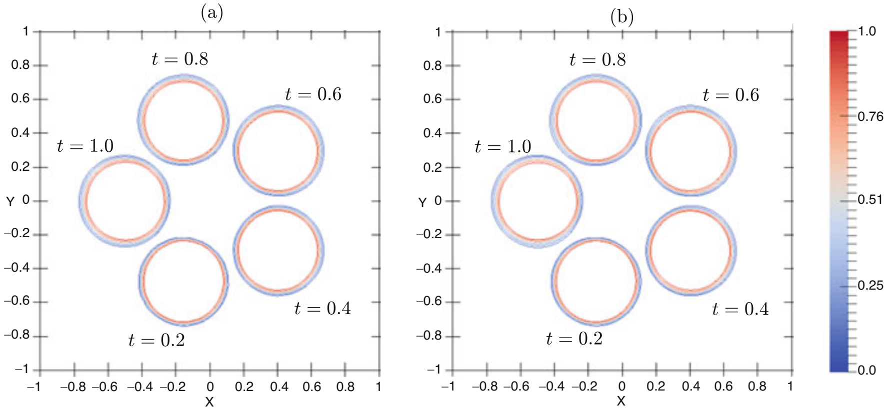

Fig. 9 Numerical solution for the 2D solid-body rotation at different stages for $N = 256$. (**a**) $\mathcal{H}_\epsilon$. (**b**) $\mathcal{H}$

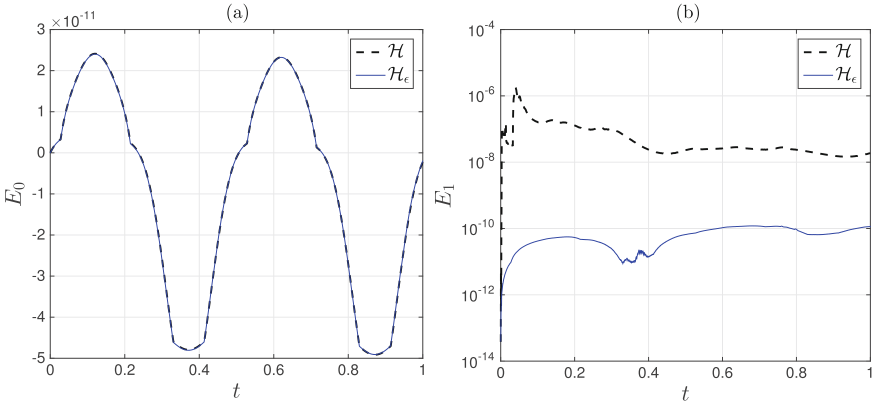

Fig. 10 Numerical solution for the 2D solid-body rotation at different stages for $N = 256$, and normalized mass conservation errors. (**a**) E_0. (**b**) E_1

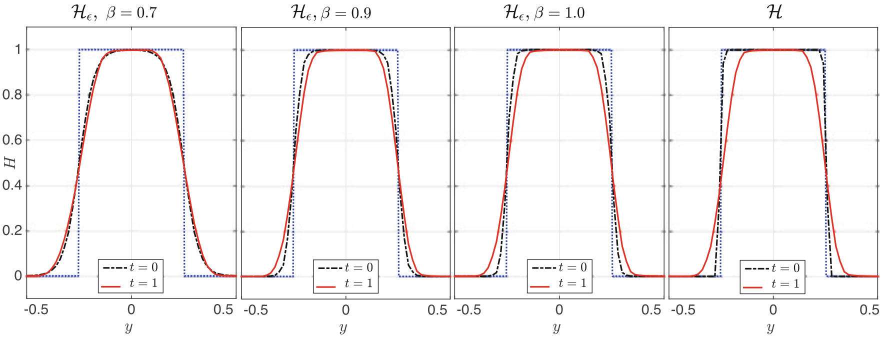

Fig. 11 Numerical solution for the 2D solid-body rotation at the initial and final stage at $x = -0.5$ using different $\epsilon = 0.5\Delta^{\beta}$ values and $N = 64$

corners are transported. Next, in the single vortex problem, we investigate the ability of the method to resolve thinner filaments.

7.2 Zalesak's Disk

For the second example, the Zalesak's disk benchmark simulates the rigid body rotation of the slotted disk with respect to a fixed point [40]. The initial shape is a disk of radius $r_0 = 0.15$ and centered at $\boldsymbol{x}_0 = (0.75, 0.5)$ with a slot of 0.05 deep and 0.125 wide, see Fig. 13. The domain is $[0, 1] \times [0, 1]$ and the velocity is given by (31). The slotted disk also completes one revolution after one unit of time.

The final interface of the slotted disk after one complete cycle using different grid resolutions is shown in Fig. 13. Note that the coarse grid gives a curve that has lost

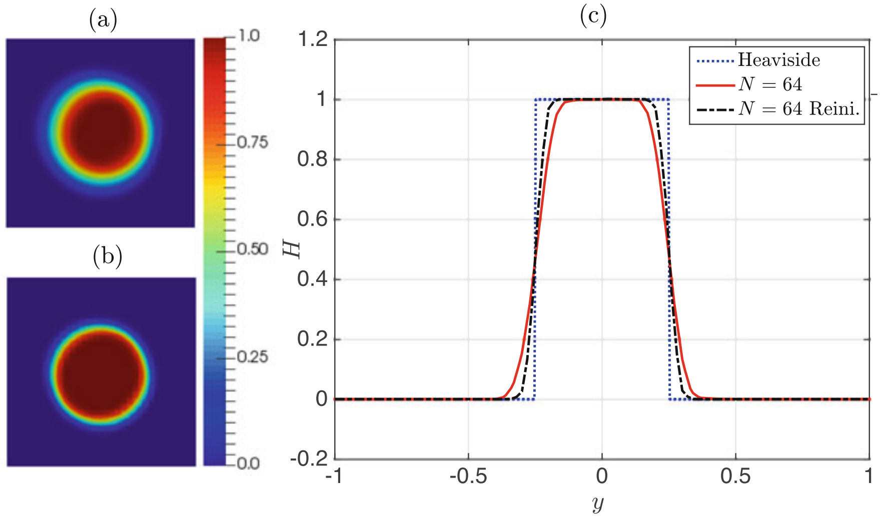

Fig. 12 Numerical solution for the 2D solid-body rotation at the final stage with and without reinitialization for a structured grid resolution of $N = 64$. (**a**) $N = 64$. (**b**) $N = 64$ Reini. (**c**) Numerical solution at $x = -0.5$

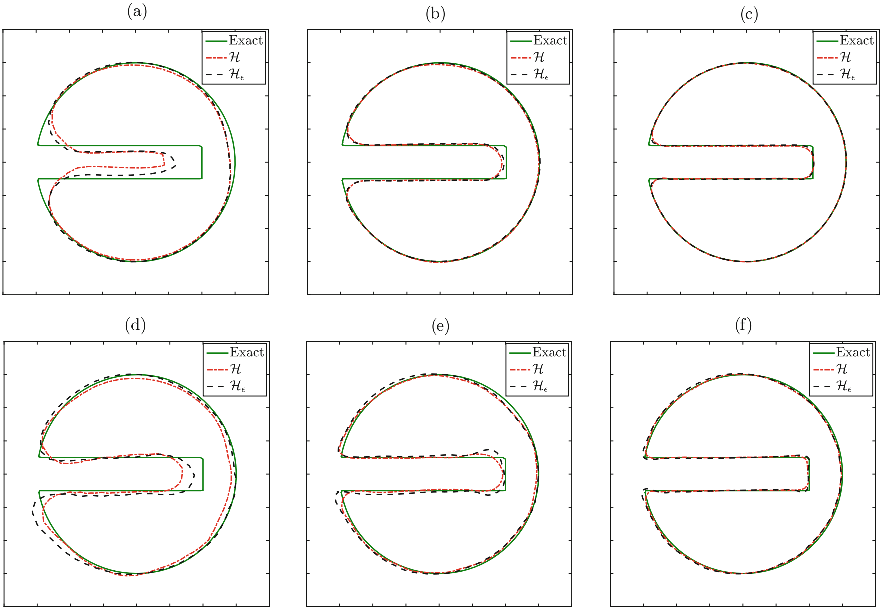

Fig. 13 Zalesak's disk final interface after a complete revolution with different grids. (**a**) Structured ($N = 64$). (**b**) Structured ($N = 128$). (**c**) Structured ($N = 256$). (**d**) Unstructured ($N = 64$). (**e**) Unstructured ($N = 128$). (**f**) Unstructured ($N = 256$)

Table 4 Normalized mass errors of the Zalesak's disk problem after one revolution

	Structured			Unstructured		
	$N = 64$	$N = 128$	$N = 256$	$N = 64$	$N = 128$	$N = 256$
$\mathcal{H}$	-21.8%	-14.6%	-8.1%	-18.9%	-7.1%	-3.6%
$\mathcal{H}_\epsilon$	-3.5%	-3.3%	-1.2%	5.4%	4.8%	3.8%

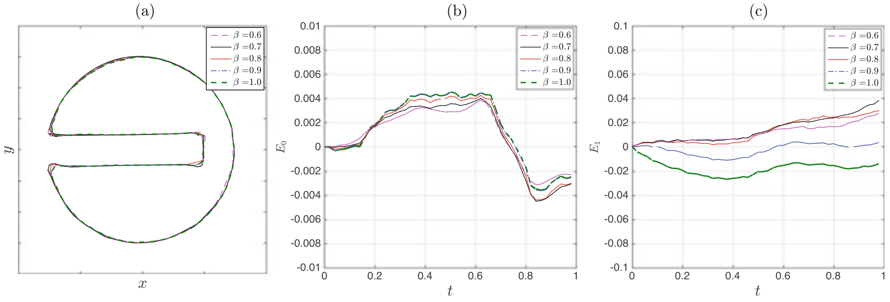

Fig. 14 Zalesak's disk final interface and evolution of the normalized mass errors E_0 and E_1 using a $N = 256$ unstructured grid resolution. Errors for different values of $\varepsilon = 0.5\Delta^\beta$. (**a**) Solution $\mathcal{H}_\epsilon$. (**b**) Relative error E_0. (**c**) Relative error E_1

its original shape. However, for $N = 256$, structured and unstructured results show an acceptable final profile for both $\mathcal{H}$ and $\mathcal{H}_\epsilon$. As expected, the most challenging part are the corners. The mass errors shown in Table 4 agree with the profiles of the slotted disk shown in Fig. 13. The mass errors are displayed using structured and unstructured grids of resolutions $N = 64$, 128, and 256. As expected, the mass conservation is improved when the grid size is smaller. A maximum deviation of 1.2% and 3.6% are reached using a structured and unstructured grid resolution of $N = 256$, respectively.

Figure 14 shows the final interface and normalized mass errors of different values of $\varepsilon = 0.5\Delta^\beta$ using an unstructured grid of resolution $N = 256$. As expected, the evolution of errors E_0 and E_1 depends on the β values. If β decreases, then E_1 becomes smaller. However, the final interfaces have imperceptible differences. The reminding simulations of this paper with $\mathcal{H}_\epsilon$ will be performed using $\beta = 1$.

Finally, as the previous example, we present the results incorporating the reinitialization algorithm, as shown in Fig. 15. Although the level set $H = 0.5$ is similar for both cases, the numerical solution of H is significantly improved, as expected.

7.3 Single Vortex Deformation of a Circle

For the final 2D test case, we study the single vortex deformation of a circle in the domain $[0, 1] \times [0, 1]$. A circle of radius $r_0 = 0.15$ is initially centered at $\boldsymbol{x}_0 =$

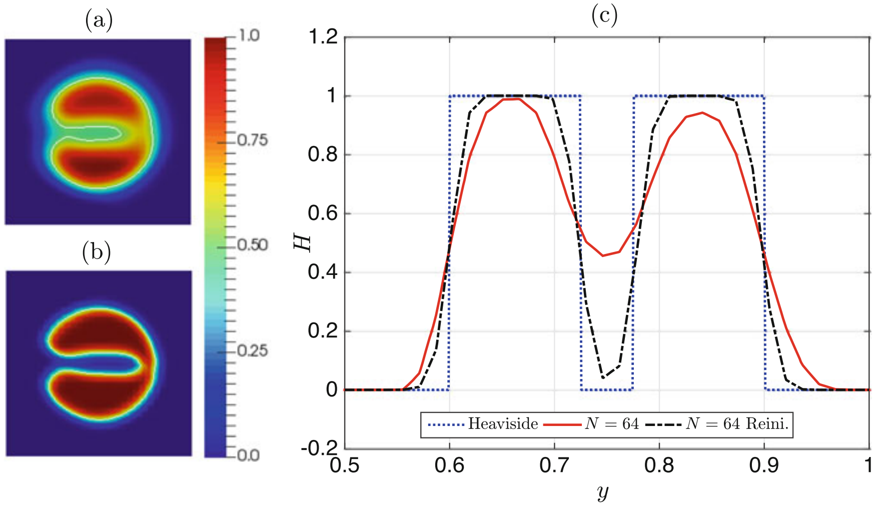

Fig. 15 Zalesak's disk final solution with and without reinitialization using a $N = 64$ structured grid resolution. The one-dimensional solution corresponds to $x = 0.5$. (**a**) $N = 64$. (**b**) $N = 64$ Reini. (**c**) Numerical solution at $x = 0.5$

(0.5, 0.75) and advected under a solenoidal velocity field given by

$$\boldsymbol{u} = \Big(-\sin^2(\pi x)\sin(2\pi y),\ \sin^2(\pi y)\sin(2\pi x)\Big), \tag{35}$$

At $t = T/2$ the flow field is reversed, so that the exact solution at $t = T$ should coincide with the initial condition. Unlike previous examples, the accuracy of the numerical method also depends on the topology changes of the initial interface. As the period T increases, the velocity field stretches the circular interface into a very long filament that spirals around the center of the domain. Thus, the final interface shape becomes more difficult to coincide with the initial condition.

Contour lines corresponding to $H = 0.1, 0.5$, and 0.9 of the evolution of the circle shape for a period $T = 8$ at eight different stages are shown in Fig. 16. We employ a structured right-angled grid resolution of $N = 256$, $\mathcal{H}_\epsilon$ as initial condition, and $\Delta t = 10^{-4}$. Note that the interface is very accurate at early stages; however, the interface tail loses its accuracy as time continues increasing. At $t = 4$, the circle reaches its maximum deformation, and the result is already deteriorated.

As expected, the final solution also depends on the grid resolution. Figure 17 shows the level-set at $H = 0.5$ for the period $T = 2$ using structured and unstructured grids. The interface has returned to a circle format, and it is more accurate as the grid resolution becomes finer. However, for unstructured grids, the profile presents some noisy at several segments of the interface. It is expected as the cell size and number of cells sharing a node change in an unstructured grid.

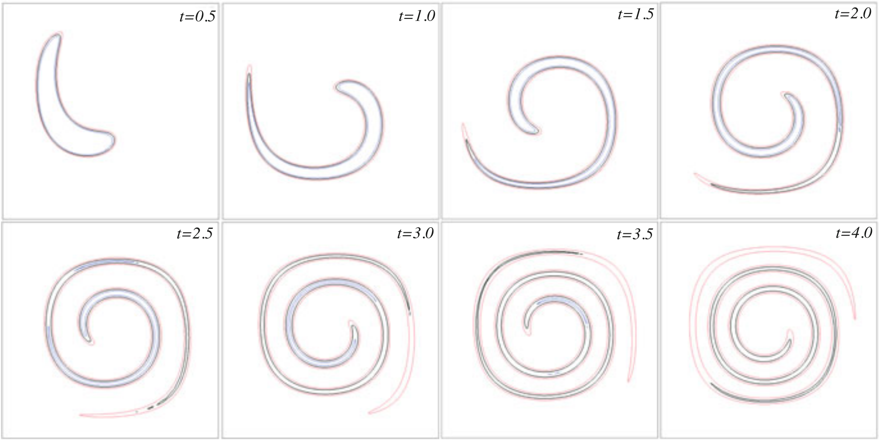

Fig. 16 Single vortex deformation of a circle at different stages using a structured grid of resolution $N = 256$. Interface location corresponds to $H = 0.1$ (red), $H = 0.5$ (black) and $H = 0.9$ (blue)

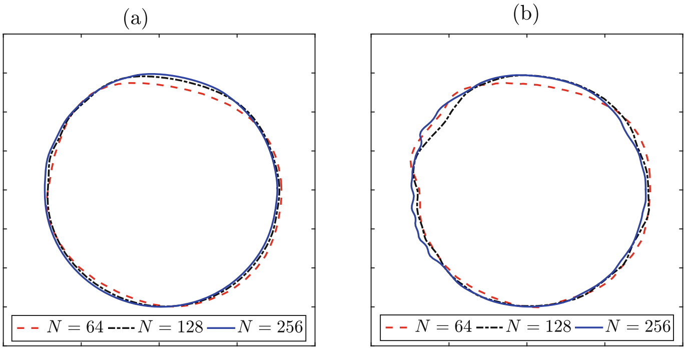

Fig. 17 Final interface location ($H = 0.5$) for the period $T = 2$ using different grid resolutions. (**a**) Structured. (**b**) Unstructured

On the other hand, the final shapes of the circles to periods $T = 1$, 2, 4 and 8 are shown in Fig. 18a using a structured of $N = 256$. For periods $T = 1$ and 2, the circle returns to its original shape with high accuracy. Furthermore, the final interface shape for period $T = 4$ still resembles a circle. However, the grid is not fine enough to resolve the interface at $T = 8$. The precision of the numerical results can be better analyzed from the interface errors shown in Fig. 18b. The interface error is calculated as $e_i = |r_0 - r_i|$, where r_i is the distance from each point $\boldsymbol{x}_i$ on the interface to the initial center $\boldsymbol{x}_0$.

Table 5 shows the L_∞- and L_2-norm errors of the final interface shape using $\mathcal{H}$ and $\mathcal{H}_\epsilon$, as level-set functions. Note that the norm errors are slightly different

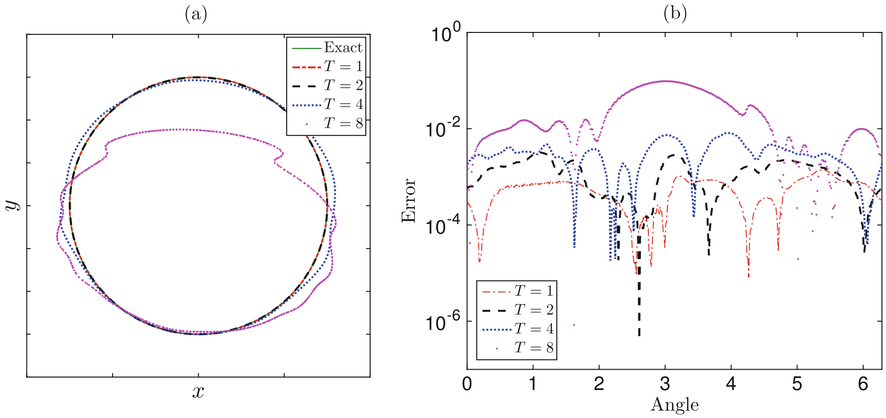

Fig. 18 Single vortex deformation of a circle: (**a**) Final interface location $H = 0.5$ for the circle for $T = 1, 2, 4, 8$ using a right-angled grid of resolution $N = 256$. Absolute interface errors using the characteristic function $\mathcal{H}_\epsilon$. (**a**) Final interface solution. (**b**) Absolute errors

Table 5 Interface errors of the single vortex problem with a right-angled grid of resolution $N = 256$ and different characteristic functions

Period (T)	Heaviside function $\mathcal{H}$		Regularized function $\mathcal{H}_\epsilon$	
	L_∞-norm	L_2-norm	L_∞-norm	L_2-norm
1	1.46e−03	1.66e−02	1.43e−03	1.49e−02
2	2.97e−03	3.55e−02	3.21e−03	3.45e−02
4	8.05e−03	8.43e−02	8.20e−03	8.42e−02
8	9.70e−02	8.48e−01	9.70e−02	8.50e−01

between the Heaviside function and the regularized function $\mathcal{H}_\epsilon$. This confirm the method's capacity to deal with the discontinuous $\mathcal{H}$ problem.

We further study the conservative level-set results for $\mathcal{H}$ and $\mathcal{H}_\epsilon$ by analyzing the loss mass for period $T = 2$. The normalized mass error E_0 is plotted in Fig. 19 for $N = 256$. The global error E_0 is close to the zero machine for structured grids and very small for unstructured grids which indicates that the proposed numerical method is conservative, as expected.

Figure 20 shows the results of the reinitialization step in the single vortex problem for $T = 2$ using a structured grid of resolution $N = 64$. Note the significant improvement in the numerical solution compared to the one without reinitialization. Finally, we remark that, even if a reinitialization step is applied, inaccurate results are presented by other state-of-the-art methods for either structured or unstructured grids [27, 29, 36].

In general, the method's accuracy of each example is sensitive to the reinitialization parameters: the number of pseudo-time steps, $\Delta\tau$, and recurrence that is applied. Future work will be done in this direction.

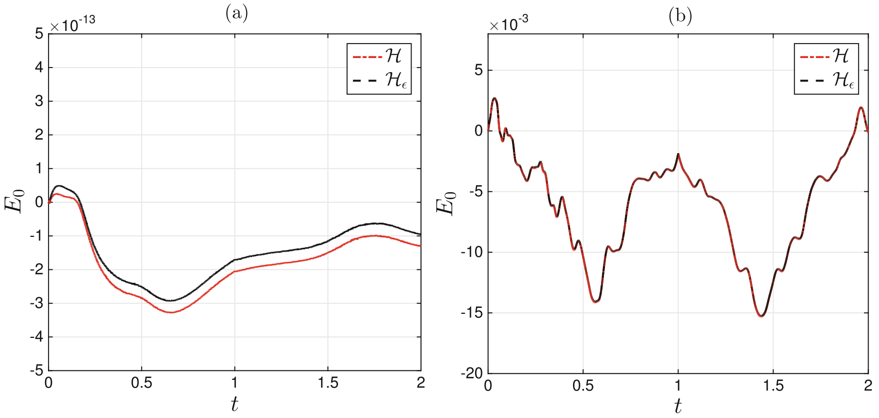

Fig. 19 Normalized mass error E_0 of the single vortex problem with period $T = 2$ using structured and unstructured grids for $N = 256$. (**a**) Structured E_0. (**b**) Unstructured E_0

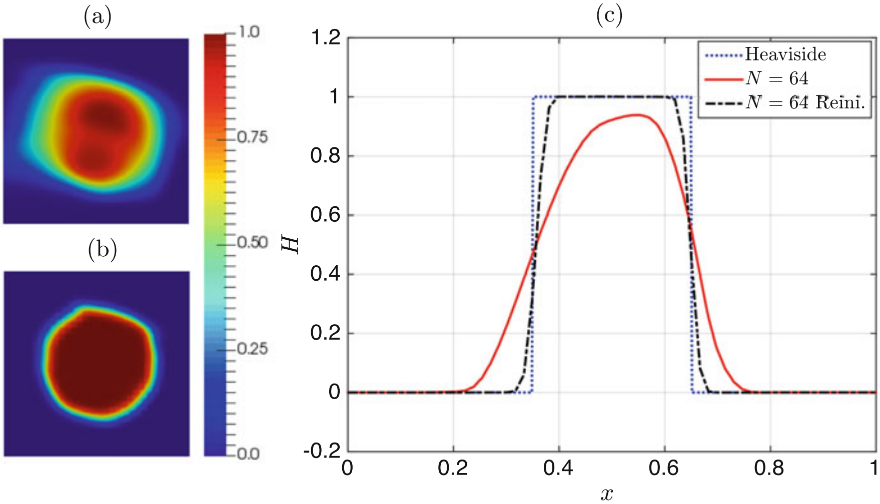

Fig. 20 Single vortex final solution ($T = 2$) with and without reinitialization using a structured grid of resolution $N = 64$. (**a**) $N = 64$. (**b**) $N = 65$ Reini. (**c**) Numerical solution at $y = 0.75$

8 Three-Dimensional Numerical Results

The ideas presented for the 2D examples can be carried out directly to 3D space. This section tests the proposed numerical method in three benchmarks problems considered by Kawano et al. [18]. The simulations are computed over the domain $\Omega = [0, 1] \times [0, 1] \times [0, 1]$. The same grid resolution was selected in each direction for structured and unstructured grids, as presented in Table 1. We apply $\Delta t = 10^{-2}$, 5×10^{-3}, and 2×10^{-3} for $N = 64$, 128, and 256, respectively.

8.1 Kawano 3D Solid-Body Translation

In this example, an interface profile as proposed by Kawano [18] is translated into Ω. The shape is defined as the union of the sets $[0.08, 0.48] \times [0.2, 0.36] \times [0.08, 0.48]$ and the sphere of radius $r_0 = 0.16$ and center $\boldsymbol{x}_0 = (0.28, 0.28, 0.28)$, see Fig. 21. The shape is translated using the uniform velocity field $\boldsymbol{u} = (1, 1, 1)$. At $t = 0.4$ the flow field is reversed using $\boldsymbol{u} = (-1, -1, -1)$, then the solid-body returns to the initial position at $t = 0.8$.

Figure 21 shows the final shapes ($t = 0.8$) using different resolutions for structured and unstructured grids and the Heaviside function. The initial body shape is recovered in all cases. Although the method produces more deformations for $N = 64$, we get accurate results for $N = 128$ and 256. For unstructured grids, results show some noise at several segments of the interface. It is expected due to the arbitrary distribution of the cell size and number of cells sharing a node. Profiles in the xy plane at $z = 0.28$ for iso-surface values $H = 0.1, 0.5,$ and 0.9 are shown in Fig. 22. Results confirm that high-resolution grids produce small deformations; however, the sharp corners are still smoothed. Figure 22 also shows the normalized mass error E_1. Note that it decreases when grid resolution is finer. Moreover, temporal evolution has a similar behavior for both structured and unstructured grids.

To conclude this example, we study the reinitialization effect in this problem. Figure 23 shows the results using a structured grid of $N = 64$ and both $\mathcal{H}$ and $\mathcal{H}_\epsilon$ as characteristic level-set functions. Note that the numerical solution for both cases is similar. As expected, the reinitialization step gives a less diffusive solution and is closer to the Heaviside profile.

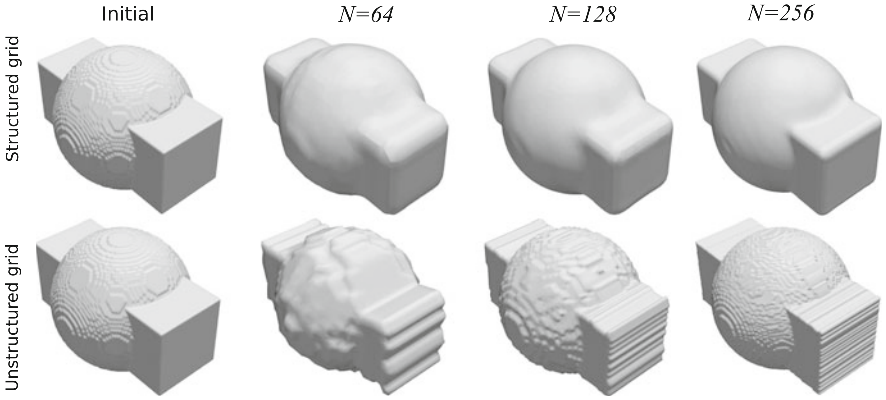

Fig. 21 Final body position ($H = 0.5$) using different structured and unstructured grid resolutions

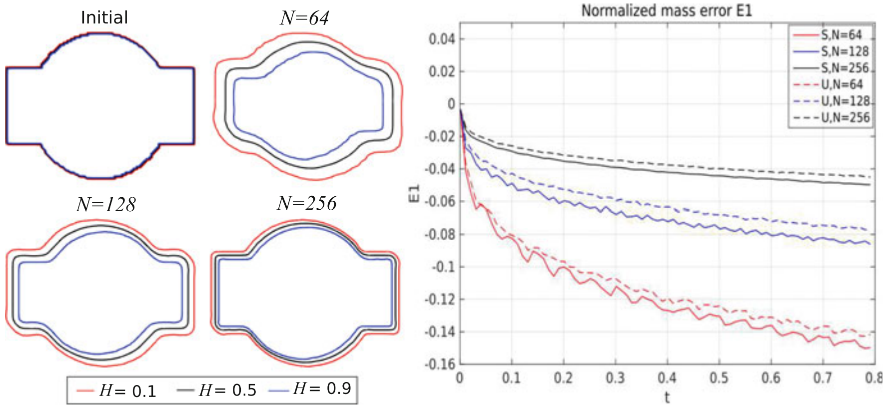

Fig. 22 Initial and final time profiles of the Kawano 3D solid-body example for structured grids, and temporal evolution of the normalized mass error E_1

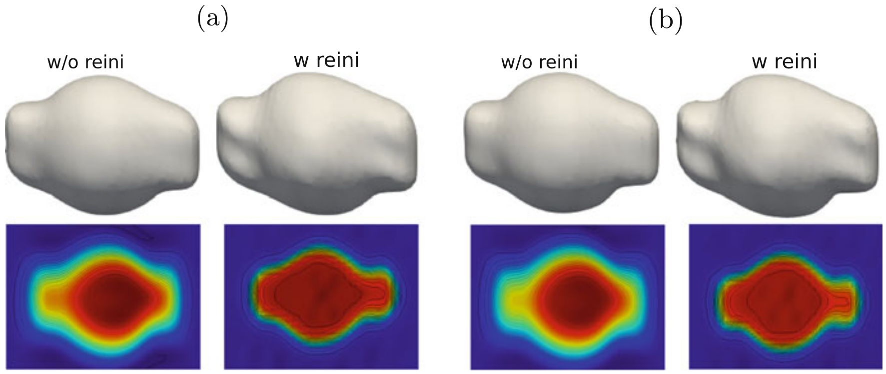

Fig. 23 Kawano 3D solid-body final solution with and without reinitialization using a $N = 64$ structured grid resolution. The results at the bottom corresponds to the xy plane at $z = 0.28$. (**a**) $\mathcal{H}$. (**b**) $\mathcal{H}_\epsilon$

8.2 Zalesak's Sphere

The second 3D example is Zalesak's sphere test [18, 41]. This example has been used extensively to characterize how the methods can accurately transport sharp corners. The shape is a sphere of $r_0 = 0.15$ and $\boldsymbol{x}_0 = (0.75, 0.25, 0.5)$ with a slot of 0.2 deep and 0.04 wide. The velocity field moves the solid body over a circular trajectory that is orthogonal to the vector $(1, 1, 1)$ returning to its original position at $t = 1$.

Numerical results using the Heaviside characteristic function are shown in Fig. 24. This figure also shows the initial and final interfaces using a structured grid of $N = 64$, 128, and 256. As expected, the numerical method can recover the initial

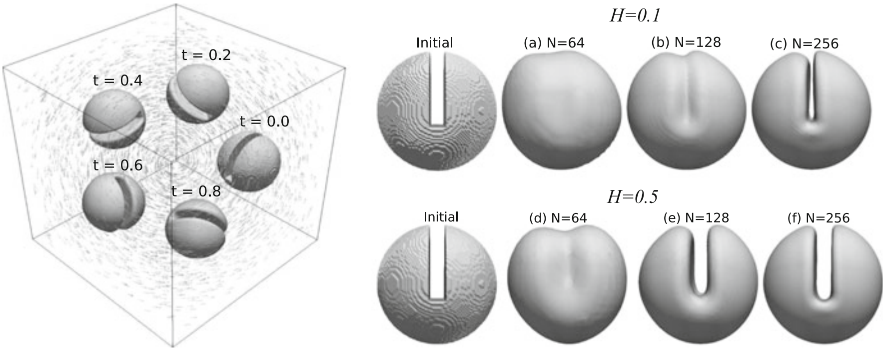

Fig. 24 Zalesak's sphere evolution at different stages using $N = 256$. At the right, iso-surfaces $H = 0.1$ (top) and $H = 0.5$ (bottom) at the initial and final time for different grid resolutions

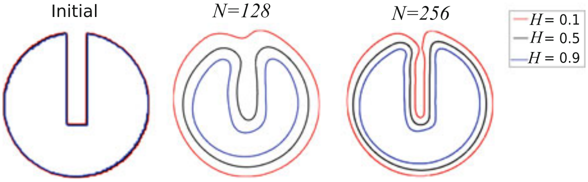

Fig. 25 Initial and final profile of the Zalesak' sphere using for different resolutions

shape for higher resolutions. The iso-surface profiles on the plane xy at $z = 0.5$ are displayed in Fig. 25a for $H = 0.1, 0.5$, and 0.9. Results confirm that high-resolution grids produces small deformations; however, the sharp corners are still smoothed in all cases.

We remark that the standard Zalesak's sphere problem is simulated using a circular rotation orthogonal to $(0, 0, 1)$ [18, 42]. However, the proposed vector field in this paper includes a transverse movement which makes it a more severe test. Although the results are not shown here, similar results are obtained using the standard rotation field.

Finally, we present the numerical simulations incorporating the reinitialization algorithm in the Zalesak's sphere test for $N = 64$. Figure 26 shows the results applying both the Heaviside and the regularized characteristic level-set functions. The numerical solution of H is significantly improved using the reinitialization, as expected. Moreover, the level set $H = 0.5$ recovers more of the initial Zalesak's sphere shape.

Vortex Deformation of a Sphere

In the final example, we consider the vortex deformation of a sphere under a velocity field which imposes large deformations to the original shape. It is considered one of

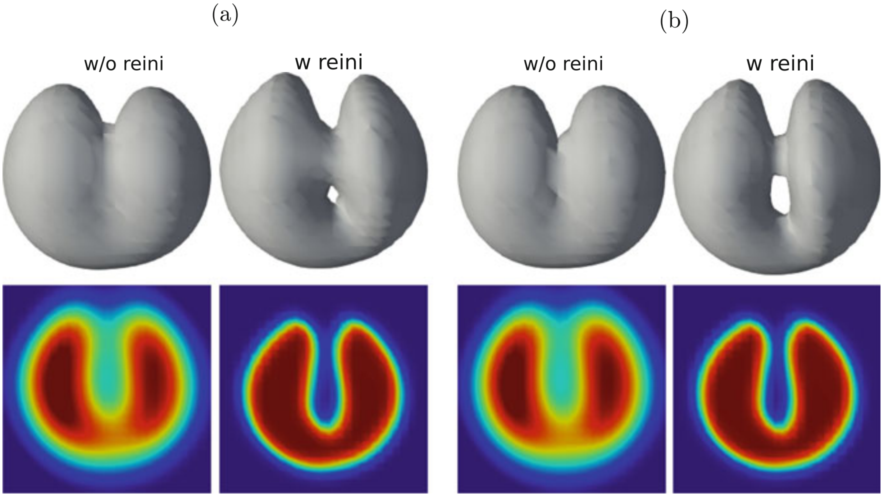

Fig. 26 Zalesak's sphere final solution with and without reinitialization using a $N = 64$ structured grid resolution. The two-dimensional solution corresponds to the xy plane at $z = 0.5$. (**a**) $\mathcal{H}$. (**b**) $\mathcal{H}_\epsilon$

the most challenging tests because it superposes simultaneously similar deformation fields in the xy and xz planes [43].

A sphere of radius $r_0 = 0.15$ and centered at $\boldsymbol{x}_0 = (0.35, 0.35, 0.35)$ is moved and deformed through Ω using the incompressible flow field proposed by LeVeque [42]:

$$\begin{aligned} u &= 2\sin^2(\pi x)\sin(2\pi y)\sin(2\pi z)\cos(\pi t/T), \\ v &= -\sin(2\pi x)\sin^2(\pi y)\sin(2\pi z)\cos(\pi t/T), \\ z &= -\sin(2\pi x)\sin(2\pi y)\sin^2(\pi z)\cos(\pi t/T), \end{aligned} \tag{36}$$

where T is the period.

The temporal evolution of the interface shape ($H = 0.5$) is shown in Fig. 27 using $\mathcal{H}_\epsilon$ as the characteristic level-set function and a structured grid resolution of $N = 256$. The velocity field forms two rotating vortices, which initially scoop out opposite sides of the sphere and then squeeze it. Then, the top and bottom of this shape are caught up again in their appropriate vortices, causing a very slim and stretched surface. At $t = T/2$, the flow field is reverted to recover the original shape. These deformations cause the collapse of some regions of the interface and mass loss consequently.

Figure 28 compares the initial and final shapes using structured grid resolutions of $N = 64$, 128, and 256. As expected, the interface shape strongly depend on the grid resolution and it is recovered increasing the number of elements. Note that a well-defined interface shape is reconstructed for the finest mesh at $t = T/2$.

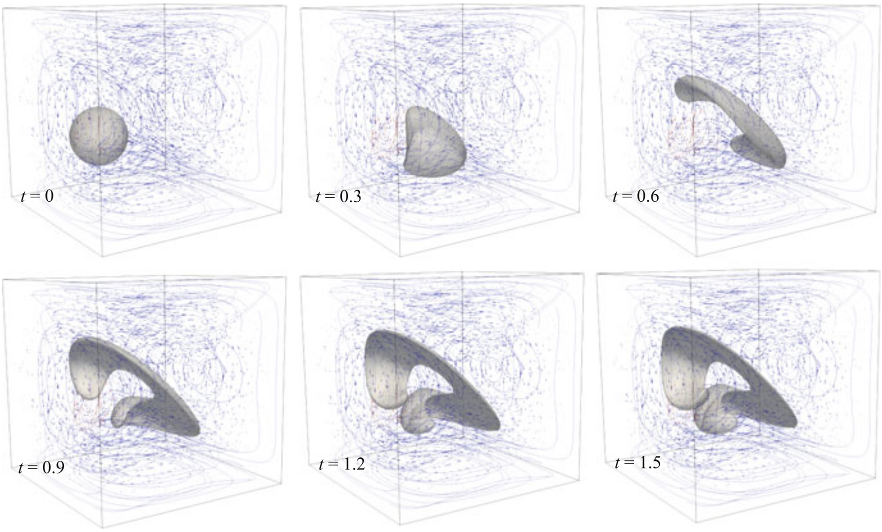

Fig. 27 Evolution of vortex deformation of a sphere calculated using $T = 3$ and $N = 256$

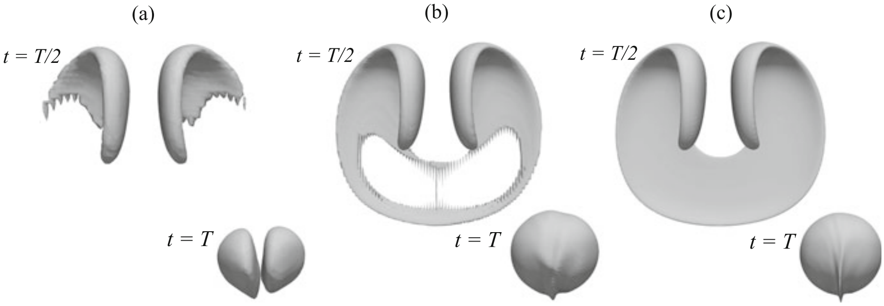

Fig. 28 Sphere deformation at the middle and final stage using different structured grid resolutions. (**a**) $N = 64$. (**b**) $N = 128$. (**c**) $N = 256$

Finally, we present the numerical simulations incorporating the reinitialization algorithm in the sphere deformation test for $N = 64$ and period $T = 1$. Figure 29 shows the final profile ($H = 0.5$) with and without the reinitialization step. As in previous examples, the numerical solution of H is closer to the initial Heaviside profile using the reinitialization. Similar to the 2D cases, the number of pseudo-time steps, $\Delta\tau$ and the application frequency plays an essential role in the final solution.

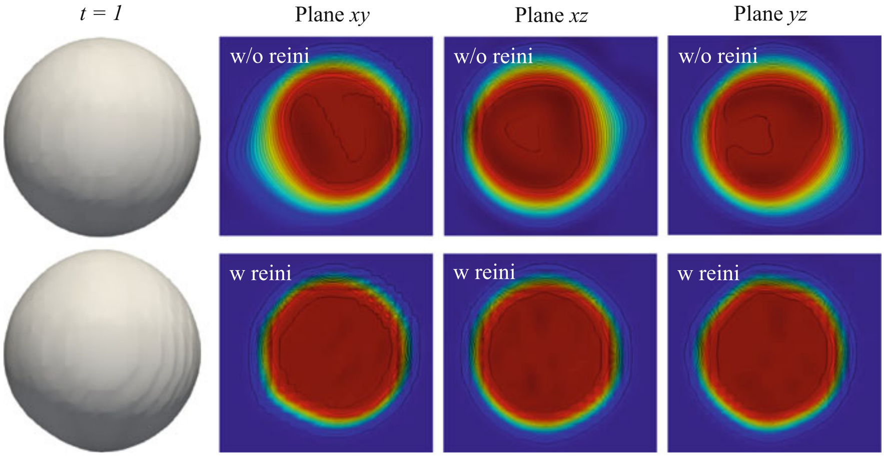

Fig. 29 Sphere deformation final solution with and without reinitialization using a $N = 64$ structured grid resolution

9 Performance

In this section, the performance of the code is reported to show the effectiveness of the proposed parallel technique. Computational performance is evaluated in terms of speedup and efficiency. The speedup S_p is defined as $S_p = t_1/t_p$ and the efficiency E is defined as $E_p = t_1/(n_p t_p)$ where t_p are the execution time of the algorithm with n_p processors. We report the results of this section on a standard twenty-core 3.0 GHz Intel Xeon. All of our codes are implemented in FORTRAN language.

We analyze the parallelization to the 3D solid-body rotation problem described in Sect. 6.2. In this example, a structured grid is applied to control the size and distribution of the sub-domains. To test the performance, we consider a grid resolution of $N = 128$ and 256 corresponding to about 4 and 33 million prisms elements, respectively. The sub-domains are taken by dividing n_p times the 3D domain in the x-direction.

The CPU time, speedup, and efficiency for one step starting from 2 up to 20 processors are shown in Fig. 30. In general, seven and nine iterations are taken to the solver to converge. As expected, the total CPU time decreases as the number of processors increases. Each time step using $N = 256$ and the maximum number of processors is simulated in approximately 1.7 s. However, the speedup deviates from the ideal speedup line as the number of processors increases because of the communication time between blocks.

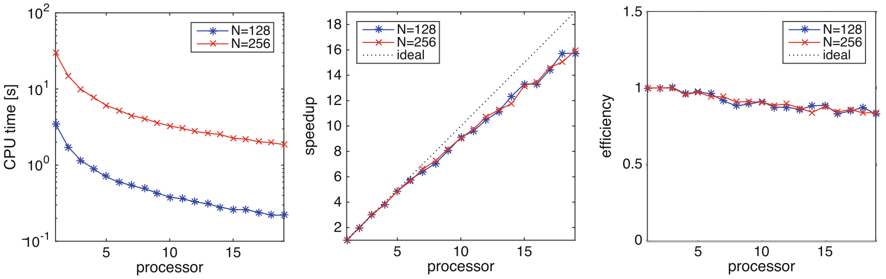

Fig. 30 3D solid-body rotation performance using different number of processors and resolutions

10 Conclusions

This work presents a second-order conservative level-set method based on an unstructured finite-volume technique. The numerical results verify the second-order accuracy in time and space. Zalesak problem has demonstrated the ability to capture the interface and maintain the sharpness of corners. The single vortex problem shows the capacity to recover the interface under large deformations. The proposed approach demonstrates a mass conservation property; however, the unstructured grid has an important influence on the method's precision. As expected, the proposed method performs well for smooth characteristic functions. Furthermore, functions with discontinuities or sharp gradient regions such as the Heaviside and regularized hyperbolic tangent function still perform well by only applying a flux-limiter technique. Simulations on multiple CPUs are essential to provide the required computational power needed to obtain fast and detailed 3D simulations. The code parallelization is straightforward due to the simplicity of both the block domain decomposition and the MSOR method. The number of communications is minimum that explains the overall efficiency in the parallel computation. Future work involves more analysis in implementing the reinitialization technique to improve the interface recovery. We will also develop a complete code to obtain 3D two-phase flow simulations on irregular domains using the proposed conservative level-set technique.

Acknowledgments The authors gratefully acknowledge the Mexican Council of Science and Technology projects Investigadoras e Investigadores por Mexico and postdoctoral for their financial supports.

References

1. T. Hoïnk, J. Schmalzl, U. Hansen, Dynamics of metal-silicate separation in a terrestrial magma ocean. Geochem. Geophys. Geosyst. **7**(9) (2006)
2. J. Monteux, Y. Ricard, N. Coltice, F. Dubuffet, M. Ulvrova, A model of metal-silicate separation on growing planets. Earth Planet. Sci. Lett. **287**, 353–362 (2009)
3. H. Schmeling et al., A benchmark comparison of spontaneous subduction models-Towards a free surface. Phys. Earth. Planet. Inter. **171**, 198–223 (2008)
4. J. van Hunen, A.P. van den Berg, N.J. Vlaar, Various mechanisms to induce present day shallow flat subduction and implications for the younger Earth: a numerical parameter study. Phys. Earth. Planet. Inter. **146**, 179–174 (2004)
5. L. Bourgouin, H.B. MÃijhlhaus, A. Jane Hale, A. Arsac, Studying the influence of a solid shell on lava dome growth and evolution using the level set method. Geophys. J. Int. **170**(3), 1431–1438 (2007)
6. A.J. Hale, L. Bourgouin, H.B. Mühlhaus, Using the level set method to model endogenous lava dome growth. J. Geophys. Res. Solid Earth **112**(B3) (2007)
7. L. Bourgouin, H.B. Mühlhaus, A.J. Hale, A. Arsac, Towards realistic simulations of lava dome growth using the level set method. Acta Geotech. **1**(4), 225–236 (2006)
8. H. Samuel, M. Evonuk, Modeling advection in geophysical flows with particle level sets. Geochem. Geophys. Geosyst. **11**(8) (2010)
9. J. Suckale, J.C. Nave, B.H. Hager, It takes three to tango: 1. Simulating buoyancy-driven flow in the presence of large viscosity contrasts. J. Geophys. Res. Solid Earth **115**(B7) (2010)
10. R. Scardovelli, S. Zaleski, Direct numerical simulation of free-surface and interfacial flow. Ann. Rev. Fluid Mech. **31**, 567–603 (1999)
11. J.M. Floryan, H. Rasmussen, Numerical methods for viscous flows with moving boundaries. Appl. Mech. Rev. **42**(12), 323–341 (1989)
12. T. Okamoto, M. Kawahara, Two-dimensional sloshing analysis by Lagrangian finite element method. Int. J. Num. Meth. Fluids **11**, 453–477 (1990)
13. G. Tryggvason et al., A front-tracking method for computations of multiphase flows. J. Comput. Phys. **169**, 708–759 (2001)
14. M. Uh, S. Xu, The immersed interface method for simulating two-fluid flows. Numer. Math. Theory Methods Appl. **7**(4), 447–472 (2014)
15. M. Kang, R.P. Fedkiw, X.D. Liu, A boundary condition capturing method for multiphase incompressible flow. J. Scient. Comput. **15**, 323–360 (2000)
16. C. Farhat, A. Rallu, S. Shankaran, A higher-order generalized ghost fluid method for the poor for the three-dimensional two-phase flow computation of underwater implosions. J. Comput. Phys. **227**, 7674–7700 (2008)
17. C.W. Hirt, B.D. Nichols, Volume of Fluid (VOF) method for the dynamics of free boundaries. J. Comput. Phys. **39**, 201–225 (1981)
18. A. Kawano, A simple volume-of-fluid reconstruction method for three-dimensional two-phase flows. Comput. Fluids **134**, 130–145 (2016)
19. S. Osher, R.P. Fedkiw, Level set method: an overview and some recent results. J. Comput. Phys. **169**, 463–502 (2001)
20. J.A. Sethian, P. Smereka, Level set methods for fluids interfaces. Ann. Rev. Fluid Mech. **35**, 341–372 (2003)
21. T. Chen, P. Minev, K. Nandakumar, A projection scheme for incompressible multiphase flow using adaptive Eulerian grid. Int. J. Numer. Meth. Fluids **45**, 1–19 (2004)
22. E. Marchandise, P. Geuzaine, N. Chevaugeon, A Quadrature free discontinuous Galerkin method for the level set equation. J. Comput. Phys. **212**, 338–357 (2006)
23. P. Frolkovic, D. Logashenko, G. Wittum, Flux-based level set method for two phase flows, in *Finite Volumes for Complex Applications*, ed. by R. Eymard, J.M. Herard (Wiley, 2008), pp. 415–422

24. X. Lv, Q. Zou, Y. Zhao, D. Reeve, A novel coupled level set and volume of fluid method for sharp interface capturing on 3D tetrahedral grids. J. Comput. Phys. **229**, 2573–2604 (2010)
25. C.E. Kees, I. Akkerman, M.W. Farthing, Y. Bazilevs, A conservative level set method suitable for variable-order approximations and unstructured meshes. J. Comput. Phys. **230**, 4536–4558 (2011)
26. K. Ito, T. Kunugi, H. Ohshima, T. Kawamura, A volume-conservative PLIC algorithm on three-dimensional fully unstructured meshes. Comput. Fluids **88**, 250–261 (2013)
27. N. Balcázar, L. Jofre, O. Lehmkuhl, J. Castro, J. Rigola, A finite-volume/level-set method for simulating two-phase flows on unstructured grids. Int. J. Multiph. Flow **64**, 55–72 (2014)
28. B. Xie, J. Peng, X. Feng, An unstructured-grid numerical model for interfacial multiphase fluids based on multi-moment finite volume formulation and THINC method. Int. J. Multiph. Flow **89**, 375–398 (2017)
29. E. Olsson, G. Kreiss, A conservative level set method for two phase flow. J. Comput. Phys. **210**, 225–246 (2005)
30. L.X. Li, H.S. Liao, L.J. Qi, An improved r-factor algorithm for TVD schemes. Int. J. Heat Mass Transf. **51**(3–4), 610–617 (2008)
31. M. Uh Zapata, R. Itzá Balam, A conservative level-set/finite-volume method on unstructured grids based on a central interpolation scheme. J. Comput. Phys. **444**, 110576 (2021)
32. F.S. Lien, A pressure-based unstructured grid method for all-speed flows. Int. J. Numer. Meth. Fluids **33**, 355–374 (2000)
33. D. Vidović, A. Segal, P. Wesseling, A superlinearly convergent Mach-uniform finite volume method for the Euler equations on staggered unstructured grids. J. Comput. Phys. **217**(2), 277–294 (2006)
34. Y. Sato, T. Hino, K. Ohashi, Parallelization of an unstructured Navier-Stokes solver using a multi-color ordering method for OpenMP. Comput. Fluids **88**, 496–509 (2013)
35. M. Uh Zapata, D. Pham Van Bang, K.D. Nguyen, Parallel SOR methods with a parabolic-diffusion acceleration technique for solving an unstructured-grid Poisson equation on 3D arbitrary geometries. Int. J. Comp. Fluid Dyn. **30**(5), 370–385 (2016)
36. L. Zhao, X. Bai, T. Li, J.J.R. Williams, Improved conservative level set method. Int. J. Numer. Meth. Fluids **75**(8), 575–590 (2014)
37. R. Eymard, T. Gallouet, R. Herbin, Finite volume methods, in *Handbook of Numerical Analysis*, vol. VII (Elsevier, North-Holland, 2000)
38. M. Uh Zapata, D. Pham Van Bang, K.D. Nguyen, An unstructured finite volume technique for the 3D Poisson equation on arbitrary geometry using a σ-coordinate system. Int. J. Numer. Meth. Fluids **76**(10), 611–631 (2014)
39. D. Kim, H. Choi, A second-order time-accurate finite volume method for unsteady incompressible flow on hybrid unstructured grids. J. Comput. Phys. **162**, 411–428 (2000)
40. S.T. Zalesak, Fully multidimensional flux-corrected transport algorithms for fluids. J. Comput. Phys. **31**(3), 335–62 (1979)
41. D. Enright, R. Fedkiw, J. Ferziger, I. Mitchell, A hybrid particle level set method for improved interface capturing. J. Comput. Phys. **183**(1), 83–116 (2002)
42. R.J. LeVeque, High-resolution conservative algorithms for advection in incompressible flow. SIAM J. Numer. Anal. **33**(2), 627–65 (1996)
43. R.N. Elias, A.L.G.A. Coutinho, Stabilized edge-based finite element simulation of free-surface flows. Int. J. Numer. Methods Fluids **54**, 965–993 (2007)

The Physics of Granular Natural Flows in Volcanic Environments

G. M. Rodríguez-Liñán, R. Torres-Orozco, V. H. Márquez, L. Capra, and V. Coviello

Abstract Active volcanoes are an incredible source of loose material, pyroclastic fragments that emplace as rain or flow on their slopes, forming m-thick deposits during explosive eruption. In particular, eruptive columns can elevate through the atmosphere for several kilometers, from which ash and pyroclastic fragments can fall, mantling the surrounding area, or can flow as turbulent, hot, pyroclastic flows. A pyroclastic flow mainly consists of a dry, basal, granular avalanche that moves along the volcanic slope, overrunned by a dilute, turbulent mixture of hot gas and fine ash. During heavy rains or abrupt release of water (such a dam failure or glacier outburst), these unconsolidated deposits can be easily eroded and remobilized as lahars, a two-phase mixture of water and granular material. These gravity-driven volcaniclastic flows are usually studied based on their deposits, where gas or water are no longer present, limiting our understanding of particle-particle or fluid-particle interaction. Numerical and analog modeling have been used to study their behavior, as well as the laws governing energy transfer between particles, and between the flow and the substratum. The mobility of a pyroclastic flow is greatly controlled by the current's mass and height of generation (potential energy), the efficiency of conversion from potential to kinetic energy within the current (i.e. loss of momentum due to frictional processes both within the current and at its edges), and the rate of atmospheric air entrainment. Lahars, in addition to the above-mentioned factors, are still more intricate since the rheology of the fluid phase (water plus fines) can modify the particle interactions, preventing energy dissipation and improving their mobility. In contrast to lahars, where real-time data is frequently collected, pyroclastic flows are rarely studied syn-eruptive due to their high velocities (35 m/s

---

G. M. Rodríguez-Liñán
Cátedras Conacyt – CGEO UNAM, Juriquilla, Querétaro, Mexico

R. Torres-Orozco · V. H. Márquez · L. Capra (✉)
Centro de Geociencias, Campus UNAM-Juriquilla, Juriquilla, Querétaro, Mexico
e-mail: lcapra@geociencias.unam.mx

V. Coviello
CNR, IRPI, Padova, Italy

G. Hernández-Dueñas, M. A. Moreles (eds.), *Mathematical and Computational Models of Flows and Waves in Geophysics*, CIMAT Lectures in Mathematical Sciences, https://doi.org/10.1007/978-3-031-12007-7_4

in average) and high temperatures (400 °C on average) making direct data collection extremely challenging, for which only few examples are available in the literature, Real-time data, however, are of paramount importance since they can provide a radiography of the flow behavior and of the mechanisms of emplacement, having crucial implications on hazard assessment. Volcán de Colima is a natural laboratory for studying volcaniclastic gravity flows. Most recent 2004–2005, 2013, and 2015 pyroclastic flows were produced by summit dome collapses; the latest of which represented the last 100 years' largest eruption. In contrast, lahars develop every year during the rainy season at a minimum 20 event/year rate inside the main ravines draining the volcano's southern sector. Since 2011, a monitoring network has been installed to get visual and seismic data from lahars, aiming at understanding their behavior and the mechanisms of transport, which depend on sediment content and on the interaction between flow, substratum and channel walls morphology. In 2015, the transit of a pyroclastic flow, never before recorded at an active volcano, was registered by one monitoring station. From these data, it was possible to better describe energy transfer between particles, and between particle and substratum, and to demonstrate that at least 1/3 of the total flow energy dissipates at channel walls. The latest conclusion was revealing since most numerical models used at reproducing gravity flow for hazard assessment, only considered energy dissipation at the substratum, overestimating flow maximum runout. More in detail, the seismic data, coupled with images of the event and field data, enabled discriminating flow sediment content, and implementing a real-time warning system to alert villages settled around main ravines. Our data demonstrate that more work is needed, and that only a multidisciplinary approach can solve yet undiscovered volcaniclastic flow internal behaviors.

1 Introduction

Volcanoes are one of the main natural threats responsible for several human tragedies. Volcanic eruptions are spectacular natural events that can destroy in a few minutes area in a radius of tens of kilometers from the volcano. Eruptive columns can elevate through the atmosphere for several kilometers, from which ash and pyroclastic fragments can fall, mantling the surrounding area, or can flow as turbulent, hot, pyroclastic flows. A worldwide analysis showed that pyroclastic density currents (PDC) and lahars represent the dominant fatal causes for incidents and fatalities [1]. Several historic eruptions such as the 79 AD Vesuvius, 1902 Mount Pelée, 1985 Nevado del Ruiz (Colombia) and the recent 2019 Volcán de Fuego (Guatemala) are examples of it. One of the main efforts in the volcanology community is to understand the nature of volcaniclastic flows and their behavior, to finally assess their hazards. PDC and lahars are among the most dangerous volcanic granular flows that, because of their characteristic and behavior (density, viscosity, temperature and velocity), represent one of the major threats during (PDC) or after (lahar) an eruption. Predicting the propagation of these flows has been one of the biggest challenges in geosciences because we lack a fundamental understanding of how complex granular media flow behaves, i.e. our understanding of their rheology is very incomplete. This gap in our knowledge makes the impacts from PDC and lahars very difficult to predict. The ability to forecast velocity and inundation areas would help to limit the loss of human life and reduce economic impacts by informing mitigation strategies such as evacuations. In the present paper we present an overview of the state of the art about PDC and lahars knowledge, with focus on experiments, numerical models and real-time monitoring, which represent the main tools used so far to better constrain volcanic granular flow behavior and define their impact. Application to active Mexican volcanoes will be here used to illustrate their application.

2 Pyroclastic Density Currents

Pyroclastic density currents (PDCs) are gravity currents consisting of mixtures of volcanic gas and particles of volcanic rocks (i.e. pyroclasts) that can range, in variable proportions, from pulverized <2 mm-diameter ash to larger and different-size particles of up to meters of diameter. These mixtures move away from their volcanic source region mainly due to gravity acting on the highest density of the current relative to the surrounding environment. The density differences result from the PDC's high temperatures (400 °C on average) and diverse concentrations of the suspended particles that prevent efficient entrainment of atmospheric gas.

PDCs can range in between two end-members based on the concentration of their particles and on the sedimentation of their deposits [2, 3]: (1) highly concentrated currents are granular flows (i.e. pyroclastic flows) that are distinguished by flowing mostly confined inside topographic channels, reaching relatively short run-out distances from source, and being dominated by grain-to-grain collisions and interstitial pore fluid pressure; and (2) low concentrated or dilute currents (i.e. pyroclastic surges) are characterized by flowing mostly unconfined, being capable of overcoming high topographic barriers and reaching the largest run-out distances during high flow dynamic pressures, transporting particles in a turbulent suspension, and being dominated by particle-gas drag forces. From the geological investigation of PDC deposits and their distribution, along with experimental and numerical modelling, a single PDC of any type can comprise the complete range of particle concentrations in space and time, i.e., transforming from flow to surge and vice-versa, depending on the PDC eruptive mechanism.

A generalized PDC consists of a dense underflow overlied by a buoyant phoenix plume, less dense than the atmosphere (Fig. 1a). The underflow consists of a basal granular flow dominated by particle–particle interactions overlied by a dilute part dominated by traction processes driven by fluid turbulence (Fig. 1a). The non-turbulent/turbulent boundary between the basal granular–fluid and upper dilute part of the PDC is characterised by a strong reduction in particle concentration by 2–3

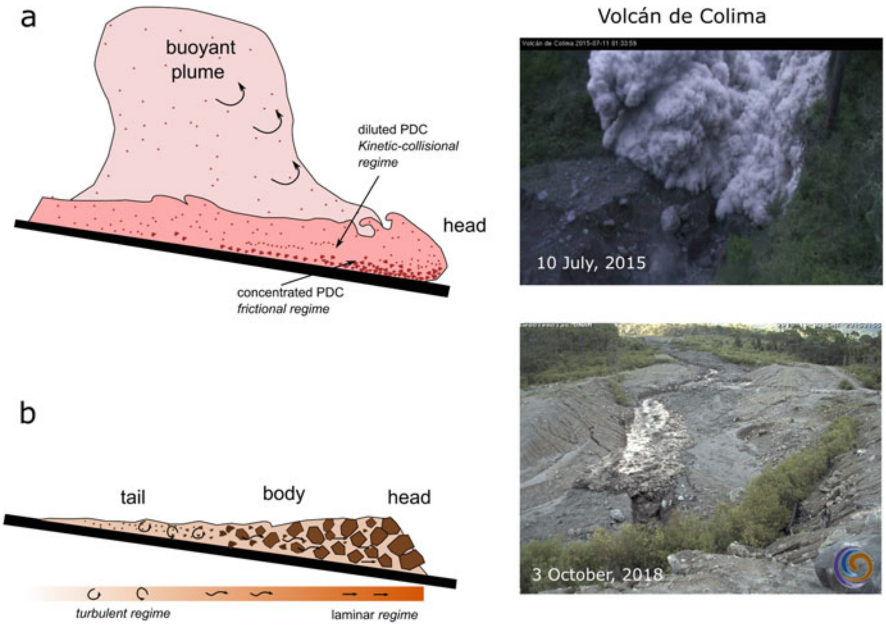

Fig. 1 Schematic profile of (**a**) pyroclastic density current and (**b**) lahar with images showing examples of flow fronts captured at Volcan de Colima monitoring site

orders of magnitude, produced by the interaction of gravity and the different sizes of particles in suspension.

All types of highly concentrated and low concentrated currents produce pyroclastic deposits once sedimentation undergoes via two different processes [4]: (1) en mass deposition, where the complete current stops flowing and forms deposits, and (2) progressive aggradation, in which particles progressively sediment from base to top parts of the current, so that vertical sections of deposits reflect only temporal variations at the base of the PDC while passing over a particular location.

Most mechanisms of PDC generation are associated with magma of different chemical composition and gas content ascending to the Earth's surface, and later on erupting from volcanoes at different intensity, in which case, the PDC mechanisms can be referred to as "hot" or eruptive.

The most widely accepted PDC eruptive mechanisms and corresponding PDC styles are (Fig. 2): (1) dome collapse block-and-ash flows, (2) laterally directed blasts, (3) column collapse PDCs, and (4) fountaining and boiling-over PDCs [4]. In particular, block-and-ash flow (BAF) PDCs, one of the most common event observed at Volcán de Colima during the last century (e.g. [5]), are produced from gravitational collapse of lava domes following dome growth to a critical size, which is attained in long periods of highly viscous lava effusion and accumulation on top of a volcano's either summit crater or peripheral secondary vents. Consequently, BAFs can occur in relatively "cold" non-eruptive conditions due to slope instability alone;

yet, most commonly, gravitational dome collapses are aided by dome fracturing and overpressurization owing to one or all of the following: volatile-rich magma remaining hot inside the least permeable interior of lava domes, persistent magma flux in volcanic conduit walls, or gas exsolution from fresh magma ascending towards the surface. In the latter cases, dome collapses and BAF generation commonly either trigger or preclude decompression of magma from different levels of the conduit, leading into explosive volcanism of varying duration and intensity, from short-lived Vulcanian burts to sustained larger events. Examples of the range of dome collapse BAF processes and ensuing different explosions were produced in the eruptions of 1902 Mount Pelée, Martinique; 1995–1999 Soufriere Hills, Montserrat; 2010 Merapi, Indonesia; 2012 Santiaguito, Guatemala; and 2015 Volcán de Colima, Mexico.

Laterally directed blast PDCs are generated from the abrupt, violent decompression and burst of magma close to the surface, followed by the rapid lateral expansion of the resulting eruptive mixture of pyroclasts. During the initial explosive phase, the pyroclastic mixture is driven by magma's internal pressure but cannot rise vertically due to limitations, mainly failed entrainment of atmospheric gas, flank oriented edifice collapse, and horizontally inclined pre- and syn-eruptive conduit and vent exit morphology ([3]). Instead, the mixture expands laterally, and most subsequent PDC transport occurs due to gravity (Fig. 2). A notorious evidence of the high dynamic pressure of blast PDCs, as recorded during historical eruptions, were volcanoes' ringplain landscapes being fully or partially damaged, and trees being knocked to the ground, parallel to the current's flow direction. Few examples of laterally directed blasts have been witnessed in recent history, where two main mechanisms for blast PDC generation were recognised. First, the eruption of May 1980 of Mount Saint Helens, USA, initiated with flank collapse of the volcanic edifice, which formed a giant landslide and decompressed magma that fed a laterally expanding blast PDC. In this case, edifice collapse instantly exposed to the surface a body of magma (i.e., a cryptodome) that had been residing for several weeks in Mount Saint Helens' uppermost conduit, early detected during this eruptive episode from edifice ground deformation. Similarly, a second blast PDC generation mechanism was exemplified by the explosive phase of 1997 of Soufriere Hills, Montserrat, and more recently during the eruption of 2014 of Kelud, Indonesia (e.g. [6, 7]). In these two explosive events, the hot interiors of large lava domes sitting over the central vents were decompressed violently, driving rapid expansion of laterally directed blasts. Magma decompression in the latter two cases was thus triggered by the fast removal of summit lava domes, producing initial BAFs, which is the mechanism for blast PDC generation more frequently identified in geological and historical records.

Collapse of eruption columns emitted vertically towards the atmosphere from a volcanic vent occurs when the mixture of pyroclasts fails to entrain enough atmospheric gas to become buoyant (Fig. 2). This can happen due to several potential and mutually related factors, including rapid loss of gas or gas exhaustion from the erupting magma, increased eruptive flux, conduit and vent widening, and mixture's entrainment of dense conduit walls [3, 4]. Whereas complete collapse

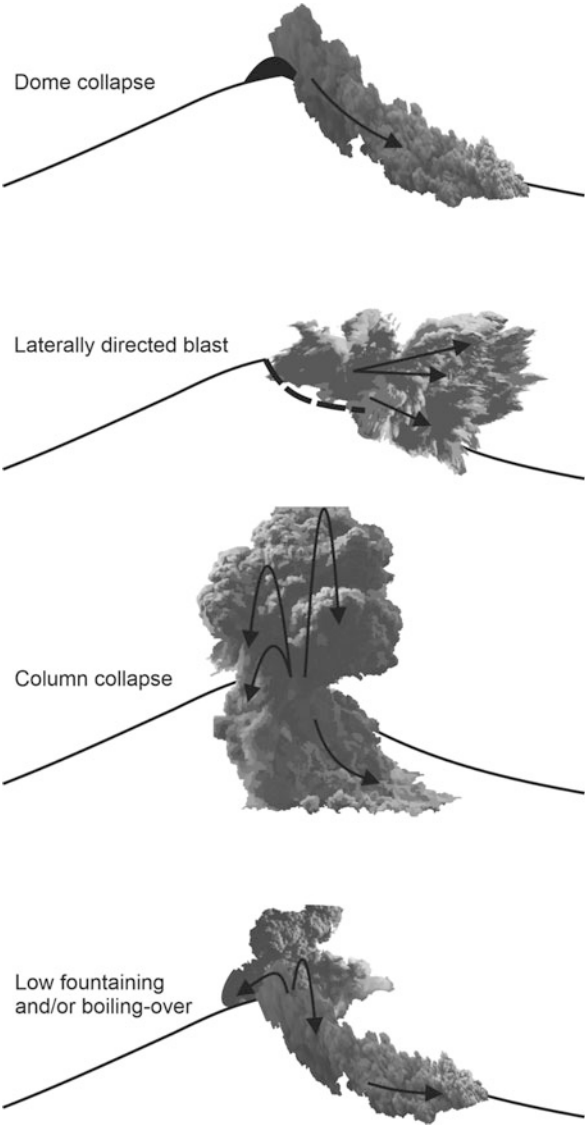

Fig. 2 Sketch of generalized main eruptive mechanisms and styles of pyroclastic density currents

comprises the entire mixture of pyroclasts collapsing and flowing over the ground by gravity, partial collapse only affects margins or small portions of the entire column, in which case both eruption columns and PDCs form together. Ultimately, the number (i.e., pulses) of column collapse PDCs that can be generated during a single eruption, and their individual starting volumes, depend on magma flux rates and eruption intensity; i.e., the larger the eruption intensity, the potentially larger the eruption column, and the more voluminous and/or numerous column collapse PDCs might form [4]. Examples of partial column collapse PDCs generated from the margins of large Plinian-type eruption columns (>20–30 km-high) were registered during the eruptions of 1980 of Mount Saint Helens, USA, and of 1991 of Mount Pinatubo, Philippines. On the other hand, deadly, and totally devastating complete column collapse PDCs were produced in the final explosive phases of the eruptions of A.D. 79 of Mount Vesuvius, Italy, and of 1883 of Krakatoa volcano, Indonesia.

Fountaining PDCs, likewise column collapse, form due to gravitational collapse of mixtures of pyroclasts, but from transient and low (meters-high) Strombolian or Vulcanian-type eruption columns [8]. In this case, intermittent magma flux inside the conduit driven by magma's highly heterogeneous gas-foam rheology produces unsteady eruption columns that rapidly lose buoyancy and collapse, forming a fountain of pyroclasts that feeds PDCs moving by gravity over the volcano flanks (Fig. 2). In these conditions, the fountain might remain relatively constant in an eruption until either the magma supply rate or the gas content decrease. Boiling-over PDCs obey similar mechanisms of PDC generation than fountaining but at lower energy, insufficient for developing any type of eruption column. Instead, the vesiculated magma directly sprouts over the crater rim, and PDCs are generated once the crater becomes inundated, so that the mixture of pyroclasts can flow out of the rim over the volcano flanks by gravity [8]. Examples covering the range from high to low energetic fountaining and the less energetic boiling-over PDCs were produced during the eruptions of 1995–1999 Soufriere Hills, Montserrat; 2000 Etna, Italy; 2006 Tungurahua, Ecuador; and 2015 Volcán de Colima, Mexico.

3 Lahar

Lahar is an Indonesian term used for describing a water-sediment mixture that flows down the slopes of a volcano. Lahars may occur during an eruption (syn-eruptive), few days or months after (post-eruptive) or during a period of eruptive quiescence (intra-eruptive) [9]. They usually form through rapid water release, from glacier melting, lake break-out or more commonly during heavy rains. At Volcan de Colima, one of the most active volcanoes in Mexico, up to 40 lahars are detected each year during the rainy season (from June to October). As water flows along the flank of a volcano on an erodible surface, sediments are progressively entrained (i.e. bulking process), forming sediment-laden flows. Depending on sediment concentration, the latter flows can be classified in debris flows and hyperconcentrated flows. In debris flows, sediment concentration is higher than ~60 vol% or more generally, with solid and liquid fractions approximately equal volumetrically [10–12]. They are laminar flows where solid and water fractions move downstream in unison, with the capacity for transporting large boulders over long distances, making them very destructive [13, 14]. Hyperconcentrated flows have sediment concentrations between 20 and 60 vol% [15]. They are turbulent, two-phase flows, and are considered to be the transition from stream flows to debris flows [10]. Such transitions are gradual and dependent on other factors such as sediment-size distribution, clay mineralogy, particle agitation, and flow energy [14].

In particular, changes in channel morphology (such as channel width, shape and slope), intersection with secondary river tributaries, bulking or debulking processes can modify the lahar behavior causing unsteady pulsating flows. This unsteadiness produces horizontal and vertical gradients in flow characteristics. A longitudinal profile of a lahar is characterized by three different sections [16] (Fig. 1b). The head consists of a dilated, high-friction, coarse-grained flow front, reaching the highest flow height and peak velocity pushed from behind by a nearly liquid, finer-grained debris body, followed by the recessional tail with the lowest sediment concentration. The vertical profile is produced due to the increment in sediment concentration towards the base of the flow. Depending on the hydraulic properties of clasts, the largest or densest particles go to the bottom of the flow because of the sedimentation processes. However, sedimentation is counteracted by the density of the interstitial fluid and clasts' dispersive pressure, which inhibits sedimentation, especially in turbulent flows.

Once fully developed, lahars flow under the influence of the following stresses: cohesive yield strength, the Mohr-Coulomb shear stress, ($\tau = \rho gHtan\delta$ where τ is the frictional shear stress, ρ is the flow density, g is the gravity, δ is the friction angle of the material, H is the flow depth), the dispersive stress, the viscous stress, and the turbulent shear stress [17]. Different models have been used to describe the stress-deformation relationship in debris flow behaviors [18]. Simple rheological models describe the bulk behavior of sediment-water flows as viscoplastic, either as Bingham plastic or Herschel-Bulkeley fluids [19, 20]. Bingham model is the simplest non-newtonian rheological model, where viscosity is independent of shear rate, in contrast to the Herschell-Bulkley model where viscosity depends to the shear strain rate. Both models fail to account particle-particle interaction. Other models, more commonly used for describing lahars with low fine sediment content, are mostly focused on dispersive stresses as the dominant mechanism of particle support and momentum transfer (i.e. inertial granular models, [21, 22]). Takahashi [22] model considers a dispersive shear stress due to collisions and momentum exchanges between adjacent particles. On the basis of the ratio of inertial to viscous shear stress, two regimens were identified: macroviscous (dominates at low shear rates) and grain-inertia (dominated by grain collision). Another approach consists of the employment of hydraulic models that solve Saint-Venant equations and incorporate Manning or Chezy coefficients, both related to the channel slope and geometry, to account for turbulence, viscosity, and friction as energy loss mechanisms [18]. Some hydraulic, depth-averaged models incorporate viscoplastic and grain inertial resistance in their constitutive equations, allowing them to calculate flow depth and velocity during transport [23, 24]. More complex multiphase models use Coulomb-Mixture theory (CMT), a depth-averaged, three dimensional mathematical model that accounts explicitly for solid- and fluid-phase forces and interactions [25]. The CMT main assumptions are that the solids behave as a Coulomb frictional material, the intergranular fluid behaves as a Newtonian viscous fluid, Terzaghi principle of effective stress and Darcy's Law (fluid drag) govern the coupling between solid and fluid components, pore fluid pressure reduces intergranular effective stresses and can evolve during flow. This model best describes the initial motion of a mass of granular material (i.e. landslide) from a static state to a debris flow, which is not always the most usual initiation process for syn- and post-eruptive lahars.

Physical and rheological characteristics of lahars are of paramount importance in hazard assessment. They were derived from empirical relationships, field measurements, and large-scale flume experiments [26]. Finally, despite the wide variety and complexity of mathematical and physical relations for describing lahar behavior, there is not a single model that represents lahar phenomena due to the complexity of triggering mechanisms, transitions between different types of lahar, and emplacement processes.

4 Numerical Simulations and Experiments

4.1 Numerical Simulations

The behavior of granular flows moving down a slope depends on a large number of parameters [27], such as grain size, polydispersity, water content, packing fraction, terrain and particle irregularities, friction coefficients, etc. This complexity leads to non-intuitive, difficult-to-predict phenomena appearing in granular flows, among which particle-size segregation is one of the most important and has great consequences when dealing with these materials [28, 29]. However, theoretical models have been developed in order to understand the underlying physical mechanisms of granular flows. Even though these models need to take into account all that large number of variables, the constitutive equations in these models can be solved numerically. Two main approaches exist to best accurately describe such flows, namely continuum models and discrete models.

Continuum models use the assumption that the granular flow can be regarded as a continuum medium, similar to a fluid [30]. These models are based on the basic principles of mass and momentum conservation to set up the needed differential equations [31–33]. However, unlike the equations governing Newtonian fluids, like the Navier-Stokes equations, granular models may require additional terms that take into account frictional and collisional loss of energy both between particles and between the medium and its substrate. In many circumstances, continuum models are accurate enough to describe all the observed phenomena. Nevertheless, they fail to describe phenomena inherent to the granularity of the medium, such as particle-size segregation [34] and high-speed ejection of individual particles [35]. This failure can be of crucial importance when assessing hazard maps for locations prone to rock avalanches and pyroclastic density currents.

Because of the lack of success at completely describing granularity-related phenomena, instead of continuum models, discrete models, which take into account the mechanics of individual particles, are also commonly used to explain the behavior of granular flows. A very common approach is the utilization of Molecular Dynamics (MD) algorithms [36], which first calculate the sum of forces experienced by each of the individual grains, and afterwards solve the equations of motion with an appropriate integrator. In this section we will only focus on the description of discrete models.

MD simulations require an initial set of positions and velocities for the i-th particle, $\{\mathbf{r}_i(t), \mathbf{v}_i(t)\}$. From this set and the calculation of the total force on the particle, the equations of motion are numerically solved and a new set of positions and velocities, $\{\mathbf{r}_i(t + \Delta t), \mathbf{v}_i(t + \Delta t)\}$, is obtained. However, the calculation of dissipative forces is usually expensive in terms of computational resources and, for this reason, most MD algorithms aimed to simulate granular flows tend to leave out popular integrators, like high-order Runge-Kutta methods [37], which require the calculation of forces several times. Even in the case of Runge-Kutta methods, such as Strong Stability-Preserving Runge-Kutta methods, that can be decomposed as a convex combination of forward Euler methods, an intermediate calculation for the forces is required between t and $t + \Delta t$, again increasing the computation time [38]. Instead, one must rely on simpler, one-time-step integrators, among which the velocity-Verlet method is quite popularly used. Nonetheless, the velocity-Verlet method has the disadvantage that it works with accelerations that do not depend on the particles' velocity, whereas most forces in granular matter, such as friction and inelastic collisions, require the knowledge of a relative velocity between particles to be computed. This inconvenience is circumvented by adding an intermediate step for a prediction of velocity before the acceleration is computed. The resulting set of equations for this velocity-Verlet corrected method is [37]

$$\boldsymbol{r_i}\,(t+\Delta t) = r_i(t) + \boldsymbol{v_i}(t)\Delta t + \frac{1}{2}a_i(t)\Delta t2 \tag{1}$$

$$v_{p,i}\,(t+\Delta t) = v_i(t) + a_i(t)\Delta t$$

$$a_i\,(t+\Delta t) = \frac{1}{m_i}f_i\left(r_i\,(t+\Delta t)\,,\, v_{p,i}\,(t+\Delta t)\right)$$

$$v_i\,(t+\Delta t) = v_{p,i}(t) + \frac{1}{2}\left[a_i\,(t+\Delta t) - a_i(t)\right]\Delta t$$

Here, $\mathbf{v}_{p,i}$ is the predicted intermediate velocity, $\mathbf{a}_i$ is the acceleration of the particle, $\mathbf{f}_i$ is the total force experienced by the particle and m_i is the particle's mass.

The previous method yields an $O(\Delta t^3)$ truncation error. More sophisticated algorithms with higher accuracy exist, for example, the sixth-order adaptation of the Adams-Bashforth-Moulton methods described by Pöschel and Schwager [39], which gives a local truncation error of $O(\Delta t^6)$. However, the computation of high-order derivatives, required by this adaptation, introduces a new source of error, since dissipative forces usually have discontinuities in their derivatives at some point, for instance, when a particle-particle contact is broken. For this reason, most numerical algorithms stick to the simpler velocity-Verlet corrected method.

As mentioned before, the calculation for the t + Δt step requires the previous computation of the total force exerted on each individual particle. In the case of dry granular matter, the only interparticle forces are non-elastic collisions and static and dynamic friction forces. Also, additional non-elastic collisions and friction forces have to be calculated for those particles interacting with the boundaries of the system—being, in the case of dry granular avalanches, the slope and the walls of the containing channel. In addition to these forces, one needs to include any force arising from external potentials. For rock avalanches and similar granular flows, the only relevant external potential is gravity.

In order for interparticle collisions to be modeled, one must first require that two conditions be fulfilled: the force between particles must be zero when they are not in contact and particle interpenetration must be avoided as much as possible. For the second condition to hold entirely, one would need something like a hard-sphere potential. However, the differential equations for such potential could not be solved with a MD method, given its divergence at zero relative particle-particle distance. Moreover, in a real physical case, even the hardest particles do interpenetrate a tiny amount when they collide, since their elasticity makes them deform a very small fraction of their size. Therefore, a commonly used model for the collisional force is the so-called spring-dashpot model [40]. This model considers the particle as a body that suffers a very small compression, whose magnitude is a tiny fraction of its diameter, and that the particle responds to this deformation with an opposing force linearly proportional to the compression. Additionally, a viscous force proportional to the rate of compression is included to account for the loss of energy of the non-elastic collision. Let the compression be denoted by ξ and the respective radii of the colliding particles be R_i and R_j. The compression is then defined as

$$\xi = \max\left(0, R_i + R_j - \left|r_i - r_j\right|\right). \tag{2}$$

The interacting force must also be always repulsive so, when the particles are moving apart from each other, they do not experience a restitution force that brings them back together. Considering this, the collisional force is

$$f_c = \min\left(0, -\kappa\xi - \gamma\frac{d\xi}{dt}\right). \tag{3}$$

The spring constant κ and the viscous constant γ can be expressed in terms of more physically relevant parameters: the coefficient of restitution ϵ and the collision time t_{coll}, which in turn is related to the particle stiffness. This yields [41]

$$\kappa = \left(\frac{\pi}{t_{coll}}\right)^2 + \left(\ln\frac{\epsilon}{t_{coll}}\right)^2; \tag{4}$$

$$\gamma = 2\ln\frac{\epsilon}{t_{coll}}. \tag{5}$$

Frictional forces, on the other hand, require a more elaborated description, since a large number of interactions occurring at the same time usually leads the particle behavior to go from the static to the dynamic regime and back. The canonical prescription for the friction forces is the Coulomb model:

$$f_{static} < \mu_s f_n; \tag{6}$$

$$f_{dynamic} = \mu_d f_n;$$

where μ_s and μ_d are the static and dynamic friction coefficients respectively, with $\mu_s > \mu_d$, and f_n is the normal component of the total force exerted on the particle. The simplest approach is to consider only the dynamic friction. This choice usually suffices when we deal with diluted rapidly moving granular flows, where we have briefly lasting interparticle contacts. However, this approach drastically fails in situations where the flowing material comes to a halt (for instance, when an avalanching material ends up in a deposition zone). In these cases, since most relative particle-particle velocities become zero, most interactions simultaneously enter the static regime. The implementation of static friction is rather complicated, since this force is, by definition, the needed force that cancels out the contribution of all other forces in order for the system to be in mechanical equilibrium and provided this needed force does not exceed the value of $\mu_s f_n$. This requires a force that is not single-valued and whose exact value depends on several parameters at once. A simple, elegant solution to this conundrum is to consider a virtual spring fixed at the contact point between particles whose elongation is the response of the other forces acting on the particles [42]. The elongation at a certain time t should be given by

$$\chi(t) = \int_{t_0}^{t} v_t(\tau)\, d\tau, \tag{7}$$

where $\mathbf{v}_t$ is the relative tangential velocity between the particles' surfaces of contact and t_0 is the time at which the contact forms. The virtual spring, thus, generates a force given by

$$f_s = -\kappa_s \chi - \gamma_s \frac{d\chi}{dt}, \tag{8}$$

where κ_s and γ_s are the spring constant and a viscous constant. The viscous term is needed in order to avoid unwanted persistent oscillations. The elongation cannot be allowed to grow indefinitely, so the force is set to be zero if $\mu_s |f_n| / \kappa_s < |\chi|$ [43]. With all these ingredients we can finally define the friction force as

$$\mathbf{f}_f = \begin{pmatrix} |\mathbf{f}_s| \quad \boldsymbol{\chi}/|\boldsymbol{\chi}| & |\mathbf{f}_s| < \mu_s f_n \\ |\mu_d f_n| \quad \boldsymbol{\chi}/|\boldsymbol{\chi}| & |\mathbf{f}_s| \geq \mu_s f_n \end{pmatrix} \tag{9}$$

Note that in the previous equation $|\mathbf{f}_s|$ is modeling the static friction force, f_{static}, when $|\mathbf{f}_s| < \mu_s f_n$. In the opposite case, when $|\mathbf{f}_s|$ overcomes $\mu_s f_n$, the force $|\mu_d f_n| \cdot \chi / |\chi|$ is now used, and this represents the change to a dynamic regime. The previous prescription for the friction force is known as the modified Cundall-Strack model and gives very good agreements when it is compared with experiments. The choice for the values of κ_s and γ_s depends on the type of particles being modeled. The interested reader may refer to Shäfer et al. [40] and Pérez [37] for reasonable values of these constants.

If we wish to accurately describe the behavior of granular particles, we have to consider that they might not necessarily be spherical, ideal objects. Therefore, we need to take into account all six degrees of freedom: three translational ones and three rotational ones. The rotational degrees of freedom are extremely important when we calculate the tangential forces between particles (i.e., friction forces), since this calculation depends upon the relative velocity of the surface of the particles at the contact point. This, in turn, depends on the angular velocity of the particles and on how far is the surface contact point from the rotation axis.

While the translational part of the calculations is simply performed by applying Eq. (1), the rotational part requires a more careful description, since we need a set of three parameters to get the orientation of the particle in space. Nevertheless, Eq. (1) can be adapted for rotational configurations by exchanging the original translational variables by their rotational counterpart (velocity and angular velocity, force and torque, etc.). By doing that, one can use the three-dimensional rotation formalism of one's fancy (rotation matrices, the quaternion rotation formalism, etc.) in order to calculate the new orientational configuration.

As previously mentioned, Eq. (1) and their rotational counterparts need the knowledge of the total forces and torques exerted on each particle. These forces need to be calculated as though they are applied on the particle-particle contact point. The easiest way to do so is to split the force into a normal component and two tangential components with respect to the surface of the particle at the contact point. The normal force, f_n, is simply the collisional force, f_c, calculated in Eq. (3). However, this force requires that we already know the relative velocities of the contact surface. The velocity of the contact point on particle i and particle j is given respectively by

$$v_c^{(i)} = v_i + \omega_i \times (r_c - r_i)\,; \tag{10}$$

$$v_c^{(j)} = v_j + \omega_j \times \left(r_c - r_j\right);$$

where $\mathbf{v}_i$ and $\mathbf{v}_j$ are the translational velocities of particles i and j, respectively, ω_i and ω_j are the corresponding angular velocities, $\mathbf{r}_c$ is the vector position of the contact point and $\mathbf{r}_i$ and $\mathbf{r}_j$ are the center of mass positions of the particles. Note that $\mathbf{r}_c$ is the same on both i and j. Next, we compute the relative contact point velocity:

$$\Delta v_c = v_c^{(j)} - v_c^{(i)}. \tag{11}$$

For a given particle geometry, we can obtain the normal component of $\Delta \mathbf{v}_c$, and this component has to be equal to the negative of the derivative of ξ with respect to time. The compression, of course, is the maximum separation between both particles' center of mass when they are barely touching minus the difference of the particles' positions at the time of calculation. With ξ and dξ/dt, we can directly compute the normal force with Eq. (3).

The tangential part of the force is given by the frictional forces calculated in Eq. (9). A prerequisite to obtain these forces is that we know the tangential part of the relative contact point velocity. This is simply obtained by subtracting the normal component to the total vector $\Delta \mathbf{v}_c$. After getting this, we just equate the tangential force to the resulting friction force calculated by the modified Cundall-Strack model, Eq. (9).

Finally, the torque exerted on the particle is obtained by adding up all the forces which are being applied at each contact point and calculating the cross product

$$\tau_i = (r_c - r_i) \times f_i . \tag{12}$$

As an example of the method previously described, we can simulate a rock avalanche by considering non-spherical particles going down an inclined plane. Equation (2) requires spheres for the compression to be computed. However, the use of spherical particles would result in an unrealistic, naive model for rock avalanches. We solve this issue by creating particles consisting of four spheres placed on the vertices of a regular tetrahedron (see Fig. 3a). A tetrahedral geometry is a simple symmetric and more realistic model that represent non-spherical particles better resembling natural clasts and, at the same time, having an easy-to-calculate tensor of inertia required for the rotational part of the algorithm in Eq. (1).

For this example, we set the values for the coefficient of restitution, the collision time, the static coefficient of friction, and the dynamic coefficient of friction as

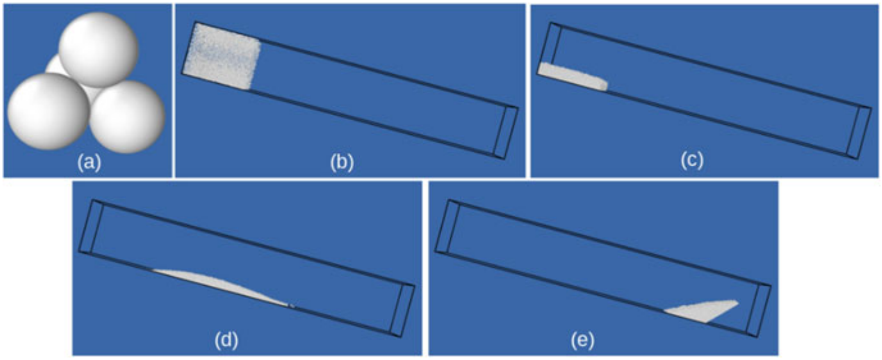

Fig. 3 (**a**) An example of the tetrahedral particles used in the simulations. (**b**) Initial cubic-lattice configuration of particles. (**c**) Particles contained in the initial hopper before the avalanche starts. (**d**) Material avalanching. (**e**) Particles reaching the final deposition zone

$\epsilon = 0.6$, $t_{coll} = 2.5\times10^{-4}$ s, $\mu_s = 0.4$, and $\mu_d = 0.32$. These values are the same for both particle-particle interactions and for particle-slope and wall interactions. Those values correspond to measured values for andesite rocks [44]. From those values we can apply Eqs. (2–6) to obtain the values of f_c, f_{static}, and $f_{dynamic}$. Additionally we set a particle density equal to the average density of andesite: 2600 kg/m^3, which is needed to obtain the mass required by the third equation in (1). The simulated material contains a total 10,000 particles whose gyration radii span from 0.5 to 2 cm, following a constant distribution for particle sizes.

The particles are first placed on a cubic lattice in a region of the simulation box that will represent a hopper initially containing the grains (Fig. 3b). The particles are given random initial velocities and angular velocities and are let to fall in order for them to fill the hopper and achieve a relaxed state (Fig. 3c). Afterwards, one of the hopper's walls is removed, and the particles begin to go down a slope (Fig. 3d), which has a preset inclination $\theta = 15°$ and a length L = 2 m. After the particles have run the entire length of the flume, they reach the horizontal zone where they are brought to stop by the basal friction; this horizontal zone represents a deposition zone (Fig. 3e).

Since Eq. (1) require the computation of the particles' positions, space orientations, translational and angular velocities, translational and angular accelerations, and forces and torques at each time t, we can obtain from the algorithm whatever set of kinematic and dynamic quantities, including, but not restricted to, linear and average angular momentum, rotational and translational kinetic energy, center-of-mass position, loss of energy by friction, and so on.

As a very simple demonstration, in Fig. 4, upper panel (red, solid line), we show the behavior of the center-of-mass velocity of the avalanche as a function of time. The behaviour of the center-of-mass velocity presents three main stages. It shows, in a first stage (0–0.5 s), a linear growing trend, during which the dominating forces are gravity and the basal friction, being both of them constant forces. The avalanching mass uniformly accelerates, thus yielding a linear growth for the velocity. In a second stage (1–4 s), the velocity acquires a constant value—a terminal velocity acquired when dissipative forces due to aerodynamic drag are balanced with gravity. In a final stage (5 s and afterwards), when the granular mass begins to enter the deposition zone, the velocity drops until the material stops. In this stage, gravity is overcome by basal friction and aerodynamic drag, and thus the material's velocity becomes zero.

The shape of the initial part of the plot in the upper panel of Fig. 4 can be easily explained if we analyze the forces exerted on the avalanching material. From this analysis, we can obtain the equation of motion. Thus, the differential equation for velocity when the granular material is going down the slope is

$$\frac{dv}{dt} = A\left(\theta, \mu_d\right) - Dv^2, \tag{13}$$

where $A(\theta,\mu_d) = g(\sin\theta - \mu_d \cos\theta)$ and D is a generalized drag coefficient, which depends on the material's mass, the shape and size of the particles and the density

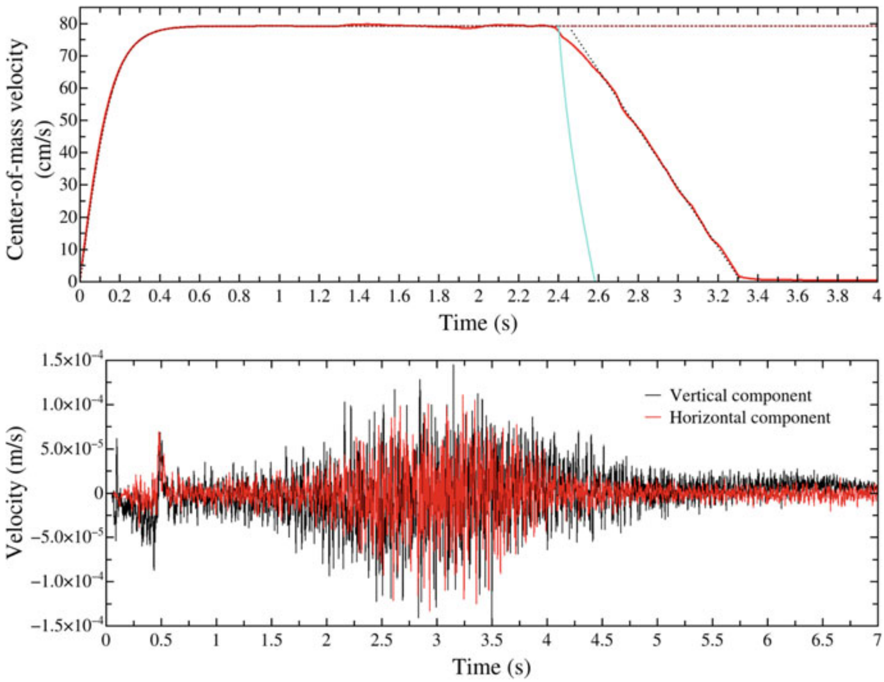

Fig. 4 (Upper panel) In solid red is shown the center-of-mass velocity for an avalanche of polydisperse particles shown in Fig. 3b, in dashed dark red is shown the function in Eq. (14) using the parameters mentioned in the body of the text, the black dashed line is a guide-to-eye straight line to show the constant deceleration rate, and the solid cyan curve corresponds to the function in Eq. (16). (Lower panel) Synthetic seismic signal obtained from the avalanche simulation

of the air. The solution for v(t) in Eq. (13) is

$$v(t) = v_T \tanh\left(\frac{A\left(\theta, \mu_d\right)}{v_T} t\right), \tag{14}$$

with $v_T = \sqrt{A/D}$ the terminal velocity. On the other hand, the differential equation for velocity when the granular material arrives in the deposition zone is

$$\frac{dv}{dt} = -\mu_d g - D v^2 \tag{15}$$

This equation has the solution

$$v(t) = v_* \tan\left[\phi - \frac{\mu_d g}{v_*}\left(t - t_{dep}\right)\right], \tag{16}$$

where $v_* = \sqrt{\mu_d g/D}$, $\phi = \tan^{-1}(v_{dep}/v_*)$, t_{dep} is the time at which the mass enters the deposition zone, and v_{dep} is the velocity the mass possesses at t_{dep}. However this is a naive approach, since the granular material does not enter the deposition zone all at once. Instead, when the front of the avalanche is reaching the deposition zone, the middle body and the tail are still sliding down, pushing the frontal grains and thus adding additional forces to the front. These forces will in turn depend on the fraction of mass of the material that remains on the slope, compared with the mass that is slowing down on the deposition zone. The analysis of such a complicated force scheme is beyond the scope of this work. All we can mention is that, from the upper panel of Fig. 4, it can be seen that the material decelerates at a constant rate. This indicates the existence of net constant force over the whole body of grains.

The dashed line in the upper panel of Fig. 4 is the plot of the function shown in Eq. (14) with the parameter values for θ and μ_d specified before. For v_T we use the saturation value observed in the plot: $v_T = 79.2$ cm/s.

From the computed data, one can also obtain information of geological interest. For instance, we can calculate the amount of momentum transferred to discrete elements of mass making up the base and walls of the flume. From that, considering the theoretical velocity of waves traveling in an andesite material, which is calculated based on the andesite Young's modulus [44], we can generate a synthetic seismic signal, which can be "detected" on an arbitrary point by adding up all the contributions of the oscillations from all the discrete mass elements. This synthetic signal is shown in Fig. 4, lower panel. This kind of signal could be, in principle, compared with real signal in rock-avalanche-prone sites to give insights of the physical mechanisms of these processes.

4.2 Experiments

Micro and meso-scale PDC flow and internal gas-particle regimes and structure in space and time have been interpreted from the pyroclastic deposits' sedimentation mechanisms and distribution, and benchtop numerically simulated using multiphase flows. In addition, large-scale, in-situ and real-time experiments of PDC flow, employing engineered channels, has allowed direct measurement of PDC's internal flow dynamics, most importantly on the evolution of particle concentration regimes and PDC's vertical stratification [32]. Large-scale experiments were also performed to simulate water-saturated mixture of mud, sand and gravel [45]; variation in basal normal stress and pore fluid pressure were estimated and correlated with flow behaviour.

5 Monitoring

Monitoring is widely employed on active volcanoes to estimate when they are likely to erupt or to detect PDC and lahar events during their propagation. The unpredictability of PDCs, their high velocity and temperature, make it difficult to set up a monitoring system, and the only few examples described in the literature represent fortuitous cases [5].

In contrast, instrumental monitoring is widely implemented on active volcanoes where lahars regularly occur during the rainy season, such as Volcán de Colima in Mexico. Collection of field measurements by in situ monitoring is a fundamental task as these data are necessary to (1) improve the knowledge of initiation mechanisms and flow dynamics, (2) develop, calibrate and validate numerical models and (3) design and implement warning or alarm systems ([46] and references therein). The best way to continue improving our knowledge on flow behaviour is combining results coming from the analysis of monitoring data with numerical and analogical modelling [47].

Since 2011, a monitoring station located at 2000 m a.s.l. along the Montegrande ravine, Volcán de Colima, collects video and seismic recording of lahars. Nowadays, the monitoring network consists of four stations equipped with seismic and infrasound instrumentation, cameras, and rain gauges. Data collected by the monitoring stations are sent in real time to the seismic observatory of the Universidad de Colima. The seismic data, coupled with images of the event and field data, allow discriminating the main characteristics of the flow (duration, magnitude, sediment content) and implementing a real-time warning system to alert villages settled along main ravines [48–50]. Also, geophysical observations of lahars can provide information on particle interaction mechanism and sediment concentration that can be used for model calibration. In the following, we present the monitoring data of a recent lahar that was recorded in the Montegrande ravine, Volcán de Colima.

Figure 5 shows the seismic signal of a lahar that occurred during the 2021 rainy season, recorded by a low cost short-period seismometer (RaspberryShake 3D). Figure 5 shows the seismogram of the vertical component (upper) and the power spectral density (PSD) (lower) of the front, of the body and of the tail of the flow, calculated by means of a Fast Fourier Transform. From the seismogram, we can infer the flow duration (about 1 h), its time of occurrence and the presence of secondary surges following the main front. The PSDs show how most energy release occurs during the passage of the front of the flow while during the body and the tail of the flow the energy radiation from the flow is 1 and 3 orders of magnitude lower, respectively. This is consistent with observations of debris flows made in alpine basins that show how the peak amplitudes are representative of the energy of each surge and most energy transfer occurs during the passage of the surge fronts [51].

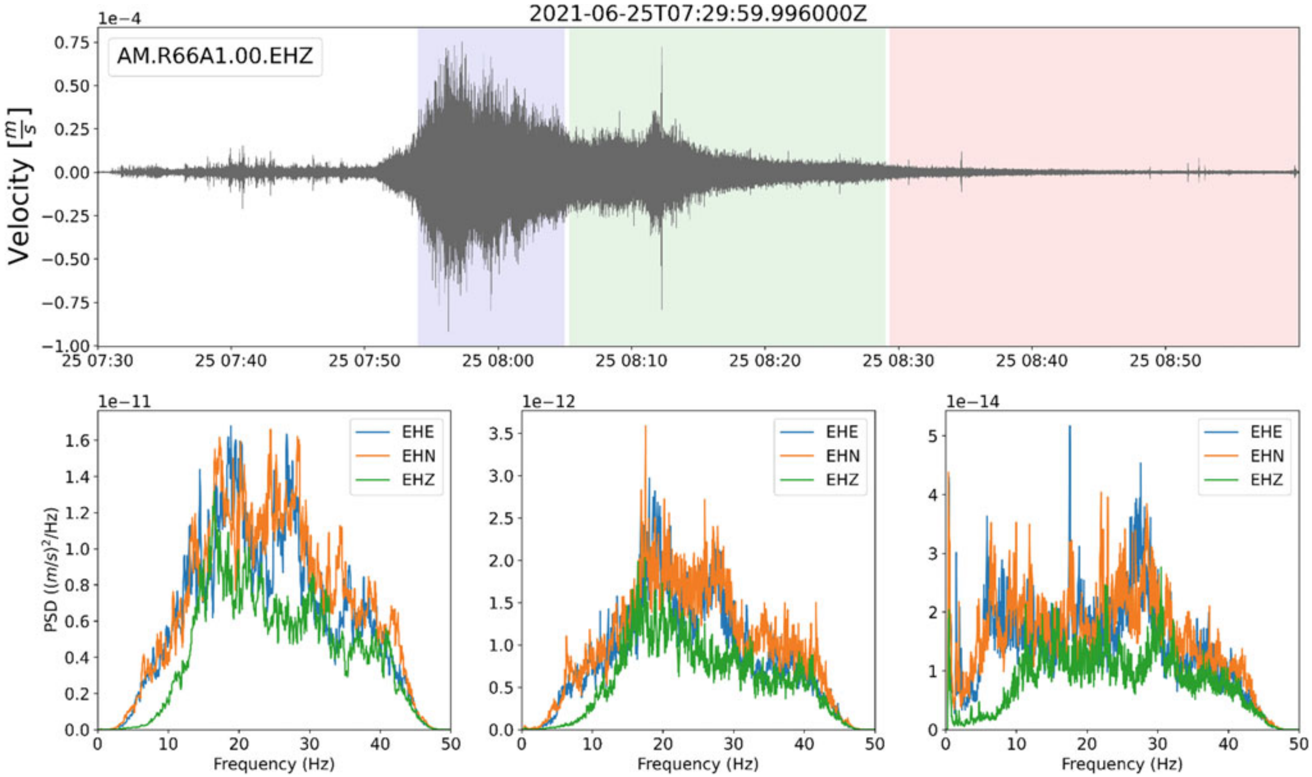

Fig. 5 Seismic signal of a lahar that occurred in the Montegrande Ravine, Volcán de Colima. Upper panel: seismogram of the vertical component; lower panels: PSD of ground velocity of the front (violet area in the seismogram), of the body (green area) and of the tail of the flow (pink area), respectively. Direction on the ground vibrations: East-west (EHE), vertical direction (EHZ) and north-south (EHN)

6 Numerical Model for Hazard Assessment

Numerical models have become one of the main instruments used to reproduce past events of volcanic granular flows or to predict their behaviour and potential hazard. Two main approaches have been used: (1) empirical models (e.g., LAHARZ, [52]; energy cone, [53]), but they fail in predicting crucial dynamic parameters as velocity and dynamic pressure; (2) geophysical mass-flow models using simplified rheological laws (e.g., TITAN2D, [54, 55]; FLO2D, [24]; VolcFlow, [56]). Beside the model approach, the resolution of Digital Elevation Model (DEM) reproducing the real topography, is of primary importance for reliable replications of simulated flow paths and inundated areas [57, 58].

The two most popular simulation tools for granular volcanic flows are FLO2D [24] for lahars and TITAN2D [54] for PDC. Both codes solve for the depth-averaged shallow-water conservation equations where the fluid is approximated as an incompressible continuum material of constant density ρ, moving across a complex topography. One of the main assumptions is that the horizontal length scales L are substantially larger than the vertical length scale H (shallow flows).

The FLO2D model [24] routes floods over natural channels solving the full dynamic wave equation. The total shear stress τ is the sum of the cohesive yield stress τc, the Mohr-Coulomb shear τmc, the viscous shear stress τv (ηdv/dy), the turbulent shear stress τt, and the dispersive shear stress τd.

$$\tau = \tau_c \quad + \tau_{mc} + \tau_v + \tau_t + \tau_d$$

The model neglects any frictional effect due to direct contacts among the coarse clasts.

The most important input parameters are an accurate DEM, an input hydrograph, the Manning coefficient (the channel's resistance to flow), and the rheological parameters for yield strength and viscosity. The viscosity and yield strength terms are scaled on user-defined empirical coefficients taking into account the exponential dependence of the rheological parameters on sediment concentration by volume [59]:

$$\tau_y = \alpha_2 e^{\beta_2 C_v}$$

$$\eta = \alpha_1 e^{\beta_1 C_v}$$

where αi and βi are rheological coefficients that depend on the fine content (silt and clay) of the flow, which can be obtained by laboratory experiments or empirical relationships [59]; Cv is the solid phase concentration.

The TITAN2D model [54] is designed to simulate dry granular flow, i.e. the basal, dense granular flow of a PDC. The conservation equations for mass and momentum are solved following the equations provided by Iverson and Denlinger [25] in the dry limit, and taking into account a Coulomb-type friction term for the

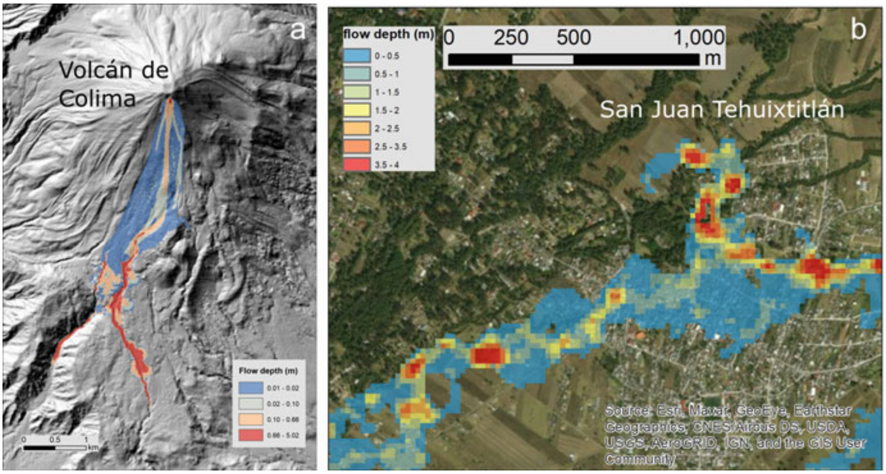

Fig. 6 Example of numerical simulations used to define inundation area for (**a**) PDC (TITAN2D) and (**b**) LAHARS (FLO-2D)

interactions between the granular medium and the basal surface [55]. In order to run a typical TITAN2D simulation, the main input parameters are: the DEM of the area of interest; the volume of the mobilized granular material, the initial grid size and the smallest computational cell allowed on the map during the course of the simulation; the internal friction angle φint and the basal friction angle φbed.

For both models, the first approach is to calibrate the input parameters by reproducing the extent of known events representing different scenarios. After calibration, simulations are run to all possible directions from the volcano summit, with a statistical distribution of all possible inputs to obtain a probabilistic map of inundated areas.

This approach has been used to elaborate recent hazards maps for Mexican active volcanoes, such as Popocatépetl [60], Ceboruco [61], Tacaná [62], Volcán de Colima [63] among others. The main output of a simulation is the flow-thickness of the total inundated area (Fig. 6); flow-velocity maps are also available, based on which impact force on infrastructures can be calculated for damage estimation.

7 Discussion and Conclusions

After more than two decades, the integration of field observation, numerical models and experiments have provided new insights into the internal structure of lahars and PDCs which are contributing to design more robust simulation codes for hazard assessment. But, as models improve our knowledge, more accuracy will be needed to estimate physical properties for natural flows, a difficult task considering the hazard that they pose during their formation and emplacement. Scaled experiments and geophysical measurements are still the best main tools to look “inside” volcanic granular flows and to quantify flow rheology. On the other hand, two-phase models able to reproduce stratified flows are still far away to be accessible for hazard assessment, and high computational cost and high simulation times will be required. Likewise, large-scale in-situ experiments using engineered channels, although being able to reproduce and record from concentrated to dilute currents in real-time and at different rates and internal flow dynamic conditions, therefore representing present’s state-of-the-art direct approaches for studying flow dynamics, are widely inaccessible due to the high costs of installation and maintenance, along with intricate experimental requirements. At present, depth-averaged models, which are computationally simple, are still widely used, even if they cannot provide a comprehensive view on all lahars and PDC regimes.

Because of the lack of detail in those simple models, there has been, in recent years, a growing trend of research aimed at looking at the grain-size-scale physics of granular flows. Although, as we just mentioned, an approach this detailed is quite time-consuming and computationally expensive, we can take the advantage of modern resources like supercomputing or graphic-process-unit parallel computing to accelerate this process. We have presented a detailed algorithm based on Molecular Dynamics simulations that can be easily applied to dry granular flows, but that can likewise be extended to water-saturated granular flows. As we have demonstrated, algorithms of this kind are able to yield insight of many dynamic and kinematic variables. This output can always be compared with real, in situ data from geological, hazard-prone locations, in order to visualize the inherent physical processes within geological flows. Of course, we just gave very simple examples, but the algorithms can be methodologically refined to better suit one’s research needs.

Acknowledgements We thank Luis Albeto Aguilar, Alejandro de León and Jair García of the Laboratorio Nacional de Visualización Científica Avanzada (UNAM) for their support during TITAN2D computer simulations. GMR would like to thank the Cátedras Conacyt fellowship program for supporting this research.

References

1. S.K. Brown, S.F. Jenkins, R.S.J. Sparks, H. Odbert, M.R. Auker, Volcanic fatalities database: analysis of volcanic threat with distance and victim classification. J Appl Volcanol **6**, 15 (2017)
2. G. Lube, E.C.P. Breard, T. Esposti-Ongaro, J. Dufek, B. Brand, Multiphase flow behaviour and hazard prediction of pyroclastic density currents. Nat. Rev. Earth Environ. **1**(7), 348–365 (2020)
3. R. Sulpizio, P. Dellino, D.M. Doronzo, D. Sarocchi, Pyroclastic density currents: state of the art and perspectives. J. Volcanol. Geotherm. Res. **283**, 36–65 (2014)
4. J. Dufek, T. Esposti-Ongaro, O. Roche, Pyroclastic density currents: processes and models, in *The Encyclopedia of Volcanoes*, (Academic Press, 2015), pp. 617–629

5. L. Capra, R. Sulpizio, V.H. Márquez-Ramirez, V. Coviello, R. Arambula-Mendoza, S. Cruz, The anatomy of a pyroclastic density current: the 10 July 2015 event at Volcán de Colima (Mexico). Bull. Volcanol. **80**(4), 34 (2018)
6. T. Esposti-Ongaro, A.B. Clarke, A. Neri, B. Voight, C. Widiwijayanti, Fluid dynamics of the 1997 Boxing Day volcanic blast on Montserrat, West Indies. J. Geophys. Res. **113**(B03211) (2008)
7. F. Maeno, S. Nakada, M. Yoshimoto, T. Shimano, N. Hokanishi, A. Zaennudin, M. Iguchi, A sequence of a plinian eruption preceded by dome destruction at Kelud volcano, Indonesia, on February 13, 2014, revealed from tephra fallout and pyroclastic density current deposits. J. Volcanol. Geotherm. Res. **382**, 24–41 (2019)
8. B. Behncke, Hazards from pyroclastic density currents at Mt. Etna (Italy). J. Volcanol. Geotherm. Res. **180**, 148–160 (2009)
9. V. Manville, K. Németh, K. Kano, Source to sink: a review of three decades of progress in the understanding of volcaniclastic processes, deposits, and hazards. Sediment. Geol. **220**(3–4), 136–161 (2009)
10. T.C. Pierson, Hyperconcentrated flow—Transitional process between water flow and debris flow, in *Debris-Flow Hazards and Related Phenomena*, (Springer, Berlin, 2005), pp. 159–202
11. T.C. Pierson, J.E. Costa, W. Vancouver, A rheologic classification of subaerial sediment-water flows. Debris flows/avalanches: process, recognition, and mitigation. reviews in engineering geology. Geol. Soc. Am. **7**, 1–12 (1987)
12. J.W. Vallance, K.M. Scott, The osceola mudflow from mount rainier: sedimentology and hazard implications of a huge clay-rich debris flow. Geol. Soc. Am. Bull. **109**, 143–163 (1997)
13. S.R. Mead, C. Magill, V. Lemiale, S.R. Mead, C. Magill, V. Lemiale, J.C. Thouret, M. Prakash, Examining the impact of lahars on buildings using numerical modelling. Nat. Hazards Earth Syst. Sci. **17**(5), 703–719 (2017)
14. J.W. Vallance, R.M. Iverson, Lahars and their deposits, in *The Encyclopedia of Volcanoes*, (Academic Press, 2015), pp. 649–664
15. J.P. Beverage, J.K. Culbertson, Hyperconcentrations of suspended sediment. J. Hydraul. Div. **90**(6), 117–128 (1964)
16. T.C. Pierson, Flow behavior of channelized debris flows. Mount St. Helens, Washington, in *Hillslope processes*, (Routledge, 1986), pp. 269–296
17. M.T. Pareschi, Physical modeling of eruptive phenomena: Lahars. Monitoring and Mitigation of Volcano Hazards, 463–489 (1996)
18. V. Manville, J.J. Major, S. Fagents, Modeling lahar behavior and hazards, in *Modeling Volcanic Processes: The Physics and Mathematics of Volcanism*, ed. by S. A. Fagents, T. K. P. Gregg, R. M. C. Lopes, (Cambridge University Press, 2013), pp. 300–330
19. P. Coussot, D. Laigle, M. Arattano, P. Coussot, D. Laigle, M. Arattano, A. Deganutti, L. Marchi, Direct determination of rheological characteristics of debris flow. J. Hydraul. Eng. **124**(8), 865–868 (1998)
20. J.J. Major, T.C. Pierson, Debris flow rheology: experimental analysis of fine-grained slurries. Water Resour. Res. **28**(3), 841–857 (1992)
21. R.A. Bagnold, Experiments on a gravity-free dispersion of large solid spheres in a Newtonian fluid under shear. Proc R Soc Lond Ser A Math Phys Sci **225**(1160), 49–63 (1954)
22. T. Takahashi, Debris flow on prismatic open channel. J. Hydraul. Div. **106**(3), 381–396 (1980)
23. P.Y. Julien, J.S. O'Brien, Selected notes on debris flow dynamics, in *Recent Developments on Debris Flows*, (Springer, Berlin, 2007), pp. 144–162
24. J.S. O'Brien, P.Y. Julien, W.T. Fullerton, Two-dimensional water flood and mudflow simulation. J. Hydraul. Eng. **119**(2), 244–261 (1993)
25. R.M. Iverson, R.P. Denlinger, Flow of variably fluidized granular masses across three-dimensional terrain: 1. Coulomb mixture theory. J. Geophys. Res. Solid Earth **106**, 537–552 (2001)
26. J.-C. Thouret, S. Antoine, C. Magill, C. Ollier, Lahars and debris flows: characteristics and impacts. Earth-Sci. Rev. **201**, 103003 (2019)

27. S.P. Pudasaini, K. Hutter, *Avalanche Dynamics: Dynamics of Rapid Flows of Dense Granular Avalanches* (Springer Science & Business Media, 2007)
28. J. Gray, Particle segregation in dense granular flows. Annu. Rev. Fluid Mech. **50**, 407–433 (2018)
29. Y.-J. Jiang, X.-Y. Fan, T.-H. Li, S.-Y. Xiao, Influence of particle-size segregation on the impact of dry granular flow. Powder Technol. **340**, 39–51 (2018)
30. S.B. Savage, K. Hutter, The dynamics of avalanches of granular materials from initiation to runout. Part I: Analysis. Acta Mechanica **86**(1), 201–223 (1991)
31. P. Bartelt, B. Salm, U. Gruber, Calculating dense-snow avalanche runout using a Voellmy-fluid model with active/passive longitudinal staining. J. Glaciol. **45**, 242–254 (1999)
32. E. Breard, J. Dufek, O. Roche, Continuum modeling of pressure-balanced and fluidized granular flows in 2-D: Comparison with glass bead experiments and implications for concentrated pyroclastic density currents. J. Geophys. Res. Solid Earth **124**(6), 5557–5583 (2019)
33. R.M. Iverson, The physics of debris flows. Rev. Geophys. **35**(3), 245 (1997)
34. R. Bartali, G.M. Rodríguez-Liñán, L. Torres-Cisneros, G. Pérez-Ángel, Y. Nahmad-Molinari, Runout transition and clustering instability in binary-mixture avalanche deposits. Granul. Matter **22**, 1–18 (2020)
35. R. Bartali, D. Sarocchi, Y. Nahmad-Molinari, Stick-slip motion and high-speed ejecta in granular avalanches detected through multi-sensors flume. Eng. Geol. **195**, 248–257 (2015)
36. H.J. Herrmann, Molecular dynamics simulations of granular materials. Int. J. Mod. Phys. C **4**(2), 309–316 (1993)
37. G. Pérez, Numerical simulations in granular matter: the discharge of a 2D silo. Pramana J. Phys. **70**(6), 989–1007 (2008)
38. S. Gottlieb, C.W. Shu, E. Tadmor, Strong stability-preserving high-order time discretization methods. SIAM Rev. **43**(1), 89–112 (2001)
39. T. Pöschel, T. Schwager, *Computational Granular Dynamics* (Springer Science & Business Media, 2005)
40. J. Shäfer, S. Dippel, D. Wolf, Force schemes in simulations of granular materials. J. Phys. **6**(1), 5–20 (1996)
41. T. Schwager, T. Pöschel, Coefficient of restitution and linear-dashpot model revisited. Granul. Matter **9**(6), 465–469 (2007)
42. P.A. Cundall, O.D.L. Strack, A discrete numerical model for granular assemblies. Geotechnique **29**(1), 47–65 (1979)
43. L. Brendel, S. Dippel, Lasting contacts in molecular dynamics simulations. Phys. Dry Granular Media NATO ASI Ser. E **350**, 313–318 (1998)
44. N. Naito, K. Maeda, H. Konno, Y. Ushiwatari, K. Suzuki, R. Kawase, Rockfall impacts on sand cushions with different soil mechanical characteristics using discrete element method. Soils Found. **60**(2), 384–397 (2020)
45. R.M. Iverson, Landslide disparities, flume discoveries, and oso despair. Perspect. Earth Space Sci. **1** (2020)
46. M. Hürlimann, V. Coviello, C. Bel, X. Guo, M. Berti, C. Graf, J. Hübl, S. Miyata, J.B. Smith, H.Y. Yin, Debris-flow monitoring and warning: review and examples. Earth Sci. Rev. **199**, 102981 (2019)
47. K.E. Allstadt, M. Farin, A.B. Lockhart, S.K. McBride, J.W. Kean, R.M. Iverson et al., Overcoming barriers to progress in seismic monitoring and characterization of debris flows and lahars, in *Proceedings of the Seventh International Conference on Debris-Flow Hazards Mitigation,* Golden, CO, 2019
48. V. Coviello, L. Capra, R. Vázquez, V.H. Márquez-Ramirez, Seismic characterization of hyperconcentrated flows in a volcanic environment. Earth Surf. Process. Landf. **43**(10), 2219–2231 (2018)
49. R. Vázquez, E. Surinach, L. Capra, R. Arambula, G. Reyes, Seismic characterisation of lahars at Volcán de Colima, Mexico. Bull. Volcanol. **78**(2), 1–14 (2016)

50. B. Walsh, V. Coviello, L. Capra, J. Procter, V. Márquez, Insights on the internal dynamics of natural lahars from the analysis of 3-component broadband seismic signals. Front. Earth Sci. **8**, 632 (2020)
51. V. Coviello, M. Arattano, F. Comiti, P. Macconi, L. Marchi, Seismic characterization of debris flows: insights into energy radiation and implications for warning. J. Geophys. Res. Earth Surf. **124**(6), 1440–1463 (2019)
52. R.M. Iverson, S.P. Schilling, J.W. Vallance, Objective delineation of lahar-inundation hazard zones. Geol. Soc. Am. Bull. **110**(8), 972–984 (1998)
53. M.C. Malin, M.F. Sheridan, Computer-assisted mapping of pyroclastic surges. Science **217**, 637–640 (1982). doi: 10.1126/science.217.4560.637
54. A.K. Patra, A.C. Bauer, C.C. Nichita, E.B. Pitman, M.F. Sheridan, M. Bursik, B. Rupp, A. Webber, A.J. Stinton, Namikawa, & L. M., Renschler, C. S., Parallel adaptive numerical simulation of dry avalanches over natural terrain. J. Volcanol. Geotherm. Res. **139**(1–2), 1–21 (2005)
55. E.B. Pitman, C. Nichita, A. Patra, Computing granular avalanches and landslides. Phys. Fluids **15**(12), 3638–3646 (2003)
56. K. Kelfoun, T.H. Druitt, Numerical modeling of the emplacement of Socompa Rock Avalanche, Chile. J. Geophys. Res. Solid Earth **110**(B12) (2005)
57. L. Capra, V.C. Manea, M. Manea, G. Norini, The importance of digital elevation model resolution on granular flow simulations: a test case for Colima Volcano usingTITAN2D computational routine. Nat. Hazards **59**(2), 665–680 (2011)
58. N.F. Stevens, V. Manville, D.W. Heron, The sensitivity of a volcanic flow model to digital elevation model accuracy: experiments with digitised map contours and interferometric SAR at Ruapehu and Taranaki volcanoes, New Zealand. J. Volcanol. Geotherm. Res. **119**(1–4), 89–105 (2003)
59. J.J. O'Brien, P.Y. Julien, Physical properties and mechanics of hyperconcentrated deiment flows. Proc. ASCE Speciality Conference on the Delineation of landslide, Flashflood and debrisl flow hazards, Utah Water Lad, Series UWRL/G-85/03, 260–279 (1985)
60. A.L. Martin del Pozzo, M. Alatorre, L. Arana, R. Bonasia, L. Capra, W. Cassata, et al., *Estudios geológicos y actualización del mapa de peligros del volcán Popocatépetl* (Memoria técnica del mapa de peligros del volcán Popocatépetl: Monografías del Instituto de Geofísica, 2017), p. 22
61. K. Sieron, D. Ferres, C. Siebe, R. Constantinescu, L. Capra, C. Connor, L. Connor, G. Groppelli, K. González Zuccolotto, Ceboruco hazard map: Part II—Modeling volcanic phenomena and construction of the general hazard map. Nat. Hazards **96**(2), 893–933 (2019)
62. R. Vázquez, J.L. Macías, J.L. Arce, Integrated hazards maps of the Tacaná Volcanic complex, Mexico-Guatemala: ashfall, block-and-ash flows, and lahars. J. S. Am. Earth Sci. **107**, 103146 (2021)
63. L. Capra, J.C. Gavilanes-Ruiz, R. Bonasia, R. Saucedo, R. Sulpizio, Re-assessing volcanic hazard zonation of Volcán de Colima, México. Nat. Hazards **76**(1), 41–61 (2015)

Cooperative Gravity and Full Waveform Inversion: Elastic Case

Raul U. Silva-Ávalos, Jonás D. De Basabe, and Mrinal K. Sen

Abstract A variety of geophysical methods can be used to acquire measurements to estimate a subsurface model. However, each method typically yields a different model and it can be challenging to merge with those obtained using other methods. We need to be able to combine the data from different geophysical methods to obtain a more detailed and consistent subsurface model. In this chapter, we present a scheme for cooperative inversion of seismic and gravity measurements. This scheme performs iteratively full-waveform inversion (FWI) and gravimetric inversion to minimize the misfit between the observed and synthetic data. We explain how to use the adjoint-state method to compute the gradient needed for FWI, the constrained conjugate gradient least-squares method to compute the gravimetric inversion, and how to incorporate petrophysical relationships to merge these methods in a cooperative scheme. The final system to be solved is large and sparse, hence the implementation relies on a large sparse matrix storage and high-performance computing. Finally, we show examples using the proposed inversion scheme and compare the results with those of FWI. The cooperative scheme yields more accurate models than those obtained from FWI with negligible additional computational cost.

R. U. Silva-Ávalos
Departamento de Geofísica Aplicada, División de Ciencias de la Tierra, CICESE, Ensenada, Mexico

J. D. De Basabe (✉)
Departamento de Sismología, División de Ciencias de la Tierra, CICESE, Ensenada, Mexico
e-mail: jonas@cicese.mx

M. K. Sen
Institute for Geophysics, John A. and Katherine G. Jackson School of Geosciences, The University of Texas at Austin, Austin, TX, USA
e-mail: mrinal@utexas.edu

G. Hernández-Dueñas, M. A. Moreles (eds.), *Mathematical and Computational Models of Flows and Waves in Geophysics*, CIMAT Lectures in Mathematical Sciences, https://doi.org/10.1007/978-3-031-12007-7_5

1 Introduction

Exploration geophysicists have developed a variety of methods to probe the subsurface using measurements that can be gathered on the ground. The interpretation of the data from these geophysical methods yields an assortment of subsurface models, and the conundrum is to merge these models into a unified model that better reflects the geometry and properties of the area of interest and fits all the available data.

Among the exploration-geophysics methods, the seismic method has been particularly successful. This method was at the heart of the energy transition that took place over one century ago [13] and continues to be widely used with an ever increasing number of applications [47]. Over its long history, this method has evolved together with the technology, becoming the basis for other state-of-the-art methods such as Full Waveform Inversion (FWI) [11].

FWI [38, 39] is a powerful seismic-imaging method used to estimate a seismic-velocity model such that the discrepancies between observed and synthetic seismograms are minimized. This method has become a popular [44] and in the recent years has improved, reducing the computational cost and enhancing the resolution of seismic images.

FWI consists of three main steps performed iteratively. The first step is to do the forward modeling starting from an initial model to compute the synthetic data, and obtain the residual by subtracting the observed data. Several authors have used the Finite Difference Method (FDM) [2, 43] for waveform modeling, however, the Finite Element Method [26], the Spectral Element Method (SEM) [22] or other methods can also be used. The second step is to back-propagate the residual wave field to obtain the adjoint field. This step includes computing a cross-correlation between the forward and the adjoint wavefield and adding over all the data points to obtain a velocity gradient. This is the well-known adjoint method [32], which reduces significantly the computational cost because only two forward modelings are required in each iteration of the inversion process. In the final step, the velocity model is updated by adding to the starting model the scaled velocity gradient using a line-search method to determine the increment. If the observed and synthetic data do not match, these steps are repeated until a stopping criterion is reached. This methodology has provided good results for stratigraphic and predominantly horizontal layered models. Despite the good results both in acoustic and elastic media, density variations have largely been ignored [44].

The gravimetric data is directly linked to the density variations in the subsoil. The observed data can be the gravity or the gravity gradient tensor on the surface [49]. As in FWI, the interpretation of this data relies on solving the forward problem. Several forward modeling methods exist to compute gravity anomalies by solving Poisson's equation for the gravitational potential. Among the best-known methods is the analytical solution for prismatic bodies [4, 29], however, solutions for other geometries are readily available [16, 20, 37, 46]. In this work, we will use the solution for uniform rectangular prisms to be congruent with the grid used in finite differences for waveform modeling.

Gravimetric inversion (GI) for density estimation is a linear problem. This method is well known for estimating structures with horizontal changes of mass distribution. The solution is straightforward using Gauss-Newton minimization [35] to obtain a density model inverting the square matrix on a single step. This method is widely used by geophysicists because of its fast convergence, however, it is computationally expensive and unfeasible for large-scale problems. One alternative to this problem is to use the Conjugate Gradient Least Squares (CGLS) method. This method solves the inverse problem without the need to form and store the square matrix [35].

Nowadays, the exploration of a region of interest for underground resources requires the measurements of several geophysical datasets which need to be interpreted for characterization. Joint inversion allows integrating these different datasets into a consistent Earth-property model. Usually the strategy consists in combining all the methods into one single inverse problem. Vozoff and Jupp [45] were the first to perform joint inversion for different geophysical data sets, namely resistivity and magnetotelluric data. Following this, numerous methodologies and different geophysical data-inversion schemes emerged for the reduction of non-uniqueness and ambiguity in the interpretation of the Earth model. Depending on the constraints in the optimization problem, the joint inversion schemes can be classified into petrophysical, structural, or statistical. Petrophysical joint inversion is based on empirical relationships of the model parameters [23, 27, 48], structural joint inversion seeks to minimize the cross product of the gradient of each model parameter [14, 15] and statistical joint inversion tries to solve the problem attaching to each grid cell of the model a mean point (fuzzy c-mean) depending on the number of c-means [31, 33].

The cooperative inversion of seismic and gravimetric data has attracted significant attention since these methods complement each other and both theories depend on the density. For example, Roy et al. [34] performed first-arrival travel time inversion jointly with gravity data using very-fast simulated annealing. Other groups have done further work using seismic and gravity data [9, 24, 25, 41]. In particular, Blom et al. [6] stressed the importance of density in geological processes and studied the role of density using seismic and gravimetric data, concluding that density estimation requires a strong a priori model to be able to determine it as an independent parameter.

In this work, we present a novel method to obtain a unified inverted model using FWI and GI in a sequential and cooperative scheme. This chapter is divided into five sections, Sect. 1 being the introduction. Section 2 presents the forward modeling on a geophysical framework and is divided in two parts for gravimetric and seismic data modeling. For gravity, we discuss Newton's law of universal gravitation and present the forward modeling based on the response of a rectangular body. For seismic modeling, we give a brief introduction to elastodynamic theory and the forward modeling for elastic and acoustic media. Section 3 discusses the inverse problem and follows the same organization as Chap. 2 for each geophysical method. We first present the general basis on inverse theory. Then we discuss the separate inversion for each method and present the the sequential inversion. The results are presented in

Sect. 4 for two synthetic models using using conventional and cooperative inversion. The conclusions are included in Sect. 5.

2 Forward Modeling of Geophysical Data

This section presents the theoretical framework for the gravimetric and seismic geophysical methods. For the gravity data, we present the solution of Newton's Law of gravitation for a parallelepiped of constant density. For seismic data, we discuss the wave equations for elastic and acoustic media and show how to solve them using finite-difference methods.

2.1 Gravimetric Forward Modeling

Newton's law of gravitation [5] provides the gravitational potential ϕ at an observation point $\mathbf{r}$ due to a body on Earth with density distribution ρ (Fig. 1) as

$$\phi(\mathbf{r}) = \int_{\Omega} \gamma \frac{\rho(\mathbf{r}')}{\|\mathbf{r} - \mathbf{r}'\|} \mathrm{d}V, \tag{1}$$

where $\gamma = 6.672 \times 10^{-11}\,\mathrm{m^3 kg^{-1} s^{-2}}$ is the universal gravitation constant, $\mathbf{r}'$ is the position for each differential element of density over the volume Ω and $\|.\|$ denotes the vector norm. The gravity acceleration field is given by the gradient of

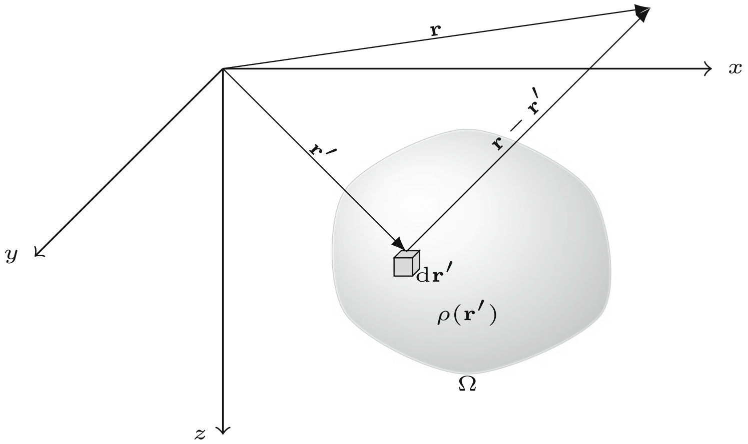

Fig. 1 Observation vector $\mathbf{r}$ and position vector $\mathbf{r}'$ for each differential volume element $\mathrm{d}\mathbf{r}'$ for a continuous of density ρ in Cartesian coordinates system

the potential,

$$\mathbf{g}(\mathbf{r}) = \nabla\phi(\mathbf{r}). \tag{2}$$

Consider an arbitrary continuous body of density ρ in Cartesian coordinates (Fig. 1), the components of the gravity acceleration are given by

$$g_x(x, y, z) = \frac{\partial\phi}{\partial x} = \gamma \int_\Omega \rho \frac{x - x'}{\left[(x - x')^2 + (y - y')^2 + (z - z')^2\right]^{3/2}} \mathrm{d}x'\mathrm{d}y'\mathrm{d}z', \tag{3}$$

$$g_y(x, y, z) = \frac{\partial\phi}{\partial y} = \gamma \int_\Omega \rho \frac{y - y'}{\left[(x - x')^2 + (y - y')^2 + (z - z')^2\right]^{3/2}} \mathrm{d}x'\mathrm{d}y'\mathrm{d}z', \tag{4}$$

$$g_z(x, y, z) = \frac{\partial\phi}{\partial z} = \gamma \int_\Omega \rho \frac{z - z'}{\left[(x - x')^2 + (y - y')^2 + (z - z')^2\right]^{3/2}} \mathrm{d}x'\mathrm{d}y'\mathrm{d}z'. \tag{5}$$

In this work, we consider only the vertical component of the gravity acceleration g_z, as usually done in geophysics.

2.2 Gravimetric Forward Modeling

In order to compute the gravimetric response at any observation point on the surface, we need a discretization of the Earth model. Given that Eq. 5 is valid for a continuous body of arbitrary shape and density distribution and taking advantage of the superposition theorem for Newton's law of gravitation, the Earth model can be discretized as a set of rectangular prism of constant density (Fig. 2). For each prism, the analytic solution of Eq. 5 is given by Banerjee and Das Gupta [3]

$$g_z = \left\{ \gamma \left[z \tan^{-1}\left(\frac{xy}{z|\Delta r|}\right) - x \ln\left(y + |\Delta r|\right) - y \ln\left(x + |\Delta r|\right) \right] \Bigg|_{\Delta x_1'}^{\Delta x_2'} \Bigg|_{\Delta y_1'}^{\Delta y_2'} \Bigg|_{\Delta z_1'}^{\Delta z_2'} \right\} \rho, \tag{6}$$

where the prime coordinates are the corners of the prism, $|\Delta r| = \sqrt{x^2 + y^2 + z^2}$, $\Delta x_k' = x - x_k'$, $\Delta y_k' = y - y_k'$ and $\Delta z' = z - z_k'$ $k = 1, 2$. This expression corresponds to the gravity measurement at the point (x, y, z) due to the prism and the part within the braces is the gravity kernel.

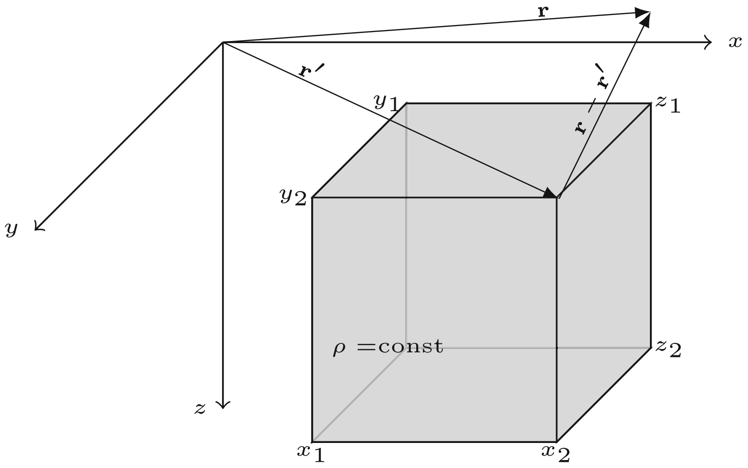

Fig. 2 Rectangular prism of constant density ρ. The coordinates x_i, y_i, z_i are the corners of the prism for $i = 1, 2$

A typical data acquisition is done on the surface for N_s observation points (gravimetric stations), hence $\mathbf{g}_z = \left[g_{z_1}, g_{z_2}, \cdots, g_{z_{N_s}}\right]^T \in \mathbb{R}^{N_s}$. Considering a model parametrization of $M = n_x \times n_y \times n_z$ prisms where n_x, n_y and n_z are the number of prisms for x, y and z directions respectively, a model vector can be arranged as $\mathbf{m}_\rho = [\rho_1, \rho_2, \cdots, \rho_M]^T \in \mathbb{R}^M$. Given this vector notation, the corresponding matrix for the kernel $\mathbf{A}$ in index notation is

$$A_{ij} = \gamma \left[z_i \tan^{-1}\left(\frac{x_i y_i}{z_i |\Delta r_i|}\right) - x_i \ln\left(y_i + |\Delta r_i|\right) - y_i \ln\left(x_i + |\Delta r_i|\right) \right] \Bigg|_{\Delta x'_{1_j}}^{\Delta x'_{2_j}} \Bigg|_{\Delta y'_{1_j}}^{\Delta y'_{2_j}} \Bigg|_{\Delta z'_{1_j}}^{\Delta z'_{2_j}}, \tag{7}$$

where $\mathbf{A} \in \mathbb{R}^{N \times M}$, thus the gravity data vector can be represented in a matrix form as

$$\mathbf{g}_z = \mathbf{A}\mathbf{m}_\rho, \tag{8}$$

corresponding to the forward modeling of the gravimetric data. This is a linear problem with respect to density.

2.3 Waveform Forward Modeling

An elastic body is governed by the generalized Hooke's law. For small deformations and ignoring attenuation, the stress and strain are directly proportional as

$$\boldsymbol{\tau} = \mathbf{c} : \epsilon, \tag{9}$$

where $\boldsymbol{\tau}$ is the stress tensor, $\boldsymbol{\epsilon}$ the strain tensor, $\mathbf{c}$ represents the fourth-order stiffness tensor containing the constants that characterize the elastic properties of the solid, and : is the double dot product for tensors. In index notation, Eq. 9 can be represented as

$$\tau_{ij} = c_{ijkl}\epsilon_{kl}. \tag{10}$$

for $i, j, k, l = 1, 2, 3$. Taking into consideration that the strain is proportional to the gradient of the displacement [1], $\boldsymbol{\epsilon} = \frac{1}{2}\left[\nabla u + (\nabla u)^T\right]$, Eq. 10 can be written as

$$\tau_{ij} = c_{ijkl}\frac{\partial u_k}{\partial x_l}, \tag{11}$$

where $u_k = \left\{u_x(x,t), u_y(x,t), u_z(x,t)\right\}$ is the displacement vector. Following [1] and assuming that the elastic body is subject to Newton's second law ($F = ma$) normalized over a volume, an equation relating displacement and stresses can be obtained

$$\rho\frac{\partial^2 u_i}{\partial t^2} = \frac{\partial \tau_{ij}}{\partial x_j} + f_i, \quad \text{in} \quad \Omega, \tag{12}$$

where Ω is the spatial domain, f_i represent an external force per unit volume, ρ is the density and the acceleration is written as the second derivative of the displacement u_i. The elastodynamic wave equation is obtained combining Eqs. 11 and 12, to obtain

$$\rho\frac{\partial^2 u_i}{\partial t^2} - \frac{\partial}{\partial x_j}\left[c_{ijkl}\frac{\partial u_k(x,t)}{\partial x_l}\right] = f_i, \tag{13}$$

valid for heterogeneous, elastic and anisotropic media, ignoring attenuation or viscoelastic effects. In this work, only isotropic media will be considered. In this case, the stiffness tensor is reduced to

$$c_{ijkl} = \lambda\delta_{ij}\delta_{kl} + \mu(\delta_{ik}\delta_{jl} + \delta_{il}\delta_{jk}), \tag{14}$$

where λ and μ are the Lamè parameters and δ_{ij} is the Kronecker delta function. Substituting Eq. 14 into 13 and reducing indexes, the elastic wave equation for isotropic media is obtained as follows

$$\rho \frac{\partial^2 u_i}{\partial t^2} = \frac{\partial}{\partial x_i}\left(\lambda \frac{\partial u_j}{\partial x_j}\right) + \frac{\partial}{\partial x_j}\left[\mu\left(\frac{\partial u_i}{\partial x_j} + \frac{\partial u_j}{\partial x_i}\right)\right] + f_i. \tag{15}$$

The media parameters of the wave equation were reduced to 3: Lamè's first parameter λ, the shear modulus μ, and the density ρ. There are other ways to write Eq. 15 depending on the choice of the elastic parameters, for example, the bulk modulus $\kappa = \lambda + \frac{2}{3}\mu$ is commonly used instead of λ. In general, these parameters can be expressed in terms of the P-wave velocity, $V_P = \sqrt{\frac{\lambda+2\mu}{\rho}}$, and the S-wave velocity, $V_S = \sqrt{\frac{\mu}{\rho}}$, which will be the parameters estimated on the inverse problem.

The elastodynamic wave equation can be simplified considering the wave propagation through acoustic media (fluids, melted bodies, liquid bodies) where there are no shear forces and therefore $\mu = 0$. Substituting this in Eq. 13 and defining $P = \lambda \nabla \cdot \mathbf{u}$, we obtain

$$\frac{1}{\lambda}\frac{\partial^2 P(\mathbf{x},t)}{\partial t^2} - \nabla \cdot \left[\frac{1}{\rho}\nabla P(\mathbf{x},t)\right] = \tilde{f}(\mathbf{x},t), \tag{16}$$

where the scalar field P is the pressure propagated in the media due to an external force $\tilde{f}$. For constant density, this expression is simplified to the well-know acoustic wave equation

$$\frac{1}{V_P^2}\frac{\partial^2 P(\mathbf{x},t)}{\partial t^2} - \nabla^2 P(\mathbf{x},t) = \tilde{f}(\mathbf{x},t), \tag{17}$$

where $V_P^2 = \frac{\lambda}{\rho}$ is the P-wave velocity. Let $\partial\Omega$ be the boundary of Ω and $\hat{n}$ be the outward unit normal vector defined in the boundary. The boundary can be decomposed as $\partial\Omega = \Gamma_D \cup \Gamma_N$, $\Gamma_D \cap \Gamma_N = \emptyset$, where Γ_D and Γ_N are the boundaries where Dirichlet and Neumann conditions are defined. The boundary conditions for Eq. 17 are given by

$$P = P_D \quad \text{on} \quad \Gamma_D, \tag{18}$$

$$\nabla P \cdot \hat{n} = P_N \quad \text{on} \quad \Gamma_N. \tag{19}$$

Despite the fact that this equation is valid for acoustic media, it is often used for forward modeling in elastic media, FWI and RTM since it is computationally less expensive than the elastodynamic wave equation and, more importantly, the results are acceptable for many applications.

In order obtain the synthetic seismograms for displacement, velocity or pressure, Eqs. 15 and 17 need to be solved under some initial conditions. Among the most used techniques for wave propagation, we have FDM for acoustic [2] or elastic media [21], SEM for acoustic [8] or elastic media [22] and Finite Difference using

Staggered Grids (SGFD) for elastic media [43]. In this work, the acoustic wave equation will be solved using FDM and the elastic wave equation using SGFD.

Consider the following standard-grid discretization for the space–time domain

$$t_n = n\Delta t, \quad n = 0, 1, 2, ..., n_t, \tag{20}$$

$$x_i = x_0 + i\Delta x, \quad i = 1, 2, 3, ..., n_x, \tag{21}$$

$$y_j = y_0 + j\Delta y, \quad j = 1, 2, 3, ..., n_y, \tag{22}$$

$$z_k = z_0 + k\Delta z, \quad k = 1, 2, 3, ..., n_z, \tag{23}$$

$$P^n_{i,j,k} = P(x_i, y_j, z_k, t_n), \tag{24}$$

where n_x, n_y and n_z are the total number of grid points in each direction, n_t is the number of time steps, Δx, Δy, Δz and Δt are the spatial and time increments, and x_0, y_0 and z_0 are the coordinates of the reference point. First, let us consider the acoustic problem. The discrete form for the spatial and time derivatives is given by Alford et al. [2]

$$P^{n+1}_{i,j,k} = 2P^n_{i,j,k} - P^{n-1}_{i,j,k} + V_P^2 \Delta t^2 \left(D_x^2 P^n_{i,j,k} + D_y^2 P^n_{i,j,k} + D_z^2 P^n_{i,j,k} \right), \tag{25}$$

where D_x^2, D_y^2 and D_z^2 are the discrete operators for the second derivative. For example, the second-order discrete operator for the second derivative centered at x is given by

$$\left(\frac{\partial^2 P}{\partial x^2} \right)_n = \frac{P^n_{i+1,j,k} - 2P^n_{i,j,k} + P^n_{i-1,j,k}}{\Delta x^2} + O(\Delta x^2) \tag{26}$$

with $O(\Delta x^2)$ the truncation error. For this order, only 3 grid points in time are required to compute the second derivative of the pressure. Since the resolution depends on the parametrization of the velocity model in space, it is preferable to use more grid points for x, y and z, as seen in Table 1 for second derivatives for different orders of precision. The visual representation of the reference and neighbouring nodes for the discretization of the acoustic wave equation in 2D is shown in Fig. 3.

The numerical simulation of Eq. 26 involves the recursive computation of the pressure P over the time steps n_t. However, this recursive computation can present incremental error over time because of the truncation of the approximated solution or because of the machine rounding error. In order to set the discretization parameters such that the errors are bounded, a Von Neumann analysis is required. Based on the work of Alford et al. [2], a stability condition can be obtained by substituting a plane-wave solution into Eq. 26 and performing some standard algebraic simplifications, to obtain

$$\Delta t \leq \frac{\Delta x}{v_{\text{MAX}} \sqrt{n_D}} \left(\sum_{i=1}^{M} a_m \right)^{-1/2}, \tag{27}$$

Table 1 Central differences coefficients for second order derivative for accuracies of 2, 4, 6 and 8th order with uniform grid spacing

	Approximation at $x = 0$ central differences								
Order of accuracy↓	-4	-3	-2	-1	0	1	2	3	4
2				1	-2	1			
4			$-\frac{1}{12}$	$\frac{4}{3}$	$-\frac{5}{2}$	$\frac{4}{3}$	$-\frac{1}{12}$		
6		$\frac{1}{90}$	$-\frac{3}{20}$	$\frac{3}{2}$	$-\frac{49}{18}$	$\frac{3}{2}$	$-\frac{3}{20}$	$\frac{1}{90}$	
8	$-\frac{1}{560}$	$\frac{8}{315}$	$-\frac{1}{5}$	$\frac{8}{5}$	$-\frac{205}{72}$	$\frac{8}{5}$	$-\frac{1}{5}$	$\frac{8}{315}$	$-\frac{1}{560}$

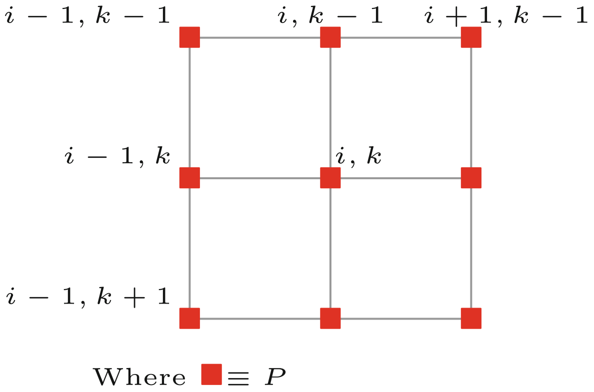

Fig. 3 Visual representation of a standard grid discretization for a 2D acoustic media for the pressure field P

where v_{MAX} is the maximum value of the velocity model, $\sum_{i=1}^{M} a_m$ is the sum over the coefficients of Table 1 for each order of precision excluding the central point, and $n_D = 1, 2, 3$ is the dimension (1D, 2D, or 3D). This condition is very important for the inverse problem; given that it depends on the maximum velocity, the velocity model obtained has to be inspected in every iteration for stability.

In order to simulate the wave propagation in time a source has to be applied at any point of the space. In this example and in all the following results for this work, a Ricker wavelet is used, given by

$$w(t) = 2(\pi \nu)^2 \left\{1 - 2\left[\pi \nu \left(t - t_0\right)\right]^2\right\} e^{-[\pi \nu (t - t_0)]^2} \tag{28}$$

where ν is the peak frequency of the pulse and t_0 is the time shift. The Ricker wavelet is also called the Mexican-hat wavelet because of its distinctive shape (see Fig. 4 for $t_0 = 0.0$ and $\nu = [2, 5, 10, 15, 25]$ Hz). For low frequencies the wavelet becomes wider and *vice versa* for high frequencies.

Concerning wave propagation in elastic media, FDM with a standard grid has grid-dispersion problems when there are significant contrast of properties [10], therefore, the forward modeling will be performed using Staggered Grid Finite Differences (SGFD) [43]. The isotropic wave equation can be expressed as the

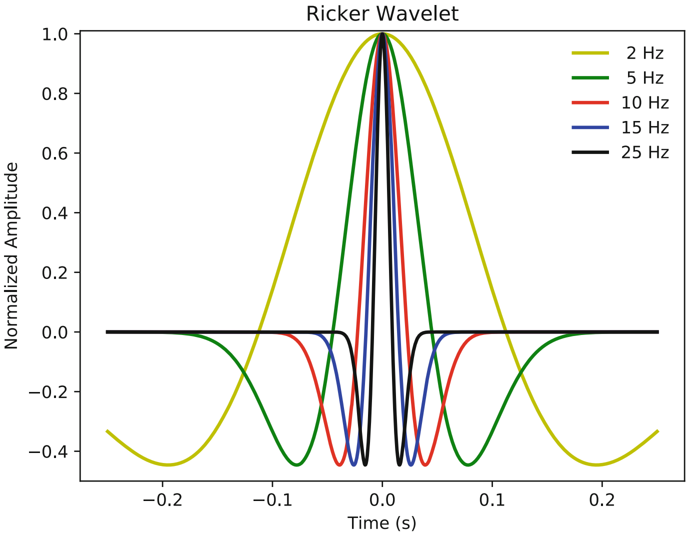

Fig. 4 Ricker wavelet function for peak frequencies 2,5,10,15 and 25 Hz. The function is centered at $t_0 = 0$

following set of equations

$$\rho\partial_{tt}u_x = \partial_x\tau_{xx} + \partial_y\tau_{xy} + \partial_z\tau_{xz} + f_x, \tag{29}$$

$$\rho\partial_{tt}u_y = \partial_x\tau_{xy} + \partial_y\tau_{yy} + \partial_z\tau_{yz} + f_y, \tag{30}$$

$$\rho\partial_{tt}u_z = \partial_x\tau_{xz} + \partial_y\tau_{yz} + \partial_z\tau_{zz} + f_z, \tag{31}$$

$$\tau_{xx} = (\lambda + 2\mu)\partial_x u_x + \lambda(\partial_y u_y + \partial_z u_z), \tag{32}$$

$$\tau_{yy} = (\lambda + 2\mu)\partial_y u_y + \lambda(\partial_x u_x + \partial_z u_z), \tag{33}$$

$$\tau_{zz} = (\lambda + 2\mu)\partial_z u_z + \lambda(\partial_x u_x + \partial_y u_y), \tag{34}$$

$$\tau_{xy} = \mu(\partial_y u_x + \partial_x u_y), \tag{35}$$

$$\tau_{xz} = \mu(\partial_z u_x + \partial_x u_z), \tag{36}$$

$$\tau_{yz} = \mu(\partial_z u_y + \partial_y u_z). \tag{37}$$

The discretization of the elastodynamic wave equation in the displacement-stress formulation is given by Virieux [43]

$$\begin{aligned}[u_x]^{n+1}_{i+1/2,j,k} &= 2[u_x]^{n}_{i+1/2,j,k} - [u_x]^{n-1}_{i+1/2,j,k} \\ &\quad + \Delta t^2\left[b_x(D_x\tau_{xx} + D_y\tau_{xy} + D_z\tau_{xz} + f_x)\right]^{n}_{i+1/2,j,k},\end{aligned} \tag{38}$$

$$\begin{aligned}\left[u_y\right]^{n+1}_{i,j+1/2,k} &= 2[u_y]^n_{i,j+1/2,k} - [u_y]^{n-1}_{i,j+1/2,k} \\ &\quad + \Delta t^2 \left[b_y(D_x\tau_{xy} + D_y\tau_{yy} + D_z\tau_{yz} + f_y)\right]^n_{i,j+1/2,k}\,, \end{aligned} \tag{39}$$

$$\begin{aligned}[u_z]^{n+1}_{i,j,k+1/2} &= 2[u_z]^n_{i,j,k+1/2} - [u_z]^{n-1}_{i,j,k+1/2} \\ &\quad + \Delta t^2 \left[b_z(D_x\tau_{xz} + D_y\tau_{yz} + D_z\tau_{zz} + f_z)\right]^n_{i,j,k+1/2}\,, \end{aligned} \tag{40}$$

for the displacement calculated on midpoints of the grid. This time D_x, D_y and D_z are the discrete operators for the first derivative in a staggered grid and $b = 1/\rho$. For stresses

$$[\tau_{xx}]^n_{i,j,k} = \left[(\lambda + 2\mu)D_x u_x + \lambda(D_y u_y + D_z u_z)\right]^n_{i,j,k}\,, \tag{41}$$

$$[\tau_{yy}]^n_{i,j,k} = \left[(\lambda + 2\mu)D_y u_y + \lambda(D_x u_x + D_z u_z)\right]^n_{i,j,k}\,, \tag{42}$$

$$[\tau_{zz}]^n_{i,j,k} = \left[(\lambda + 2\mu)D_z u_z + \lambda(D_x u_x + D_y u_y)\right]^n_{i,j,k}\,, \tag{43}$$

$$[\tau_{xy}]^n_{i+1/2,j+1/2,k} = \left[\mu_{xy}(D_y u_z + D_x u_y)\right]^n_{i+1/2,j+1/2,k}\,. \tag{44}$$

$$[\tau_{xz}]^n_{i+1/2,j,k+1/2} = [\mu_{xz}(D_z u_x + D_x u_z)]^n_{i+1/2,j,k+1/2}\,. \tag{45}$$

$$[\tau_{yz}]^n_{i,j+1/2,k+1/2} = \left[\mu_{yz}(D_z u_y + D_y u_z)\right]^n_{i,j+1/2,k+1/2}\,. \tag{46}$$

The simplification from 3D to 2D media is straightforward ignoring the y-dependent terms. The finite difference coefficients for staggered grid are shown in the Table 2. Figure 5 shows a visual representation of a staggered grid.

Table 2 Central differences coefficients for first order derivatives for accuracies of 2, 4, 6 and 8th order with uniform grid spacing corresponding to staggered grid

	Approximation at $x = 0$ $x-$coordinates at nodes							
Order of accuracy↓	$-\frac{7}{2}$	$-\frac{5}{2}$	$-\frac{3}{2}$	$-\frac{1}{2}$	$\frac{1}{2}$	$\frac{3}{2}$	$\frac{5}{2}$	$\frac{7}{2}$
2				-1	1			
4			$\frac{1}{24}$	$-\frac{9}{8}$	$\frac{9}{8}$	$-\frac{1}{24}$		
6		$-\frac{3}{640}$	$\frac{25}{384}$	$-\frac{75}{64}$	$\frac{75}{64}$	$-\frac{25}{384}$	$\frac{3}{640}$	
8	$\frac{5}{7168}$	$-\frac{49}{5120}$	$\frac{245}{3072}$	$-\frac{1225}{1024}$	$\frac{1225}{1024}$	$-\frac{245}{3072}$	$\frac{49}{5120}$	$-\frac{5}{7168}$

Fig. 5 Visual representation of a staggered grid discretization for a 2D elastic media in terms of displacements (u_x and u_z) stresses (τ_{xx}, τ_{zz} and τ_{xz})

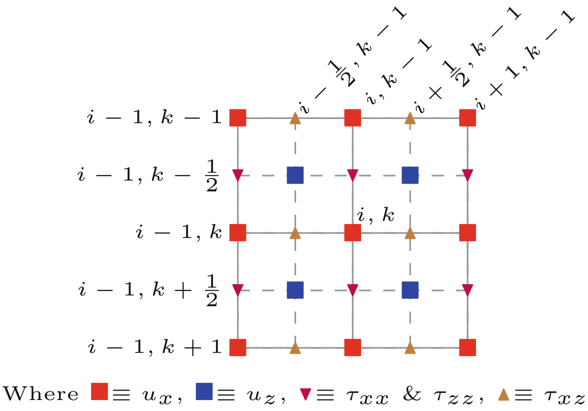

Fig. 6 Illustration of the concept of forward and the inverse problems

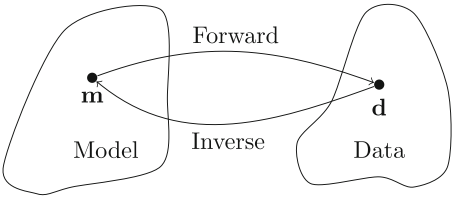

3 Inverse Theory for Geophysical Data

This section presents the basic concepts of inverse theory, providing the theoretical framework for GI and FWI for heterogeneous acoustic or elastic media, with an emphasis on the adjoint-state method for FWI. Starting from an Earth model, the forward problem computes theoretical data which will be compared to real data observations. Conversely, the inverse problem starts from the data and aims to compute an Earth model. A simple illustration of this statement is shown in Fig. 6. In general, the inverse problem is computationally more intensive, requires more sophisticated techniques and the interpretation of the results is more involved due to insufficient, inaccurate, noisy or inconsistent data [19]. In order to solve inverse problems, the following elements are essential in its formulation (see Table 3)

- Data,
- Model parameters,
- Forward problem,
- Cost/Objective/Error/Misfit function, and
- Optimization method.

Let us define a general formulation for inverse theory. The function (**F**) that involves such elements needs to be stated. The objective function (also known as cost, error or misfit function) compares the differences between the observed and

Table 3 Elements of inverse theory, where N is the number of data points and M the number of model parameters. In general $N \neq M$

Data vector	$\mathbf{d}^{\mathrm{obs}} = [d_1\ d_2\ d_3 \cdots d_N]^T$
Model vector	$\mathbf{m} = [m_1\ m_2\ m_3 \cdots m_M]^T$
Forward modeling	$\mathbf{d}^{\mathrm{cal}} = \mathbf{F}(\mathbf{m})$
Objective function	$Q = Q(\mathbf{d}^{\mathrm{obs}}, \mathbf{d}^{\mathrm{cal}} \vert \mathbf{m})$

synthetic data vectors as follows

$$Q(\mathbf{m}) = \|\mathbf{d} - \mathbf{F}(\mathbf{m})\|_p\,, \tag{47}$$

where $\|\cdot\|_p$ is the L_p norm and Q the objective function. A general form of the L_p norm [28] is defined as

$$\|\mathbf{v}\| := \left[\sum_{i=1}^{N} |v_i|^p\right]^{1/p} \qquad \forall\ \mathbf{v} \in \mathbb{R}^n, \tag{48}$$

where N is the number of data points and p determines the norm order. Some typical norms are

$$L_1 : \quad \|\mathbf{d} - \mathbf{F}(\mathbf{m})\|_1 := \sum_{i=1}^{N} |d_i - F_i(\mathbf{m})| \tag{49}$$

$$L_2 : \quad \|\mathbf{d} - \mathbf{F}(\mathbf{m})\|_2 := \left[\sum_{i=1}^{N} |d_i - F_i(\mathbf{m})|^2\right]^{1/2} \tag{50}$$

$$L_\infty : \quad \|\mathbf{d} - \mathbf{F}(\mathbf{m})\|_\infty := \max_i |d_i - F_i(\mathbf{m})|\,. \tag{51}$$

The L_2 norm is used more often in geophysical applications, however, the L_1 norm is also largely studied despite the fact that it has a discontinuity in the derivative. When using the L_2 norm, it is often more practical to work with the square of the objective function, $Q = Q^2$. For illustration purposes, we show in Fig. 7 a comparison of a straight-line fit using the L_1, L_2 and L_∞ norms. Notice that the norms for higher values of p are more biased towards outliers.

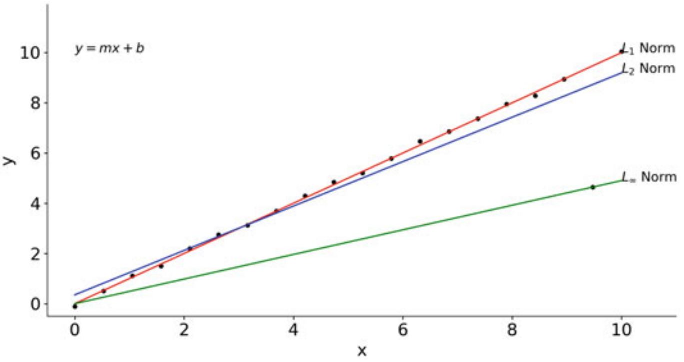

Fig. 7 L_p norm for some values of p corresponding to the fit of a straight line $\mathbf{y} = \mathbf{F}(\mathbf{x}) = a\mathbf{x} + b$

3.1 Gravimetric Inversion

The objective function for density estimation due to measurements of the vertical component of the acceleration ($\mathbf{g}_z^{\text{obs}}$) using the L_2 norm is given by

$$Q(\mathbf{m}_\rho) = \sum_{i=1}^{N_s} \left|\left| \frac{\mathbf{g}_{z_i}^{\text{obs}} - \mathbf{g}_{z_i}^{\text{cal}}}{\sigma_{\mathbf{g}_{z_i}}} \right|\right|^2 + \alpha_{\text{reg}}^2 ||\mathbf{D}\mathbf{m}_\rho||^2, \tag{52}$$

where α_{reg} is the regularization parameter, $\mathbf{D}$ is the discrete operator for the gradient and $\sigma_{\mathbf{g}_{z_i}}$ is the standard deviation of the ith data point. Solving the least-squares problem from Eq. 52 using Gauss-Newton method [35] an estimated model $\mathbf{m}_\rho$ can be obtained as

$$\mathbf{m}_\rho = \left[\mathbf{A}^T \mathbf{C}_{dd}^{-1} \mathbf{A} + \alpha_{\text{reg}} \mathbf{D}^T \mathbf{D}\right]^{-1} \mathbf{A}^T \mathbf{C}_{dd}^{-1} \mathbf{g}_z^{\text{obs}}, \tag{53}$$

where $\mathbf{C}_{dd}^{-1}$ is the diagonal covariance matrix and $\mathbf{A}$ is given in equation7. This least-squares implementation requires to store and invert a square matrix with dimensions depending on the discretization of the model, namely, $M \times M$. We need a fine discretization of the model to achieve a good resolution for the seismic inversion and therefore the joint inversion, nevertheless, we may encounter storage problems in a straight-forward implementation of Eq. 53.

An alternative to solving Eq. 53 is the use of the Conjugate Gradient Least Squares (CGLS) method. This method minimizes the objective function of Eq. 52 without the need to form and store the square matrix from Eq. 53 [35] using a conjugate gradient technique. This method requires as an input $\mathbf{G}$ and $\mathbf{d}$ to find a solution, in this case, the density model ($\mathbf{m}_\rho$) for $\mathbf{G}\mathbf{m}_\rho = \mathbf{d}$, these matrices are given by

$$\mathbf{G} = \begin{bmatrix} \mathbf{C}_{dd}^{-1/2}\mathbf{A} \\ \alpha_{\text{reg}}\mathbf{D} \end{bmatrix} \tag{54}$$

$$\mathbf{d} = \begin{bmatrix} \mathbf{C}_{dd}^{-1/2}\mathbf{g}_z^{\text{obs}} \\ 0 \end{bmatrix}, \tag{55}$$

in this case, the matrix $\mathbf{G}$ will be large and sparse due to the discrete operations for the Tikhonov regularization, the model vector $\mathbf{m}_\rho$ is not modified.

3.2 *Acoustic Full Waveform Inversion*

We now proceed to describe the methodology of Acoustic Full Waveform Inversion (AFWI). The least-squares functional for minimizing the misfit between the observed and the synthetic pressure due to a single shot is given by the L_2 norm of the residual

$$Q = \frac{1}{2}\sum_r \int_0^T \left[P_r^{\text{obs}} - P_r^{\text{cal}}\right]^2 \mathrm{d}t, \tag{56}$$

where P_r^{obs} is the observed pressure and P_r^{cal} is the synthetic pressure computed using Eq. 17. T is the total recording time and r denotes the index for the receiver. Implicitly the P_r^{cal} depends on the model parameter $\mathbf{m}$ as $P_r^{\text{cal}} = P_r^{\text{cal}}(\mathbf{m})$. This model needs to be found in such a way Eq. 56 is minimized. Taking the derivative with respect to a model perturbation

$$\partial Q = -\sum_r \int_0^T \int \left[P_r^{\text{obs}} - P_r^{\text{cal}}\right] \delta P(\mathbf{x}, t)\mathrm{d}t, \tag{57}$$

where δP is a perturbation of P aiding to compute the Frèchet derivative, which represents the sensibility for each data point and for each model parameter. This derivative is computed by making a small perturbation in each model parameter and performing a forward modeling for each data point, therefore $M \times N$ forward modelings are needed to obtain the derivative, which is impractical to implement even with the advances in computational resources, therefore, alternative methods for minimizing the problem are required.

A more efficient way to minimize Eq. 56 relies on the use of the adjoint state method for the acoustic waveform. Let us minimize the augmented misfit function subject to the wave equation multiplied by an arbitrary, well behaved and derivable

Lagrange multiplier $\Lambda := \Lambda(\mathbf{x}, t)$ remaining to be defined [32] then

$$
\begin{aligned}
Q = \frac{1}{2} \sum_r \int_0^T \int_\Omega \left[P_r^{\text{obs}} - P_r^{\text{cal}} \right]^2 \delta(\mathbf{x} - \mathbf{x}_r)\, \mathrm{d}^3x\, \mathrm{d}t \\
- \int_0^T \int_\Omega \Lambda \left[\frac{1}{V_P^2} \frac{\partial^2 P}{\partial t^2} - \nabla^2 P - f \right]^2 \mathrm{d}^3x\, \mathrm{d}t,
\end{aligned} \tag{58}
$$

notice that the last term of Eq. 58 is zero, corresponding to the wave equation acting as constriction, therefore the problem is consistent. Taking the total derivative

$$
\begin{aligned}
\delta Q = & - \sum_r \int_0^T \int_\Omega \left[P_r^{\text{obs}} - P_r^{\text{cal}} \right] \delta(\mathbf{x} - \mathbf{x}_r) \delta P \mathrm{d}^3x \mathrm{d}t \\
& - \int_0^T \int_\Omega \Lambda \left[- \frac{2}{V_P^3} \frac{\partial^2 P}{\partial t^2} \right] \mathrm{d}^3x\, \mathrm{d}t \\
& - \int_0^T \int_\Omega \Lambda \left[\frac{1}{V_P^2} \frac{\partial^2 \delta P}{\partial t^2} - \nabla^2 \delta P \right] \mathrm{d}^3x\, \mathrm{d}t,
\end{aligned} \tag{59}
$$

where the source is considered as independent of the model parameter perturbation. Notice that the perturbation δP appears on the first and last term. In the last term, the linear operator of the wave equation ($\mathcal{L} = \frac{1}{V_P^2} \frac{\partial^2}{\partial t^2} - \nabla^2$) is acting over δP which is a computation that we are looking to avoid. For this, let us first integrate by parts two times for t as

$$
\int_0^T \Lambda \left[\frac{\partial^2 \delta P}{\partial t^2} \right] \mathrm{d}t = \left(\Lambda \frac{\partial \delta P}{\partial t} \right) \Bigg|_0^T - \left(\frac{\partial \Lambda}{\partial t} \delta P \right) \Bigg|_0^T + \int_0^T \left[\frac{\partial^2 \Lambda}{\partial t^2} \right] \delta P\, \mathrm{d}t. \tag{60}
$$

Setting $\Lambda(x, t = T) = \frac{\partial \Lambda}{\partial t}(x, t = T) = 0$, yields

$$
\int_0^T \Lambda \left[\frac{\partial^2 \delta P}{\partial t^2} \right] \mathrm{d}t = \int_0^T \left[\frac{\partial^2 \Lambda}{\partial t^2} \right] \delta P \mathrm{d}t, \tag{61}
$$

this means that the second derivative is a self-adjoint operator ($\mathcal{L} = \mathcal{L}^*$). For the Laplacian operator ∇ the same procedure can be done, setting the correct boundary conditions in space. Consider the last term of Eq. 59,

$$
\int_\Omega \Lambda \left[\nabla^2 \delta P \right] \mathrm{d}^3x. \tag{62}
$$

Taking into consideration the identity $\psi\nabla^2\phi - \phi\nabla^2\psi = \nabla\cdot(\psi\nabla\phi - \phi\nabla\psi)$, then

$$\int_\Omega \Lambda\left[\nabla^2\delta P\right]\mathrm{d}^3x = \int_\Omega \delta P\left[\nabla^2\Lambda\right]\mathrm{d}^3x + \int_\Omega \nabla\cdot[\Lambda\nabla\delta P - \delta P\nabla\Lambda]\,\mathrm{d}^3x. \tag{63}$$

Applying Gauss theorem on the last term of the equation

$$\int_\Omega \nabla\cdot[\Lambda\nabla\delta P - \delta P\nabla\Lambda]\,\mathrm{d}^3x = \int_{\partial\Omega}[\Lambda\nabla\delta P - \delta P\nabla\Lambda]\cdot\hat{n}dS, \tag{64}$$

where the integral was changed from volumetric to surface. In order to cancel the boundary integral in the above equation, we set the following boundary conditions for δP and Λ [12]

$$\delta P = 0, \quad \text{on} \quad \Gamma_D, \quad \nabla\delta P\cdot\hat{n} = 0, \quad \text{on} \quad \Gamma_N, \tag{65}$$

and

$$\Lambda = 0, \quad \text{on} \quad \Gamma_D, \quad \nabla\Lambda\cdot\hat{n} = 0, \quad \text{on} \quad \Gamma_N. \tag{66}$$

Therefore,

$$\int_{\partial\Omega}[\Lambda\nabla\delta P - \delta P\nabla\Lambda]\cdot\hat{n}dS = 0. \tag{67}$$

In this way, Eq. 59 can be rewritten as

$$\begin{aligned}
\delta Q = &-\sum_r\int_0^T\int_\Omega\left[P_r^{\mathrm{obs}} - P_r^{\mathrm{cal}}\right]\delta(\mathbf{x}-\mathbf{x}_r)\delta P\,\mathrm{d}^3x\,\mathrm{d}t \qquad (68)\\
&-\int_0^T\int_\Omega\Lambda\left[-\frac{2}{V_P^3}\frac{\partial^2 P}{\partial t^2}\right]\mathrm{d}^3x\,\mathrm{d}t\\
&-\int_0^T\int_\Omega\left[\frac{1}{V_P^2}\frac{\partial^2\Lambda}{\partial t^2} - \nabla^2\Lambda\right]\delta P\,\mathrm{d}^3x\,\mathrm{d}t,\\
= &-\int_0^T\int_\Omega\left\{\frac{1}{V_P^2}\frac{\partial^2\Lambda}{\partial t^2} - \nabla^2\Lambda + \sum_r\left[P_s^{\mathrm{obs}} - P_s^{\mathrm{cal}}\right]\delta(x-x_r)\right\}\delta P\,\mathrm{d}^3x\,\mathrm{d}t\\
&-\int_0^T\int_\Omega\Lambda\left[-\frac{2}{V_P^3}\frac{\partial^2 P}{\partial t^2}\right]\mathrm{d}^3x\,\mathrm{d}t. \qquad (69)
\end{aligned}$$

Let us define the Lagrange multiplier Λ in such a way that the first term of Eq. 69 is canceled. Then

$$\frac{1}{V_P^2}\frac{\partial^2 \Lambda}{\partial t^2} - \nabla^2 \Lambda = -\sum_r \left[P_r^{\text{obs}} - P_r^{\text{cal}}\right] \delta(\mathbf{x} - \mathbf{x}_r), \tag{70}$$

which corresponds to another wave equation using the residuals at the seismogram locations as a source. The importance of this result relies on the computation of the gradient without the need to compute the perturbation of P and therefore Frèchet derivatives, instead, a single additional forward modeling needs to be performed using the same wave propagation method but with the residuals as a source. Finally, to give more meaning to the Lagrange multiplier let us define $\Lambda(x, t) \equiv P^\dagger(x, T - t)$, thus the gradient

$$\partial V = \frac{2}{V_P^3} \int_0^T P^\dagger(\mathbf{x}, T - t) \frac{\partial^2 P(\mathbf{x}, t)}{\partial t^2} \mathrm{d}t, \tag{71}$$

which is a convolution of the pressure and adjoint wave fields. Using multiple seismic sources requires a summation as follows

$$\partial V = \frac{2}{V_P^3} \sum_s^{n_s} \int_0^T P^\dagger(\mathbf{x}, T - t) \frac{\partial^2 P(\mathbf{x}, t)}{\partial t^2} \mathrm{d}t. \tag{72}$$

where n_s is the total number of shots. Notice that the pressure and adjoint wavefields are computed in opposite directions for the time stepping: $P(\mathbf{x}, t)$ is going forward in time and $P^\dagger(\mathbf{x}, T - t)$ is going backward in time.

3.3 Gradient Based Optimization

With the velocity gradient, we can update the velocity model minimizing the cost of 56, but first let us illustrate how such gradient is constructed. Consider the modified Marmousi model and a starting 2D velocity model of Fig. 8. This model involves slightly folded layers similar to a bookshelf sliding fault system and a discordance event at the bottom. The velocity range was shortened to 1500–3500 km/s covering a depth of 1000 m and a horizontal distance of 2000 m on a grid of $n_x = 200$ and $n_z = 100$ grid nodes. The starting model is a smoothed version (Gaussian smoothing) of the true velocity model and the water layer is considered to be known in both models. Table 4 summarizes the parameters used for the forward modeling and the construction of the gradient for this example. The parameters satisfy the stability condition of Eq. 27 for a 10th order FDM in 2D media. The receivers and sources locations are equally spaced along the surface, 10 m spacing between seismograms and 20 m spacing for sources (shots). For this example, the seismic traces are shown in Fig. 9 for some shots. This data acquisition correspond

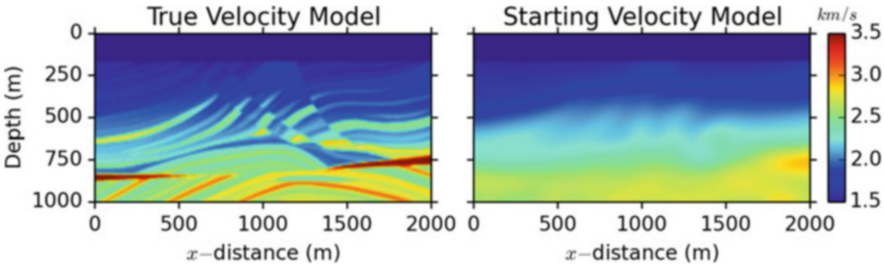

Fig. 8 Modified Marmousi velocity model (left) and starting velocity model (right). The velocity was shortened to 3500 m/s

Table 4 Parameters used for the construction of the gradient for the Marmousi model

Parameter	Value	Unit	Description
x_{MIN}	0	m	Starting horizontal distance
x_{MAX}	2000	m	Final horizontal distance
z_{MIN}	0	m	Starting depth
z_{MAX}	1000	m	Final depth
n_x	200		Grid nodes for x
n_z	100		Grid nodes for z
T	2	s	Recording time
n_t	1500		Grid nodes for t
v_{MAX}	3500	m/s	Maximum velocity
f	15	Hz	Ricket wavelet's peak frequency
n_r	200		Number of receivers
n_s	100		Number of sources

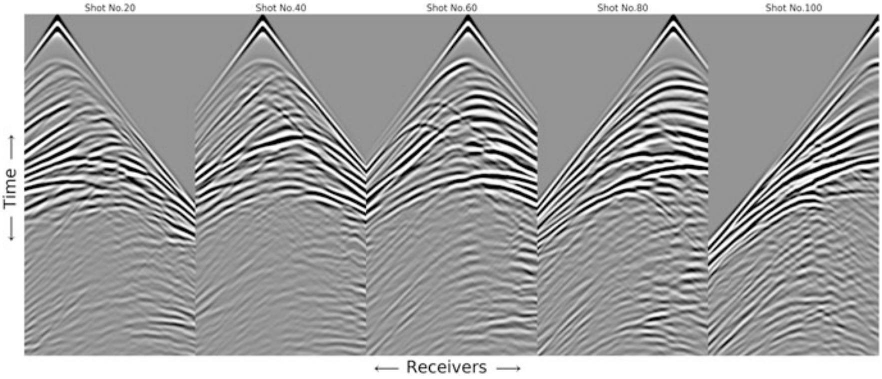

Fig. 9 Synthetic seismic data acquisition for the Marmousi model example at shots number 20, 40, 60, 80 and 100 corresponding to 200 receivers equally spaced along the surface

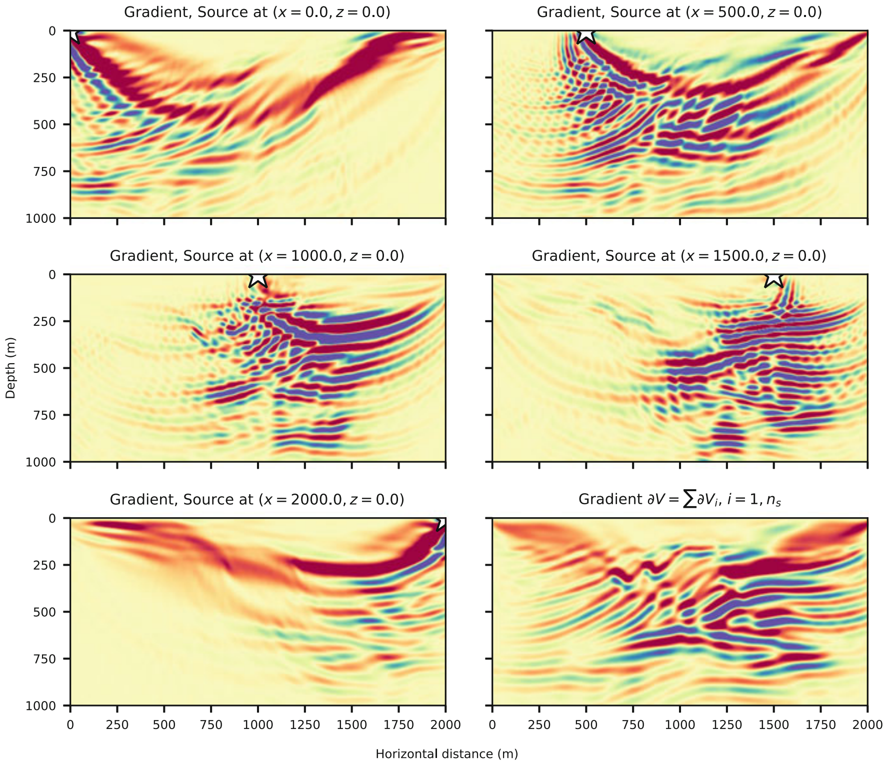

Fig. 10 Velocity gradient for several source locations $x_s = 0, 500, 1000, 1500$ and 2000 using the whole stream of receivers (200). The white star represents the different source positions. The bottom right gradient consist on the addition of all gradients

to the observed data vector $\mathbf{P}^{\text{obs}} \in \mathbb{R}^N$, $N = n_t n_r n_s$, which in this case is a vector of $1500 \times 200 \times 100 = 30$ Million data elements.

Let us consider several source positions at the surface, $x_s = 0, 500, 1000, 1500$ and 2000 m for a depth $z = 0$. The gradient for each source as well as the gradient stacked for all sources ($\partial V = \sum \partial V_i$) is shown at Fig. 10. Each gradient exhibits more sensibility beneath its position at the surface, even though the surface is fully covered with receivers. While the image is not clear for each one, the addition of all gradients into a single one produces a velocity gradient with fine resolution.

Computing the gradient is readily parallelizable. We implemented this part of our problem using Message Passing Interface (MPI) in Fortran 90 and compute the gradient for each source in parallel in a computer cluster.[1] Taking advantage

---

[1] We used the cluster Lamb of the supercomputing lab at the Specialized Labs System of the Earth Sciences Division of CICESE. Each node is equipped with 20 cores and we used for all examples 5 nodes, for a total of 5×20=100 MPI cores, equal to the number of sources.

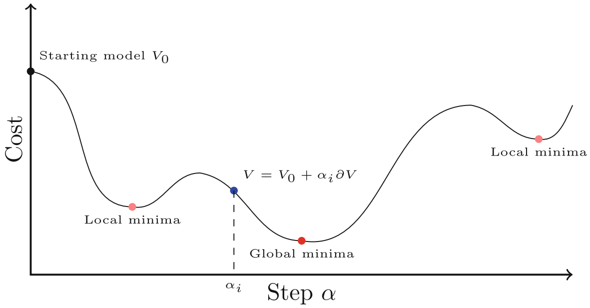

Fig. 11 Illustration of a cost function as a function of the steps α_i. An ideal step size would be the one leading closer to the global minimum

of the fact that each source-gradient computation is independent of the others, we compute each gradient simultaneously following Eq. 71, then Eq. 72 is obtained by combining the values from all processes into a main MPI core using an *MPI_ALLREDUCE* operation.

The total gradient (Fig. 10 bottom right) resembles the footprint of the layers for the Marmousi model and it is similar to a typical seismic migration. This velocity model is added to the starting model using a scalar factor that needs to be carefully chosen. The gradient-based optimization minimizes Eq. 56 by updating the velocity model iteratively as follows

$$V_{n+1} = V_n + \alpha_n \partial V, \tag{73}$$

where the scalar α_n is the step length which represents how much the current model V_n moves along the direction ∂V at the n-th iteration. The efficiency of the minimization depends on the choice of the step α_n which can lead to local or global minima as illustrated in Fig. 11.

There are several algorithms for the search of the optimal step length α_n [30]. For this work we used a step line search method using interval reduction. Consider the range of values of steps $\alpha_1 < \alpha_2 < \alpha_3 < \cdots < \alpha_k$ with k the number of test points with their respective costs $\text{cost}_1, \text{cost}_2, \text{cost}_3, \cdots, \text{cost}_k$. In this method, we select the value of α which corresponds to the minimum cost. If the minimum cost corresponds to the first test value then for the next iteration a *zoom in* is performed for the test points $[\alpha_1, \alpha_2, \alpha_3, \cdots, \alpha_k] \times \text{zoom}$ with $\text{zoom} < 1$, on the other hand if the optimal step correspond to the final point test a *zoom out* is performed as $[\alpha_1, \alpha_2, \alpha_3, \cdots, \alpha_k]/\text{zoom}$. A typical value of zoom is $\frac{\sqrt{5}-1}{2}$ corresponding to the reciprocal of the Golden ratio. The evaluation of the cost function for k different step sizes is computationally expensive, however, it is compensated by the effectiveness due to the optimal choice of α_n. The AFWI iterative scheme combining all the components is shown in algorithm 1.

Continuing with the example from Fig. 8 and Table 4, we show in Fig. 12 the inversion results at some of the iterations. For this example we used 10 test points in the step line search method ($k = 10$). In the first 10 iterations the stratigraphic features are recovered. Thereafter, the velocity values at each point of the model are

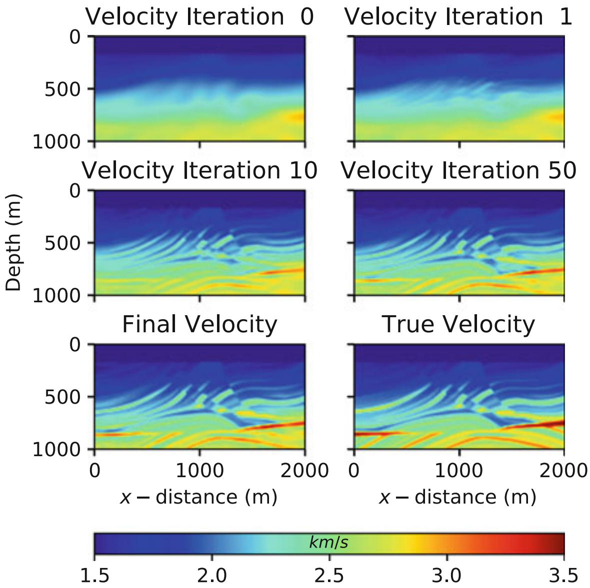

Fig. 12 Velocity Marmousi model after some iterations of FWI. The true velocity model is at the bottom-right

steadily recovered, with more resolution on the central part of the survey. The final velocity model after 228 iterations (Fig. 12 bottom left) closely resembles the true model.

To further illustrate how AFWI works, we show in Fig. 13 the seismogram from the station at (1000, 0) m with 5% of Gaussian noise and the seismograms computed using the starting and final models. Notice that the seismogram from the final model closely follows the observed seismogram.

A more accurate indicator for the quality of the FWI iterative process is the analysis of the objective function for each iteration (Fig. 14). The objective function for this example is reduced faster at early iterations and becomes slower for later iterations, because the stratigraphic information has been recovered first and, at the end of the process, only the velocity value is getting recovered slowly.

Algorithm 1: Typical AFWI process

```
Data: Observed pressure $P^{obs}[n_t, n_r, n_s]$, starting velocity model $V$
Input  : FWI iterations $n_{iter}$ .
for $i_{iter} = 1 : n_{iter}$ do
    Computes forward modeling and adjoint field;
    Performs step-line search for $\alpha$;
    Update velocity model $V_{iter+1} = V_{iter} + \alpha \partial V$
Output: Velocity model $V$, data residual $R[n_t, n_r, n_s]$
```

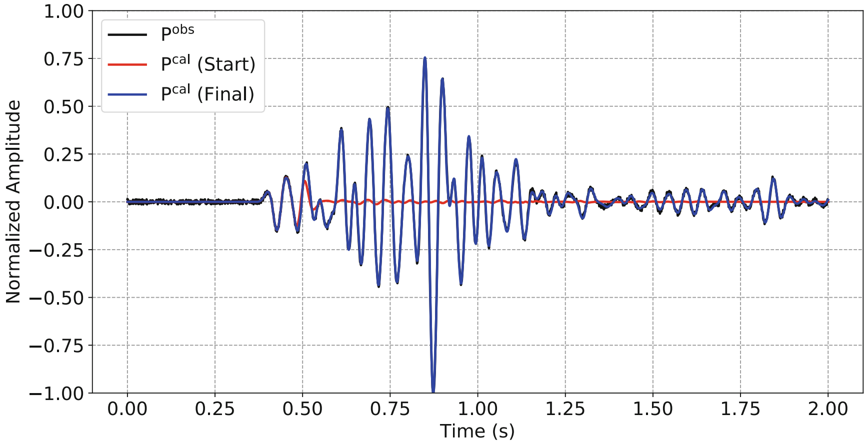

Fig. 13 Seismogram comparison for starting (red) and final (blue) synthetic data with respect to the observed data corresponding to a single source and a single receiver for the Marmousi model FWI example

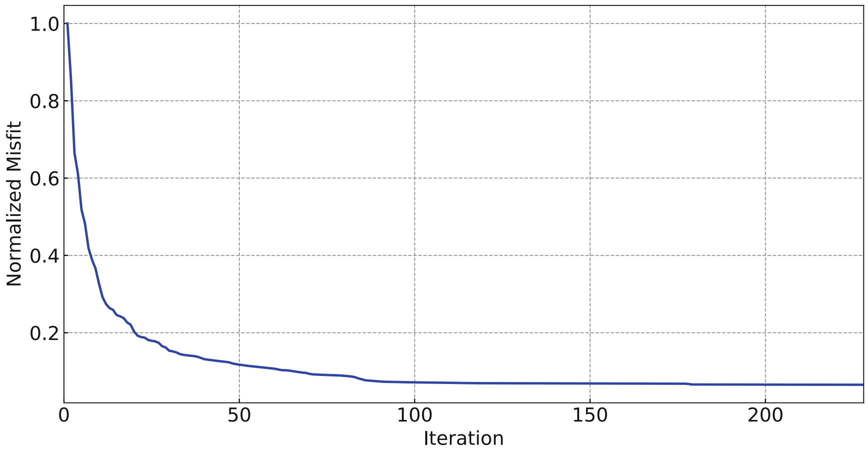

Fig. 14 Objective function (cost, misfit) reduction for 228 iterations of FWI for the Marmousi model example

3.4 Elastic Full Waveform Inversion

The tools and algorithm applied to the acoustic case can be used for Elastic FWI (EFWI) by replacing the forward modeling. The objective function for EFWI is given by

$$Q(m) = \frac{1}{2} \sum_s \sum_r \int_0^T ||\mathbf{u}_{r,s}^{\text{obs}} - \mathbf{u}_{r,s}^{\text{cal}}||^2 \, dt, \tag{74}$$

where $\mathbf{u}_{r,s}^{\text{obs}}$ is the observed displacement and $\mathbf{u}_{r,s}^{\text{cal}}$ is the synthetic displacement computed using the elastodynamic wave equation. T is the total time of recording, r is the receiver index and s is the source index. The displacements can be u_x, u_y and/or u_z (or velocities v_x, v_y, v_z) for a model m which depends on the Lamè parameters and density (or velocities V_P and V_S).

As in the acoustic case, the direct minimization of Eq. 74 involves the computation of the perturbations, which increase even more the computational cost for elastic media because the displacement (or velocity) fields are vectors. The same procedure as AFWI can be pursued using the adjoint-state method. The mathematical deduction of the gradients will not be detailed, however, notice that the second-order derivatives are self-adjoint operators. See [42] for further details of the adjoint method for elastic media.

For an isotropic media we require the gradients for density (δ_ρ), shear modulus (δ_μ) and bulks modulus (δ_κ), given by Tromp et al. [42]

$$\delta_\rho(\mathbf{x}) = -\sum_r \int_0^T \rho(\mathbf{x})\mathbf{u}^\dagger(\mathbf{x}, T-t) \cdot \partial_t^2 \mathbf{u}(\mathbf{x}, t)\, dt \tag{75}$$

$$\delta_\mu(\mathbf{x}) = -\sum_r \int_0^T 2\mu(\mathbf{x})\mathbf{D}^\dagger(\mathbf{x}, T-t) : \mathbf{D}(\mathbf{x}, t)\, dt \tag{76}$$

$$\delta_\kappa(\mathbf{x}) = -\sum_r \int_0^T \kappa(\mathbf{x})[\nabla \cdot \mathbf{u}^\dagger(\mathbf{x}, T-t)][\nabla \cdot \mathbf{u}(\mathbf{x}, t)]\, dt \tag{77}$$

where **:** is a double dot product operator between tensors, and **D** denotes the deviatoric strain, defined as

$$\mathbf{D} = \frac{1}{2}\left[\nabla\mathbf{u} + (\nabla\mathbf{u})^T\right] - \frac{1}{3}(\nabla \cdot \mathbf{u})\mathbf{I}. \tag{78}$$

Notice that these computations involve more complex operations than in the acoustic case. The adjoint deviatoric strain $\mathbf{D}^\dagger$ is computed using the equation for $\mathbf{D}$ but using $\mathbf{u}^\dagger$. The elastic gradient can be expressed in terms of the shear-wave

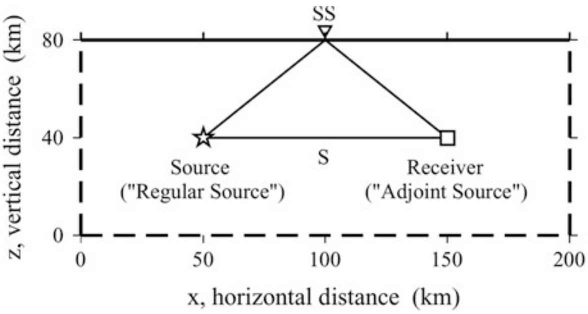

Fig. 15 Source—receiver geometry for the computation of the elastic kernels. Taken from [42]

velocity

$$\delta_{V_S}(\mathbf{x}) = 2\left(\delta_\mu - \frac{4}{3}\frac{\mu}{\kappa}\delta_\kappa\right), \tag{79}$$

and the compressional-wave velocity

$$\delta_{V_P}(\mathbf{x}) = 2\left(1 + \frac{4}{3}\frac{\mu}{\kappa}\delta_\kappa\right), \tag{80}$$

then, a step line search can be used to obtain the model parameters iteratively. Following the work of Tromp et al. [42], the source-receiver geometry for an isotropic elastic media with homogeneous properties (Fig. 15) is used.

Following the same procedure as in the previous section for acoustic media, the wave propagation for the horizontal displacement and the back-propagation for the adjoint horizontal displacement is shown in Fig. 16 for 52 seconds of recording time. For illustration purposes, the P-wave velocity kernel is shown in the third column. The gradient shows the so-called banana-doughnut shape, which is related to the ray path [42].

3.5 Cooperative Inversion

In a joint-inversion scheme, different geophysical forward problems are solved to obtain a consistent Earth-property model that matches the respective data sets measured at the surface. Usually, the strategy consists of combining all the parameters into one objective function, leading to a large system of often disparate parameters [34]. There are mainly three types of joint inversion techniques, depending on the construction of the cost function:

- Petrophysical joint inversion, where the models are constrained by an empirical relationship [6, 25, 34, 36],

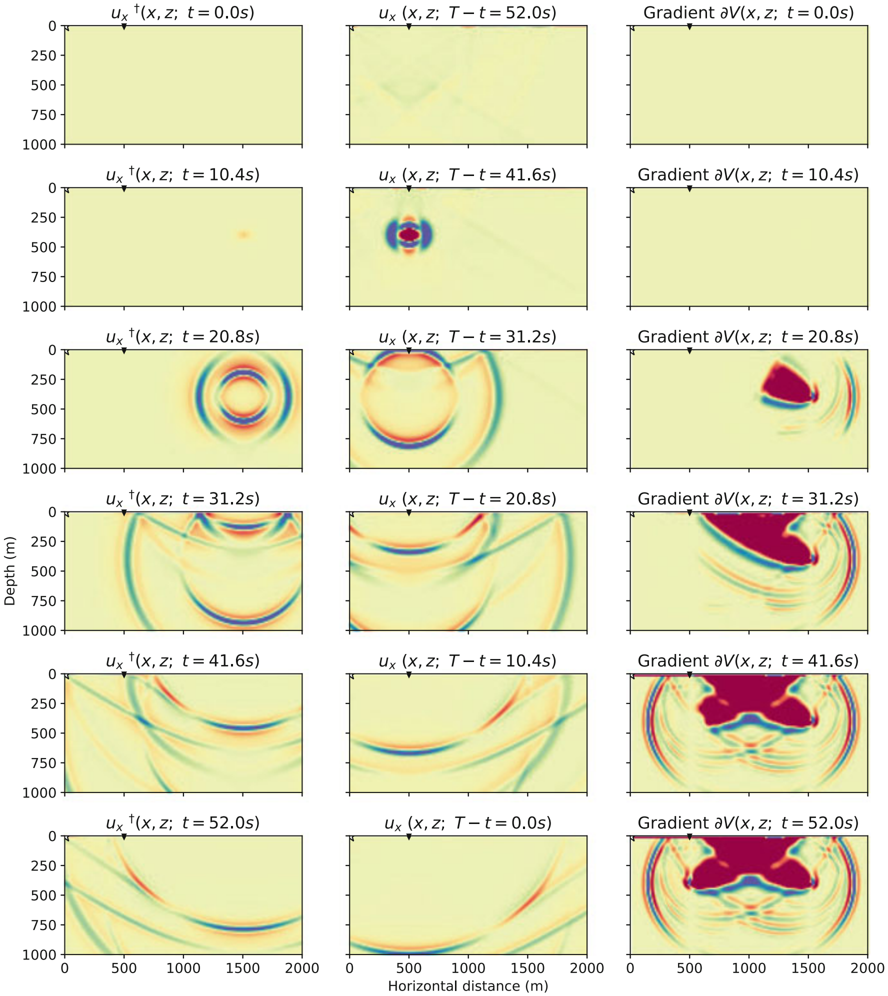

Fig. 16 Regular displacement u_x and adjoint displacement $u_x^\dagger$ wave propagation for 52 seconds of recording time for the construction of the P-wave velocity kernel

- Structural joint inversion [14, 15], where the functional is used to match the structure for both models trough the cross gradient, and
- Statistical joint inversion, e.g. using the fuzzy c-means technique [31, 33].

We will focus on the petrophysical joint inversion to combine FWI and GI. We propose a cooperative and sequential approach in which we solve at different stages for the densities and velocities. The resulting system is, therefore, more manageable and there is more control over the parameters at each stage. We call this a cooperative strategy to distinguish it from the joint strategies that solve all the geophysical parameters together at every iteration. Unlike conventional joint inversions, where the problem is to minimize a two-part objective function (e.g. seismic and gravity errors), this cooperative inversion is based on alternately minimizing the errors in seismic and gravity data iteratively [36]. The main reasons to perform these sequentially are to increase robustness, reduce the computational cost, and keep always a strong control in the GI, avoiding the natural behavior of this potential method to yield shallower models. Furthermore, in the proposed scheme we do not need to impose depth-dependent weights or constraints to the GI to avoid shallower models, this is achieved instead by using the velocity model from FWI as the a priori gravimetric model. Another advantage of this approach is that, regardless of the model obtained from fitting a gravity anomaly, the total mass is uniquely recovered as implied by Gauss' theorem [18]. This means that, although gravity is a low-resolution geophysical tool, it does provide unique information linked to the velocity model. We seek to minimize the gravimetric data constrained with the velocity model obtained after an FWI process using the following objective function

$$Q(\mathbf{m}_\rho) = \sum_{i=1}^{N_s} \left|\left| \frac{\mathbf{g}_{z_i}^{\text{obs}} - \mathbf{A}\mathbf{m}_\rho}{\sigma_{\mathbf{g}_{z_i}}} \right|\right|^2 + \alpha_{\text{reg}}^2 ||\nabla \mathbf{m}_\rho||^2 + \beta^2 ||\mathbf{m}_\rho - \mathbf{m}_{\rho(V)}||^2, \tag{81}$$

where $\mathbf{m}_\rho$ is the density model obtained using a petrophysical relationship as a function of the velocity model obtained from AFWI or EFWI. β is the parameter that weights the role on the inversion of seismic versus GI. Higher values of β yield results closer to the seismic model and vice versa. Our results will focus more on the velocity model from FWI to avoid shallower models due to a weakly-restricted GI. Then the density model will give feedback to the velocity model using an empirical relationship for the next FWI iteration. We use the following relationship from Gardner et al. [17] as petrophysical constraint,

$$\mathbf{m}_{\rho(V)} = \rho = \rho_0 V_P^{k_0}, \tag{82}$$

with $\rho_0 = 0.31$ g/cm^3 and $k_0 = 0.25$. Other density-velocity petrophysical relationships are readily available in the literature and can easily be incorporated into our proposed scheme. For example, Brocher [7] computed the following polynomial fits for density as a function of velocity

$$\rho(\text{g/cm}^3) = 1.6612 V_P(\text{km/s}) - 0.4721 V_P^2 + 0.0671 V_P^3 - 0.0043 V_P^4 + 0.000106 V_P^5, \tag{83}$$

and velocity as a function of density

$$V_P(\rho) = 39.128\rho - 63.064\rho^2 + 37.083\rho^3 - 9.1819\rho^4 + 0.8228\rho^5. \tag{84}$$

These are valid for densities between $2.0 < \rho < 3.5\,\mathrm{g/cm^3}$ and velocities in the range $1.5 < V_P < 8.5\,\mathrm{km/s}$ respectively. However, since both of Brocher's equations are based on polynomial fits, they are not inversely related. An iterative procedure using Eqs. 83 and 84 will not lead to the same velocity-density values. For example, starting from a velocity of 3500 m/s, a density of $2.318\,\mathrm{g/cm^3}$ is computed using Eq. 83, then, using Eq. 84 to get the corresponding velocity, we obtain a value of 3692.34 m/s, a change of 192.34 m/s (5.49%). Therefore, since we require that the two functions be inverse of each other, we would have to do some adjustments to incorporate these petrophysical relations into our scheme.

The CGLS method is implemented in a straightforward way modifying **G** and **d** from Eqs. 54 and 55 as follows

$$\mathbf{G} = \begin{bmatrix} \mathbf{C}_{dd}^{-1/2}\mathbf{A} \\ \alpha_{\text{reg}}\mathbf{D} \\ \beta\mathbf{I} \end{bmatrix}, \tag{85}$$

$$\mathbf{d}^{\text{CG}} = \begin{bmatrix} \mathbf{C}_{dd}^{-1/2}\mathbf{g}_z^{\text{obs}} \\ 0 \\ \beta\mathbf{m}_{\rho(V_P)} \end{bmatrix}, \tag{86}$$

where **I** is the identity matrix. Once again, **G** is a large and sparse matrix. For example, for a discretization with $n_x = 5$, $n_y = 4$ and $n_z = 3$, we would have a matrix of 15,600 element, of which only 1706 are non zero elements (a sparsity of 10.9%, see Fig. 17), whereas the square matrix of a Gauss-Newton implementation would have to store 3600 elements. The procedure to solve the system $\mathbf{Gm} = \mathbf{d}^{\text{CG}}$ is shown in algorithm 2 [35]. An efficient implementation of this algorithm requires that all the matrices be stored in a sparse representation, we use Coordinate Format (COO) sparse matrices for this.

In summary, this cooperative inversion scheme for gravity and seismic data consists of the following iterative steps: From a starting velocity model, we perform FWI to update the velocity model, then, using Gardner's density-velocity relationship, we perform constrained GI to update the density model, finally, using Gardner's velocity-density relationship, a velocity model is obtained that will be the starting model to solve FWI.

Fig. 17 Large sparse structure of the matrix **G** for the CGLS method. The blue spots represent non-zero elements and the white spaces zero elements

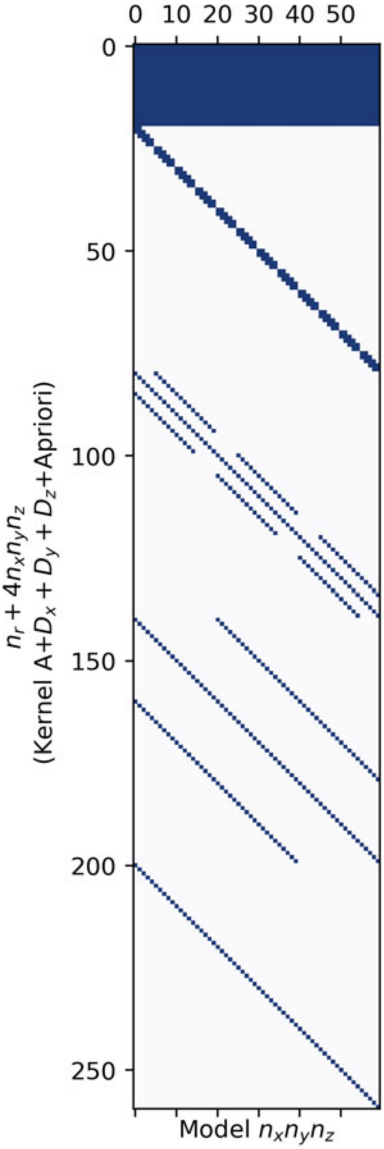

Algorithm 2: CGLS algorithm to iteratively solve the problem $Gm = d^{\mathrm{CG}}$

```
Data:
$m_0, d_0 = d^{\mathrm{CG}}, r_0 = G^T d^{\mathrm{CG}}$
$p_0 = r_0, t_0 = Ap_0$, $n$-iterations
Result: model $m_k$
while $k < n$ and $||r_k|| < 10^{-15}$ do
    $\alpha_k = ||r_{k-1}||^2/||t_{k-1}||^2$
    $m_k = m_{k-1} + \alpha_k p_{k-1}$
    $d_k = d_{k-1} - \alpha_k t_{k-1}$
    $r_k = G^T d_k$
    $\beta_k = ||r_k||^2/||r_{k-1}||^2$
    $p_k = r_k + \beta_k p_{k-1}$
    $t_k = Gp_k$
    $k \leftarrow k + 1$
```

4 Results

In order to test the proposed cooperative inversion algorithm and demonstrate its advantages, we apply this method on two synthetic examples for 2D elastic media.

4.1 EFWI: Marmousi Model

Let us consider again the Marmousi model. The geometry and parameters are the same as those of the example in Sect. 3.3 (see Fig. 8 and Table 4). The S-wave velocity is computed using $V_S = V_P/\sqrt{3}$ and the density is obtained using Gardner petrophysical relationship; the models for V_S and ρ are not shown. Only the vertical component of the displacement is considered and we use 10 test points for the step line search. We did not add Gaussian noise to the data in this example.

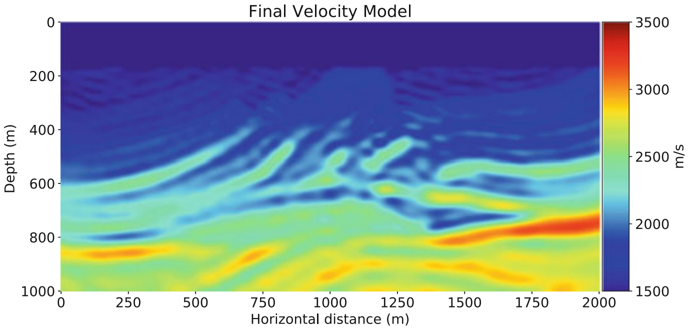

Fig. 18 The final velocity model after 100 iterations of EFWI for the Marmousi example

The velocity model obtained after 100 iterations, shown in Fig. 18, resembles the stratigraphic information of the Marmousi model (Fig. 8). This result shows spurious artifacts in the final model. This problem is attributed to the problem of the limited bandwidth of the observed data [40]. The artifacts are also related to the S-waves since they are usually not present in AFWI. These artifacts yield small errors between the observed and computed seismograms but contaminates the iterative process and affect the convergence.

The convergence of the EFWI iterative process can be analysed from the behaviour of the objective function. We observe from Fig. 19 that the objective function for this example converges fast at early iterations and becomes stagnant for later iterations. This is mostly due to the presence of the spurious artifacts mentioned before.

We show in Fig. 20 the observed and computed seismograms for the station located at (1000, 0) m corresponding to the 20th source located at (404.04, 0) m. Overall, the seismogram for the final model closely approximates the observed data. The phase of all the events is matched very well, however, there are discrepancies

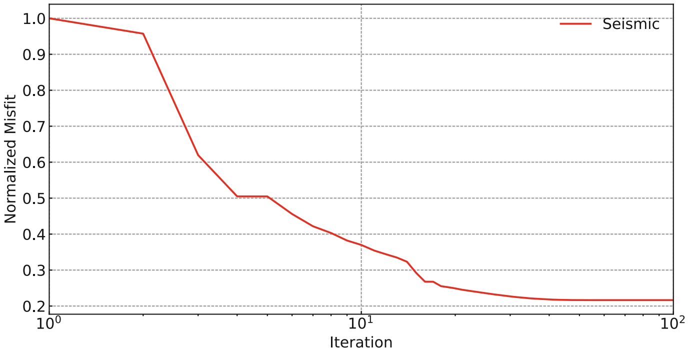

Fig. 19 Normalized objective function for the Marmousi model using EFWI

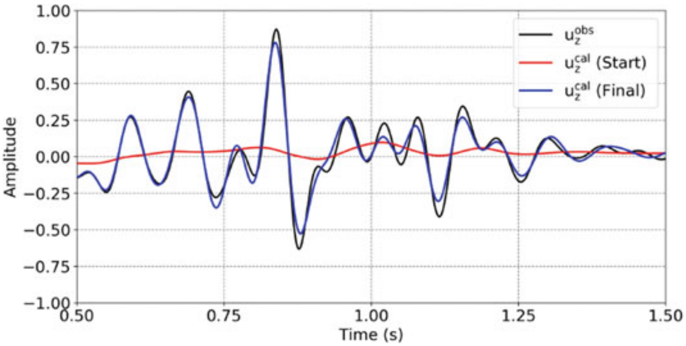

Fig. 20 Seismogram comparison of starting (red) and final (blue) synthetic data for EFWI with the observed data (black) corresponding to a single source and a receiver located at (1000, 0) m

in the amplitudes. Unfortunately, these results can not be improved using more iterations, we would have to rely on the implementation of additional techniques to get a better approximation.

4.2 EFWI: Texas-Shaped Model

For this example, we created a laterally heterogeneous layered model covering a horizontal distance of 2000 m and a depth of 1000 m for both seismic and gravimetric data. Beneath the low-velocity layers, we place a structure with the shape of Texas, as shown in Fig. 21a. The shallow layers have lower velocities (between 1500 and 2000 m/s) with respect to the deepest layer (∼3500 m/s). The S-wave velocity is computed using $V_S = V_P/\sqrt{3}$ and we used Gardner's density-velocity relationship to obtain the density model. Notice that the maximum velocity used for this example is 3500 m/s, hence Gardner's equation applies to this example. We use the same discretization parameters from the previous example (Table 4).

The initial model and the result after 48 iterations are shown in Fig. 21b, c. The top layers show many spurious artifacts similar to those in the previous example. These artifacts persist if we continue iterating the method. The objective function, shown in Fig. 22, exhibits a convergent behaviour until 40th iterations where stagnation is reached.

4.3 Cooperative Inversion: Marmousi Model

Let us apply the cooperative scheme on the Marmousi model (Fig. 8). We used the same model parameters of Table 4, with the addition of 200 equispaced gravimetric stations in the surface. The true velocity model and the starting model are the same as in the AFWI example of Sect. 3.3, and the S-wave velocity and density models are the same as in Sect. 4.1.

In order to compare the result, we performed 100 iterations of the cooperative inversion and show the results, together with those of EFWI, in Fig. 23. Incorporating GI helps to eliminate the spurious artifacts and smooths the model (Fig. 23b). This is because GI acts as a filter in the cooperative inversion. Each iteration has a computational cost of 75 minutes for EFWI and 76 minutes for the cooperative scheme.

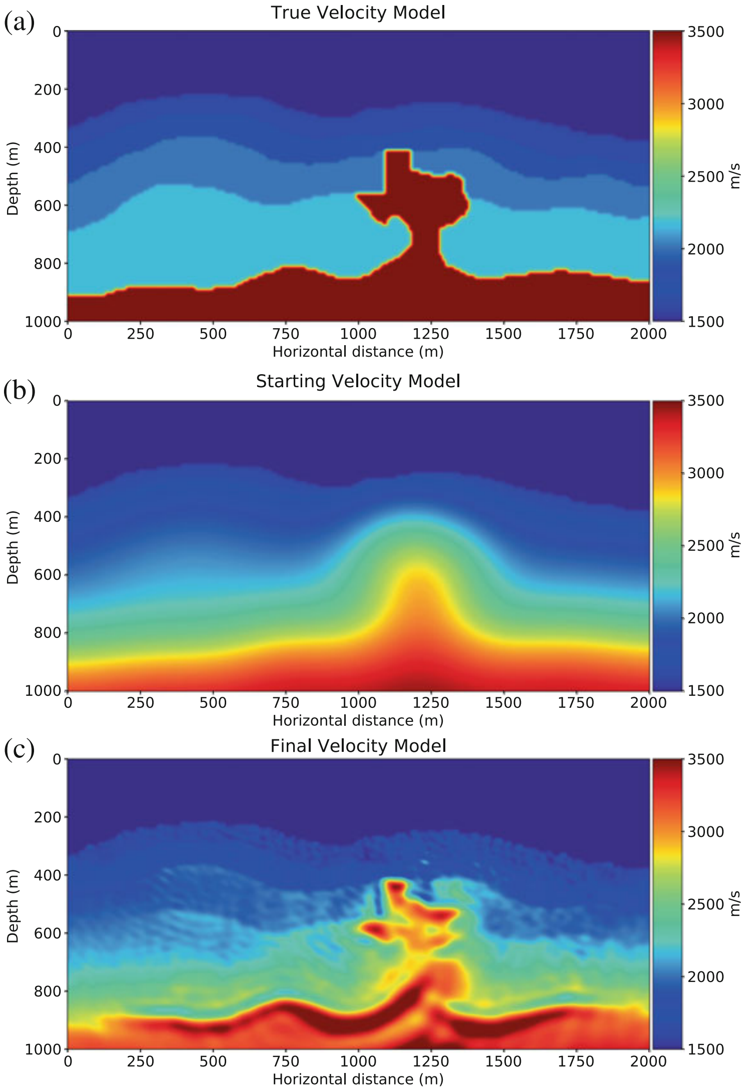

Fig. 21 (**a**) Texas-shape true velocity model, and (**b**) and its smoothing set as a starting model. (**c**) Final velocity model after EFWI

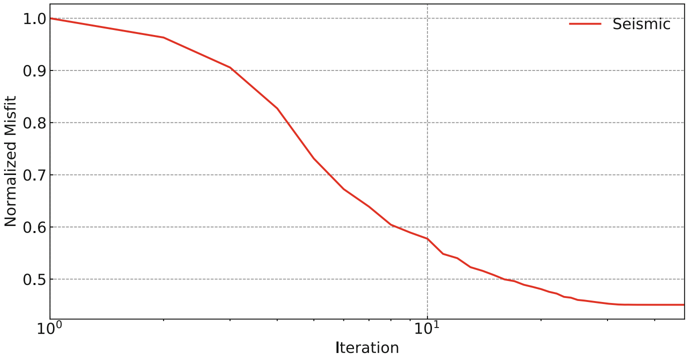

Fig. 22 Normalized misfit for seismic data for the Texas-shape model after EFWI

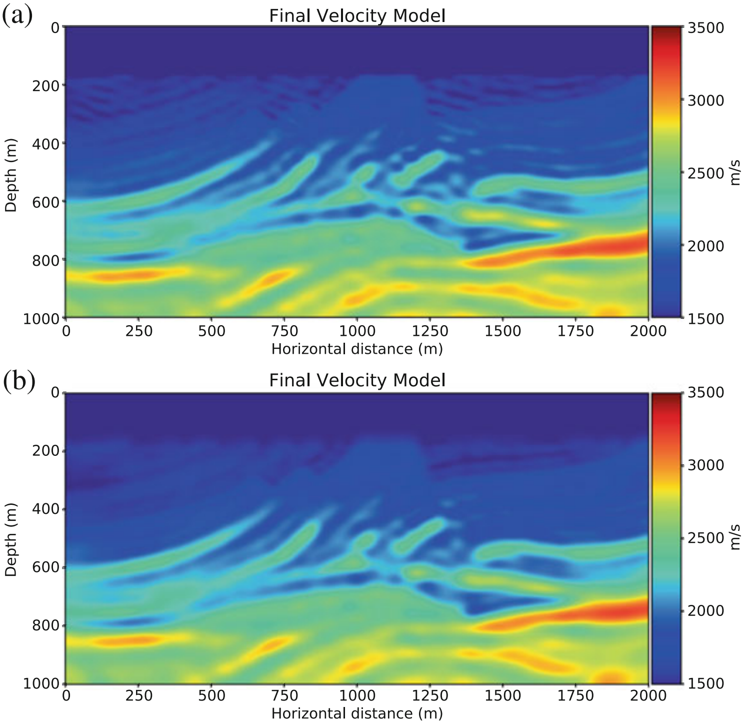

Fig. 23 Marmousi final velocity model obtained using (**a**) conventional EFWI, and (**b**) the cooperative inversion (EFWI and GI).

4.4 Cooperative Inversion: Texas-Shaped Model

As a final example, let us apply cooperative inversion to the Texas-shaped model of Fig. 21a. The true velocity model, the starting model and other parameters are the same as in Sect. 4.2. The final velocity model after 48 iterations is shown in Fig. 24 together with the results of EFWI to facilitate the comparison. Comparing Fig. 24a, b, we observe that cooperative inversion reduces the artifacts that pollute the EFWI results. The density models obtained from conventional GI and cooperative inversion are shown in Fig. 25. Figure 25a shows the typical behavior of conventional GI of giving preference to shallower models, whereas the model obtained from cooperative inversion (Fig. 25b) yields significantly better model. In order to illustrate the data fit, we show in Fig. 26 the seismograms for a station at (1000, 0) m from a source at (404.04, 0) m, and the gravimetric anomaly. The seismogram for the final model show a good agreement with the observed seismogram, with small discrepancies in phase and amplitude (Fig. 26a). The computed gravimetric anomaly has small discrepancies with the observed anomaly (Fig. 26b). We emphasize that

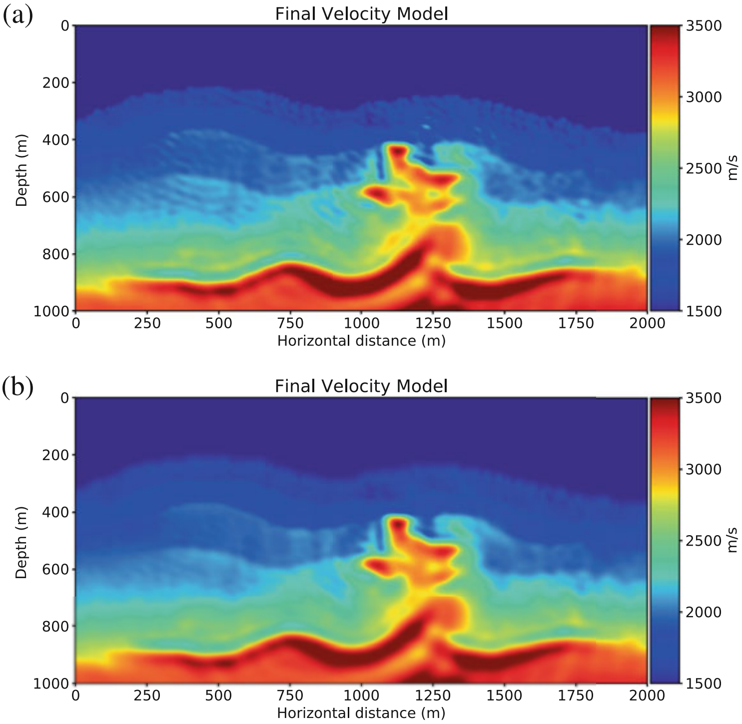

Fig. 24 Texas-shape final velocity model after 48 iterations, comparison between (**a**) conventional EFWI, and (**b**) the cooperative inversion

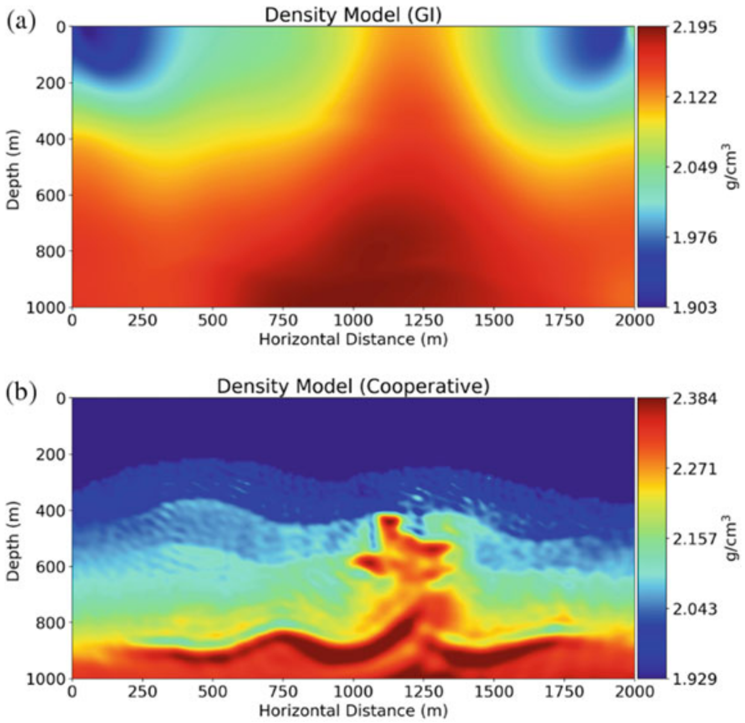

Fig. 25 Texas-shape final density model after 48 iterations, comparison between (**a**) conventional gravimetric inversion (GI), and (**b**) the cooperative inversion

the cooperative inversion does not aim to exactly fit all the data but to obtain a realistic model.

A comparison of the seismic misfit for EFWI and the cooperative scheme is presented in Fig. 27. The misfits exhibit a similar reduction at earlier iterations, however, later the cooperative inversion adjusts better the seismic traces given the elimination of the artifacts.

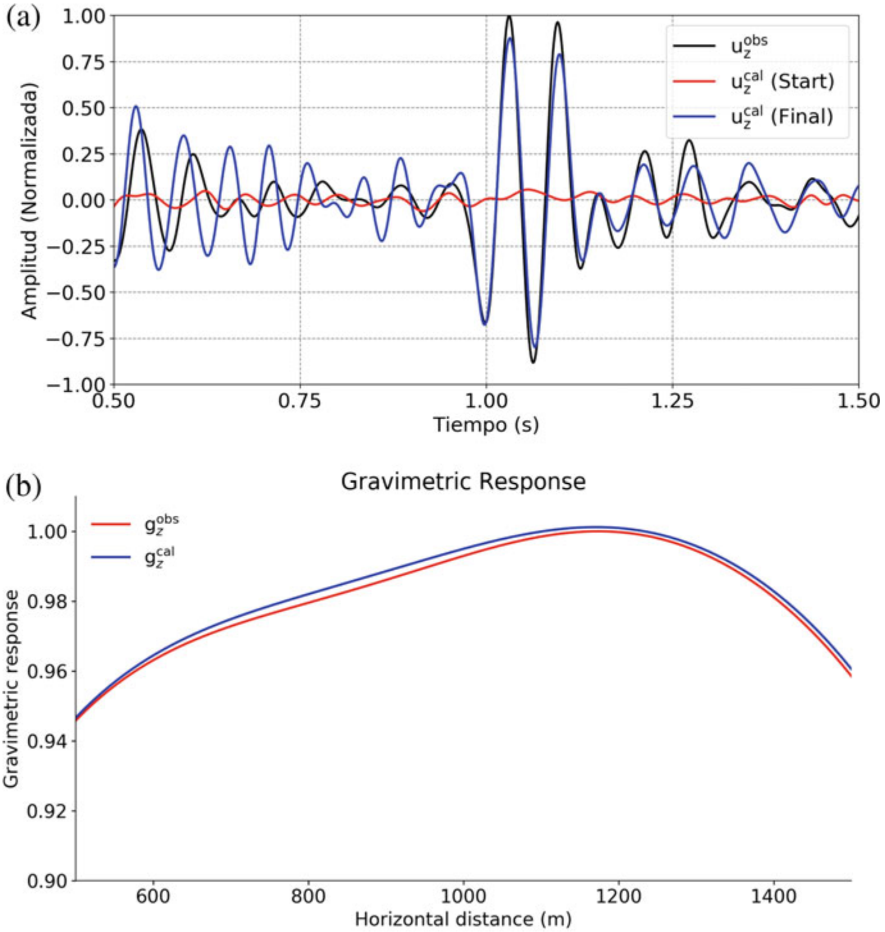

Fig. 26 Data fit for the Texas-shape model after 48 iterations of the cooperative scheme. (**a**) Vertical-displacement seismograms for a station at (1000, 0) m from a source at (404.04, 0) m, and (**b**) Observed and computed gravity anomaly

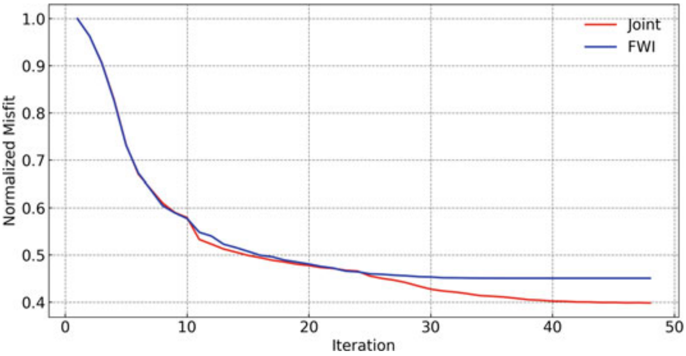

Fig. 27 Normalized misfit reduction for seismic data for cooperative inversion (red) and separated inversion (blue)

5 Conclusions

We have developed a cooperative scheme that combines GI and FWI. The methods are combined in an iterative scheme based on petrophysical relationships that can be used to characterize typical geological environments found in real field data such as irregular high velocity bodies embedded in complex horizontal layers, thrust and dominoes fault systems, for both acoustic and elastic media.

The synthetic examples for elastic media show that both methods converge as long as the starting model is acceptable and FWI has more weight in the cooperative inversion algorithm. The models recover the stratigraphic part, the fault dip, the discordances and the top and shape of the high velocity and density bodies. The weights in the cost function play a critical role in the trade off between the convergence rate and the accuracy of the resulting models. Further analysis is required to determine optimal weights.

Comparing the results obtained by separate and cooperative inversion, we observe that the cooperative scheme helps improve the density models of GI by constraining them to the FWI models. FWI also benefits from the cooperative inversion, avoiding the saturation in parts of the model and reducing the presence of the spurious reflectors. Finally, the sequential implementation of the cooperative scheme has a negligible additional computational cost compared to the classical FWI.

Acknowledgments We want to thank CONACYT and CeMIEGeo for their financial support. The numerical computations were performed using the cluster Lamb of the supercomputing lab at the Specialized Labs System of the Earth Sciences Division of CICESE.

References

1. K. Aki, P.G. Richards, *Quantitative Seismology*, vol. 1 (University Science Books, Sausalito, 2002)
2. R. Alford, K. Kelly, D.M. Boore, Accuracy of finite-difference modeling of the acoustic wave equation. Geophysics **39**(6), 834–842 (1974)
3. B. Banerjee, S. Das Gupta, Gravitational attraction of a rectangular parallelepiped. Geophysics **42**(5), 1053–1055 (1977)
4. B. Bhattacharyya, L.-K. Leu, Spectral analysis of gravity and magnetic anomalies due to rectangular prismatic bodies. Geophysics **42**(1), 41–50 (1977)
5. R.J. Blakely, *Potential Theory in Gravity and Magnetic Applications* (Cambridge University Press, Cambridge, 1996)
6. N. Blom, C. Boehm, A. Fichtner, Synthetic inversions for density using seismic and gravity data. Geophys. J. Int. **209**(2), 1204–1220 (2017)
7. T.M. Brocher, Empirical relations between elastic wavespeeds and density in the earth's crust. Bull. Seismol. Soc. Am. **95**(6), 2081–2092 (2005)
8. G. Cohen, *Higher-Order Numerical Methods for Transient Wave Equations* (Springer, Berlin, 2012)
9. D. Colombo, D. Rovetta, Coupling strategies in multiparameter geophysical joint inversion. Geophys. J. Int. **215**(2), 1171–1184 (2018)

10. J.D. De Basabe, M.K. Sen, A comparison of finite-difference and spectral-element methods for elastic wave propagation in media with a fluid-solid interface. Geophys. J. Int. **200**(1), 278–298 (2015)
11. A. Fichtner, *Full Seismic Waveform Modelling and Inversion* (Springer, Berlin, 2010)
12. A. Fichtner, H.-P. Bunge, H. Igel, The adjoint method in seismology: I. Theory. Phys. Earth Planet. Interiors **157**(1–2), 86–104 (2006)
13. B. Frehner, Monumental geophysics: J. clarence karcher and the reflection method. Lead. Edge **40**(6), 404–407 (2021). https://doi.org/10.1190/tle40060404.1
14. L.A. Gallardo, M.A. Meju, Characterization of heterogeneous near-surface materials by joint 2D inversion of dc resistivity and seismic data. Geophys. Res. Lett. **30**(13), 1658–1661 (2003)
15. L.A. Gallardo, M.A. Meju, Joint two-dimensional dc resistivity and seismic travel time inversion with cross-gradients constraints. J. Geophys. Res. Solid Earth **109**(B3), B03311 (2004)
16. J. García-Abdeslem, The gravitational attraction of a right rectangular prism with density varying with depth following a cubic polynomial. Geophysics **70**(6), J39–J42 (2005)
17. G. Gardner, L. Gardner, A. Gregory, Formation velocity and density–the diagnostic basics for stratigraphic traps. Geophysics **39**(6), 770–780 (1974)
18. F.S. Grant, G.F. West, Interpretation theory in applied geophysics (New York: McGraw-Hill, 1965)
19. D.D. Jackson, Interpretation of inaccurate, insufficient and inconsistent data. Geophys. J. Int. **28**(2), 97–109 (1972)
20. L.R. Johnson, J.J. Litehiser, A method for computing the gravitational attraction of three-dimensional bodies in a spherical or ellipsoidal earth. J. Geophys. Res. **77**(35), 6999–7009 (1972)
21. K. Kelly, R. Ward, S. Treitel, R. Alford, Synthetic seismograms; a finite-difference approach. Geophysics **41**(1), 2–27 (1976)
22. D. Komatitsch, J. Tromp, Introduction to the spectral element method for three-dimensional seismic wave propagation. Geophys. J. Int. **139**(3), 806–822 (1999)
23. J.M. Lees, J. VanDecar, Seismic tomography constrained by bouguer gravity anomalies: applications in Western Washington. Pure Appl. Geophys. **135**(1), 31–52 (1991)
24. F.-C. Lin, B. Schmandt, V.C. Tsai, Joint inversion of rayleigh wave phase velocity and ellipticity using usarray: constraining velocity and density structure in the upper crust. Geophys. Res. Lett. **39**(12), L12303 (2012)
25. W. Lin, M. Zhdanov, Joint inversion of seismic and gravity gradiometry data using gramian constraints, in *SEG Technical Program Expanded Abstracts 2017* (Society of Exploration Geophysicists, Houston, 2017)
26. K.J. Marfurt, Accuracy of finite-difference and finite-element modeling of the scalar and elastic wave equations. Geophysics **49**(5), 533–549 (1984)
27. V. Menichetti, A. Guillen, Simultaneous interactive magnetic and gravity inversion. Geophys. Prospect. **31**(6), 929–944 (1983)
28. W. Menke, *Geophysical Data Analysis: Discrete Inverse Theory* (Academic Press, Cambridge, 2018)
29. D. Nagy, The gravitational attraction of a right rectangular prism. Geophysics **31**(2), 362–371 (1966)
30. J. Nocedal, S. Wright, *Numerical Optimization* (Springer, Berlin, 2006)
31. H. Paasche, J. Tronicke, Cooperative inversion of 2D geophysical data sets: a zonal approach based on fuzzy c-means cluster analysis. Geophysics **72**(3), A35–A39 (2007)
32. R.-E. Plessix, A review of the adjoint-state method for computing the gradient of a functional with geophysical applications. Geophys. J. Int. **167**(2), 495–503 (2006)
33. A. Romero, L.A. Gallardo, Borehole constrained inversion of geophysical data based on fuzzy clustering, in *SEG Technical Program Expanded Abstracts 2015* (Society of Exploration Geophysicists, Houston, 2015), pp. 1792–1796
34. L. Roy, M.K. Sen, K. McIntosh, P.L. Stoffa, Y. Nakamura, Joint inversion of first arrival seismic travel-time and gravity data. J. Geophys. Eng. **2**(3), 277 (2005)

35. M.K. Sen, P.L. Stoffa, *Global Optimization Methods in Geophysical Inversion* (Cambridge University Press, Cambridge, 2013)
36. R.U. Silva, J.D. De Basabe, M.K. Sen, M. Gonzalez-Escobar, E. Gomez-Trevino, S. Solorza-Calderon, Cooperative full waveform and gravimetric inversion. J. Seismic Exploration **29**(6), 549–573 (2020)
37. M. Talwani, Computation with the help of a digital computer of magnetic anomalies caused by bodies of arbitrary shape. Geophysics **30**(5), 797–817 (1965)
38. A. Tarantola, Inversion of seismic reflection data in the acoustic approximation. Geophysics **49**(8), 1259–1266 (1984)
39. A. Tarantola, A strategy for non linear inversion of seismic reflection data. Geophysics **51**(10), 1893–1903 (1986)
40. F. ten Kroode, S. Bergler, C. Corsten, J.W. de Maag, F. Strijbos, H. Tijhof, Broadband seismic data – the importance of low frequencies. Geophysics **78**(2), WA3–WA14 (2013). https://doi.org/10.1190/geo2012-0294.1
41. R. Tondi, U. Achauer, M. Landes, R. Daví, L. Besutiu, Unveiling seismic and density structure beneath the vrancea seismogenic zone, Romania. J. Geophys. Res. Solid Earth **114**(B11), B11307 (2009)
42. J. Tromp, C. Tape, Q. Liu, Seismic tomography, adjoint methods, time reversal and banana-doughnut kernels. Geophys. J. Int. **160**(1), 195–216 (2005)
43. J. Virieux, P-SV wave propagation in heterogeneous media: velocity-stress finite-difference method. Geophysics **51**(4), 889–901 (1986)
44. J. Virieux, S. Operto, An overview of full-waveform inversion in exploration geophysics. Geophysics **74**(6), WCC1–WCC26 (2009)
45. K. Vozoff, D. Jupp, Joint inversion of geophysical data. Geophys. J. Int. **42**(3), 977–991 (1975)
46. R.A. Werner, The gravitational potential of a homogeneous polyhedron or don't cut corners. Celestial Mech. Dyn. Astron. **59**(3), 253–278 (1994)
47. O. Yilmaz, *Seismic Data Analysis* (Society of Exploration Geophysicists, Houston, 2001). ISBN 978-1-56080-098-9. https://doi.org/10.1190/1.9781560801580
48. H. Zeyen, J. Pous, 3-D joint inversion of magnetic and gravimetric data with a priori information. Geophys. J. Int. **112**(2), 244–256 (1993)
49. M.S. Zhdanov, R. Ellis, S. Mukherjee, Three-dimensional regularized focusing inversion of gravity gradient tensor component data. Geophysics **69**(4), 925–937 (2004)

Modelling the 3D Electromagnetic Wave Equation: Negative Apparent Conductivities and Phase Changes

Beatriz Valdés-Moreno, Marco A. Pérez-Flores, and Jonás D. De Basabe

Abstract We often use electromagnetic methods in exploration geophysics to map the resistive structure of the subsurface using instruments that work at low induction numbers. These instruments are usually very portable and versatile, they can be used at the surface, mounted on an airplane or placed inside a wellbore. To process the data acquired with these methods, we need to be able to compute the electric and magnetic fields by numerically solving Maxwell's equations in the low induction-number domain. Previous studies have used the integral form of Maxwell's equations, however, these approaches only calculate an approximation of the apparent conductivity. In this chapter, we solved Maxwell's equations on the frequency domain using the finite-difference method with a staggered grid for the electric field and compute the apparent conductivities with post-processing. We show the results of four different examples, and consider sources on the ground, on the air, and in a wellbore. Negative apparent conductivities and phase changes are observed whenever there is a high conductivity contrasts, the induction-number is low and the source is a vertical magnetic dipole. With these conditions, there is a polarity reversal on the imaginary component of the magnetic field. Furthermore, the results indicate that it is crucial to consider the real component on the measurements, which has previously been ignored.

B. Valdés-Moreno · M. A. Pérez-Flores
Departamento de Geofísica Aplicada, División de Ciencias de la Tierra, CICESE, Ensenada, Mexico
e-mail: valdesb@cicese.edu.mx; mperez@cicese.mx

J. D. De Basabe (✉)
Departamento de Sismología, División de Ciencias de la Tierra, CICESE, Ensenada, Mexico
e-mail: jonas@cicese.mx

G. Hernández-Dueñas, M. A. Moreles (eds.), *Mathematical and Computational Models of Flows and Waves in Geophysics*, CIMAT Lectures in Mathematical Sciences, https://doi.org/10.1007/978-3-031-12007-7_6

1 Introduction

Measurements of electric and magnetic fields at various frequencies or times ranges are used in most electromagnetic soundings. These fields contain information of the underground conductivity variation. In particular, electromagnetic instruments at low induction numbers (LIN), sometimes called terrain conductivity meters, use magnetic field measurements to compute the apparent electrical conductivity (σ_a) on the ground. This measurement yields a complex average of the terrain conductivity over a specific depth range. On one hand, equipment operating at LIN offer many advantages, for example, it is easy and fast to take measurements, they do not require injecting current into the subsoil, and they can be used in highly resistive environments. On the other hand, targets must be superficial (less than 30 m deep). These methods have been successfully applied to archaeological studies [16, 23], groundwater characterization [19], contaminant migration [3], mineral alteration mapping [22], and have also been recently applied to explore sinkholes and water conduits on a calcareous platform in Yucatan, Mexico [15]. Nevertheless, these instruments have not been used in the air or inside a wellbore.

Numerical simulations are important tools to interpret the electromagnetic measurements. Maxwell's equations are generally solved to study the electromagnetic phenomenon and its interaction with the Earth. These equations can be solved using numerical methods, e.g., the integral equation (IEM)[2, 11], finite difference (FDM) [8, 13, 21], finite volume (FVM) [6, 26], or finite element (FEM) methods [5, 7, 12]. Often the integral expressions of Maxwell's equations at LIN are used to compute the apparent conductivity [11]. Wait [24] found that the solution of Maxwell's equations for a magnetic coil at low frequencies provided certain simplifications; hence he was the first to develop the LIN approximation. Subsequently, McNeill [9] used the LIN approximation to explain the operation principles of instruments such as EM31, EM34, and EM38 of *Geonics*. Méndez-Delgado et al. [11] presented an integral equation technique for modeling 3D bodies. Later Pérez-Flores et al. [14] applied the imaging technique to LIN data to solve the inverse problem using a weighting function. Recently Selepeng et al. [20] extended the research of Pérez-Flores et al. [14] by modeling real field data.

We compute the magnetic field solving the differential form of Maxwell's equations using the parsimonious finite-difference method. This approach is more accurate than the one based on the integral form with the LIN approximation [4]. The finite-difference method with a magnetic coil as a source has been previously used for airborne and ground EM [13, 17, 18]; however, they did not compute the apparent conductivity. We solve the 3D numerical problem and integrate the LIN conditions using the range of frequencies at which the transmitter coil of typical instruments operate. Furthermore, we compute the apparent conductivities following the approach of McNeill [9] for a homogeneous half-space. We find that the apparent conductivity can be negative when a high conductivity contrast is present.

2 Modeling Scheme

Maxwell's equations related the magnetic field $\boldsymbol{H}$ and the electric field $\boldsymbol{E}$. Assuming a time-dependence of $e^{i\omega t}$, these fields are given by

$$\nabla \times \boldsymbol{E}(\boldsymbol{r}) + i\omega\mu \boldsymbol{H}(\boldsymbol{r}) = 0 \tag{1}$$

and

$$\nabla \times \boldsymbol{H}(\boldsymbol{r}) - i\omega\varepsilon \boldsymbol{E}(\boldsymbol{r}) = \boldsymbol{J}(\boldsymbol{r}), \tag{2}$$

where $\boldsymbol{r}$ is the position vector, $\boldsymbol{J}(\boldsymbol{r})$ is the electric current density, $i^2 = -1$, and ω is the angular frequency. The magnetic permeability μ and the dielectric permittivity ε are assumed as constant and equal to the corresponding value for a vacuum ($\mu_0 = 4\pi \times 10^{-7}\,\mathrm{Hm}^{-1}$ and $\varepsilon_0 = 8.854 \times 10^{-12}\,\mathrm{Fm}^{-1}$). The electric current density $\boldsymbol{J}(\boldsymbol{r})$ can be divided into a source term $\boldsymbol{J_p}(\boldsymbol{r})$ and a conduction current $\boldsymbol{J_c}(\boldsymbol{r})$ as follows

$$\boldsymbol{J}(\boldsymbol{r}) = \boldsymbol{J_p}(\boldsymbol{r}) + \boldsymbol{J_c}(\boldsymbol{r}). \tag{3}$$

The conduction current is given by Ohm's law

$$\boldsymbol{J_c}(\boldsymbol{r}) = \sigma(\boldsymbol{r})\boldsymbol{E}(\boldsymbol{r}), \tag{4}$$

where $\sigma(\boldsymbol{r})$ is the electrical conductivity as a function of position. Under this consideration, Eq. (2) can be written as

$$\nabla \times \boldsymbol{H}(\boldsymbol{r}) - i\omega\varepsilon \boldsymbol{E}(\boldsymbol{r}) - \sigma(\boldsymbol{r})\boldsymbol{E}(\boldsymbol{r}) = \boldsymbol{J_p}(\boldsymbol{r}). \tag{5}$$

In problems involving the electromagnetic fields in the air, this equation can be problematic because these fields vary quickly near the source position. To avoid this issue, we followed the approach of Newman and Alumbaugh [13], in which the electric and magnetic fields are separated into primary and secondary fields. By primary fields we mean those induced by the source on a homogeneous space model and the secondary (or scattered) fields are those computed considering the heterogeneities in the model and using the primary fields as source. The secondary fields are more straightforward to simulate numerically than the total fields because they have a smoother spatial dependence on the source positions. Besides, using these fields, we can avoid convergence problems associated with the singularity at the source location. Maxwell's equations for the secondary fields are given by

$$\nabla \times \boldsymbol{E_s}(\boldsymbol{r}) + i\omega\mu \boldsymbol{H_s}(\boldsymbol{r}) = 0 \tag{6}$$

and

$$\nabla \times \boldsymbol{H_s}(\boldsymbol{r}) - i\omega\varepsilon \boldsymbol{E_s}(\boldsymbol{r}) - \sigma(\boldsymbol{r})\boldsymbol{E_s}(\boldsymbol{r}) = \boldsymbol{J_s}(\boldsymbol{r}), \tag{7}$$

where $\boldsymbol{H_s}(\boldsymbol{r})$ and $\boldsymbol{E_s}(\boldsymbol{r})$ are the secondary magnetic and electric fields respectively. We also define an equivalent source $\boldsymbol{J}_s$ given by

$$\boldsymbol{J}_s(\boldsymbol{r}) = (\sigma(\boldsymbol{r}) - \sigma_p(\boldsymbol{r}))\boldsymbol{E_p}(\boldsymbol{r}), \tag{8}$$

where $\boldsymbol{E_p}(\boldsymbol{r})$ is the primary electric field of a whole space and σ_p is the reference conductivity. Now, taking the curl of Eq. (6) and substituting into Eq. (7) we obtain

$$\nabla \times (\nabla \times \boldsymbol{E_s}(\boldsymbol{r})) + (i\omega\mu\sigma(\boldsymbol{r}) - \omega^2\mu\varepsilon)\boldsymbol{E_s}(\boldsymbol{r}) = -i\omega\mu \boldsymbol{J}_s(\boldsymbol{r}). \tag{9}$$

For Earth materials at frequencies less than 10^5 Hz the propagation term $\omega^2\mu\varepsilon$ can be neglected because it is many orders of magnitude smaller than the conduction term $\omega\mu\sigma(\boldsymbol{r})$. Therefore, Eq. (9) can be rewritten as

$$\begin{aligned} \nabla \times (\nabla \times \boldsymbol{E}_s(\boldsymbol{r})) + i\omega\mu\sigma(\boldsymbol{r})\boldsymbol{E}_s(\boldsymbol{r}) &= -i\omega\mu \boldsymbol{J}_s(\boldsymbol{r}), \qquad \forall\, r \in \Omega \\ \boldsymbol{E}_s(\boldsymbol{r}) &= 0, \qquad \forall\, r \in \partial\Omega \end{aligned} \tag{10}$$

where Ω is the domain and $\partial\Omega$ is the boundary of Ω. Finally, the total electric and magnetic fields are obtained by

$$\boldsymbol{E}(\boldsymbol{r}) = \boldsymbol{E_p}(\boldsymbol{r}) + \boldsymbol{E_s}(\boldsymbol{r}) \tag{11}$$

and

$$\boldsymbol{H}(\boldsymbol{r}) = \boldsymbol{H_p}(\boldsymbol{r}) + \boldsymbol{H_s}(\boldsymbol{r}). \tag{12}$$

We solve Eq. (10) using FDM on a regular staggered grid (see Fig. 1 and Appendix 1; [27]). After discretizing the vector Helmholtz equation, we obtain a system of linear equations given by

$$\boldsymbol{A}\boldsymbol{u} = \boldsymbol{b}, \tag{13}$$

where $\boldsymbol{A}$ is a square matrix of dimension $(3N)^2$, $N = N_x \times N_y \times N_z$, and N_x, N_y and N_z are the numbers of nodes in the x, y, and z directions respectively; $\boldsymbol{u}$ is the unknowns vector of the secondary electric field of dimension $3N$, and $\boldsymbol{b}$ is the source vector with dimension $3N$. The matrix $\boldsymbol{A}$ is complex valued and sparse with up to 13 nonzero elements per row.

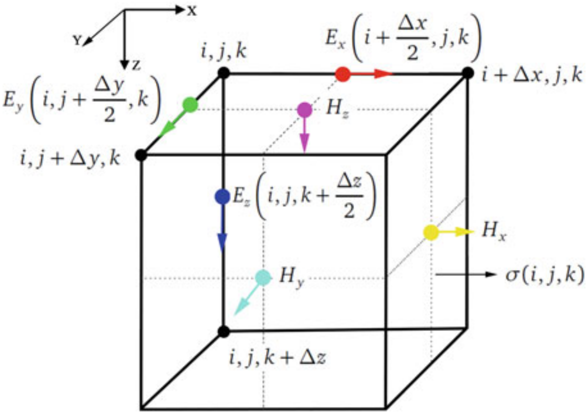

Fig. 1 Yee's scheme defines the positions of electric and magnetic components. The electric field is assigned to the edges of the cell and the magnetic field is assigned to the cell faces. The cell conductivity is $\sigma(i, j, k)$

After computing the secondary electric field, we use Faraday's law (Eq. (1)) to obtain the secondary magnetic fields using an explicit scheme of central finite differences (see Appendix 2). Finally, in order to obtain the total electric and magnetic fields, the primary and the secondary fields are added.

3 Apparent Conductivities at LIN

We consider a data-acquisition setup involving two co-planar coils either as vertical magnetic dipoles (VMD) or horizontal magnetic dipoles (HMD) separated by an offset s (Fig. 2). The induction number is given by the ratio

$$B = \frac{s}{\delta}, \tag{14}$$

where δ is the skin depth, defined as the distance a wave must travel before its amplitude decays by a factor of $1/e$, and is given by

$$\delta = \sqrt{\frac{2}{\omega\mu\sigma}}. \tag{15}$$

Therefore, the induction number can be rewritten as

$$B = s\sqrt{\pi f \mu\sigma}, \tag{16}$$

where f is the frequency of the source, and it is related to the angular frequency by $\omega = 2\pi f$. McNeill [9] obtained an expression to compute the ratio between the

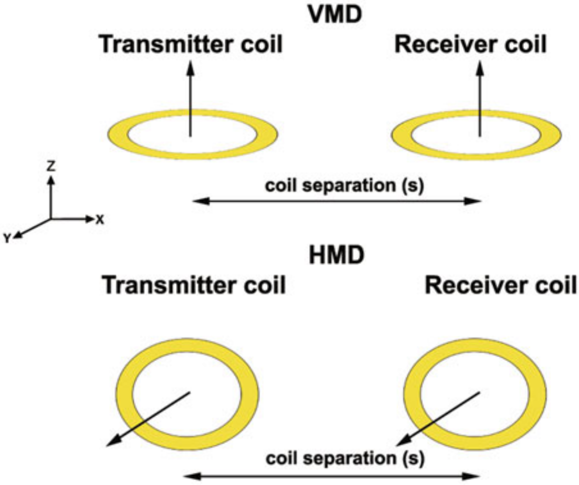

Fig. 2 General coil configurations. The transmitter and receiver coils are separated by a certain distance s. In VMD both coils lie flat on the ground and in HMD both coils are upright and coplanar

total magnetic and the primary magnetic fields at LIN, given by

$$\frac{H}{H_p} = \frac{H_p + H_s}{H_p} = 1 + i\frac{\omega\mu\sigma s^2}{4}, \tag{17}$$

where H is the total magnetic field obtained by adding the primary and secondary magnetic fields, and H_p is the primary magnetic field generated by a VMD or HMD.

Figure 3 shows that, when the induction numbers are less than 1 (LIN restriction), the imaginary part of the ratio between the total magnetic field and the primary magnetic field is related to the ground conductivity and linear with respect to B, and the real part remains stable and equal to 1. Nevertheless, when $B > 1$, the behavior of the real and imaginary parts of the ratio H/H_p are not linear.

To get the apparent conductivity using the LIN approach, we need the ratio between the secondary and primary magnetic fields, which corresponds to the imaginary part of H/H_p, whereas the real part of this ratio is neglected. Then, the apparent conductivity is proportional to the ratio between the secondary and primary magnetic fields [9] as follows

$$\sigma_a = \frac{4}{\omega\mu s^2}\left(\frac{H_s}{H_p}\right). \tag{18}$$

This approach is based on the assumptions that the induction number is small ($B < 1$) and that the instrument operates at zero elevation over a homogeneous half-space [9].

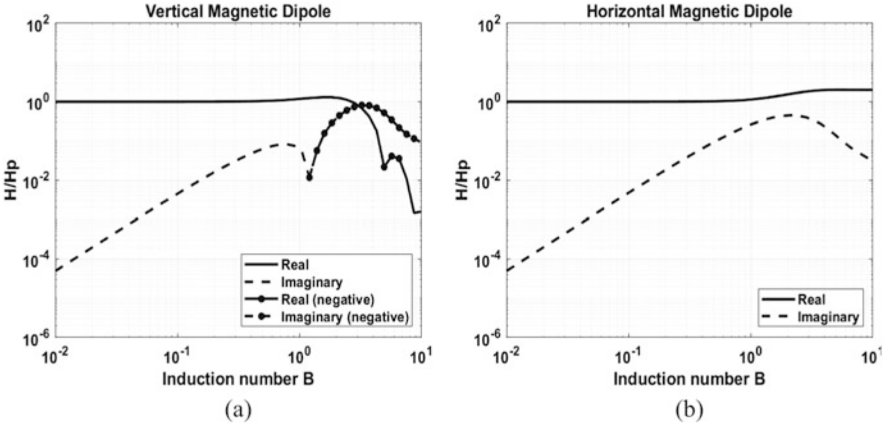

(a) (b)

Fig. 3 Induction numbers and real and imaginary part of H/H_p. (**a**) Real and imaginary part using a VMD. (**b**) Real and imaginary part using a HMD

4 Code Validation

The finite-difference code was developed in Fortran and parallelized with OpenMP. Despite restrictions at LIN, we keep a general implementation; therefore, we can use low and high inductions numbers and modify the position of transmitters and receivers.

It was compiled and executed in a computer with 20 cores (2.5 GHz) and 128 GB of RAM (the source code is available upon request). The system of equations is solved using the PARDISO 5.0 function from Intel's MKL.[1] In order to validate the implementation, we use the analytic solution for a half-space [25] using Anderson's filter [1] to solve the Hankel transform. Following [13], we considered $\sigma = 0.01\,\mathrm{Sm}^{-1}$ for the half-space model with two sources (VMD or HMD) operating at 30 kHz and located at 20 m, above the surface. The receivers have 5 m of separation between each one and they are at the same height as the source. The dimensions of our numerical model are $400 \times 400 \times 400$ m and is discretized with a finite-difference mesh of 512,000 cells using spatial increment of 5 m (Fig. 4), including air and Earth.

Figure 5 shows the vertical magnetic field (H_z) over a half-space for VMD and HMD. To evaluate the accuracy of the numerical modeling, the root mean square errors (RMSE) were calculated by

$$\mathrm{RMSE} = \sqrt{\frac{1}{N}\sum_{n=1}^{N} x_n^2} \tag{19}$$

---

[1] https://software.intel.com/content/www/us/en/develop/articles/pardiso-parameter-table.html.

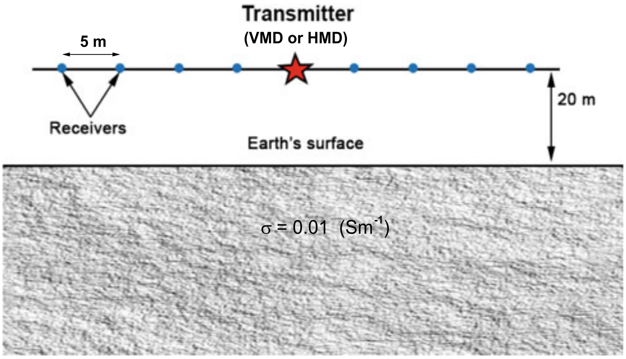

Fig. 4 Conductivity model for the validation example, it includes Earth and air. The transmitter coil operates at 30 kHz and it is located at 20 m above the surface; receivers are at the same height, 5 m from each other. The Earth conductivity is $\sigma = 0.01\ \mathrm{Sm}^{-1}$

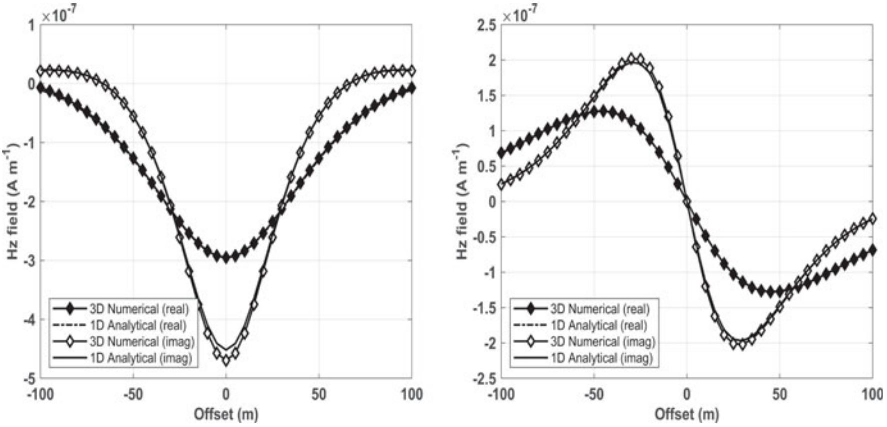

(a) (b)

Fig. 5 Comparison of the analytical (1D) and numerical (3D) vertical magnetic fields (real and imaginary parts) for the conductivity model. (**a**) Comparison of H_z for VMD. (**b**) Comparison of H_z for HMD

where $N = 41$ is the number of data points and x_n is the difference between the analytical and numerical solution at the n-th receiver.

The RMSE of the vertical magnetic field in the VMD case are $1.09 \times 10^{-8}\ \mathrm{A\,m}^{-1}$ (real part) and $5.85 \times 10^{-9}\ \mathrm{A\,m}^{-1}$ (imaginary part), and for the HMD case are $3.25 \times 10^{-9}\ \mathrm{A\,m}^{-1}$ (real part) and $2.73 \times 10^{-9}\ \mathrm{A\,m}^{-1}$ (imaginary part). The discrepancies are very small and therefore we conclude that the implementation of the 3D forward modeling method yields accurate results.

Table 1 Frequency, offset and induction number for *Geonics* conductivity meters

Equipment	Frequency (kHz)	Offset (m)	Induction number $\sigma = 0.01\ \mathrm{Sm}^{-1}$
EM34	6.4	10	0.1590
	1.6	20	
	0.4	40	
EM31	9.8	3.66	0.0720
EM38	14.6	1	0.0240

5 Applications

In this research, we simulated four electromagnetic scenarios with three-dimensional conductivity models where the EM instruments at LIN can be used: on the ground, in the air, and within a wellbore. For the examples on the ground we use the frequencies and offsets of the *Geonics* equipment (see Table 1). For the air and wellbore examples we use realistic frequencies. The conductivity model uses 80 nodes in each direction, thus requiring a solution of 1,536,000 equations. The cell size is modified according to the depth of exploration in a homogeneous half-space depending on frequency, transmitter-receiver distance, dipole orientation and ground conductivity [9].

5.1 *Sinkhole Model*

This examples' conductivity models consist of a 3D sinkhole within a resistive half-space; each sinkhole contains only air, water, seawater and a layered model, as shown in Fig. 6. The sinkhole was discretized in a parallelepiped measuring 50 m in the x- and y-directions and 27 m in z-direction.

We computed the response at 6400 Hz and 10 m offset using HMD and VMD; we show in Fig. 7 the profiles for all the models. The highest responses correspond to model A3 since the highest conductivity contrast is between limestone and seawater. Notice that this conductivity contrast does not represent a limitation of the finite difference method for geophysical applications because the cell's size are small compared to the target's size.

On the other hand, VMD detects better the lateral conductivity contrast, as shown in Fig. 7. We observed in the A3 profile an increase in σ_a before the contact, subsequently σ_a decreases up to the contact location and finally increases again until it reaches the maximum value. On the other hand, we cannot distinguish in the HMD profile the location of the lateral edges (Fig. 7).

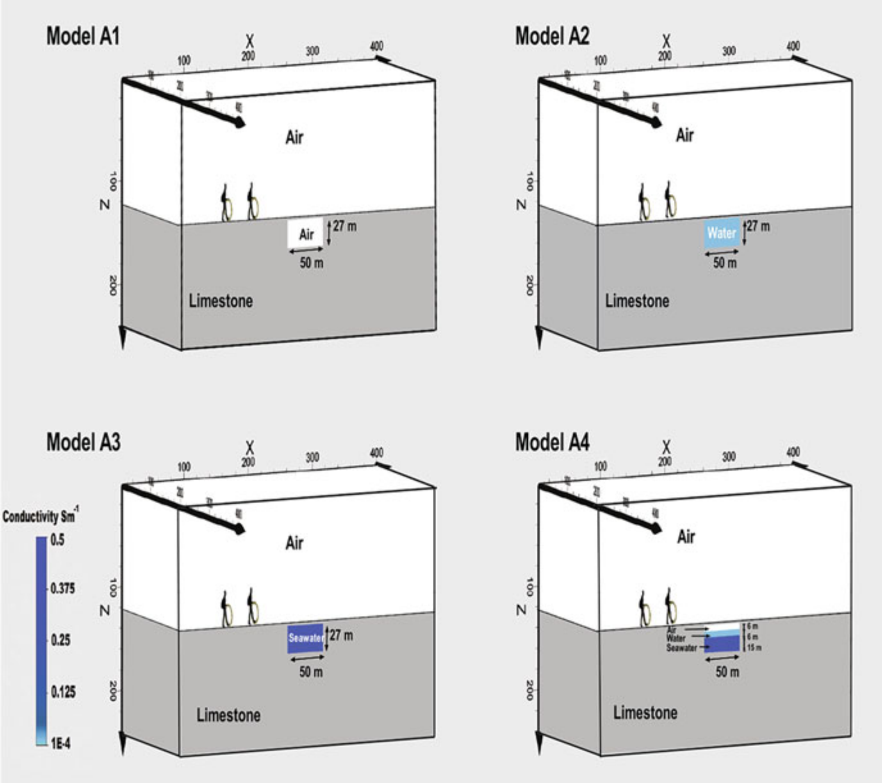

Fig. 6 Conductivity models for the sinkhole example. Sinkholes are located at 3 m depth within a resistive half-space ($\sigma = 1 \times 10^{-4}\,\mathrm{Sm}^{-1}$). (A1) Air sinkhole ($\sigma = 0\,\mathrm{Sm}^{-1}$). (A2) Water sinkhole ($\sigma = 0.0125\,\mathrm{Sm}^{-1}$). (A3) Seawater sinkhole ($\sigma = 0.5\,\mathrm{Sm}^{-1}$). (A4) A layered model with air, water and seawater

5.2 *Two Nearby Sinkholes*

With this experiment, we show that it is challenging to distinguish buried conductive bodies if they are very close to each other because the anomalies can be misinterpreted. The experiment consists of two sinkholes that are separated from each other by a specific variable distance (Fig. 8). Each sinkhole contains air ($\sigma = 0\,\mathrm{Sm}^{-1}$), water ($\sigma = 0.0125\,\mathrm{Sm}^{-1}$), seawater ($\sigma = 0.5\,\mathrm{Sm}^{-1}$), a water invasion ($\sigma = 0.005\,\mathrm{Sm}^{-1}$) and a seawater invasion ($\sigma = 0.05\,\mathrm{Sm}^{-1}$) within a limestone half-space ($\sigma = 1 \times 10^{-4}\,\mathrm{Sm}^{-1}$).

Figure 9 shows the apparent-conductivity responses over the ground for the models in Fig. 8 using VMD and HMD. The VMD responses at 10 m (6400 Hz) and 40 m (400 Hz) offsets show a relevant difference between models B1 and B2. In models B3 and B4 we notice changes due to the resistive zone at the center of the array for both frequencies or offsets. The HMD responses have similar behaviors at

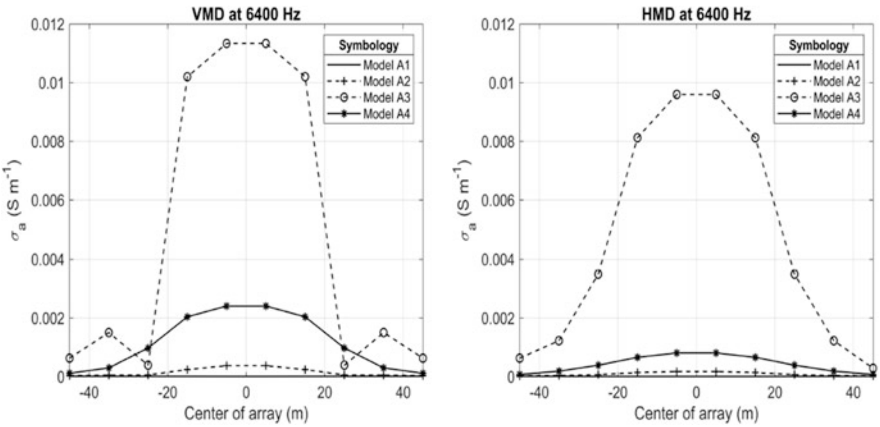

Fig. 7 Numerical response of four conductivity models at 6400 Hz. (Left) VMD apparent conductivity. (Right) HMD apparent conductivity

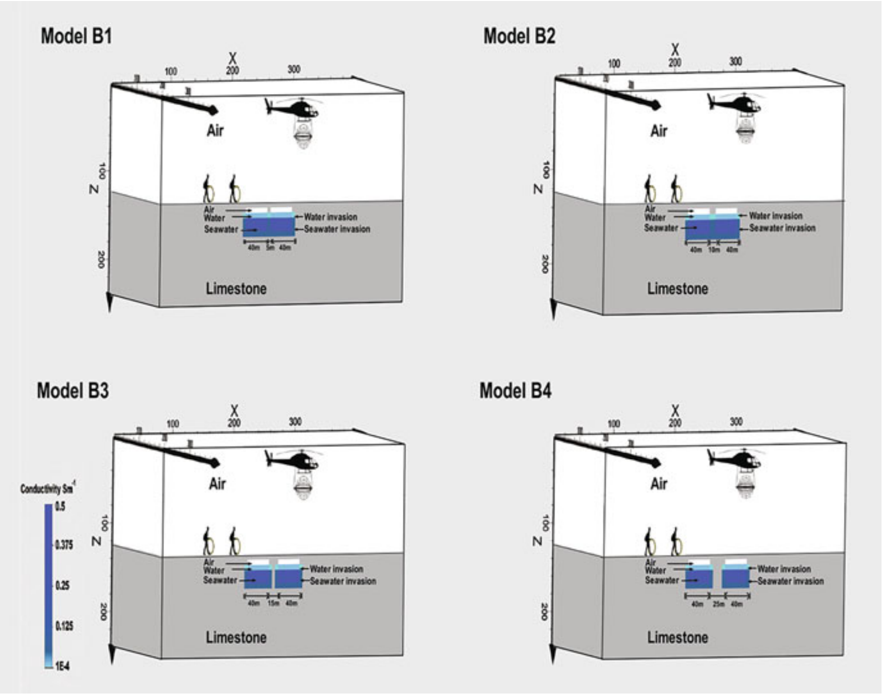

Fig. 8 Conductivity model of two sinkholes at different separations. (B1) 5 m separation joined by an invaded zone. (B2) 10 m separation joined by an invaded zone. (B3) 15 m separation of which 5 comprise the resistive zone. (B4) 25 m separation of which 15 comprise the resistive zone

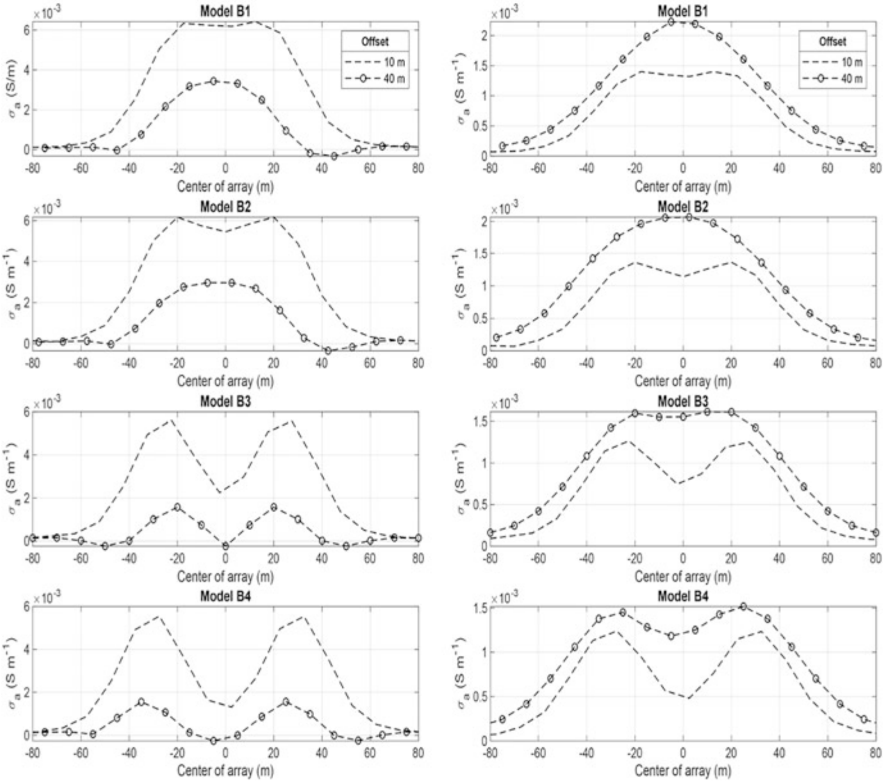

Fig. 9 Apparent conductivities for the models in Fig. 8 using 10 m offset (at 6400 Hz) and 40 m offset (at 400 Hz). (Left) VMD responses and (right) HMD responses

40 m offset for models B1, B2 and B3; Moreover, at 10 m offset, all models showed significant differences. On the other hand, using VMD with a 40 m offset, some negative apparent conductivities are observed in all models in the sudden changes in conductivity, such as in the limit between the half-space and the sinkholes.

Figure 10 shows the apparent-conductivity response in the air at 40 m above the surface. We used VMD and HMD at 12.8, 20, 30 and 40 kHz with a 10 m offset for all frequencies; the receptor coil is located at the same height as the transmitter coil. Generally, as the frequency increases, the response in both configurations decreases and the apparent-conductivity plot looks flatter; in particular, VMD provides a higher response for all frequencies. Notice that the only case in which the anomaly allows us to distinguish two distinct bodies is in the model B4 with VMD and 12.8 kHz. In models B1, B2, and B3 with both configurations, the higher response corresponds to the center of the array, meaning that we cannot distinguish two sinkholes with aero-electromagnetic methods. Pérez-Flores et al. [15] observe that there is no significant difference between the sinkhole and the bedrock. According to our results, this happens because there is an intrusion of water in the bedrock that

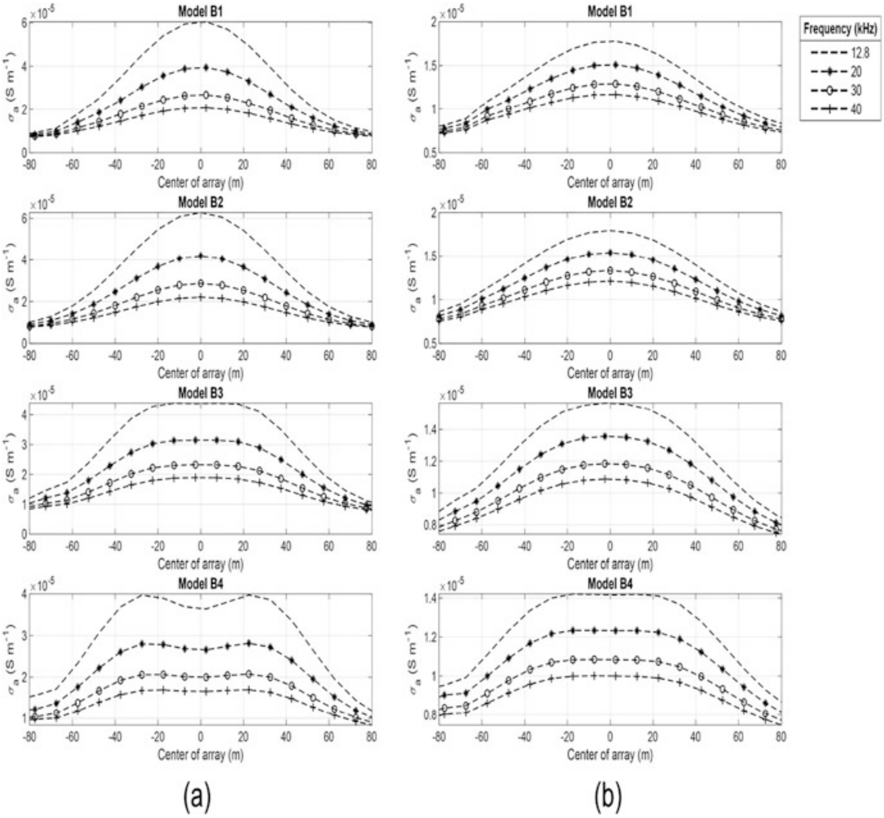

Fig. 10 Apparent conductivities for the models in Fig. 8 computed at 40 m above the surface at 12.8, 20, 30 and 40 kHz with 10 m offset. (**a**) VMD responses and (**b**) HMD responses

does not allow to differentiate the sinkhole and the bedrock due to a low conductivity contrast.

5.3 *Layered Conductivity Model with a Wellbore*

For this example we use a layered conductivity model with a wellbore (Fig. 11). It contains a conductive layer ($\sigma = 0.5\,\text{Sm}^{-1}$) within a resistive half-space ($\sigma = 1\times10^{-4}\,\text{Sm}^{-1}$) We use a VMD configuration with the receiver and transmitter along the wellbore, the transmitter operates at 20 kHz and it is located over the receptor coil in a collinear array with 1 m and 2 m offsets.

We compute σ_a for the three models shown in Fig. 11 and observe larger responses with 1 m offset for models C1 and C3 (see Fig. 12). In C2, the apparent conductivity converges to the half-space conductivity for both offsets; however,

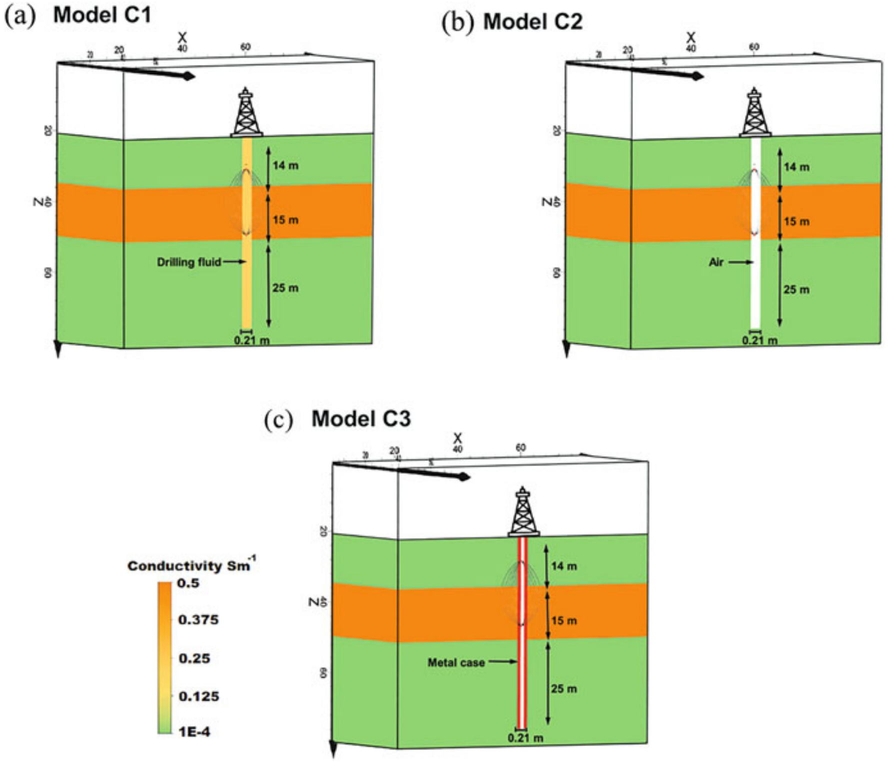

Fig. 11 Layered conductivity model with a wellbore: (**a**) C1 is filled with water-based drilling fluid ($\sigma = 0.2\,\mathrm{Sm}^{-1}$); (**b**) C2 is dry (only air) ($\sigma = 0\,\mathrm{Sm}^{-1}$) and (**c**) C3 is a metal cased hole with $\sigma = 30\,\mathrm{Sm}^{-1}$ and, for modeling purposes, a metal thickness of 0.07 m

in models C1 and C3, the half-space apparent conductivity for both offsets do not converge because the drilling fluid and the metal case conductivities are very different to the conductivity of the surrounding layered earth. Furthermore, we obtain negative apparent conductivity values for all models.

We further compare the response in model C3 at different frequencies (see Fig. 13). Notice that we can distinguish the conductive layer in spite of the metal case. When we compare the responses at 12.8, 6.4, 1.6 and 0.4 kHz, we obtain the same response for all the frequencies; however, we obtain a higher response at 1 m offset than at 2 m. Frequencies 1.6 and 0.4 kHz are under LIN conditions for both offsets.

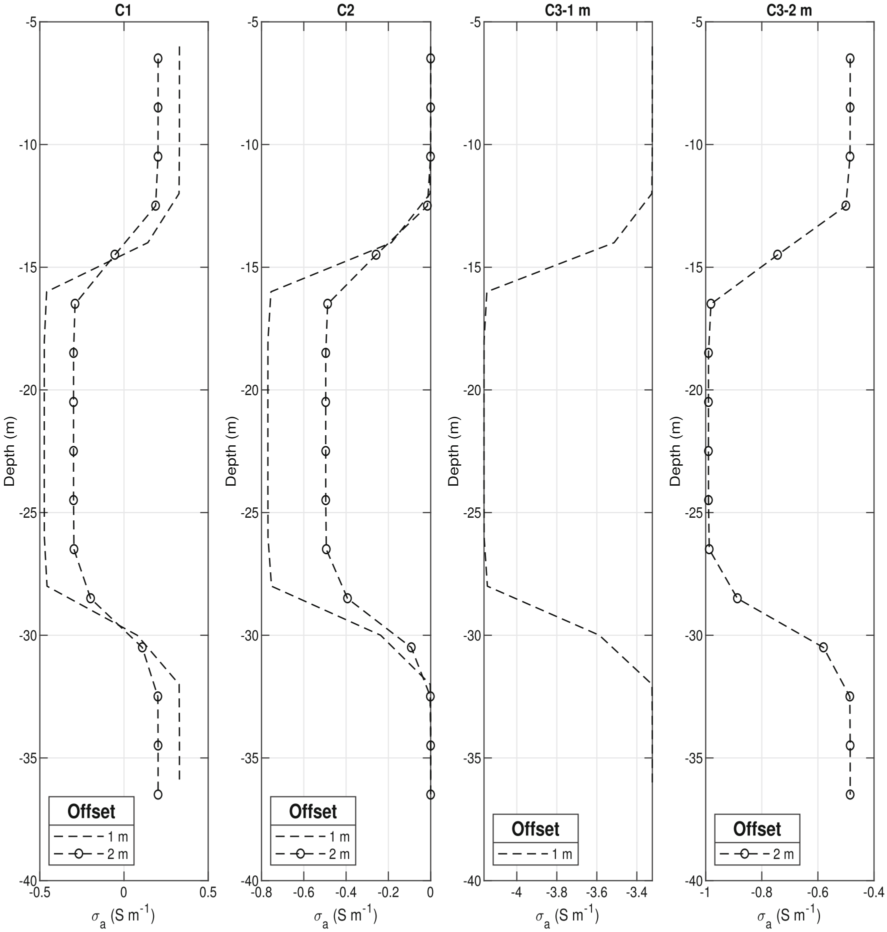

Fig. 12 Apparent conductivities in the wellbore models at 20 kHz with a 1 and 2 m offsets

5.4 Vertical-Contact Model

The final example is a model consisting of a vertical contact between a resistive and a conductive zone. We keep fixed the conductivity in the resistive zone ($\sigma = 0.0001\,\mathrm{S m^{-1}}$) and let it vary in the conductive zone from 10^1 to 10^3 times more conductive than in the resistive zone (Fig. 14). We show in Table 2 the induction numbers for each conductivity in the conductive zone.

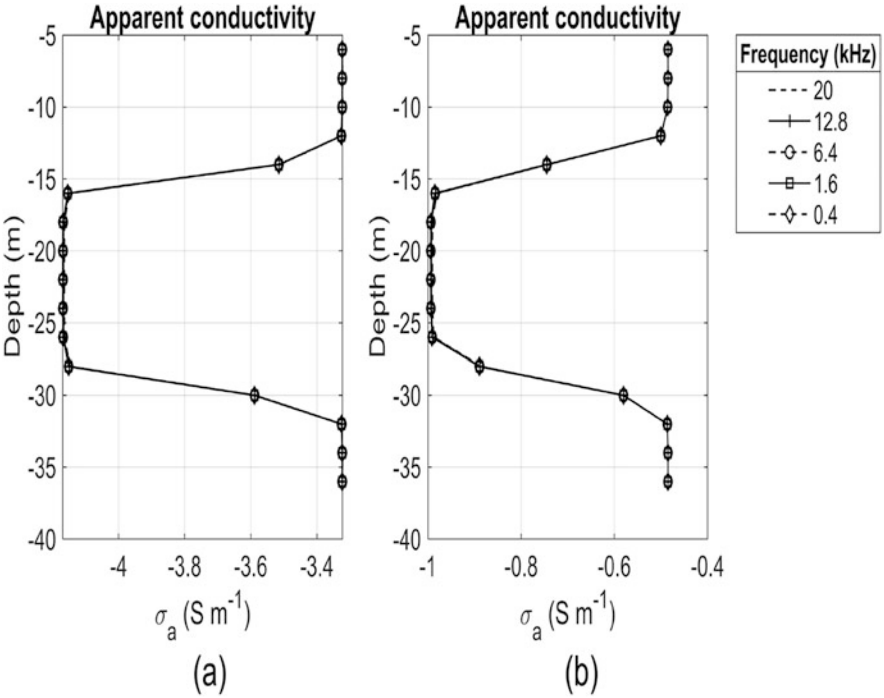

Fig. 13 Apparent conductivities computed using the model C3 and different offsets. Numerical response at 20, 12.8, 6.4, 1.6 and 0.4 kHz. (**a**) 1 m offset and (**b**) 2 m offset

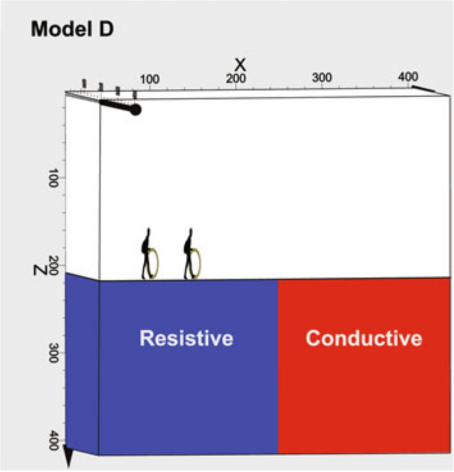

Fig. 14 Conductivity model of a vertical contact. The blue zone represents the resistive zone and the red one the conductive zone

Table 2 Induction numbers (B) for each conductivity in the vertical contact model

σ (Sm^{-1})	B
0.001	0.0503
0.01	0.1590
0.1	0.5027

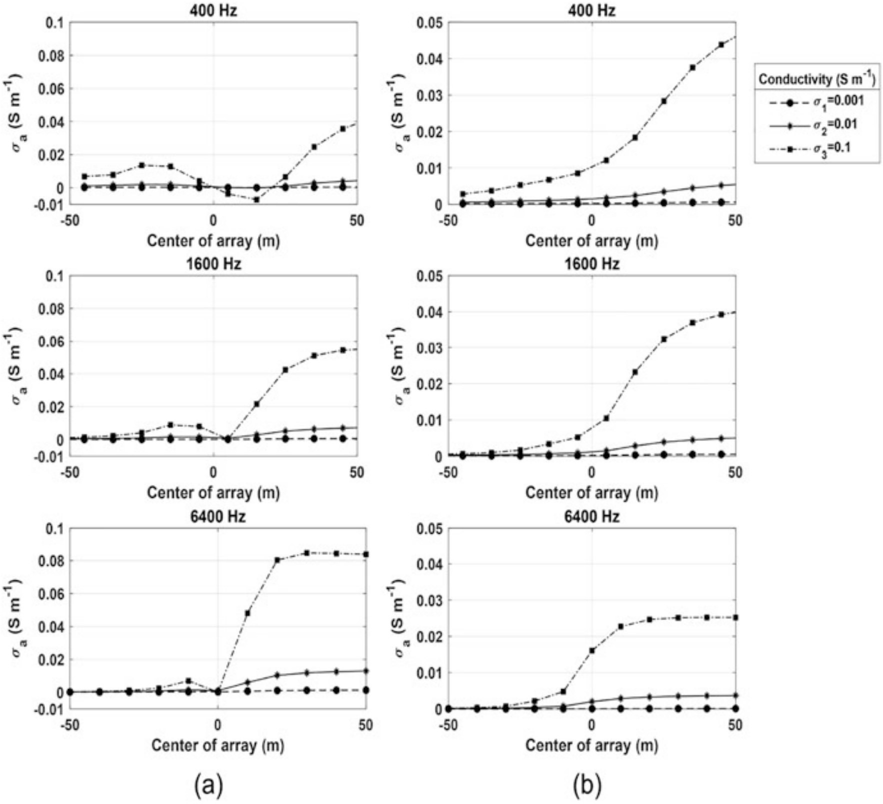

(a) (b)

Fig. 15 Apparent conductivities for the vertical-contact model using 400, 1600 and 6400 Hz (40, 20 and 10 m offsets respectively). (**a**) VMD response at the surface. (**b**) HMD response at the surface

Figure 15 shows the apparent conductivity responses for the models using VMD and HMV at the surface ($z = 0$) varying the offset and frequency. We obtain negative apparent conductivities using VMD and a high conductivity contrast, as shown in Fig. 15a. For 400 Hz (40 m offset), we obtained negative σ_a values between $x = 0$ m and $x = 20$ m. We do not observe a negative σ_a using HMD; however, we observe an obvious change in the apparent conductivity produced by the conductivity contrast. Within the LIN domain, the highest conductivity contrast generates a larger anomaly. According to Eq. (18), the secondary magnetic field changes sign in the vertical contact, meaning that the secondary magnetic field

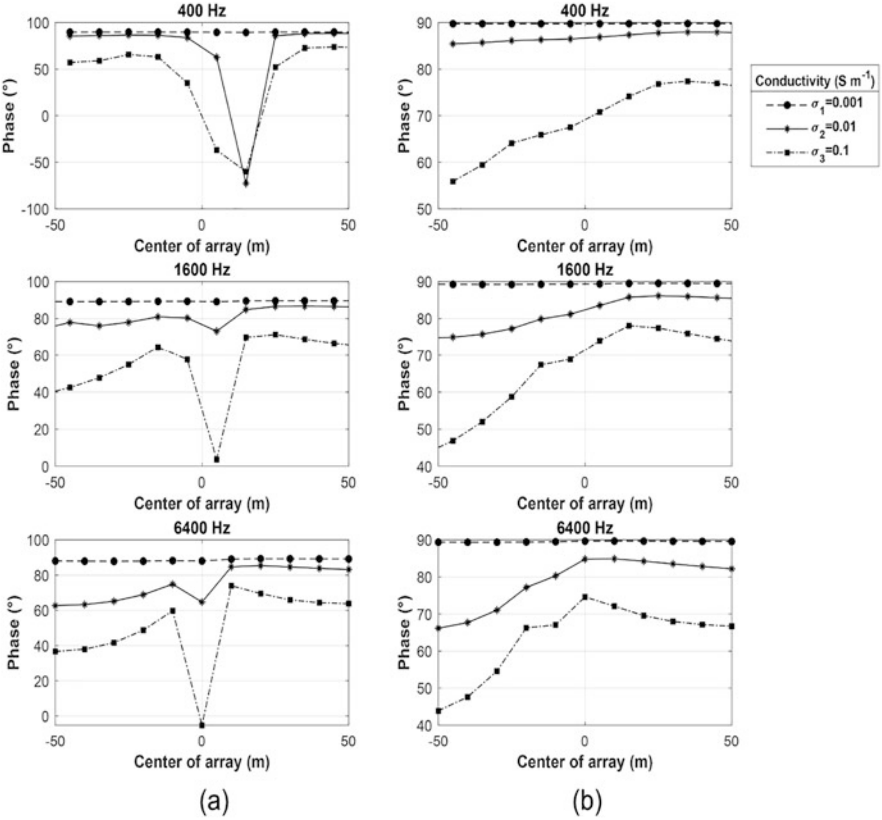

Fig. 16 Phases for the vertical-contact model at 400, 1600 and 6400 Hz (40, 20 and 10 m offsets respectively). (**a**) VMD response at the surface. (**b**) HMD response at the surface

vector is in the opposite direction of the primary magnetic field, just where the high-conductivity contrast is present.

Recall that only the imaginary part of the secondary and primary magnetic fields ratio is used to compute LIN's apparent conductivity. We consider that the real part of the secondary magnetic field is zero, and therefore the phase of the secondary magnetic field is 90°. We analyzed the secondary magnetic field for models in Fig. 14 and computed phases for each model (Fig. 16). Phases are stable and equal to 90° when using σ_1 for both dipole configurations and for all frequencies. Phases with σ_2 shows a large phase change near the vertical contact although it indicates a change to a negative phase at 400 Hz using VMD but towards the ends of the model it remains stable. At 1600 and 6400 Hz the phases show a slight change close to the vertical contact. When we used an HMD, the phases do not exhibit abrupt changes in the contact. The phases using VMD with σ_3 show notable phase changes close to the vertical contact, and in the anomalies at 6400 and 400 Hz exist a change of the phase sign. In the resistive zone, phases increase up to the conductive zone in all frequencies, when employing HMD.

This last experiment shows that, although we are in the LIN domain, the secondary magnetic field's real part is non-zero in the vertical contact when the conductivity contrast is large. If we consider the real part of Eq. (18), the apparent conductivities become fully complex and consequently, it is necessary to reformulate McNeill's equation.

6 Discussion

Electromagnetic equipment at LIN can be used for several applications. Our experiments show that VMD allows us to obtain a better resolution of superficial conductive structures. Furthermore, the effective exploration depth of VMD is higher than that of HMD [9]. Unlike other electromagnetic methods in which the penetration depth depends on the frequency and the medium conductivity, at low induction numbers this depth of exploration depends on: (1) the separation between the source and the receiver and (2) The dipole configuration. However, LIN conditions require using the instruments in a low-conductivity terrain, and we cannot always satisfy this. We need to exercise caution when making qualitative interpretations outside the LIN domain because the secondary magnetic field's imaginary part is not linear with respect to electrical conductivity.

In the literature, several authors have reported negative apparent conductivities. McNeill [10] was the first to report this negative response. He indicated that a vertical dike (with $\sigma = 1\,\mathrm{Sm}^{-1}$) produced a negative response of σ_a using VMD at 1600 Hz. Subsequently, Méndez-Delgado et al. [11] observed that using a VMD and if the receiver-transmitter distances are larger than the thickness of the conductor can yield a negative σ_a. Pérez-Flores et al. [14] used the integral form of Maxwell's equations approximation at LIN and found that the weighting functions they used in shallow conductors with both coil configurations can produce negative σ_a.

We found that VMD can produce negative σ_a values under certain circumstances as some transmitter-receiver distances and high-conductivity contrast. We observed that, if the conductivity contrast between two mediums differs by at least two orders of magnitude, it can produce a phase change even when both conductivities are within the LIN domain.

Namely, we observed that the phase of the secondary magnetic field is significantly different than 90° or 270°. Therefore, the secondary magnetic field's real part, previously neglected, should be considered for the apparent-conductivity analysis.

7 Conclusions

We have computed apparent conductivities for 3D bodies by solving Maxwell's equations numerically in the frequency domain, using the finite differences method with a staggered grid. We compared our results with an analytical solution for a homogeneous and isotropic half-space to validate the magnetic field's numerical solution. We used the parameters for low induction numbers standard equipment and the VMD and HMD modes of operation.

Using VMD can disclose the conductor's edge location and yields a significant larger response than HMD. Nevertheless, we cannot distinguish between two or more conductive bodies if they are very close. The qualitative interpretation in this case can be misleading because we obtained only one anomaly. Furthermore, this problem increases when using the equipment in the air.

We have also simulated an electromagnetic device running inside a wellbore. We observed that the wellbore filled with drilling fluid and the cased hole produced different σ_a values in the resistive zone for each offset. Surprisingly, the wellbore with a metal case showed measurable changes of σ_a in the conductive layer.

The response of a vertical contact between the resistive and conductive zones showed that; (1) Using both configurations, σ_a values increase before the contact for all conductivity models; (2) Using VMD at 400 Hz, we obtained negative apparent conductivities near the contact with the highest conductivity zone ($\sigma = 0.1\,\mathrm{Sm}^{-1}$). This anomaly reveals that the secondary magnetic field goes in the opposite direction of the primary magnetic field. Additionally, both coil configurations yield stable phases in minor conductivity contrasts, i.e., between the resistive zone $\sigma = 0.0001\,\mathrm{Sm}^{-1}$ and the conductive zone with $\sigma = 0.001\,\mathrm{Sm}^{-1}$.

We noted that the phase values change swiftly when the conductivity contrast increases, even under LIN conditions. Furthermore, we found a meaningful phase change at all frequencies near the vertical contact with the highest conductivity contrast with $\sigma = 0.1\,\mathrm{Sm}^{-1}$; We also observed the highest phase change at 10 m from the vertical contact when we used VMD at 400 Hz. Accordingly, we need a fully complex equation when computing the apparent conductivity in VMD on mediums with high conductivity contrast.

Acknowledgments We want to thank CONACYT for the scholarship and CeMIEGeo for their financial support. The numerical computations were performed using the cluster Lamb of the supercomputing lab at the Specialized Labs System of the Earth Sciences Division of CICESE.

Appendix 1

Equation (10) was discretized using an scheme of central finite differences into a regular grid. The secondary electric field is computed using the following finite difference equations

$$
\begin{aligned}
&\frac{1}{\Delta x\,\Delta y}\left(E^{sy}_{i+1,j+\frac{1}{2},k} - E^{sy}_{i+1,j-\frac{1}{2},k} - E^{sy}_{i,j+\frac{1}{2},k} + E^{sy}_{i,j-\frac{1}{2},k}\right)\\
&- \frac{1}{\Delta y^2}\left(E^{sx}_{i+\frac{1}{2},j+1,k} - 2E^{sx}_{i+\frac{1}{2},j,k} + E^{sx}_{i+\frac{1}{2},j-1,k}\right)\\
&- \frac{1}{\Delta z^2}\left(E^{sx}_{i+\frac{1}{2},j,k+1} - 2E^{sx}_{i+\frac{1}{2},j,k} + E^{sx}_{i+\frac{1}{2},j,k-1}\right)\\
&+ \frac{1}{\Delta x\,\Delta z}\left(E^{sz}_{i+1,j,k+\frac{1}{2}} - E^{sz}_{i+1,j,k-\frac{1}{2}} - E^{sz}_{i,j,k+\frac{1}{2}} + E^{sz}_{i,j,k-\frac{1}{2}}\right)\\
&+ i\omega\mu\sigma_{i+\frac{1}{2},j,k}E^{sx}_{i+\frac{1}{2},j,k} = -i\omega\mu\left(\sigma_{i+\frac{1}{2},j,k} - \sigma^{p}_{i+\frac{1}{2},j,k}\right)E^{px}_{i+\frac{1}{2},j,k},
\end{aligned}
\tag{20}
$$

$$
\begin{aligned}
&\frac{1}{\Delta y\,\Delta z}\left(E^{sz}_{i,j+1,k+\frac{1}{2}} - E^{sz}_{i,j+1,k-\frac{1}{2}} - E^{sz}_{i,j,k+\frac{1}{2}} + E^{sz}_{i,j,k-\frac{1}{2}}\right)\\
&- \frac{1}{\Delta z^2}\left(E^{sy}_{i,j+\frac{1}{2},k+1} - 2E^{sy}_{i,j+\frac{1}{2},k} + E^{sy}_{i,j+\frac{1}{2},k-1}\right)\\
&- \frac{1}{\Delta x^2}\left(E^{sy}_{i+1,j+\frac{1}{2},k} - 2E^{sy}_{i,j+\frac{1}{2},k} + E^{sy}_{i-1,j+\frac{1}{2},k}\right)\\
&+ \frac{1}{\Delta x\,\Delta y}\left(E^{sx}_{i+\frac{1}{2},j+1,k} - E^{sx}_{i+\frac{1}{2},j,k} - E^{sx}_{i-\frac{1}{2},j+1,k} + E^{sx}_{i-\frac{1}{2},j,k}\right)\\
&+ i\omega\mu\sigma_{i,j+\frac{1}{2},k}E^{sy}_{i,j+\frac{1}{2},k} = -i\omega\mu\left(\sigma_{i,j+\frac{1}{2},k} - \sigma^{p}_{i,j+\frac{1}{2},k}\right)E^{py}_{i,j+\frac{1}{2},k}
\end{aligned}
\tag{21}
$$

and

$$
\begin{aligned}
&\frac{1}{\Delta x\,\Delta z}\left(E^{sx}_{i+\frac{1}{2},j,k+1} - E^{sx}_{i+\frac{1}{2},j,k} - E^{sx}_{i-\frac{1}{2},j,k+1} + E^{sx}_{i-\frac{1}{2},j,k}\right)\\
&- \frac{1}{\Delta x^2}\left(E^{sz}_{i+1,j,k+\frac{1}{2}} - 2E^{sz}_{i,j,k+\frac{1}{2}} + E^{sz}_{i-1,j,k+\frac{1}{2}}\right)\\
&- \frac{1}{\Delta y^2}\left(E^{sz}_{i,j+1,k+\frac{1}{2}} - 2E^{sz}_{i,j,k+\frac{1}{2}} + E^{sz}_{i,j-1,k+\frac{1}{2}}\right)\\
&+ \frac{1}{\Delta y\,\Delta z}\left(E^{sy}_{i,j+\frac{1}{2},k+1} - E^{sy}_{i,j+\frac{1}{2},k} - E^{sy}_{i,j-\frac{1}{2},k+1} + E^{sy}_{i,j-\frac{1}{2},k}\right)\\
&+ i\omega\mu\sigma_{i,j,k+\frac{1}{2}}E^{sz}_{i,j,k+\frac{1}{2}} = -i\omega\mu\left(\sigma_{i,j,k+\frac{1}{2}} - \sigma^{p}_{i,j,k+\frac{1}{2}}\right)E^{pz}_{i,j,k+\frac{1}{2}}.
\end{aligned}
\tag{22}
$$

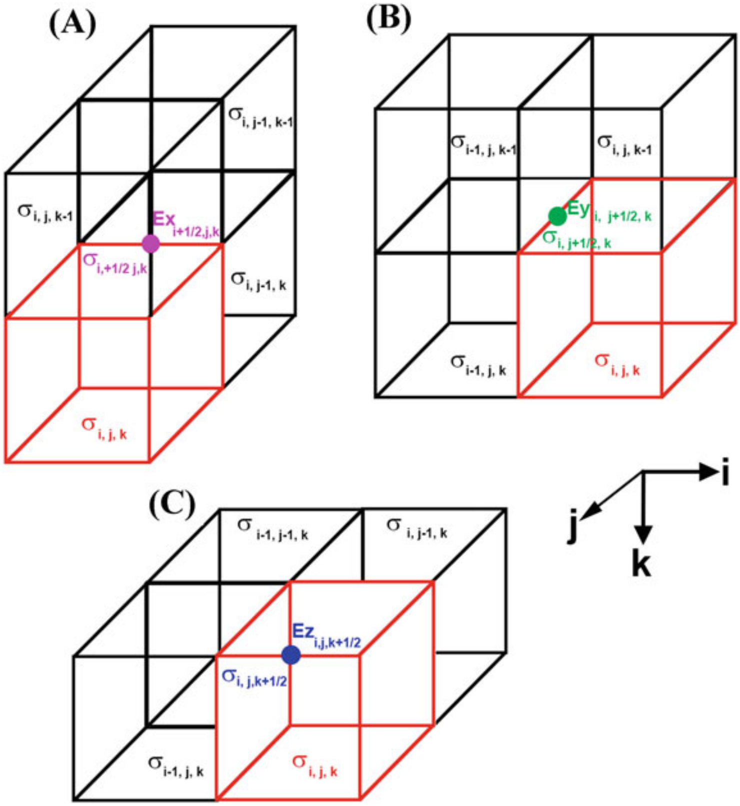

Fig. 17 Conductivity cells. (**a**) Conductivity associated to $E^{sx}_{i+\frac{1}{2},j,k}$, (**b**) Conductivity associated to $E^{sy}_{i,j+\frac{1}{2},k}$, and (**c**) Conductivity associated to $E^{sz}_{i,j,k+\frac{1}{2}}$

To compute conductivities at the edge of each cell, we use a conductivity average with four adjacent cells (see Fig. 17). In our approach, for a regular grid, the conductivity in $\sigma_{i+\frac{1}{2},j,k}$ is defined by

$$\sigma_{i+\frac{1}{2},j,k} = \frac{\sigma_{i,j,k} + \sigma_{i,j-1,k} + \sigma_{i,j,k-1} + \sigma_{i,j-1,k-1}}{4}, \tag{23}$$

in $\sigma_{i,j+\frac{1}{2},k}$ we have

$$\sigma_{i,j+\frac{1}{2},k} = \frac{\sigma_{i,j,k} + \sigma_{i-1,j,k} + \sigma_{i,j,k-1} + \sigma_{i-1,j,k-1}}{4}, \tag{24}$$

and $\sigma_{i,j,k+\frac{1}{2}}$ is defined as

$$\sigma_{i,j,k+\frac{1}{2}} = \frac{\sigma_{i,j,k} + \sigma_{i-1,j,k} + \sigma_{i,j-1,k} + \sigma_{i-1,j-1,k}}{4}. \tag{25}$$

In this approach we have used homogeneous Dirichlet boundary conditions [13, 21], where the electric field is equal to zero at the boundaries (Eq. (10)). Other authors have used Neumann boundary conditions [21], where the first derivative of the tangential electric field is equal to zero at the boundaries, then on the boundaries we could use a backward scheme.

Appendix 2

Faraday's law in differential form is given by

$$H_{sx} = -\frac{1}{i\omega\mu}\left(\frac{\partial E_{sz}}{\partial y} - \frac{\partial E_{sy}}{\partial z}\right), \tag{26}$$

$$H_{sy} = -\frac{1}{i\omega\mu}\left(\frac{\partial E_{sx}}{\partial z} - \frac{\partial E_{sz}}{\partial x}\right) \tag{27}$$

and

$$H_{sz} = -\frac{1}{i\omega\mu}\left(\frac{\partial E_{sy}}{\partial x} - \frac{\partial E_{sx}}{\partial y}\right). \tag{28}$$

These equations are discretized with a staggered grid central finite differences. The magnetic field is located at face's cells (see Fig. 1) so, we obtain:

$$H^{sx}_{i,j+\frac{1}{2},k+\frac{1}{2}} = -\frac{1}{i\omega\mu}\left(\frac{E^{sz}_{i,j+1,k+\frac{1}{2}} - E^{sz}_{i,j,k+\frac{1}{2}}}{\Delta x} - \frac{E^{sy}_{i,j+\frac{1}{2},k+1} - E^{sy}_{i,j+\frac{1}{2},k}}{\Delta z}\right), \tag{29}$$

$$H^{sy}_{i+\frac{1}{2},j,k+\frac{1}{2}} = -\frac{1}{i\omega\mu}\left(\frac{E^{sx}_{i+\frac{1}{2},j,k+1} - E^{sx}_{i+\frac{1}{2},j,k}}{\Delta z} - \frac{E^{sz}_{i+1,j,k+\frac{1}{2}} - E^{sz}_{i,j,k+\frac{1}{2}}}{\Delta x}\right) \tag{30}$$

and

$$H^{sz}_{i+\frac{1}{2},j+\frac{1}{2},k} = -\frac{1}{i\omega\mu}\left(\frac{E^{sy}_{i+1,j+\frac{1}{2},k} - E^{sy}_{i,j+\frac{1}{2},k}}{\Delta x} - \frac{E^{sx}_{i+\frac{1}{2},j+1,k} - E^{sx}_{i+\frac{1}{2},j,k}}{\Delta y}\right). \tag{31}$$

With this formulation we obtain a second-order accuracy scheme as a consequence of the centered finite-differences stencil used to compute the magnetic field.

References

1. W. Anderson, Numerical integration of related Hankel transforms of order 0 and 1 by adaptive digital filtering. Geophysics **44**(7), 1287–1305 (1979). https://doi.org/10.1190/1.1441007
2. D. Avdeev, A. Kuvshinov, O. Pankratov, G. Newman, Three-dimensional induction logging problems, Part I: An integral equation solution and model comparisons. Geophysics **67**(2), 413–426 (2002). https://doi.org/10.1190/1.1468601
3. E. Boateng, V. Sarpong, S. Danuour, Detection and delineation of contaminant migration using the terrain conductivity technique outside the perimeters of the Dompoase Landfill Facility in Kumasi-Ghana. J. Environ. Earth Sci. **3**(2), 13–24 (2013)
4. J. Callegary, T. Ferré, R. Groom, Vertical spatial sensitivity and exploration depth of low-induction-number electromagnetic-induction instruments. Vadose Zone J. **6**, 158–167 (2007). https://doi.org/10.2136/vzj2006.0120
5. P. Gauzellino, F. Zyserman, J. Santos, Nonconforming finite element methods for the three-dimensional Helmholtz equation: Iterative domain decomposition or global solution? J. Comput. Acoust. **17**(2), 159–173 (2009). https://doi.org/10.1142/S0218396X09003902
6. E. Haber, U. Ascher, Fast finite volume simulation of 3D Electromagnetic problems with highly discontinuous coefficients. SIAM J. Sci. Comput. **22**(6), 1943–1961 (2001). https://doi.org/10.1137/S1064827599360741
7. H. Jahandari, S. MacLachlan, R. Haynes, N. Madden, Finite element modelling of geophysical electromagnetic data with goal-oriented hr-adaptivity. Comput. Geosci. **24**, 1257–1283 (2020). https://doi.org/10.1007/s10596-020-09944-7
8. P. Jaysaval, D. Shantsev, S. de la Kethulle de Ryhove, Efficient 3-D controlled-source electromagnetic modelling using an exponential finite-difference method. Geophys. J. Int. **203**(3), 1541–1574 (2015). https://doi.org/10.1093/gji/ggv377
9. D. McNeill, *Electromagnetic Terrain Conductivity Measurements at Low Induction Numbers*. GEONICS LIMITED NT-6 (1980)
10. D. McNeill, *EM34-3 Survey Interpretation Techniques*. GEONICS LIMITED NT-8 (1983)
11. S. Méndez-Delgado, E. Gómez-Treviño, M. Pérez-Flores, Forward modelling of direct current and low-frequency electromagnetic fields using integral equations. Geophys. J. Int. **137**(2), 336–352 (1999). https://doi.org/10.1046/j.1365-246X.1999.00826.x
12. Y. Mitsuhata, 2-D electromagnetic modeling by finite-element method with a dipole source and topography. Geophysics **65**(2), 465–475 (2000). https://doi.org/10.1190/1.1444740
13. G. Newman, D. Alumbaugh, Frequency-domain modelling of airborne electromagnetic responses using staggered finite differences. Geophys. Prospect. **43**, 1021–1042 (1995). https://doi.org/10.1111/j.1365-2478.1995.tb00294.x
14. M. Pérez-Flores, R. Antonio-Carpio, E. Gómez-Treviño, I. Ferguson, S. Méndez-Delgado, Imaging of 3D electromagnetic data at low-induction numbers. Geophysics **77**(4), 47–57 (2012). https://doi.org/10.1190/geo2011-0368.1

15. M. Pérez-Flores, L. Ochoa-Tinajero, A. Villela, Three-dimensional inverse modeling of EMLIN data for the exploration of coastal sinkholes in Quintana Roo, Mexico. Nat. Hazards Earth Syst. Sci. **19**, 1779–1787 (2019). https://doi.org/10.5194/nhess-19-1779-2019
16. A. Sarris, T. Kalayci, I. Moffat, M. Manataki, An introduction to geophysical and geochemical methods in digital geoarchaeology, in *Digital Geoarchaeology: New Techniques for Interdisciplinary Human-Environmental Research*, ed. by C. Siart, M. Forbriger, O. Bubenzer (Springer International Publishing, Berlin, 2018), pp. 215–236. https://doi.org/10.1007/978-3-319-25316-914
17. Y. Sasaki, Full 3-D inversion of electromagnetic data on PC. J. Appl. Geophys. **46**, 45–54 (2001). https://doi.org/10.1016/S0926-9851(00)00038-0
18. Y. Sasaki, M.A. Meju, A multidimensional horizontal-loop controlled source electromagnetic inversion method and its use to characterize heterogeneity in aquiferous fractured crystalline rocks. Geophys. J. Int. **166**, 59–66 (2006). https://doi.org/10.1111/j.1365-246X.2006.02957.x
19. B. Scanlon, J. Paine, R. Goldsmith, Evaluation of electromagnetic induction as a reconnaissance technique to characterize unsaturated flow in a arid setting. Archaeometry **12**(1), 97–104 (1970). https://doi.org/10.1111/j.1475-4754.1970.tb00010.x
20. A. Selepeng, S. Sakanaka, T. Nishitani, 3D numerical modelling of negative apparent conductivity anomalies in loop-loop electromagnetic measurements: a case study at a dacite intrusion in Sugisawa, Akita Prefecture, Japan. Exp. Geophys. **48**(3), 177–191 (2018). https://doi.org/10.1071/EG16027
21. R. Streich, 3D finite-difference frequency-domain modeling of controlled-source electromagnetic data: direct solution and optimization for high accuracy. Geophysics **74**(5), F95–F105 (2009). https://doi.org/10.1190/1.3196241
22. K. Sudduth, N. Kitchen, B. Myers, S. Drummond, Mapping depth to argillic soil horizons using apparent electrical conductivity. J. Environ. Eng. Geophys. **13**(3), 135–146 (2010). https://doi.org/10.2113/JEEG15.3.135
23. A. Tabbagh, Applications and advantages of the Slingram electromagnetic method for archaeological prospecting. Geophysics **51**(3), 576–584 (1986). https://doi.org/10.1190/1.1442112
24. J. Wait, A note on the electromagnetic response of a stratified earth. Geophysics **27**(3), 382–385 (1962). https://doi.org/10.1190/1.1439028
25. S. Ward, G. Hohmann, in *Electromagnetic Theory for Geophysical Applications*, ed. by M. Nabighian. Electromagnetic Methods in Applied Geophysics, vol. I (Society of Exploration Geophysicists, Houston, 1987), pp. 113–312. https://doi.org/10.1190/1.9781560802631.ch4
26. C. Weiss, S. Constable, Mapping thin resistors and hydrocarbons with marine EM methods, Part II-Modeling and analysis in 3D. Geophysics **71**(6), G321–G332 (2006). https://doi.org/10.1190/1.2356908
27. K. Yee, Numerical solution of initial boundary value problems involving Maxwell's equations in isotropic media. IEEE Trans. Antennas Propag. 302–307 (1966). https://doi.org/10.1109/TAP.1966.1138693